Experimental and Observational Studies of Molecular Hydrogen in Interstellar and Circumstellar Environments

by

Keri Hoadley

B.S., Florida Institute of Technology, 2011

A thesis submitted to the

Faculty of the Graduate School of the

University of Colorado in partial fulfillment

of the requirements for the degree of

Doctor of Philosophy

Department of Astrophysical & Planetary Sciences

2017

This thesis entitled:
Experimental and Observational Studies of Molecular Hydrogen in Interstellar and Circumstellar Environments
written by Keri Hoadley
has been approved for the Department of Astrophysical & Planetary Sciences

Prof. Kevin France

Prof. James Green

Prof. Phil Armitage

Prof. Ann-Marie Madigan

Prof. Veronica Bierbaum

Date

The final copy of this thesis has been examined by the signatories, and we find that both the content and the form meet acceptable presentation standards of scholarly work in the above mentioned discipline.

Hoadley, Keri (Ph.D., Astrophysics)

Experimental and Observational Studies of Molecular Hydrogen in Interstellar and Circumstellar Environments

Thesis directed by Prof. Kevin France

Understanding the evolution of gas over the lifetime of protoplanetary disks provides us with important clues about how planet formation mechanisms drive the diversity of exoplanetary systems observed to date. In my thesis, I discuss how I observe warm molecular hydrogen (H_2) in the far-ultraviolet (far-UV) with the Hubble Space Telescope to study the innermost regions (a $<$ 10 AU) of planet-forming disks. I have created analytic disk models, which produce synthetic H_2 emission profiles and compare each disk realization with the data. The modeled radial distributions of H_2 help provide important constraints on the radiation properties of gas left in the inner disk of protoplanetary disks as they evolve. Additionally, I analyzed the absorption component of these fluorescence features, embedded within the hydrogen Lyman-α emission profile of the host protostar. I present column density and temperature estimates for the H_2 populations in each disk sightline, and discuss the behavior and possible spatial origins of these hot molecules.

I also address observational requirements needed to gain further insights into the behavior of the gaseous protoplanetary disk, focusing on a testbed instrument, the Colorado High-resolution Echelle Stellar Spectrograph (CHESS), built as a demonstration of one component of the LUVOIR spectrograph and new technological improvements to UV optical components for the next generation of near- to far-UV astrophysical observatories. CHESS is a far-UV sounding rocket experiment designed to probe the warm and cool gas around sites of recent star formation in the local interstellar medium. I present the science goals, design, research and development components, and calibration of the CHESS instrument. I provide a detailed analysis of the ϵ Per sightline, as inferred from the CHESS-2 flight data. I conclude by discussing future work and estimates on the performance of a CHESS-like instrument on LUVOIR when studying planet-forming disks.

Dedication

For my Mom, my Dad, and my sister Kelly: you provided me with the love and support I needed to pursue my dreams. This accomplishment is as much yours and it is mine.

For my Pepere and Memere, who were an endless source of wisdom and motivation. You truly believed I could be anything if I put my effort into it, and now I know you were completely correct. I wish you were both here to celebrate with me; I miss you everyday.

To my husband, Charles: Even in my darkest hours, you kept me grounded and held me up high; when everything seemed bleak, you always presented a positive perspective; you remind me that my increasing number of white hairs are just my super hero powers breaking through! I can never repay the moral support you have always provided, which has guided me steadily through both my work and our life. <3

Acknowledgements

All of the hard work required to create this thesis would have never been possible without the love, support, and guidance from my wonderful family, friends, and colleagues. First and foremost, I owe unending gratitude towards my Mom and Dad, who never quite understood why their 10-year-old wanted to wear lab coats and study the night sky, but nevertheless encouraged my curiosity and supported me in my pursuit towards a scientific career. My little sister, Kelly, I want to thank for giving me a reason to think of my actions and their impact on your growth; while I didn't always enjoy being a role model, it has kept me motivated to follow my dreams in the face of temptation to step off this path. My grandparents, particularly my Pepere and Memere, who loved me unconditionally and were convinced that, no matter what I did, I would leave a significant impact on the world. And all my new family - my in-laws and step parents - for providing unconditional love and support through this whole process. Finally, my husband, Charles, who left his comfort zone to move with me and allow me to pursue my dreams. I can never repay your love, support, and willingness to follow me through everything and anything.

For all my friends, old and new: Thank you for providing me the necessary outlet for stress and relaxation at times I needed it most. Aleida and Paul (and Toothless) - from the very beginning of this journey to grad school, you were both a huge support system during the entire process. All my new friends in graduate school - Katy, Chris, Matt, Allison, Eric, Eddy, Jen, and many many others - going through this experience with you made it much more enjoyable, and I will always cherish our time together.

My colleagues, who challenged me in ways I never expected and made me realize I can some-

how survive even the toughest of trials. Thank you to the wonderful support teams of NSROC, NMSU, and WSMR staff and military for providing the support that saw my sounding rocket experiments through two incredibly successful launches. The researchers, staff, and undergraduates who worked with me closely through my 6 years at ARL - Bobby and Nico, Micheal ("Jackson"/"Jamal"/"Lone Ranger"/etc) Kaiser, Ted, and Brian - thank you for overloading me with information on a daily basis and helping me to appreciate that even the smallest details matter. I'll never forget your patience as I slowly learned the intricate science of sounding rockets, and you all earn my unending gratitude. And all the students I've had the honor and privilege of helping to shape your education - Jack, Jacob, Eliot, and Nick K., Nick E., Nicole - thank you for challenging me and constantly making me doubt what I think I know. The constant pursuit of knowledge and truth is the correct path forward, and thank you for reminding me that I am still learning, too.

Finally, these acknowledgments would not be complete without offering my eternal gratitude to my research advisor, Kevin France, and my honorary advisor, Jim Green. Jim: You have offered me many hours of advice and knowledge through the sounding rocket program and astrophysics in general; thank you so much for taking time to teach me so much in your down time! Kevin: It baffles me when I think about how much faith you chose to put in me, above any others, to take on such a challenging research path. Your patience and tolerance as I stumbled through my projects, whether they were in the lab or in data analysis, are truly remarkable. I truly appreciate all of the precious time you have taken to teach me how to be an incredible scientist. Your shoes are going to be very difficult to fill, but I hope that, one day, you will be pleased with the scientist you shaped to be a productive member of the community.

Contents

Chapter

Tables

Table

Figures

Figure

Chapter 1

Introduction

"It's a turtle. It doesn't know the difference between you or a robot. It's not a dog. It don't love you."

- Larry Conser, lamenting that his son wanted a turtle for his birthday.

Since the Big Bang and the first coagulation of materials into dense structures, stars have played a critical role in the energy transport and nucleosynthetic evolution of the observable universe. The first generations of stars (Population III) likely formed from the primordial, warm baryonic matter produced by the Big Bang - made primarily of hydrogen (75%) and helium (∼25%) - making them massive, hot, and short-lived. Population III stars allowed for the synthesis of hydrogen and helium into heavier elements (metals), such as carbon, oxygen, silicon, and iron. Metallic elements are important for helping to regulate heat transport through the intervening medium by effectively cooling surrounding material with the release of low-energy radiation (far-infrared and longer wavelengths). This cooling also allows for the formation of lower-mass, longer-lived stellar populations, which we observe in abundance at the present epoch of the universe.

One of the greatest scientific challenges - the Epoch of Reionization (EoR) - includes hypotheses which rely upon stellar populations to regulate the output of ionizing radiation from their galactic hosts[1] . At the present epoch, stars make up the majority of baryonic matter found in galaxies. They regulate the energy exchange through galaxies via irradiation, winds, and evo-

[1] The Epoch of Reionization defines when and how, during the history of the universe, the pervasive populations of hydrogen in intergalactic space transitioned from a predominantly neutral phase (H I) to a completely ionized medium (H II). Observationally, we measure the end of the EoR at a redshift (z) $\approx$ 7 (e.g., Bolton and Haehnelt 2007, Clément et al. 2012).

lutionary processes. At the end of their lifetimes, stars replenish their surrounding media with nucleosynthetic materials and help trigger new bouts of star formation. Each phase of star formation shapes the media between stars in galaxies and defines the initial conditions of raw materials that form the next generations of stars and stellar systems. However, some star-formation processes remain observationally elusive.

During the last stages of star formation, remnant interstellar material gravitationally bound to the stellar object can form into a dense disk of matter rotating around the growing object. It is in this dense disk of dust and gas that planets are thought to form. However, during most of the planet-formation phase, optically thick dust and gas shroud the environment, preventing observers from directly probing how small dust grains grow into large planetary bodies. Over the last 25 years, we have discovered that extrasolar systems are not uncommon (Figure 1.1; NASA Exoplanet Archive). However, as the statistical parameter space of planetary properties grows with each new exoplanet discovered, our models of planet formation are continually being challenged. Exoplanets and extrasolar systems come in more varieties than originally thought possible. In fact, solar system-analogues remain elusive (though, presently, this may be an observational bias). The most common type of planet observed thus far has no analog in our solar system; so-called "Super Earths", they are larger than Earth but smaller than Neptune. Additionally, extrasolar systems with these "Super Earths" are typically found with multiples of them in compact, nearly circular orbits very close to their host star. As larger telescopes and better instruments come online in the next generations of astrophysical research (like *TESS*, *JWST*, and many others), the database of exoplanetary systems and properties will continue to fill in the gaps of unobserved, exoplanetary parameter space, and understanding how these planetary systems form and evolve will be crucial for inferring conditions favorable for life to thrive.

While stars may contain the bulk of the baryonic mass in galaxies at the present epoch of the universe, it is estimated that the average number of planets each star in the Milky Way hosts is $\sim$2, making planetary bodies more numerous throughout the Milky Way galaxy than even stars. Despite their differences, both astrophysical objects must draw their mass, compositions, and final

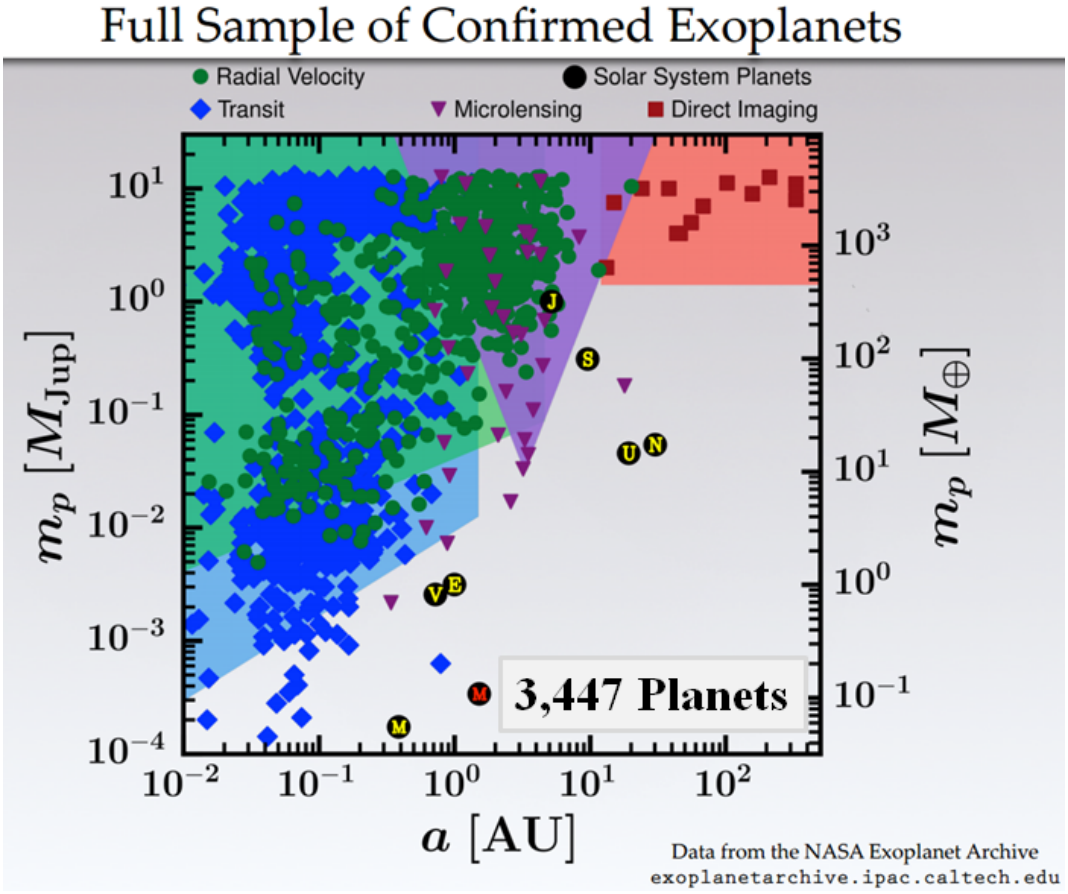

Figure 1.1 The full sample of confirmed exoplanets, as of February 2017. There are almost 3,500 confirmed exoplanets to date. The exoplanetary parameters are plotted as functions of planetary mass (M_{Jup} and $M_\oplus$) and semi-major axis from their host star (a). Each colored point represents the detection method of the original discovery of the planet (for confirmation, follow-up detection is required with an independent measurement with either the same detection method or a different technique). The colored regions show the parameter space that each detection method probes. Currently, technological development is needed on all fronts to expand the parameter space for exoplanetary detection. The solar system planets are included, with the first letters of their names used to point out the planets. Exoplanetary systems cover a large range of architectures that were not expected. Understanding how such systems can exist has shaped the field of planetary formation. (credit: *NASA Exoplanet Archive*)

properties from the same initial reservoir of material - the interstellar medium (ISM).

1.1 The Interstellar Medium

The ISM is the gas and dust in a galaxy that exist between stars and provides the raw materials that form the next generations of stars and planets. It is estimated that, at the present epoch, the ISM makes up as much as 10% of the baryonic mass found in the Milky Way (Draine 2011). The ISM of the Milky Way is comprised of 90% hydrogen, ∼9% helium, and the rest is made up of metals (i.e. any element heavier than helium). An understanding of the history of interstellar materials also provides clues to the nucleosynthetic production of metals, through stellar life and death cycles, which were not present at the start of the universe. Despite ongoing processing of Big Bang matter into heavier elements through stellar recycling, hydrogen remains the primary constituent of interstellar gas and is found in neutral (H I), ionized (H II), and molecular (H_2) forms. While it is still unknown exactly how Population III stars formed near the beginning of the universe, one hypothesis suggests that the formation of molecular hydrogen helped cool the hot, primordial materials to below a few tens of thousands of Kelvin, which provided the conditions which allowed the formation of the first stars (Palla et al. 1983, Flower and Harris 2007).

The ISM is not homogeneous. The gas in the ISM is found with different temperature, ionization, and density structures, all of which depend heavily on the evolution of the ISM through the galactic record (e.g., Linsky and Wood 1996, Linsky et al. 2000, Redfield and Linsky 2002; 2004; 2008, Kimura et al. 2003, Lehner et al. 2003, Gudennavar et al. 2012). Diffuse phases of the ISM, known as the diffuse ISM or translucent clouds, have average temperatures of several tens of Kelvin to several hundred Kelvin and have appreciable column densities of neutral and molecular hydrogen ($N(H\ I + 2H_2) \lesssim 10^{22}$ cm^{-2}, Savage et al. 1977, Diplas and Savage 1994, Rachford et al. 2009). Denser ISM phases results in cooler material (T ∼ 10 - 50 K), known as giant molecular clouds (GMCs). It is in these cool, dense clouds that star formation occurs (Shukurov et al. 2004, Martínez-García et al. 2009, Eden et al. 2015, Schinnerer et al. 2017). While the material from the ISM forms stars, stars in turn regulate several phases of the ISM. Hot, short-lived, massive (M

Figure 1.2 The Lobster Nebula, known formally as NGC 6357, located in the Scorpius constellation, is a site of some of the most massive stars known in the universe. The red glow shows emission from H II regions in the form of Hα emission, and blue spheres and glow show blue reflection nebulae being illuminated by massive young stars. Dark lanes make dense GMCs of cool, molecular gas and dust, which are potential sites of future star formation. Stellar winds shape the structure of the boundary between the hot, ionized medium and the cool, denser molecular boundaries to the GMCs, and may help trigger a new round of star formation. (credit: *NASA-APOD; ESO, VLT*)

$\geq 8M_{\odot}$) stars actively ionize and heat the surrounding ISM with their intense ultraviolet (UV) radiation and stellar winds. These phases of the ISM are known as H II regions, where hydrogen is predominantly found in its ionized form (T(H II regions) $\sim 10^4$ K). The interface between H II regions and translucent clouds are known as H I regions, where a layer of neutral hydrogen protects the molecular hydrogen in translucent materials from ionizing radiation (T(H I regions) $\sim$ 100 - 5000 K). There are ISM regions where recent star formation has produced lower-mass stars, which do not significantly output ionizing radiation. Instead, the shorter wavelength light produced by these stars scatters off of dust grains in the intervening ISM. These regions are know as reflection nebulae. All these different phases of the ISM can be viewed in regions of active star formation, such as the Lobster Nebula (Figure 1.2), and are important to understand the initial conditions of star formation, including the materials that go into forming stars and the processes that allow star formation to happen.

1.2 How Stars Form

As stated above, star formation happens in GMCs. This phase of the ISM is cool (T $\sim$ 10 K) and dense ($n_H \gtrsim 10^3$ cm^{-3}), allowing gas and dust to condense into clumps and dense cores (Solomon et al. 1987). Molecular clouds cool by radiative cooling, meaning that dust, molecules, and far-IR fine structure line cooling from metals radiate energy out of the system.

Dust is made primarily of heavier, reprocessed stellar elements - carbon and silicon - which can build into large ($\sim \mu$m diameter) chains of complex molecules, or grains (Pagani et al. 2010). The physical size of dust grains regulates the scattering properties of the the dust ($\sigma_d \propto a^2$, for $\lambda < a$). Radiation with wavelengths less than the size of a typical dust grain are more likely to be scattered, which is observed in systems like blue reflection nebulae (Figure 1.2). Additionally, the large densities of dust and H I scatter photo-dissociating radiation away from the bulk of the molecular cloud, making GMCs optically thick to UV radiation that can dissociate H_2 (Speck et al. 2002, Meixner et al. 2005).

Dust also provides a site for hydrogen atoms to meet and a sink for the binding energy of the

reaction to allow H_2 to detach from the dust grain (Hollenbach and Salpeter 1969). Dust grains, being many orders of magnitude larger than individual hydrogen atoms, give hydrogen a site to gather many atoms, which "stick" to the cold dust grain once attached because each individual atom does not have the energy required to detach from the cold dust. Atomic hydrogen preferentially wants to form a bond with another hydrogen atom, because in the molecular form, both protons of hydrogen fill their 1s shells with two electrons. The formation of H_2 is an exothermic reaction ($E_{bind} \approx 4.5$ eV), which heats the dust formation site and liberates the molecule from the grain (Cazaux and Tielens 2004). At the present epoch, the primary formation sites of H_2 are dust grains, which have a higher probability for molecular formation than hydrogen atoms bonding via collisional processes in the ISM, in either two- or three-body collisions (e.g., Palla et al. 1983, Flower and Harris 2007, Hollenbach and Tielens 1997, Fleming et al. 2010).

GMCs typically appear clumpy with dense, dark cloud complexes, and within these complexes, warm regions can be probed in the infrared. These warm regions (known as hot cores; Figure 1.3) are thought to point to the first observable signs of star formation in action, where the energy released during the initial collapse of material into a pre-stellar object heats the surrounding dust. However, the initial stages in the star-forming process, from GMC to hot cores, are difficult to observe, both being obscured by dense columns of dust and occurring over short astrophysical timescales. Instead, the physical processes involved in star formation are inferred from the physics of gravitational collapse. The simplest models of star formation require that the mass encapsulated in a given volume must surmount a critical limit, known as the Jeans mass, for gravitational collapse to overcome the collisional pressure of the gas[2] (Jeans 1902). Once gravitational collapse begins, the potential energy of the in-falling matter is released and escapes from the system while the material gathering in the core of the collapse is optically-thin to the radiation. This radiation heats the surrounding dust grains, which radiate the energy away from the system. This efficiently

[2] In reality, the simplest model assumptions do not take into account important physical mechanisms expected to play a key role in cloud collapse and star formation, particularly external pressure mechanisms. External pressure mechanisms can include density deviations introduced along the spiral arm structures of spiral galaxies, pressure waves induced by supernovae explosions, cloud rotation, turbulence, magnetic fields, and feedback from active galactic nuclei (AGN) (e.g., Dale et al. 2012, Maruta et al. 2010, Bieri et al. 2015).

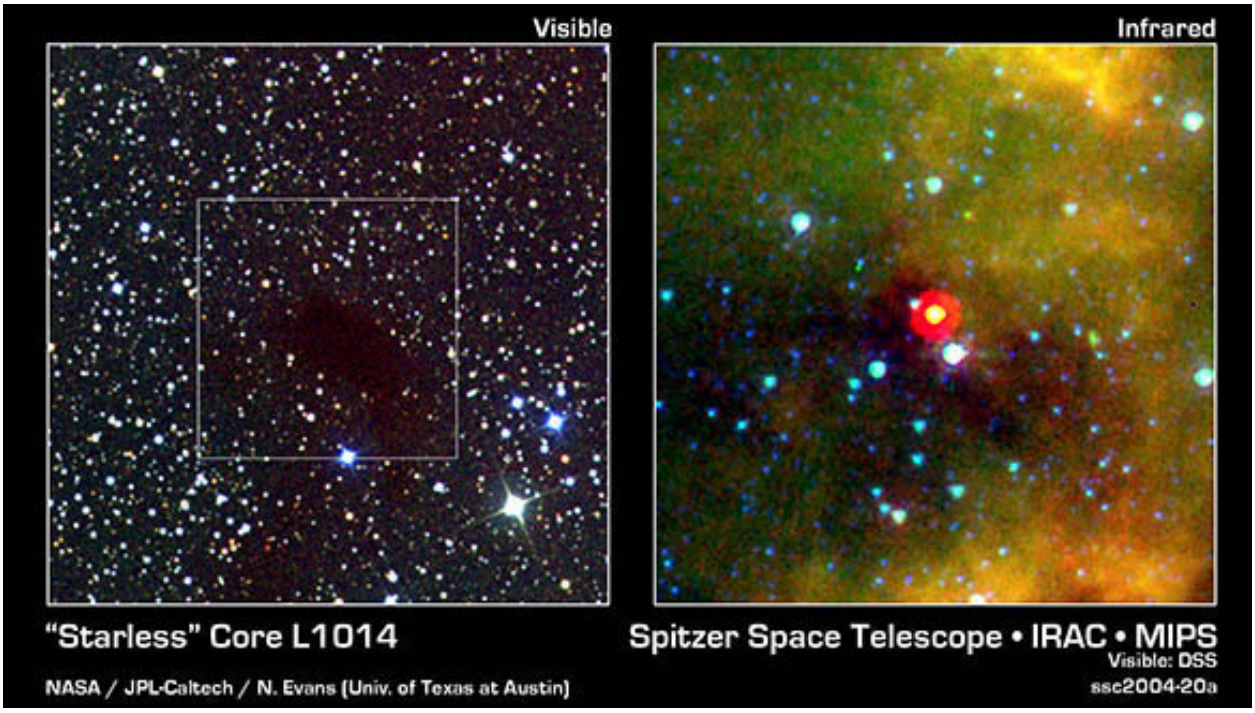

Figure 1.3 Images of the GMC L1014 in Cygnus, taken at visible wavelengths (*left*) and in the infrared (*right*), at 3.6 μm (blue), 8.0 μm (green), and 24.0 μm (red). Dust blocks the view of forming stars in the visible bandpass, but the thermal emission from forming, pre-stellar cores embedded in the dense clouds glows in the infrared. (credit: *NASA, JPL, Caltech, UT Austin*)

allows the energy from gravitational collapse to leave the system, enabling more material to collapse into a core (Penston 1967, Bodenheimer and Sweigart 1968, Larson 1969).

Once the core becomes dense enough to no longer allow radiation to escape efficiently, the object begins to increase in temperature (Gaustad 1963, Hayashi 1965; 1966, Larson 1969). This slows the process of gravitational collapse, as the gravitational force of collapse begins to match the collisional force of the warm material in the object (i.e., hydrostatic equilibrium; Larson 1969). Material from the dense, collapsing cloud is still falling onto the object, which is thought to accrete onto the core and create shock regions, which further heat the object and the surrounding medium (Larson 1969). The temperature of the pre-stellar object is expected to increase quickly at this point. At T $\sim$ 1000 K, the dust sublimation temperature is reached, which evaporates dust in the object and loses an important cooling agent in the star-formation process (Reif 1965, Kelley 1973). Once dust sublimates from the system, molecular and fine-structure metallic line emission (for example, [CII] 158μm, [OI] 63μm, [SiII] 35μm, and [OI] 6300Å) remain as dominant cooling mechanisms for the pre-stellar object. Therefore, molecules and metals help keep the core in hydrostatic equilibrium while material continues to accrete onto the outer photosphere of the core. However, as temperatures in the pre-stellar core continue to rise, molecules sensitive to temperature, like CO and H_2, begin to photo-dissociate, and the opacity provided by these molecules to prevent further gravitation collapse by balancing with the internal radiation pressure is lost (Larson 1969, Kwan et al. 1977, Alexander et al. 1983). The pre-stellar core is expected to undergo a second free-fall collapse, where the object collapses down to what is known as a protostar (Larson 1969). The density and temperature provide the correct conditions for convection to begin in the core. Convection allows the interior of the star to radiatively cool and initiate further stellar contraction (Hayashi 1966). The protostar continues to increase in temperature until hydrostatic equilibrium is once again achieved (Gaustad 1963, Hayashi 1966, Larson 1969, Salaris and Cassisi 2005).

During the entire process of star formation, from the initial collapse to the convective protostar, the pre-stellar object gains angular momentum as material is added to the dense core. Initially, this results in an increase in rotational velocity of the object, but through the star-forming phases,

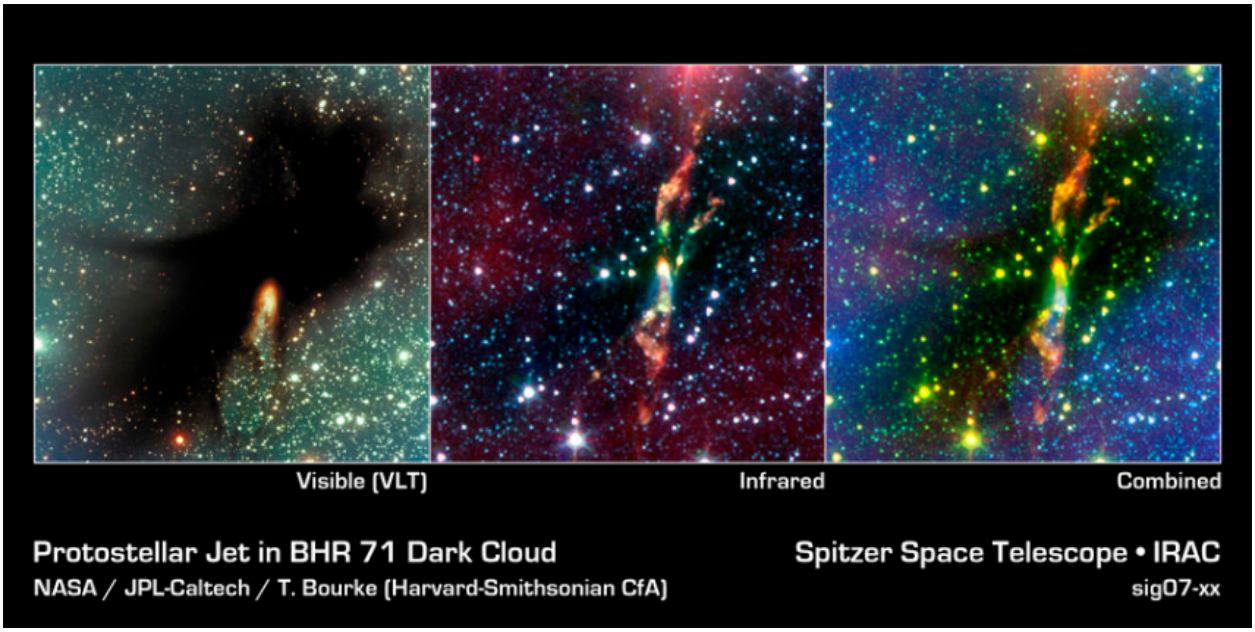

Figure 1.4 Images of the BHR 71 Dark Cloud Complex in the constellation Musca, taken at visible wavelengths (*left*) and in the infrared (*center*) at 3.6 μm (blue), 8.0 μm (green), and 24.0 μm (red). A combined image is shown on the *right*. The hot, collimated jets produced at the poles of the forming protostar heat the surrounding medium, which emits radiation in the infrared. Bi-polar jets are one of several physical mechanisms that allow protostars to eject angular momentum from the system and clear the region of the remaining envelope around the protostar. (credit: *NASA, JPL, Caltech, Harvard-Smithsonian CfA*)

gravitationally-bound cloud material gathers preferentially along the spin-axis of the protostar to help the accreting object shed excess angular momentum (e.g., Norman et al. 1980, Larson 1983). Further accretion of cloud material onto the protostar means more angular momentum added to the object, which, towards the end of the second gravitational-collapse phase, is diminished via rotationally-driven winds/turbulence (e.g., Hartmann and MacGregor 1982, Salmeron et al. 2007) and/or magnetic braking and collimated jets (e.g., Mouschovias 1979, Joos et al. 2012; Figure 1.4). These mechanisms not only help the star shed excess angular momentum, but clear the remaining cloud envelope around the protostar. What remains is the gravitationally-bound disk of material around the rotational axis of the protostar. This is the material from which planetary systems are thought to form (Lynden-Bell and Pringle 1974 and references therein).

1.3 How Planets Form

The initial stages of star formation are expected to last $t_{form} \sim 0.1$ - 1 Myr. After this, the protostellar system consists of a central protostar and a thick, dusty disk of material which orbits along the protostellar rotation axis. This disk of material is known as the *protoplanetary disk*, and it sets the initial conditions - in terms of material abundances, compositions, and densities of gas and solids - for planet formation processes (Brown et al. 2009, Woitke et al. 2009a, Dullemond and Monnier 2010). There is a vast diversity of observed exoplanetary architectures (Figure 1.1), so understanding the initial conditions in protoplanetary disks and how they evolve to form planets is critical for explaining the statistical sample of observed planetary systems.

Planets form from the solids (dust) available in the protoplanetary disk. Even gas giant planets are thought to require solid planetary cores to allow the accretion of appreciable atmospheres (Mizuno et al. 1978, Pollack et al. 1996, Wuchterl et al. 2000). Unfortunately, observing planet-formation processes directly is difficult, given the optically-thick columns of dust and gas in planet-forming disks (Kominami and Ida 2002, Trilling et al. 2002, Armitage et al. 2003). Therefore, theorists have relied upon anticipated conditions in planet-forming regions of protoplanetary disks to explain how dust grains form into larger, solid bodies over the observed lifetimes of proto-

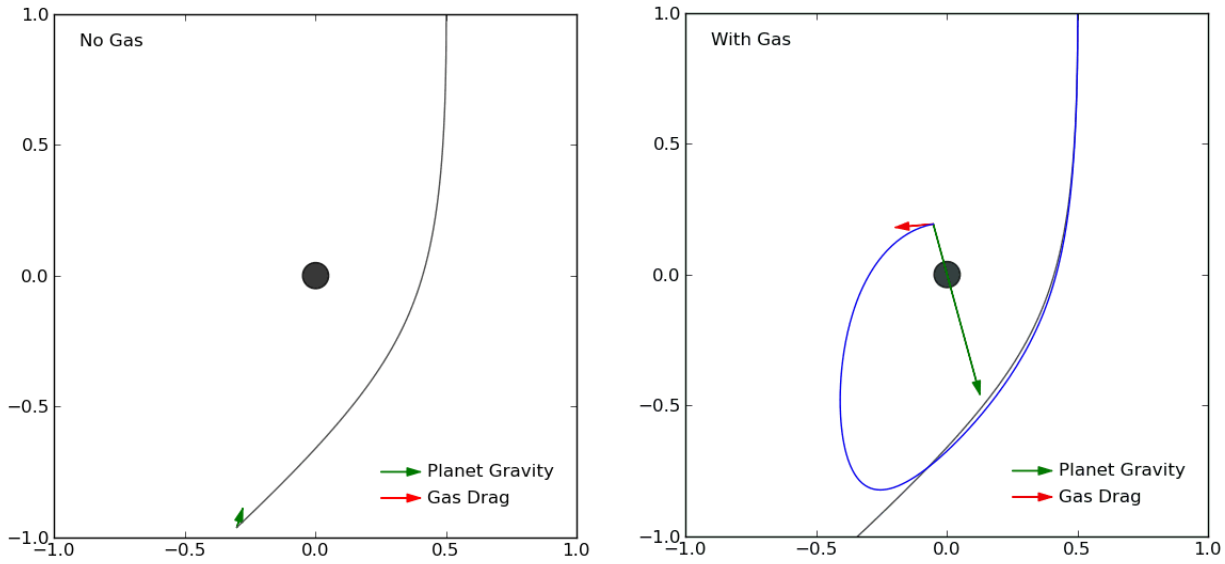

Figure 1.5 Simple simulation results showing how small pebbles in planet-forming disks are expected to react to the presence of larger planetary bodies with no gas (*left*) and with gas (*right*). The green arrow on the particle shows the force the pebble feels from the gravitational interaction with the larger planetary body, while the red arrow shows the force direction exerted on the pebble from gas drag. Without gas, pebbles can pass closely by larger bodies with only a small perturbation to their orbits. In the presence of gas drag, however, pebbles are decelerated, such that they eventually accumulate onto the larger body. Pebble accretion theory helps explain how both terrestrial and gas giant planets can gather most of their solid material in the first few Myr of planet formation. (credit: Bottke et al. 2010, Levison et al. 2015a;b).

planetary disks (1 - 10 Myr; Haisch et al. 2001).

Building dust into $\sim$ centimeter-sized particles is reproducible in astrophysical laboratory experiments, which have shown that dust can coagulate into larger grains as large as $\sim$ 5 cm in diameter with the presence of ices on grains (Weidenschilling and Cuzzi 1993, Dominik and Tielens 1997, Wurm and Blum 1998, Blum and Wurm 2000, Heißelmann et al. 2007). However, building solid bodies from centimeter-sized pebbles to kilometer-sized planetesimals has been a major challenge in planet formation models (Goldreich et al. 2004, Levison et al. 2010). Due to the size of the pebbles and the gas drag through the disk, centimeter- to meter-size rubble are expected to spiral into the protostar with radial drift timescales of the order of 100 years (Weidenschilling 1977, Takeuchi and Lin 2002, Takeuchi et al. 2005, Durisen et al. 2005, Rice et al. 2004), making the timescale required to build several kilometer-sized planetesimals shorter than the drift time of pebbles. Additionally, laboratory experiments find the aggregation threshold of icy pebbles to be of order several centimeters in diameter (Blum 2004, Blum et al. 2006), which means it is unlikely that pebbles continue to grow past several centimeters in diameter into planetesimals.

One method proposed for rapid accretion of smaller pebbles to larger objects is the pebble accretion hypothesis (Lambrechts and Johansen 2012), where centimeter- to meter-sized rubble are first concentrated by aerodynamic drag and gravitationally collapse to form kilometer-sized planetesimals (Cuzzi et al. 2001, Youdin and Goodman 2005, Youdin 2011, Johansen et al. 2007). Once this initial, large body it formed, it is expected to continue accreting pebbles, effectively clearing out the vicinity of the disk within its Roche limit (Bottke et al. 2010, Levison et al. 2015a). The pebble accretion method has demonstrated the creation of large planetary cores within only a few thousand years (Lambrechts and Johansen 2014, Kretke and Levison 2014), allowing ample time for these cores to accrete significant gas envelopes and build into gas giant planets. Pebble accretion models have even been used to successfully build Solar System-analog planetary architectures, including Mars and Mercury analogs, which are notoriously difficult to reproduce in standard planet-formation models (Levison et al. 2015a;b).

One of the key physical mechanisms of the pebble accretion method is aerodynamic drag,

which decelerates particles at a rate which would otherwise not be achieved without the presence of gas (as shown in Figure 1.5). Likewise, in almost all other planet formation scenarios (i.e., streaming instabilities, local pressure maxima, two-body collisions, turbulence, etc.), gas plays a key role in the formation of planetary systems. Therefore, the presence of gas in the protoplanetary disks plays a critical role in planet formation processes, from the build-up of large bodies to the accretion of primordial atmospheres of gas giants and, potentially, terrestrial planets.

1.4 The Role of Molecular Gas in Star and Planet Formation

For both star and planet formation processes, gas is expected to comprise the bulk of the mass in the system. In particular, molecules play a key role in regulating the thermal and chemical structure of the environments where star and planet formation occur (Hollenbach et al. 1971, Dalgarno and Roberge 1979, Lepp and Shull 1983). Studies have demonstrated significant correlations between the star formation rate and molecular gas surface density for almost any given observed star formation environment in galaxies (e.g., the Kennicutt-Schmidt law - Schmidt 1959, Kennicutt 1998), suggesting strongly that molecular gas is necessary for star formation to occur (Wong and Blitz 2002, Boissier et al. 2003, Schaye 2004, Krumholz and McKee 2005, Krumholz et al. 2009, Elmegreen 2007, Kennicutt et al. 2007, Bigiel et al. 2008, Schruba et al. 2011). This correlation naturally arises because cool environments are necessary for gravitational collapse to begin, which is regulated by dust, metal lines, and molecules, and molecules form in cool environments, where dissociating radiation typically cannot penetrate (Glover and Clark 2012a). Additionally, molecular hydrogen cooling plays an important role in enabling the formation of molecular clouds in the early (low metallicity) universe (Clark and Glover 2014, Glover and Clark 2014).

In protoplanetary disks, molecules play a crucial role in defining the abundances, chemistry, and density structure of gas from which proto-planets gather materials and evolve. Throughout the lifetime of protoplanetary disks, the gas component contains 99% of the disk mass and sets the initial conditions for planet formation. Additionally, the gaseous disk reservoir continues to

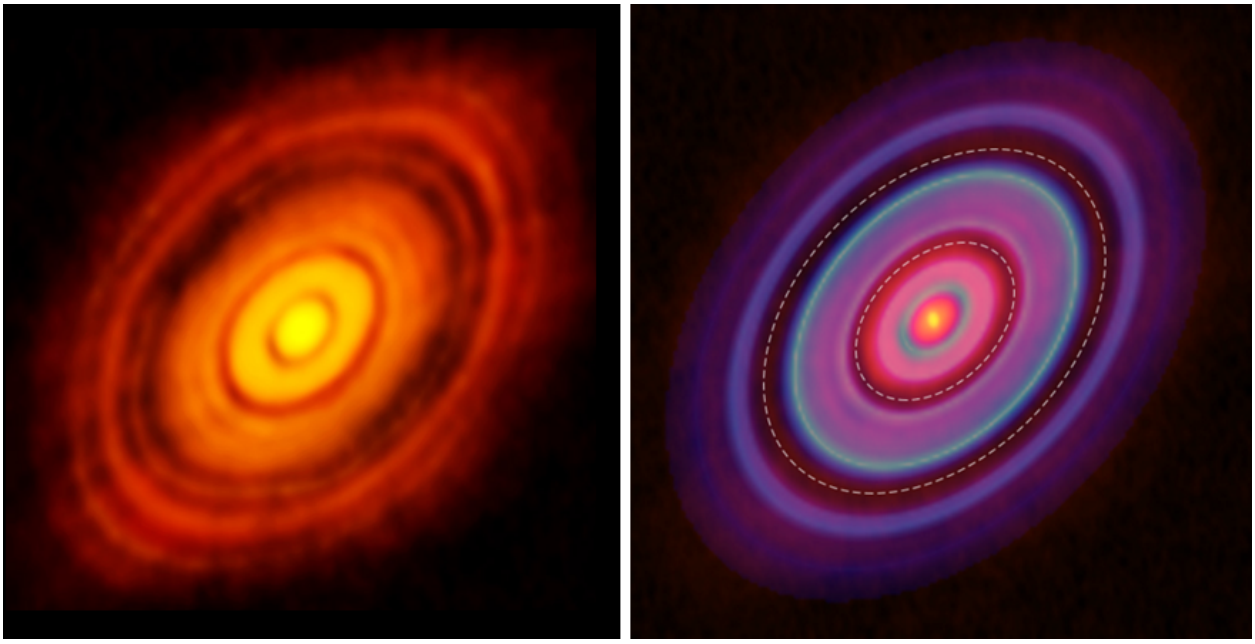

Figure 1.6 The protoplanetary disk around HL Tau, which has famously revealed the complex structure of cold, mm-sized dust by the ALMA observatory (*left*, orange). However, the dust disk does not disclose the full story happening in the planet-forming environment. When paired with the structure of gas (*right*, in blue (HCO+) with mm-sized dust in pink), it becomes apparent that all dust cavity sites may not indicate locations of planet formation. Rather, two main sites are pointed out, where large cavities of both dust and gas exist, that may point to the formation of two protoplanets (credit: ALMA/ESO/NAOJ/NRAO, ALMA Partnership 2015, Yen et al. 2016).

contribute to the final star-formation phases of the protostar by actively accreting material onto the stellar object (Muzerolle et al. 2000, Andrews and Williams 2007, Ingleby et al. 2013). This leads to a constantly evolving environment, both structurally and chemically, which sets important timescales and conditions for planetary systems to form and mature. However, most of the current knowledge about the structure and evolution of protoplanetary disks comes from observations of dust. Traditionally, the evolutionary state of planet-forming disks is determined by the depletion of warm, IR scattered light observed in a disk's broad-band spectral energy distribution (SED). The loss of near- to mid-IR dust is thought to indicate significant dust growth and/or settling in disks and may point to the presence of dust disk gaps and cavities, particularly at the innermost radii of the disk (Strom et al. 1989, Sato and Nakagawa 1999, Calvet et al. 2002; 2005, Tanaka et al. 2005, Espaillat et al. 2007a;b; 2014, Furlan et al. 2009).

It is becoming increasingly clear that the molecular disk plays a key role in understanding the evolution of protoplanetary disks (e.g., see Woitke et al. 2009a, France et al. 2012a, Hoadley et al. 2015, Banzatti and Pontoppidan 2015). For example, the interplay between dust and gas in planet-forming disks may define zones where protoplanets may more likely form and evolve, as revealed by new, spatially-resolved ALMA observations of gas and dust, as shown in Figure 1.6. While it remains unclear what exactly drives the final dispersal of gas from planet-forming disks (a number of such mechanisms include photoevaporation: Hollenbach et al. 1994, Alexander et al. 2006; 2014, Alexander and Armitage 2007, Gorti et al. 2009; dynamical clearing by proto-planets: Calvet et al. 2002, Rice et al. 2003, Dodson-Robinson and Salyk 2011; and dust growth: Tanaka et al. 2005), the removal of virtually all gas from the disk marks the end of proto-stellar formation and the beginning of the debris disk (e.g., France et al. 2007), where the essence of the planetary system formed within the protoplanetary disk settles into its final architecture.

1.5 Molecular Hydrogen

This section provides a review of molecular physics and, specifically, molecular hydrogen, and I draw inspiration from molecular astrophysical reviews, including Herzberg (1950), Field et al.

(1966), Shull and Beckwith (1982), Williams and Murdin (2000), Draine (2011).

Throughout the universe, H_2 is expected to be the dominant molecular constituent in both abundance and mass, only behind atomic hydrogen, helium, and their ions. The next most abundant molecule, carbon monoxide (CO), is typically assumed to be roughly 10^{-4} as plentiful as H_2 (e.g., Encrenaz et al. 1975, Black and Willner 1984, Black et al. 1990, Lacy et al. 1994, France et al. 2014a). In the interstellar medium, 10-20% of the mass of molecular clouds may reside in molecular hydrogen. In planet-forming disks, H_2 is expected to make up the bulk of the molecular disk reservior at all evolutionary stages of the disk lifetime, up to the ultimate dissipation of the gas from the system. However, studies of star- and planet-formation environments typically rely on observations of CO as a *tracer* of H_2 to understand the physics of these astrophysical phenomena. Due to the underlying physics properties of the hydrogen molecule, H_2 has been challenging to observe. Since the 1930s, it had been suggested that hydrogen exists in molecular form in portions of the cool interstellar medium, but it was not until the observation of ξ Persei with a rocket-borne UV spectrometer by Carruthers (1970) that the electronic absorption spectrum of H_2 was detected. Here, I will outline the intrinsic physics of the hydrogen molecule to explore why H_2, while abundant throughout the universe, has proven difficult to study, and why other simple diatomic molecules, like CO, are easier to observe.

1.5.1 The Modes of Diatomic Molecules

Molecules are made up of two or more atoms which share electron clouds. For simplicity, I will only be discussing the physics of diatomic molecules, or molecules made up of two atoms sharing electron wave functions. Diatomic molecules have several modes by which they can move and exchange energy - they can stretch along the internuclear axis (*vibration*; Figure 1.7), rotate around the axis perpendicular to the internuclear axis (*rotation*; Figure 1.8), or the electrons orbiting around the molecular nucleus can interchange between electron cloud orbitals (*electronic*). A molecule can be described at any given time by its electronic, vibrational, and rotational behaviors. The electronic level of a molecule is defined by the energy of the motion of electrons through the

nuclear electric field. The vibration and rotation levels, meanwhile, are related to the nuclear characteristics of the molecule, specifically the potential energy curves made up of the Coulomb potential of the nuclei, and are described by their quantum numbers, v (vibration) and J (rotation), which are integer in value for a given vibration-rotation coupling.

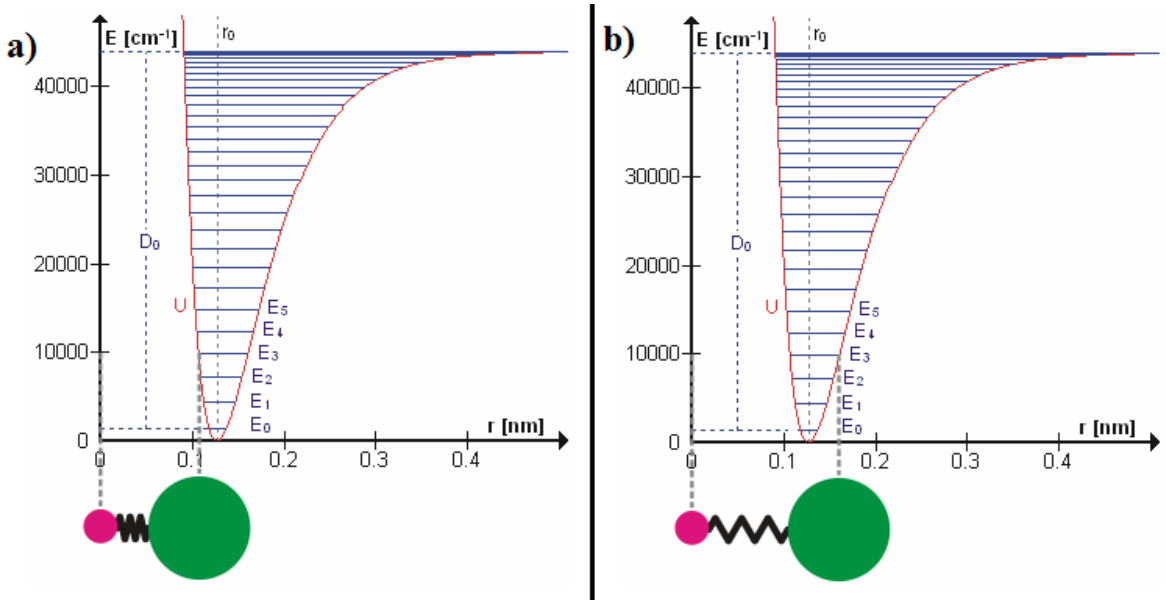

Figure 1.7 A schematic showing how molecules vibrate alone their internuclear axis. The physical length of stretching and compression is limited by the energy range in the Coulomb potential well at a given quantum vibration level.

Molecular energy levels are typically designated by term symbols for identification, written by the following formalism:

$$^{(2\Sigma+1)}\mathcal{L}_{J_e}, \tag{1.1}$$

where Σ is the projection of the electron spin angular momentum onto the internuclear axis (in units of $\hbar$), $\mathcal{L}$ is the projection of the electron orbital angular momentum onto the internuclear axis ($\equiv \Lambda$, in units of $\hbar$), defined as $\mathcal{L} = \Sigma, \Pi, \ldots$ for $\Lambda = 0, 1, \ldots$, and J_e is the projection of the total electronic angular spin onto the internucleus axis (in units of $\hbar$), defined by $J_e = |\Lambda \pm \Sigma|$. For homonuclear molecules, or diatomic molecules with identical nuclei (e.g., H_2, O_2, N_2...), J_e is replaced by either u or g. The designation of u or g is defined by whether the nuclear spin wave function is symmetric (g, "gerade") or antisymmetric (u, "ungerade") under reflection through the

center of mass of the molecular nucleus. Additionally, in the case that $\mathcal{L} = \Sigma$, the term symbol is written as

$$^{(2\Sigma+1)}\Sigma^{\pm}_{J_e}, \tag{1.2}$$

where the new superscript $\pm$ appears, which specifies the symmetry of the wave function under reflection through the plane of the molecular nucleus. If the the wave function is symmetric through the nucleus, the superscript is $+$, while if the wave function is antisymmetric, the term symbol is designated with the $-$.

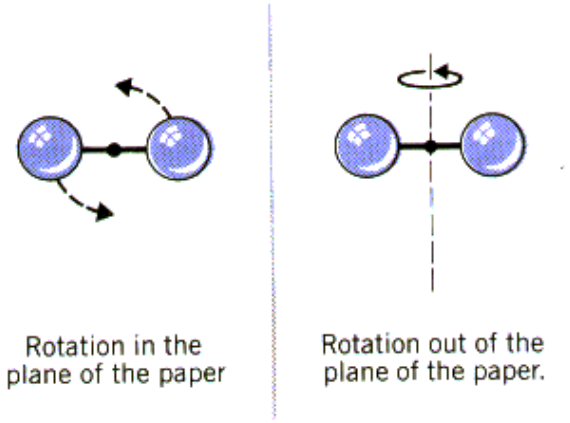

Figure 1.8 A schematic showing the modes of rotation of a molecule.

The term symbol represents the state of the molecular symmetry in a given electronic state. However, the electronic state in which the molecule is found for a given set of term symbols has its own designation, typically distinguished by a letter: X, A, B, ..., which appears in front of the term symbol. For example, the ground state for H_2 is described as: $X^1\Sigma^+_g$, where X is a designation set for the ground electronic band of a given molecule. For the first excited electronic level of H_2, the new term symbol becomes $B^1\Sigma^+_u$. For a non-homonuclear molecule, like CO, the ground electronic band term symbol is: $X^1\Sigma^+_0$. For diatomic molecules with unpaired spin (e.g., OH, where O has an integer spin and H has 1/2 spin), the ground electronic band term symbol is written as: $X^2\Pi_{3/2,1/2}$.

1.5.1.1 Molecular Energy Levels

In the Born-Oppenheimer approximation, or assuming that the nuclei are fixed and only electrons are free to move, the electronic, vibrational, and rotational energy levels can be considered separately. Thus, the total energy of the molecule can be considered as the sum of individual energy levels (electronic, vibration, and rotation) in the molecule:

$$E_q(v, J) = E_{elec} + E_{vib} + E_{rot} \tag{1.3}$$

where E_{elec} is the energy term describing the minimum potential in the specified electronic band of the molecule (for the ground electronic level, $E_{elec} \equiv 0$), E_{vib} is the energy describing the vibrational state of the molecule, and E_{rot} is the energy describing the rotational state of the molecule.

The vibrational behavior of molecules is very similar to that of the classic simple harmonic oscillator with small-amplitude vibrations, such that the potential of the vibrational modes can be expressed as

$$V_{vib}(r) \approx V_{vib}(r_0) + \frac{1}{2}k(r - r_0)^2 \tag{1.4}$$

where r_0 is the nuclear separation of the molecular nuclei when $V_{vib}(r)$ is minimized and k is a "spring constant". In this scenario, k closely relates to the bond between atomic constituents in the molecule. The solutions for the energy levels of vibrational bands in molecules, when expanded to include corrections to the energy levels due to molecules not being rigid springs, can be expressed as:

$$E_{vib}(v) = \omega_e \left(v + \frac{1}{2}\right) - x_e\omega_e \left(v + \frac{1}{2}\right)^2 + y_e\omega_e \left(v + \frac{1}{2}\right)^3 + ... \tag{1.5}$$

where $\omega_e = h\nu_0$, where ν_0 is the molecular natural oscillator frequency, and x_e, y_e are expansion terms. All coefficients are measured constants (Herzberg 1950, Huber and Herzberg 1979).

The rotational behavior of molecules can also be estimated from the rotational motion of the two molecular nuclei around their mutual center of mass. Classically, this motion resembles that of the rotational kinetic energy of a rigid rotor, such that $E = (J\hbar)^2/2I$, where I is the moment of inertia ($I = m_r r_0^2$). By replacing the J^2 classical term with the $J(J+1)$ quantum-mechanical

expression, the rotational energy levels of molecules can be approximated as:

$$E_{rot}(J) \approx J(J+1)\hbar^2/2m_r r_0^2 \tag{1.6}$$

However, the molecules are not rigid rotors, meaning that I will have some dependence on the state of vibration and rotation (e.g., at high J, the molecule gets stretched, which results in larger I). Therefore, in the expanded rotational energy level expression, J and v are not entirely decoupled:

$$E_{rot}(J,v) = B_v J(J+1) - D_v[J(J+1)]^2 + ... \tag{1.7}$$

where $B_v = B_e$ - $\alpha_e(v+\frac{1}{2})$ + ... $\cong$ constant, and $D_v = D_e$ - $\beta_e(v+\frac{1}{2})$ + ... $\cong$ constant (Herzberg 1950, Huber and Herzberg 1979).

Each electronic band of a molecule supports a vibration-rotation structure of energy levels, defined by $E_q(v,J)$. Constants important to the determination of vibrational and rotational energy levels are intrinsic to specific electronic bands and will change if the molecule is found in a different electronic state. For example, if a molecule is in an excited electronic state, the values of B_v and ν_0, which define the simplest approximation of the vibrational and rotational energy levels, yet depend on r_0 and k, will be different than B_v and ν_0 determined for the ground electronic band of the molecule. Figure 1.9 presents the Coulomb potential wells for the ground, first excited, and second excited electronic bands of H_2. Figure 1.10 shows the vibration-rotation structure of the ground electronic level of H_2.

1.5.1.2 Selection Rules for Molecular Transitions

The rotational levels of molecules are specified by a single vibrational (v) and rotational (J) quantum number, which I will henceforth call rovibrational levels. Molecules can transition between rovibrational levels in three different ways. From the lowest energy transitions to the highest, molecules can undergo purely rotational transitions ($\Delta v = 0$; observed in the far-IR and radio), rovibrational transitions from the same electronic band (IR), or rovibrational transitions between different electronic bands (UV).

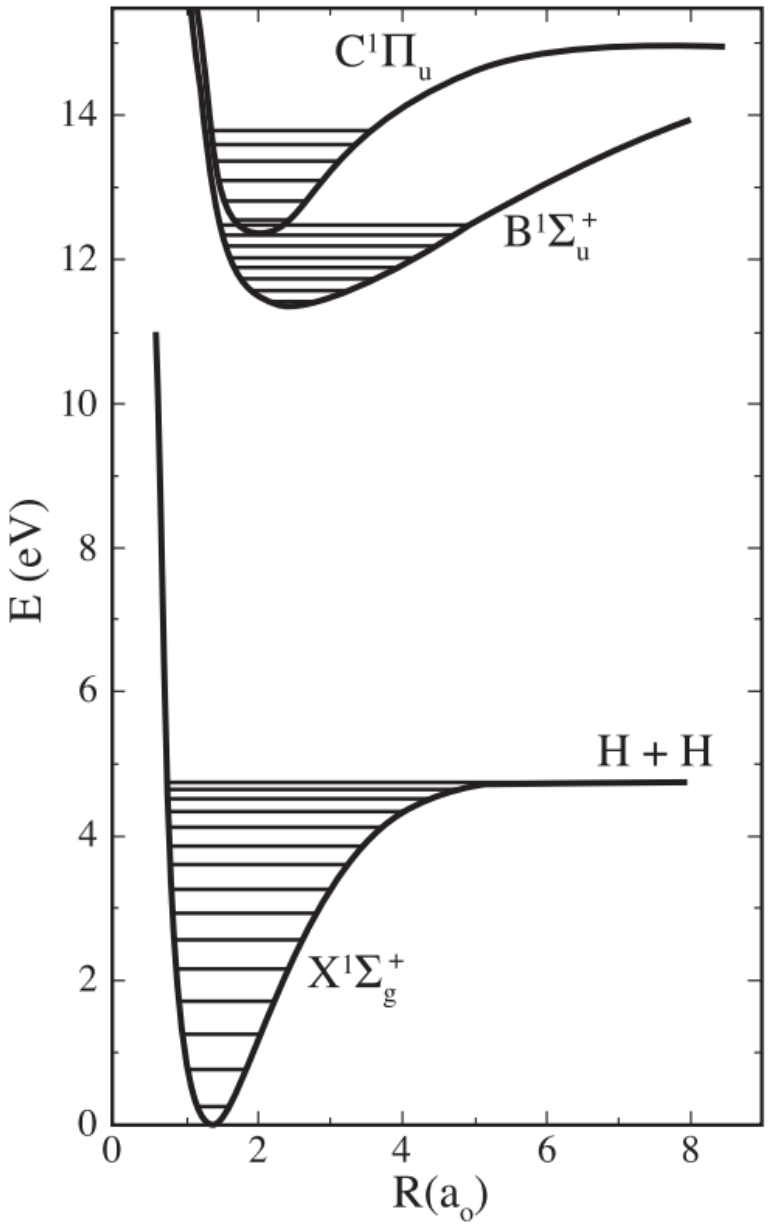

Figure 1.9 A schematic showing the ground ($X^1\Sigma_g^+$), first excited ($B^1\Sigma_u^+$), and second excited ($C^1\Pi_u$) electronic states of H_2. The "H + H" on the ground state band represents the dissociation potential energy, where H_2 has enough excess energy to dissociate into two hydrogen atoms. (credit: Draine 2011)

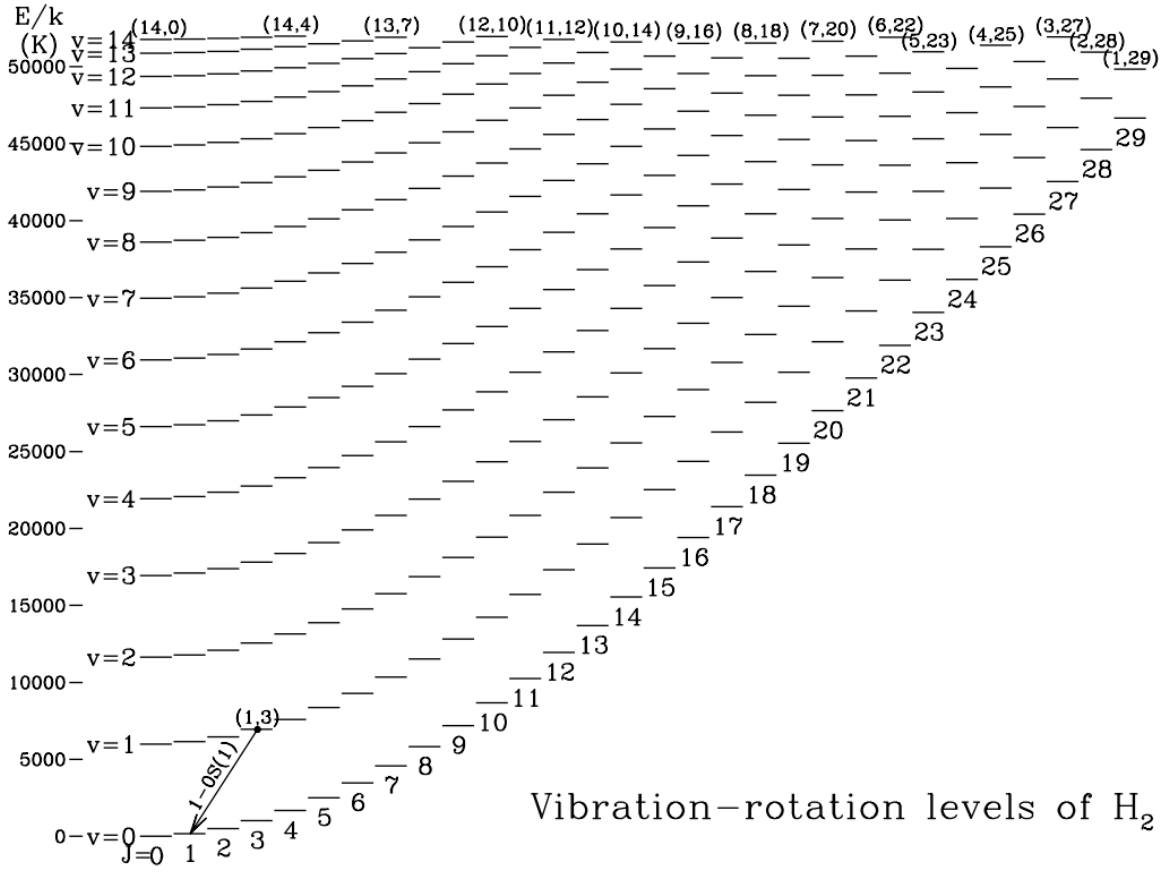

Figure 1.10 A schematic showing the vibration-rotation structure of the ground state electronic band of H_2. It is limited to $v \leq 14$ and $J \leq 29$. (credit: Draine 2011)

For purely rotational transitions, allowed transitions are dictated by the behavior of a classic rotating system, such that the classic rotating system will only radiate if its dipole moment changes. If the diatomic molecule of interest harbors a permanent electric dipole moment, or the measure of the separation of positive and negative electric charges in the molecule gives the molecule an overall net polarity that is nonzero, then it is assumed that the electric dipole moment of the molecule follows the behavior of the rigid rotor during a transition. This leads to the selection rule of $\Delta J = \pm 1$ for purely rotational transitions, with $\Delta J = 0$ forbidden. If $\Delta J = 0$ were allowed, then the rotating system cannot radiate classically. The allowed transitions of $\Delta J = \pm 1$, however, follow directly that the parity of the dipole moment must change in a dipole transition. For diatomic molecules without permanent electric dipole moments (i.e., homonuclear molecules, like H_2), pure rotational transitions ($\Delta J = \pm 1$) are forbidden. However, because diatomic molecules are not rigid rotors, higher order terms in their energy equations allow higher order moments, such as electric quadrupole moments, to exist, such that $\Delta J = \pm 2$ are allowed. Homonuclear molecules, therefore, may undergo purely rotational transitions via quadrupole-allowed transitions; however, these transitions are weaker than their dipole-allowed counterparts, making them occur less frequently and more difficult to observe.

For rovibrational transitions in the ground electronic band of a molecule, the same principle holds as pure rotational transitions: the allowed transitions must also work for classical rotating and simple harmonic oscillator systems. This means that the dipole moment must change for the system to radiate ($\Delta v = \pm 1$). Like the classic rotating system, the harmonic oscillator system must change in parity if the vibrational state changes. The selection rules for ΔJ also apply for the rovibrational transition, with the exception that Λ now plays a role in whether ΔJ is allowed to be zero. Rovibrational transitions still require that the electric parity must change in a dipole transition. When $\Lambda = 0$, the parity is determined by the rotational quantum number only, as the projected electric orbital angular momentum on the internuclear axis is zero. As such, $\Delta J = \pm 1$ observes this rule. However, if $\Lambda \neq 0$, rotational levels can split into two levels with $+\Lambda$ and $-\Lambda$ (or Λ-doubling). These different levels have opposite parity, which allows the molecular parity to

change when $\Delta J = 0$. Therefore, for electronic bands with $\Lambda \neq 0$, $\Delta J = 0$ and ± 1 (with $J \rightarrow J'$ 0-0 transitions forbidden). For homonuclear molecules, transitions with $\Delta J = \pm 1$ are forbidden because these molecules do not have an electric dipole moment. However, $\Delta J = 0, \pm 2$ are allowed and observed throughout the IR. Homonuclear molecules, therefore, may undergo rovibrational transitions but under quadrupole-allowed selection rules; again, these quadrupole transitions are weaker than molecular species with dipole-allowed rovibrational transitions.

Electronic dipole transitions are allowed for all molecules, even those without permanent dipole moments, because the projection of the electronic angular momentum (Λ) changes by either $\Delta\Lambda = 0, \pm 1$ during the electronic transition, which handles the dipole parity change required for rovibrational transitions. This also means that there is no restriction on Δv for this transition, as the dipole parity change occurs in the electronic angular momentum exchange. Since all diatomic molecules now have dipole-allowed transitions in the electronic band exchange, $\Delta J = 0, \pm 1$, with the exception that $\Delta J = 0$ is not allowed for either $\Lambda = 0 \rightarrow \Lambda' = 0$ or $J = 0 \rightarrow J' = 0$.

Molecular transitions between energy levels are expressed by specific terminology to represent the exact quantum level changes in electronic, vibrational, and rotational states. Customarily, transitions are identified by specifying the upper and lower electronic state, upper and lower vibrational levels, and a letter term to express the change in rotational levels, ΔJ. The letter terms are: $O(J_l)$, $P(J_l)$, $Q(J_l)$, $R(J_l)$, $S(J_l)$, for ΔJ = -2, -1, 0, +1, +2, respectively, and J_l denotes the lower rotational level. For example, a transition from the ground electronic level $v_l = 5$, $J_l = 3$ to the first excited electronic level $v_u = 1$, $J_u = 4$ of a molecule would be written as $B - X$(1-5)R(3). Meanwhile, if the molecule in this first excited electronic level then fluoresces back to the ground electronic level $v_l = 6$, $J_l = 5$, the notation would be written as $B - X$(1-6)P(5). For rovibrational transitions within the same electronic state, for example the H_2 transition from $v_u = 1$, $J_u = 3$ to $v_l = 0$, $J_l = 1$, the electronic notation can be dropped and the transition can be expressed as (1-0)S(1), as shown in Figure 1.10.

1.5.2 Molecular Properties of the Hydrogen Molecule

Molecular hydrogen is made of one hydrogen atom + one hydrogen atom, making it a homonuclear molecule. Each proton and electron in the H_2 molecule is a fermion, meaning they each have 1/2 spin. Therefore, the total nuclear spin of H_2 can either be symmetric (S = 1) or antisymmetric (S = 0). By the Pauli exclusion principle, the electronic and nuclear wave functions must together be antisymmetric in spin symmetry. This means that symmetric spin H_2 (S = 1) must have an antisymmetric electronic wave function, such that only odd quantum rotational levels are allowed (J = 1, 3, 5, ...) in the ground electronic level of H_2. Conversely, the antisymmetric nuclear spin H_2 (S = 0) molecules will have symmetric electronic wave functions, allowing for only even number rotational levels in the ground electronic level (J = 0, 2, 4, ...). Figure 1.11 shows a schematic of the spin states and wave functions of the two H_2 spin isomers, which are denoted as para-H_2 (S = 0) and ortho-H_2 (S = 1). This behavior leads to H_2 having no permanent electronic dipole and, as such, only rotational transitions with $\Delta J = 0, \pm 2$ are allowed within an electronic band (dipole transitions between electronic bands are allowed). The spin-coupling of the total nuclear spins of ortho- and para-H_2 are very weakly coupled to the electromagnetic field, and thus the two spin isomers of H_2 act as almost distinct species, with ortho-to-para and para-to-ortho conversions happening very slowly (of order the forbidden transition rate of the atomic hydrogen spin-flip; $A_{flip} \sim 10^{-15}$ s^{-1}).

1.5.2.1 Rotational and Rovibrational Transitions of H_2

H_2 can be excited collisionally (thermally) or radiatively. If H_2 populations are in thermal equilibrium (i.e. are populated by thermally-excited H_2 described by some temperature $T(H_2)$), then the populations of H_2 can be determined with the Boltzmann equation:

$$\frac{N(v,J)}{N_{H_2,total}} = \frac{g_J}{Z} e^{-E(v,J)/k_B T(H_2)} \tag{1.8}$$

where Z is the partition function of the molecule, or the probability density distribution of

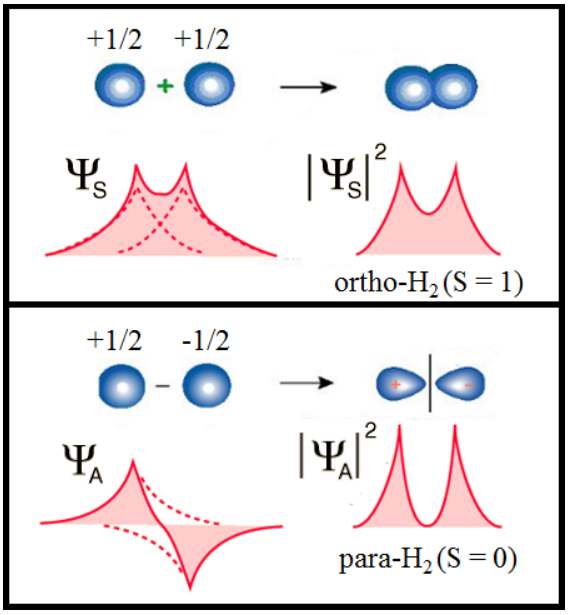

Figure 1.11 A schematic showing how the electronic wave functions pair in H_2 to create the distinct ortho- (*top*) and para- (*bottom*) species of the molecule. The blue orbitals show the spin orientation of the electron clouds, with the red curves representing their wave functions. The symmetric H_2 species have wave functions which overlap. The antisymmetric H_2 spin states have wave functions which are distinctly separated.

H_2 being in some state [v',J'] at a temperature T:

$$Z = \sum_{v',J'} g_{J'} e^{-E(v',J')/k_B T(H_2)} \tag{1.9}$$

$N(v,J)/N_{H_2,total}$ is the fractional column density of H_2 in state [v,J] to the total column density of H_2 (in units of cm^{-2}), g_J is the statistical weight of [v,J], defined by the degeneracy of the spin symmetry and rotational level of the molecule, $g_J \equiv g_s(2J+1)$[3] . $E(v,J)$ is the energy of the state [v,J], k_B is the Boltzmann constant, and $T(H_2)$ is the kinetic temperature of the molecules.

The lowest energy state of para-H_2 ($v = 0$, $J = 0$) is lower than the lowest energy state of ortho-H_2 ($v = 0$, $J = 1$). This is defined by the difference in rotational level energies, primarily dictated by the intrinsic properties of the molecule: $\Delta E = 2B_v J$ where $B_v = \hbar^2/2I$. Molecular hydrogen has a very small I because the reduced mass of the molecule is small: $m_{H_2} = m_H/2$. This leads to large energy differences between rotational levels of H_2. While the para-H_2 [$v = 0$, $J = 0$] level has $E_{[0,0]} = T([0,0]) = 0$ K, the lowest energy level of ortho-H_2 has $E_{[0,1]}/k_B = T([0,1]) = 175$ K. In typical star-formation settings, like GMCs ($T_{GMC} \sim 10$ K), only the $v = 0$, $J = 0$ level of H_2 is collisionally excited. In the diffuse ISM, where $T_{ISM} \sim 100$ K, then the $J = 0$, 1 levels of H_2 are expected to be collisionally excited. However, looking to the temperature states of H_2 levels $v = 0$, $J = 2$ and 3, the energy levels are collisionally populated at $T[0,2] = 510$ K and $T[0,3] \sim 1000$ K. In order for H_2 to radiate via rotational transitions (for example, (0-0)$S(0)$ at λ 28 μm or (0-0)$S(1)$ at λ 17 μm), H_2 must have collisionally excited column densities in the $J = 2$ and 3 levels. At typical temperatures of GMCs and the diffuse ISM, though, H_2 rotational levels with $J \geq 2$ are not collisionally excited. This makes H_2 very difficult to observe in cool astrophysical settings. For warmer astrophysical environments (e.g., shock or highly irradiated regions; $T_{env} \geq 500$ K), H_2 does have observable quadrupole-allowed rovibrational transitions ($J' = J \pm 2$), which occur in the near- to mid-IR (1 - 30 μm). However, these transitions are weak and rely on the molecules transitioning from relatively excited ground vibration levels (e.g., Sellgren et al. 1983,

[3] For para-H_2 (S = 0), the nuclei pair to be spin singlet, so $g_s = (2S+1) = 1$; for ortho-H_2 (S = 1), the nuclei pair to form a spin triplet molecule, so $g_s = (2S+1) = 3$.

Sellgren 1984, Martini et al. 1999, France et al. 2007).

Historically, other molecules with dipole-allowed rotational transitions and lower energy differences between rotational levels, like CO, have been used as a proxy for H_2 in star- and planet-formation environments. Carbon monoxide has a permanent electric dipole, which allows for $\Delta J = \pm 1$ within an electronic band of the molecule. Additionally, CO has a much larger moment of inertia than H_2 ($m_{CO} \approx 6.9 m_H$), which allows for much more closely spaced rotational levels with lower kinetic temperatures than H_2 (for example, the CO $v = 0$, $J = 1$ level is at $T([0,1]) = 5.5$ K and the CO $v = 0$, $J = 2$ level is at $T([0,2]) = 16.6$ K). This allows several rotational levels of CO to be collisionally excited in cold astrophysical environments. The lower temperature and higher moment of inertia of CO leads to longer wavelength radiation, which is observed in the radio band from the ground (the $J = 1 \rightarrow 0$ transitions radiates at $\nu = 115$ GHz, or λ 2.6 mm). For CO, cold conditions in GMCs and regions near the cold, dense midplanes of protoplanetary disks are adequate to excite the molecule to higher rotational levels, and dipole-allowed transitions give observers access to information about the molecular material and structure that cannot be traced via cold H_2.

In star-forming regions of galaxies, measurements of cool CO are used as a proxy to estimate the amount of molecular material in the ISM and draw conclusions about the role of molecules in star-forming processes (e.g., Donovan Meyer et al. 2012, Glover and Clark 2012b, Daddi et al. 2015, Muraoka et al. 2016, Shetty et al. 2016). In the local universe, measurements of cold CO in GMCs and clumps can unveil important information about interstellar conditions, structure and stellar formation sites (e.g., Bally et al. 1987, Dame et al. 2001, Schultheis et al. 2014, Burleigh et al. 2013, Barnes et al. 2016). In protoplanetary disks, cold and warm CO have revealed a wealth of knowledge about the behavior of gas in planet-forming regions. Freeze-out zones of CO have been identified by ALMA (e.g., Qi et al. 2011; 2013, Mathews et al. 2013, Martin and Livio 2014, Guidi et al. 2016), while ro-vibrational transitions of CO in the near-IR have revealed the behavior of gas at terrestrial planet-forming radii over the lifetime of disks (e.g., Salyk et al. 2011a, Brown et al. 2013, Banzatti and Pontoppidan 2015). Unfortunately, relying on molecular tracers

like CO requires extensive knowledge about the relationship between the abundances of CO to H_2 in any given astrophysical system, which may not always be accurate. While the ratio of CO-to-H_2 is typically assumed to be $\sim 10^{-4}$ for all systems, studies have observed astronomical examples where this estimate may be grossly off in the diffuse ISM and translucent clouds (Burgh et al. 2007; 2010) and the planet-forming regions of protoplanetary disks (e.g., Reboussin et al. 2015, Schwarz et al. 2016). This may be due simply to the depletion of carbon-based species onto dust grains in different environments. However, this lack of knowledge can lead to erroneous conclusions about the physical structure and behavior of certain astrophysical systems, which is why directly observing H_2 is so crucial.

1.5.2.2 Electronic Transitions of H_2

Molecular hydrogen has dipole-allowed rovibrational transitions between electronic bands. These electronic transitions cannot be thermally-populated, however, as can be seen in Figure 1.9; the lowest energy level of the first excited electronic level of H_2 is still much larger than the rovibration tiers of the ground electronic band potential well. This means that thermally-excited H_2 will reach the dissociation potential, or where the energy of the molecules overcomes the potential well of the ground electronic level, before it can begin populating the vibration-rotation ladder of excited electronic states.

The only way for H_2 to populate vibration-rotation levels in excited electronic bands is for H_2 in the ground electronic state to be photo-excited to another electronic state, such that the hydrogen molecule must absorb a photon with a minimum energy $h\nu$ to reach another electronic state. For H_2, this minimum energy is $E_{min} \approx 6.6$ eV, assuming H_2 at the highest energy levels of the ground electronic vibration-rotation ladder ($E_{gr} \sim 4.4$ eV, where $E_{diss} \cong 4.45$ eV) is being pumped to $v = 0$, $J = 0$ of the first excited electronic band ($E_{exc} \sim 11.2$ eV). Therefore, the longest wavelength photon that can pump an H_2 molecule to the excited electronic bands from the ground electronic level is $\lambda \sim 1830$ Å. Conversely, to pump H_2 found in the $v = 0$, $J = 0$ of the ground electronic band to the $v = 0$, $J = 0$ of the first excited electronic band, H_2 must absorb

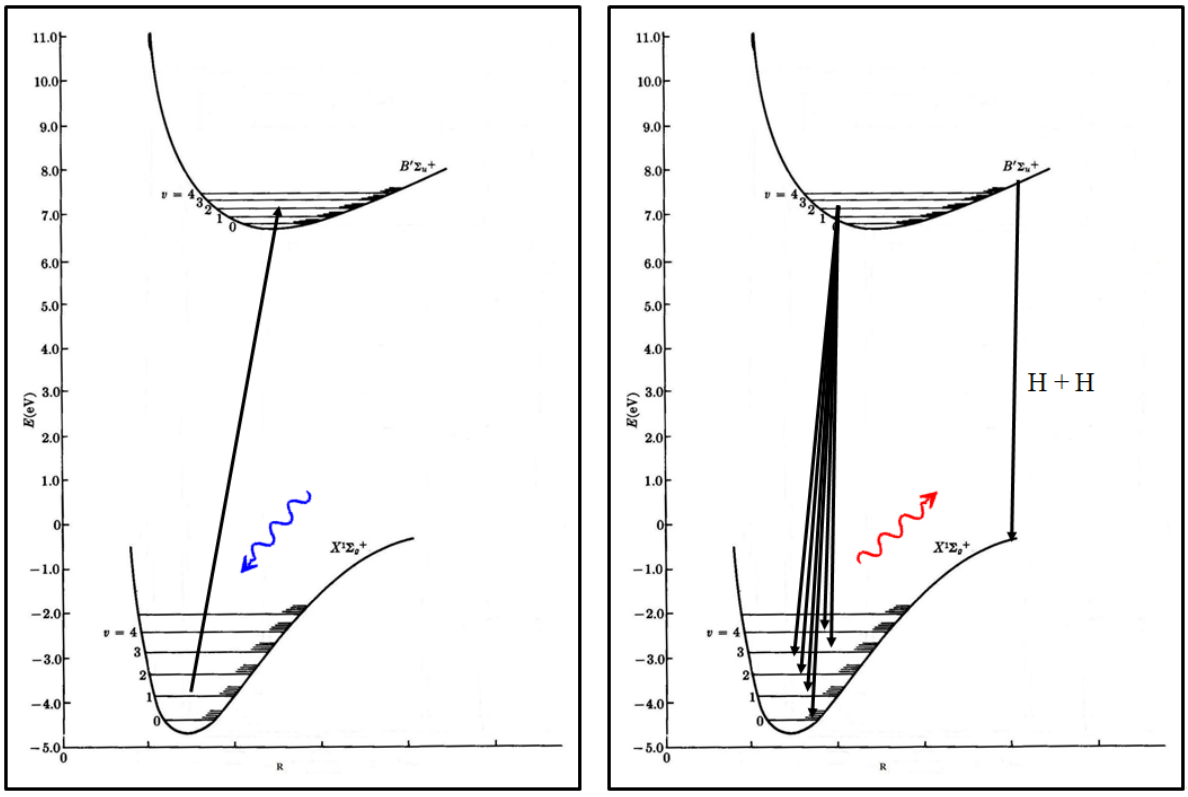

Figure 1.12 A schematic showing the ground and first excited electronic states of H_2, and how the photo-excited fluorescence process works. Each horizontal band per electronic state represents the vibrational level in the state, and hashes on the right of the potential well show rotational levels. For H_2 to undergo the fluorescence process, it must absorb a photon with sufficient energy (typically far-UV photons achieve this criterion) to excite it from the ground state to an excited electronic state, as shown on the *left*, with H_2 absorbing the blue photon. The *right* shows the decay of H_2 from the excited electronic state, which results in one of many different tracks back to the ground level. (Note: the decay is expected to occur straight down from the electronic level to the ground level. Deviations from this are shown to highlight a selection of possible routes back to the ground electronic band from the excited electronic state.) This is the fluorescence cascade, and, depending on the fluorescence track back to the ground state, H_2 will emit a photon with energy equal to the difference between the excited and ground electronic states (shown with the red photon). If H_2 is photo-excited to an excited electronic level where it has little-to-no routes available back to a vibration-rotation level in the ground electronic band, it will decay to the dissociation potential, thus unbinding H_2 into two H atoms.

a photon of $\lambda \sim 1110$ Å. In reality, H_2 in many different ground vibration-rotation levels can be photo-excited to many different vibration-rotation levels in not just the first excited electronic level (called the Lyman band) but the second excited electronic state (called the Werner band) and beyond. The minimum energy required to pump H_2 out of the ground electronic band, however, requires that H_2 molecules absorb far-UV photons ($\lambda\lambda$ 900 - 1800 Å) to undergo dipole-allowed electronic transitions.

The absorption of a far-UV photon by H_2 to undergo an electronic band transition is defined by the cross-section of H_2 in state [v,J] (in units of cm^2) with a photon of wavelength λ, which can be expressed as:

$$\sigma_{H_2[v,J]} = \frac{\sqrt{\pi}e^2}{m_e c b_{H_2}} \lambda f_{[v,J]\rightarrow[v',J']} \tag{1.10}$$

where $\sigma_{H_2[v,J]}$ is the cross-section of absorption of λ by $H_2[v,J]$, $\pi e^2/m_e c$ is the classical cross-section constant, b_{H_2} is the b-value of H_2, defined as the Doppler shift of the molecule and dominates the width of the cross-sectional area to absorb the photon, and $f_{[v,J]\rightarrow[v',J']}$ is the oscillator strength of the transition of H_2 from ground electronic level [v,J] to excited electronic state [v',J']. The oscillator strength is a measure of the strength or probability of the transition to occur and is directly related to the Einstein A coefficient of the transition, A_{ul}:

$$f_{[v,J]\rightarrow[v',J']} = \frac{m_e c}{8\pi^2 e^2} \frac{g_{[v',J']}}{g_{[v,J]}} \lambda^2_{[v,J]\rightarrow[v',J']} A_{ul} \tag{1.11}$$

where the subscript ul denotes the transition from upper to lower vibration-rotation levels. For far-UV photons with energies coincident with a potential energy difference between H_2 in ground electronic level [v,J] and a dipole transition to an excited electronic vibration-rotation level [v',J'] (i.e., $h\nu = E_{exc}[v', J'] - E_{gr}[v, J]$), $\sigma_{H_2[v,J]}$ can be quite large ($\sim 10^{-14}$ - 10^{-15} cm^2, which is several orders of magnitude larger than the physical cross-section of the molecule).

The Einstein A coefficient represents the rate of spontaneous emission from the electronic excited band back to the ground state, which is dependent on intrinsic transition physics from upper state [v',J'] to lower level [v'',J''] and, therefore, has no dependence on the radiation field. The Einstein A coefficients for H_2 dipole-allowed transitions are quite large: $A_{ul} \sim 10^7$ - 10^8 s^{-1}

(Abgrall et al. 1993a;b), which is due to the strong tendency for the excited electron to return back towards the positively-charged nuclei. Because the electronic transition is dipole-allowed and has no selection rule for Δv, H_2 can return back to the ground level via multiple routes ("fluorescence"). Each transition has its own spontaneous emission probability, which differs depending on the intrinsic state of the molecular vibration (stretching), as explained with the Franck-Condon principle: during an electronic transition, a change from one vibrational energy level to another will be more likely to happen if the two vibrational wave functions overlap significantly. The strength of one transition from a given electronic vibration-rotation level can be expressed as a "branching ratio" (B_{ul}),

$$B_{ul} = \frac{A_{ul}[[v', J'] \rightarrow [v'', J'']]}{\sum_{ul} A_{ul}} \tag{1.12}$$

where $\sum_{ul} A_{ul}$ is the total of all transition possibilities from [v',J'] to the ground electronic band. The branching ratio is directly proportional to the expected ratio of emission line strengths observed from the H_2 electronic transition. The fluorescence process is schematically portrayed in Figure 1.12.

Additionally, depending on the excited electronic band, H_2 may have a non-zero probability to dissociate into two hydrogen atoms. This can happen when the vibration (stretching) of the excited H_2 is too large to accommodate any vibration-rotation levels in the ground state. The only possible route back to the ground level, therefore, is along the dissociation potential of the molecule, as demonstrated in Figure 1.12.

The advantage of H_2 electronic transitions is that, theoretically, there should be two signatures available to detect the transitions: the absorption of discrete far-UV photons which excite H_2 to excited electronic bands, and emission of H_2 from the fluorescence back to the ground electronic band. Figure 1.13 presents a prime example of both absorption and emission from H_2 electronic transitions in a protoplanetary disk setting. While H_2 emission dominates the H_2 signatures, absorption in strong atomic accretion features, like HI-Lyα (λ 1215.67 Å) and CIV (λ 1548.82, 1550.77 Å), drives the appreciable flux in the H_2 emission features. In the ISM, particularly in sightlines with strong far-UV continuum, absorption signatures of low energy ($v = 0$) H_2 being pumped out

of lower energy vibration-rotation levels in the ground electronic level to excited electronic states are observed from $\lambda\lambda$ 900 - 1120 Å.

The dipole-allowed electronic transitions of H_2 have much larger transition probabilities (A_{ul} $\sim 10^8$ s^{-1}; Abgrall et al. 1993a;b) than quadrupole-allowed rovibrational transitions in the IR ($A_{ul} \sim 10^{-7}$ s^{-1}; Wolniewicz et al. 1998). Therefore, electronic dipole transitions of H_2 should be easier to detect than rovibrational quadrupole transitions. However, to observe these strong electronic transitions in the far-UV, both in absorption (photo-pumping signatures) and emission (fluorescent cascade transitions), space-based observatories become necessary, as the Earth's atmosphere becomes opaque to radiation with $\lambda < 3000$ Å. Studies of these H_2 transitions have been made possible since $\sim$ 1970, with sub-orbital rocket experiments and long-duration observations, such as *Copernicus*, the *International Ultraviolet Explorer* (*IUE*), the *Far Ultraviolet Spectroscopic Explorer* (*FUSE*), the *Galaxy Evolution Explorer* (*GALEX*), and instruments aboard the *Hubble Space Telescope* (*HST*). For astrophysical environments where plenty of far-UV photons are present to excite H_2 molecules, far-UV observations of H_2 electronic transitions have enabled the physical characterization of a wide range of objects, including diffuse ISM and translucent clouds (e.g., Spitzer et al. 1974, Rachford et al. 2002, France et al. 2013b), photodissociation regions (e.g., Hollenbach and Tielens 1997, France and McCandliss 2005, France et al. 2007), atmospheres of low mass stars (e.g., Redfield and Linsky 2002, Kruczek et al. Submitted), protoplanetary disks (e.g., Herczeg et al. 2002, France et al. 2011b; 2012a, Schindhelm et al. 2012b, and shown in Figure 1.13), planetary nebulae (e.g., Zuckerman and Gatley 1988, Speck et al. 2002), and many other astrophysical settings.

1.6 Scientific Objectives

The purpose of this thesis is to provide new insights into the behavior of molecular hydrogen in star- and planet-forming environments, which cannot be achieved with observations of trace molecules alone. To accomplish this, I study observational signatures of H_2 throughout the far-UV, which give access to both absorption and emission tracers of the molecule in a variety of rovibra-

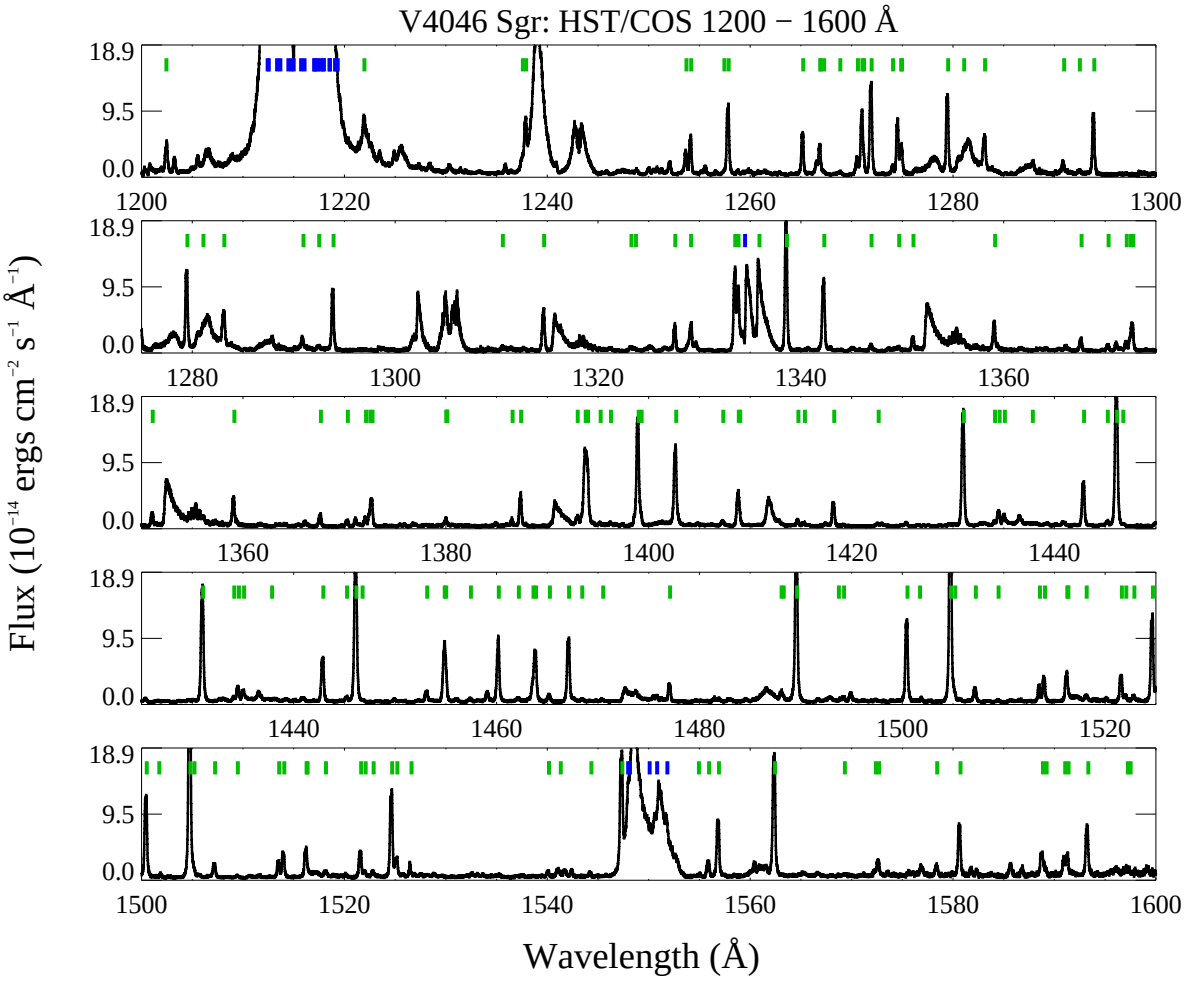

Figure 1.13 The far-UV spectrum of V4046 Sgr, a well-studied planet-forming disk at roughly 100 pc. The spectrum was obtained with *HST*/COS and covered from 1150 - 1750 Å (though only 1200 - 1600 Å is shown). The strongest fluorescence lines are pointed out with dashes - blue represent absorption transitions, while green identify emission features. The far-UV gives access to hundreds of H_2 features in both emission and absorption signatures.

tional ground states. Unfortunately, H_2 is not observable in cold, pristine environments favorable for stellar formation. Instead, I focus on characterizing the behavior and structure of H_2 in the diffuse ISM and translucent clouds, which interact with UV-bright sources (i.e. O- and B-type stars), to understand the physical conditions and abundance of H_2 at the interface to denser, molecular cloud materials. In protoplanetary disks, warmer ro-vibrational H_2 populations, which are photo-pumped by primarily Lyα radiation generated at the protostellar accretion shock, are observed in an abundance of emission features throughout the far-UV. These emission features have line widths much larger than the spectral resolutions of the UV instruments used to probe them - the *HST*-Cosmic Origins Spectrograph (COS) and Space Telescope Imaging Spectrograph (STIS) - which contain important velocity information about the warm H_2 in these environments. Additionally, signatures of H_2 absorption embedded in Lyα emission features of a selection of protoplanetary disk sightlines are detectable, which provide critical information about the circumstellar environment, specifically the excitation structure and abundances of molecular material in each target. Together, I use observed H_2 emission and absorption diagnostics to constrain the structure and behavior of the molecular protoplanetary disk as planet-forming disks evolve.

In Chapter 2, I will describe Keplerian rotation models of planet-forming disks I have created to reproduce observed emission profiles of H_2 in the far-UV, which I use to describe where in protoplanetary disks the H_2 emission is produced. I compare these H_2 models to 14 different observed protoplanetary sightlines over a variety of disk ages, which are inferred from the degree of dust evolution in the disks (as determined by their near- to mid-IR SEDs). In Chapter 3, I describe an empirical study of H_2 absorption signatures observed in the protostellar Lyα wings of 22 different protoplanetary disk sightlines. In this study, I describe the behavior of ro-vibrational ground states of H_2 in each sightline and estimate the total column densities of H_2 in each circumstellar environment. In Chapter 4, I describe a sub-orbital sounding rocket experiment - the *Colorado High-resolution Echelle Stellar Spectrograph* (CHESS) - which is designed to study the behavior of interstellar H_2 in translucent clouds in the sightlines to UV-bright O- and B-type stars in the local stellar group ($d < 500$ pc). CHESS is a high-resolution objective echelle spectrograph, designed to

achieve a resolving power R $\sim$ 100,000, and observes in the far-UV from $\lambda\lambda$ 1000 - 1600 Å. I have launched CHESS two times - in 2014, CHESS observed α Virgo (d $\sim$ 40 pc; B1 III-IV + B2 V), and in 2016, where it observed ϵ Persei (d $\sim$ 300 pc; B0.5 III). I will discuss design, component testing, ray trace simulations, build-up procedures, calibration, data reduction, and final science products from the launch of CHESS-1 and CHESS-2. Finally, Chapter 5 summarizes all of my major scientific findings and discusses future work to be accomplished in light of these results.

Chapter 2

Fluorescence Signatures of Molecular Hydrogen in Protoplanetary Disks

"We're gonna need a pressure washer after this."
- Larry Conser, reflecting on an upcoming dinner at State Line BBQ.

2.1 Introduction & Scientific Motivation

Protoplanetary disks (PPDs) provide the raw materials for the formation of stellar systems (Brown et al. 2009, Woitke et al. 2009b, Dullemond and Monnier 2010). Planet formation occurs near the midplane of a PPD, where column densities and optical depths are high (Trilling et al. 2002, Armitage et al. 2003), making it difficult to directly observe the material involved in the formation process (Kominami and Ida 2002). Current understanding of the formation and evolution of planetary systems in gaseous disks comes from studies of molecular content above or near disk midplanes, which place limits on the composition and density distribution of the gas and dust content in the inner ($r \leq 10$ AU) planet-forming regions (Agúndez et al. 2008, Carr and Najita 2008; 2011, Salyk et al. 2008; 2011a, Woitke et al. 2009b, Willacy and Woods 2009, Heinzeller et al. 2011, Najita et al. 2011). "Transition" disks refer to a class of PPDs with an optically thick outer zone but an inner region significantly depleted of dust grains (Sato and Nakagawa 1999, Calvet et al. 2002, Salyk et al. 2009) and are traditionally identified by the deficiency in near-infrared (IR) flux and steep rise of far-IR flux in the observed SED (Strom et al. 1989, Calvet et al. 2002; 2005, Espaillat et al. 2007a). Several theories exist for how dust gaps are opened in transition disks, including photoevaporation (Hollenbach et al. 1994, Alexander et al. 2006, Alexander and Armitage

2007, Gorti et al. 2009), dynamical clearing by protoplanetary systems (Calvet et al. 2002, Rice et al. 2003, Dodson-Robinson and Salyk 2011), and dust grain growth (Tanaka et al. 2005).

Discoveries of significant quantities of gas left within the dust gaps of transition disks (see Najita et al. 2003, Rettig et al. 2004, Salyk et al. 2007) and sharp "walls" between the thin and thick dust disk regions (Brown et al. 2008) support the possibility of transition disks being carved out by giant planet formation and evolution (Salyk et al. 2009, Dodson-Robinson and Salyk 2011, Dong et al. 2015). The remnant gas disks provide constraints on the processes that create the final structure of planetary systems, such as the transfer of gas from the PPD to circumplanetary disks, potentially leading to growth of protoplanets (Lubow et al. 1999, Lubow and D'Angelo 2006, Ayliffe and Bate 2010, Beck et al. 2012). Additionally, the molecular atmosphere of transition disks may respond to the dynamical perturbations caused by the presence of giant protoplanets and can lead to potentially observable effects, such as line asymmetries and distortions in near-IR CO emission profiles (Regály et al. 2010). The strength of molecular emission originating from the inner radii of PPDs is dependent on the gas temperature, density, and degree of grain growth (Salyk et al. 2011b). Molecular line surveys therefore provide the opportunity for a broad examination of the gas distributions in circumstellar environments (Brown et al. 2013).

Molecular hydrogen (H_2) has been measured to be $\sim 10^4$ times more abundant than any other molecule in the inner disks of PPDs (France et al. 2014a). Depending on the density, H_2 can survive at temperatures up to 5000 K (Williams and Murdin 2000) and self-shield against UV radiation, making it robust to both collisional- and photo-dissociation (Beckwith et al. 1978, Beckwith and Zuckerman 1982, Beckwith et al. 1983). Molecular hydrogen provides a diagnostic for the spatial and structural extent of the warm molecular surface of PPDs (Ardila et al. 2002, Herczeg et al. 2004, Yang et al. 2011). While photo-excited H_2 does not interact strongly with evolving protoplanets, it traces the underlying distribution of gas at planet-forming radii (Ardila et al. 2002, Herczeg et al. 2004; 2006, France et al. 2012b). However, H_2 is difficult to observe, as explained in the previous Chapter. Therefore, studies of molecular matter in disks have typically relied on other tracers available in the near- and mid-IR, such as CO and H_2O, to estimate

the molecular disk environment and mass of the underlying H_2 reservoir in disks.

However, the strongest transitions of H_2 are found in the far-UV (FUV) ($\lambda\lambda$ 912 - 1700 Å), where dipole-allowed electronic transitions are primarily photo-excited ("pumped") by Lyα photons generated near the protostellar surface (France et al. 2012c, Schindhelm et al. 2012b). Warm H_2 (T $\gtrsim$ 1500K) has a significant population in excited vibration (v = 1, 2) and rotation quantum states of the ground electronic band ($X^1\Sigma_g^+$) (Shull 1978). When a Lyα photon interacts with a warm H_2 molecule in the correct rovibration level [v,J], the H_2 molecule absorbs the photon, exciting it to vibration levels ($v' \rightarrow$ 0-4) of the first electronic band ($B^1\Sigma_u^+$). Since molecular hydrogen has strong ($A_{ul} \sim 10^8 s^{-1}$; see Abgrall et al. 1993a) electronic transitions in the FUV, the excited H_2 "immediately" decays back to the ground state, emitting a fluorescent photon, observed as an FUV emission line. The probability for an H_2 excitation-to-ground state transition to emit a photon with wavelength λ depends on the branching ratio of the allowed transitions to the ground electronic state. The brightest H_2 emission lines arise from excited states [v', J'] = [1,4], [1,7], [0,1], and [0,2], which have absorption coincidences with Lyα within 0 and 600 km s^{-1} of the Lyα line center, large oscillator strengths, and relatively low energy ground-state levels (Herczeg et al. 2002; 2005). The set of emission lines produced in the [v', J'] $\rightarrow$ [v'', J''] decay is refered to as a progression.

Previous work on FUV fluorescent H_2 emission utilized basic profile fitting or small-sample parametric sets to estimate inner disk diagnostics, such as column density and temperature of the radiating molecular populations (see Herczeg et al. 2004, France et al. 2012b;c). One of the first works extensively covering the presence of fluorescent H_2 emission from PPDs, Herczeg et al. (2002), laid the framework for determining likely origins and pumping mechanisms to explain the bright emission observed from TW Hya, one of the closest and most well-studied PPDs (e.g., Herczeg et al. 2002; 2006, France et al. 2012c, Schindhelm et al. 2012b, Rosenfeld et al. 2012a, McJunkin et al. 2014, Andrews et al. 2016, Bergin et al. 2016, Kastner et al. 2016 and many other studies). Since then, others have sought to correlate the behavior H_2 fluorescence from PPDs to the evolution of the innermost molecular disk for PPD hosts at different evolutionary phases of their disk lifetime (e.g., France et al. 2012c), the same way as is being done with warm molecular disk tracers observed

in the IR (Salyk et al. 2011a, Brown et al. 2013, Banzatti and Pontoppidan 2015).

For this study, I created a robust 2D radiative transfer model of PPD atmospheres to reproduce FUV H_2 emission lines observed from a variety of PPDs at different evolutionary phases. The models simulate a disk with radial temperature and density distributions, which depend on physical parameters of the stellar system, such as the disk inclination angle and stellar Lyα radiation profile (derived from Schindhelm et al. 2012b). Using four of the strongest Lyα-pumped H_2 progressions, I compare radiative transfer emission models to the spectra of 14 Classical T Tauri Stars (CTTSs) (8 primordial and 6 transition disks) observed with the *Hubble Space Telescope* (*HST*)/Cosmic Origins Spectrograph (COS) and Space Telescope Imaging Spectrograph (STIS). The goal of this work was to examine the relationship between the evolution of warm dust in PPDs and the radial distribution of H_2 in the disk atmosphere. I aimed to understand how the spatial distribution of warm H_2 relates to the structure of the dust disk and other well-studied molecular disk tracers, such as carbon monoxide (CO) and water (H_2O).

2.2 Observations

I sample a large collection of *HST*-COS and *HST*-STIS (for TW Hya) FUV H_2 data to understand the relative changes in the radiation distributions of H_2 arising from the inner regions of primordial and transition disks. The observations were obtained through the DAO of Tau guest observing program (PID 11616; PI - G. Herczeg), the COS Guaranteed Time Observing program (PIDs 11533 and 12036; PI - J. Green), and *HST* Program GTO-8041 (PI - J. Linsky). The observations have been presented in previous literature (for examples, see Herczeg et al. 2006, Ingleby et al. 2011, Yang et al. 2011, France et al. 2012c; 2014b, Schindhelm et al. 2012a, Ardila et al. 2013).

The medium-resolution G130M and G160M FUV modes of COS (Green et al. 2012) were utilized for all targets except TW Hya, which was observed with the E140M mode (1170 - 1710 Å) with the $0.5'' \times 0.5''$ aperture of STIS at a resolving power of 25,000 (see Herczeg et al. 2006). The point-source resolution for each mode on COS is $\Delta v \approx 17$ km s^{-1} with 7 pixels per resolution element (Osterman et al. 2011) and $\Delta v \approx 12$ km s^{-1} for the STIS E140M observing mode of TW

Hya (Leitherer 2001). The COS data were smoothed by 3 pixels for analysis. The one-dimensional spectra of COS were produced using the CALCOS COS calibration pipeline, which were aligned and coadded using a custom software procedure (Danforth et al. 2010). The STIS data were reduced using the CALSTIS STScI reduction pipeline (Lindler 1999), with calibration lamp spectra obtained during observations to assign wavelength solutions.

Stellar properties, such as mass, accretion rate, and inclination angle are used to constrain the underlying model framework. All disk inclination angles have been estimated from sub-mm/IR interferometric studies (e.g, Simon et al. 2000, Johns-Krull and Valenti 2001, Espaillat et al. 2007a, Andrews et al. 2011, Rosenfeld et al. 2012a). Stellar masses and extinction estimates were derived from pre-main sequence stellar evolutionary tracks (Hartmann et al. 1998). Mass accretion rates were estimated from measurements of the accretion luminosity (Ingleby et al. 2013). Refer to Table 2.1 for lists of all the relevant stellar parameters, with references therein.

2.3 H_2 Emission Line Selection

The *HST*-COS FUV spectra of all CTTSs from 1300 - 1600 Å reveal a suite of H_2 fluorescence features linked to Lyα-pumping. I chose to use the strongest transitions from the electronically-excited progressions $[v', J'] = [0,1]$, $[0,2]$, $[1,4]$, and $[1,7]$ for the purposes of studying the underlying general characteristics of the bulk gas disk. I sample 3 emission features from each progression, which give access to strong, non-blended emission lines that are well-defined from the FUV continuum while balancing the CPU time required for detailed line profile analysis. I selected H_2 emission features by locating the strongest transitions for each progression, following the outline provided by Herczeg et al. (2002). See Table 2.2 for the full outline of transitions chosen.

2.4 Modeling Analysis

I created models of warm H_2 in PPDs to constrain the radial distribution of fluorescent H_2 emission in disk atmospheres. My goal was to understand the relative changes in the H_2 distributions as a function of dust disk evolution. The fluorescent emission line shape and intensity

Table 2.1. Protoplanetary Disks: Stellar & Disk Parameters

Target	Spect. Type	$M_\star$ ($M_\odot$)	d (pc)	A_v	i_d (°)	Age (Myr)	vsini (km s^{-1})	ref.[a]
AA Tau	K7	0.8	140	0.5	75	6.4 ± 0.2	11.4	2,8,9,11,12,15,17,25
BP Tau	K7	0.73	140	0.5	30	5.9 ± 0.3	7.8	4,8,9,12,15,17,18,30
CS Cha	K6	1.05	160	0.8	60	6.4 ± 0.1	...	5,6,15,19,22
DF Tau A	M2	0.19	140	0.6	85	6.3 ± 0.5	16.1	9,11,12,16,17,18
DM Tau	M1.5	0.5	140	0.0	35	6.6 ± 0.2	10.0	3,11,12,15,17,25
GM Aur	K5.5	1.20	140	0.1	55	6.9 ± 0.2	12.4	3,8,9,11,12,15,17,25
HN Tau A	K5	0.85	140	0.5	40	1.9 ± 0.9	52.8	7,9,11,18,23
LkCa15	K3	0.85	140	0.6	49	6.4 ± 0.3	12.5	3,8,10,12,15,17,18
RECX 11	K4	0.80	97	0.0	70	4.0 ± 1.5	...	14,15,20,21
RECX 15	M2	0.40	97	0.0	60	6.0 ± 1.0	...	15,20,21,32
SU Aur	G1	2.30	140	0.9	62	2.5 ± 0.9	65.0	1,4,9,11,18
TW Hya	K6	0.60	54	0.0	4	10.0 ± 6.0	6.0	3,13,16,24,28,29,31
UX Tau A	K2	1.30	140	0.2	35	6.1 ± 0.3	25.4	3,8,11,17,19
V4046 Sgr	K5	1.75	83	0.0	34	6.9 ± 0.1	14.2(+13.7)	25,27,28,29

[a] (1) Akeson et al. (2002); (2) Andrews and Williams (2007); (3) Andrews et al. (2011); (4) Bouvier (1990); (5) Espaillat et al. (2007a); (6) Espaillat et al. (2011); (7) France et al. (2012c); (8) Furlan et al. (2011); (9) Gullbring et al. (1998); (10) Hartmann et al. (1987); (11) Hartmann and Stauffer (1989); (12) Hartmann et al. (1998); (13) Herczeg and Hillenbrand (2008); (14) Ingleby et al. (2011); (15) Ingleby et al. (2013); (16) Johns-Krull and Valenti (2001); (17) Kenyon et al. (1994); (18) Kraus and Hillenbrand (2009); (19) Lawson et al. (1996); (20) Lawson et al. (2001); (21) Lawson et al. (2004); (22) Luhman (2004); (23) McJunkin et al. (2013); (24) Pontoppidan et al. (2008); (25) Quast et al. (2000); (26) Ricci et al. (2010); (27) Rodriguez et al. (2010); (28) Rosenfeld et al. (2012a); (29) Rosenfeld et al. (2013); (30) Simon et al. (2000); (31) Webb et al. (1999); (32) Woitke et al. (2013).

Table 2.2. Selected H_2 Emission Lines & Properties of H_2 Pumping Transitions

λ_{lab} (Å)	Progression	Line ID[a]	λ_{pump} (Å)	v_{trans}[b] (km s^{-1})	A_{ul}[c] (10^8 s^{-1})	f[d] (10^{-3})
1442.87	[1,7]	$(1-6)R(6)$	1215.726	14	0.9	34.8
1467.08		$(1-6)P(8)$			1.3	
1500.45		$(1-7)R(6)$			1.7	
1524.65		$(1-7)P(8)$			1.9	
1556.87		$(1-8)R(6)$			1.3	
1580.67		$(1-8)P(8)$			1.1	
1431.01	[1,4]	$(1-6)R(3)$	1216.070	99	1.0	28.9
1446.12		$(1-6)P(5)$			1.4	
1489.57		$(1-7)R(3)$			1.6	
1504.76		$(1-7)P(5)$			2.0	
1547.34		$(1-8)R(3)$			1.1	
1338.56	[0,1]	$(0-4)P(2)$	1217.205	379	3.1	44.0
1398.95		$(0-5)P(2)$			2.6	
1460.17		$(0-6)P(2)$			1.5	
1521.59		$(0-2)P(2)$			0.6	
1342.26	[0,2]	$(0-4)P(3)$	1217.643	487	2.8	28.9
1393.96		$(0-5)R(1)$			1.6	
1402.65		$(0-5)P(3)$			2.3	
1463.83		$(0-6)P(3)$			1.4	
1525.15		$(0-7)P(3)$			0.5	

[a] Transitions are from the Lyman-excited to ground electronic states of the H_2 band system, $B^1\Sigma_u^+ - X^1\Sigma_g^+$.

[b] Velocity from line center of the pumping transition of Lyα.

[c] Einstein coefficient, describing the spontaneous decay rate from the electronically-excited Lyman band, taken from Abgrall et al. (1993a).

[d] Oscillator strengths from Abgrall et al. (1993a).

depend on the physical conditions of the gas, while the observed line width depends predominantly on the disk inclination. I constructed a physical model of the disk structure, motivated by the disk modeling analysis performed by Rosenfeld et al. (2012a).

The models make several basic assumptions on the disk properties: (a) the disk material orbits in Keplerian rotation around a central point mass, representing the stellar mass; (b) the H_2 fluorescence occurs in a shallow, warm layer on the disk surface; and (c) the level populations of warm H_2 that absorb the incident stellar Lyα radiation field are in local thermodynamic equilibrium (LTE). (a) implies that the gas disk mass is a small fraction of the stellar mass ($M_d/M_\star \ll 1$). Studies have shown that the disk mass to stellar mass ratio ($M_d/M_\star$) $< 1\%$, making this assumption plausible (Andrews et al. 2013). In the case of a binary system (i.e., V4046 Sgr), both stellar masses are represented as one central mass point. For (b), Herczeg et al. (2004) find that the warm H_2 disk layer interacting with the stellar Lyα to produced the observed fluorescence lines corresponds to mass column density of $\sim 10^{-5}$ g cm^{-2}, which is a much smaller mass column density predicted to be within 1 AU by D'Alessio et al. (1999). This suggests that the Lyα-pumped fluorescent emission originates from a tenuous layer of warm H_2 on the disk surface and supports a purely radial thermal distribution $T(r)$ (the warm molecular layer is also found by Ádámkovics et al. 2016). For (c), the combination of collisional excitation and radiative de-excitation is assumed to be in equilibrium to keep the H_2 gas near the disk surface at warm temperatures (T $>$ 1000 K; Nomura et al. 2005; 2007). Previous studies of FUV H_2 emission have argued both for and against this assumption (Ardila et al. 2002, Herczeg et al. 2006). However, LTE conditions keep the assumed parameters straightforward, so I assume LTE conditions to create models which simulate H_2 ground-state populations as a "snapshot" of the disk atmosphere as it was observed.

The warm H_2 atmosphere is described by the surface density and temperature distribution of gas, which characterizes how much of the warm H_2 is populating excited ground-states [v,J]. I reference these physical quantities in cylindrical coordinate positions in the disk (r,ϕ,z). When I consider that a parcel of warm H_2 gas on the disk surface is characterized by its radial position, vertical height from the disk midplane, and velocity distribution (r, z, $v_\phi(r)$), the velocity of the

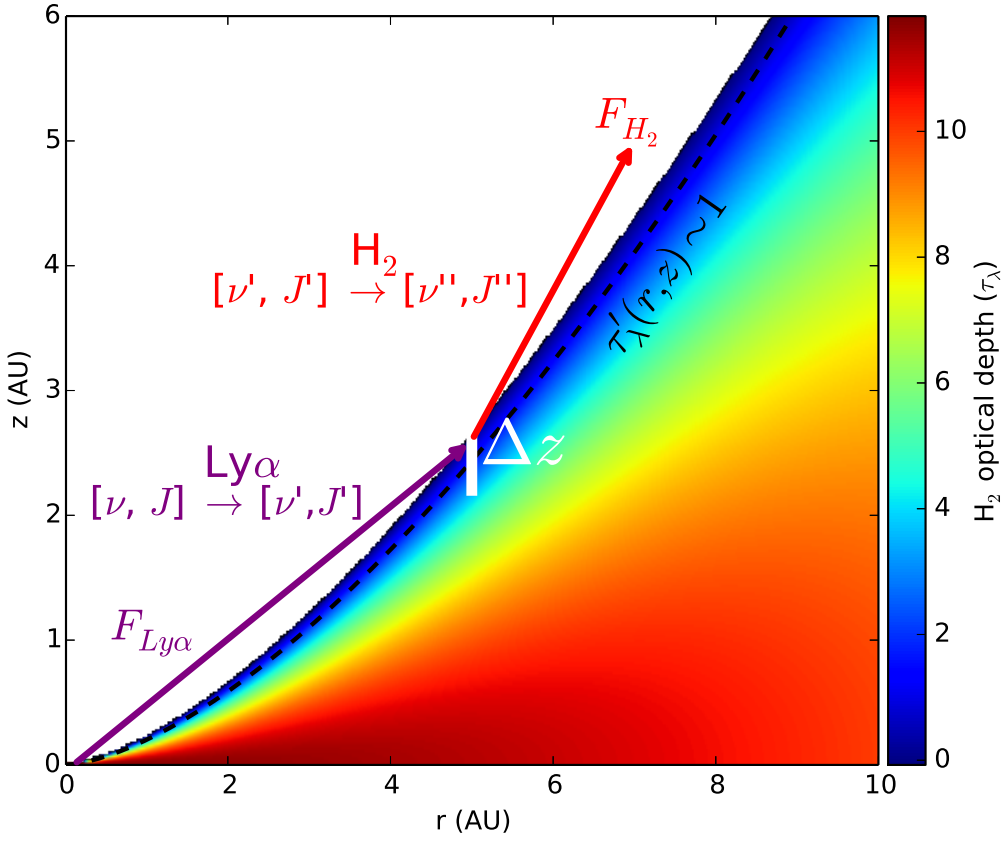

Figure 2.1 A graphical representation of the H_2 disk atmosphere model. The disk contours represent the warm H_2 optical depth ($\tau_\lambda(r,z)$) to stellar Lyα radiation being pumped to state [v',J'] = [1,4]. The dashed line marks off the approximate location of $\tau'_\lambda \approx 1$, which is where the H_2 disk atmosphere becomes optically thick to the penetrating Lyα photons. The stellar Lyα radiation (purple arrow) is absorbed by the by the warm H_2, which is excited to state [v',J'] and emits a photon (λ_{H_2}; red arrow) to decay back to ground state [v'',J''].

gas parcel, $v_\phi(r)$, can be described by Keplerian rotation in $\hat{\phi}$ only:

$$v_\phi(r) = v_k = \sqrt{\frac{GM_\star}{r}}; v_r = v_z = 0, \tag{2.1}$$

where G is the gravitational constant and $M_\star$ is the central stellar mass. The mass density at the warm H_2 disk surface is a function of the radial and vertical height in the disk,

$$\rho(r,z) = \frac{\Sigma(r)}{\sqrt{2\pi}H_p} \exp\left[-\frac{1}{2}\left(\frac{z}{H_p}\right)^2\right], \tag{2.2}$$

where $\Sigma(r)$ is the radial surface density distribution of H_2, and H_p is the pressure scale height as a function of radius, defined as:

$$H_p = \frac{c_s}{\Omega} = \sqrt{\frac{kT(r)}{\mu m_H} \cdot \frac{r^3}{GM_\star}}, \tag{2.3}$$

where c_s is the sound speed, Ω is the angular velocity of the gas, k is the Boltzmann constant, $T(r)$ is the radial temperature profile of the warm H_2 disk atmosphere, μ is the "mean molecular weight" of the gas, and m_H is the mass of a hydrogen atom. The temperature distribution of the disk atmosphere is approximated as a power-law function:

$$T(r) = T_{1AU}\left(\frac{r}{1AU}\right)^{-q}, \tag{2.4}$$

where T_{1AU} is the temperature of the warm H_2 at r = 1 AU, and q is the temperature gradient.

I assume a radial surface density for a static accretion disk, represented by a power-law viscosity profile (see Lynden-Bell and Pringle 1974),

$$\Sigma(r) = \Sigma_c\left(\frac{r}{r_c}\right)^{-\gamma} \exp\left[-\left(\frac{r}{r_c}\right)^{2-\gamma}\right], \tag{2.5}$$

where γ is the density gradient, r_c is the characteristic radius of the gas in the disk, and Σ_c is a normalization factor for the surface density distribution, dependent on the total H_2 mass contributing to the emission lines simulated by these models. The characteristic radius describes the transition from a power-law dominated density distribution to an exponentially-dominated density fall-off in the disk (Lynden-Bell and Pringle 1974, Hartmann et al. 1998). It is important to note that $\Sigma(r)$ contains a normalization factor (Σ_c), which normalizes to the disk midplane

density. My models only attempt to describe the behavior of the disk atmosphere, where the warm, tenuous H_2 resides. As a consequence, the functionality of $\Sigma(r)$ serves as a structural layout of the radial H_2 disk atmosphere. Since I normalize $\Sigma(r)$ with a factor describing the disk midplane density, the solutions of $\Sigma(r)$ describe the radial distributions of warm H_2, but the resulting H_2 mass estimates are not meaningful.

The level populations of warm, ground state H_2 contributing to the emission line are assumed to be in LTE and are determined using the Boltzmann equation,

$$n_{[v,J]}(r,z) = \frac{\rho\,(r,z)\,X_{H_2}}{\mu m_H} \times \frac{\mathrm{g}_{[v,J]}}{Z_{[v,J]}\,(T)} \times \exp\left(\frac{-E_{[v,J]}}{kT\,(r)}\right), \tag{2.6}$$

where X_{H_2} is the fraction of the total H_2 gas mass contributing to the fluorescence observed in the FUV, $g_{[v,J]}$ is the statistical weight of the level population, $Z_{[v,J]}(T)$ is the partition function describing the likelihood that the warm H_2 is in state $[v,J]$, and $E_{[v,J]}$ is the energy of warm H_2 in ground state $[v, J]$.

The radial distribution of molecular hydrogen has two normalization factors (X_{H_2} and Σ_c) that are not independent of disk conditions and are defined by their product in $n_{[v,J]}(r, z)$. The product of these factors describes the total mass of warm H_2 available for photo-excitation to state $[v',J']$ (M_{H_2}), which is obtained by integrating the distribution over (r,ϕ,z): $M_{H_2} = X_{H_2}\Sigma_c \left(2\pi r_c^2\right) / (2-\gamma)$.

The radiative transfer calculation required to reproduce the observed fluorescent H_2 emission happens in two steps: 1) the warm H_2 in ground state population $[X : v,J]$ is pumped into a rovibrational level $[B : v',J']$ of the excited electronic (Lyman band) state by the absorption of an incident stellar Lyα with wavelength $\lambda_{Ly\alpha}$, and 2) the excited H_2 molecule decays back to some ground electronic state $[X : v'',J'']$, emitting a FUV photon with wavelength λ_{H_2}. Molecular hydrogen has an absorption cross section (σ_{H_2}) defined by the area around the molecule that can intersect an incoming photon with the appropriate energy for photo-excitation:

$$\sigma_{H_2} = \frac{\lambda_{Ly\alpha}^3}{8\pi c} \frac{\mathrm{g}_{[B:v',J']}}{\mathrm{g}_{[X:v,J]}} A_{lu}, \tag{2.7}$$

where $\lambda_{Ly\alpha}$ is the rest frame wavelength of the stellar Lyα line profile needed to excite the warm

H_2 in ground state $[X : v, J]$ up to energy level $[B : v', J']$, and A_{lu} is the probability that H_2 in population $[X : v, J]$ will be "pumped" to electronic state $[B : v', J']$.

Assuming an absorption coefficient $\kappa_\lambda(r,z) = \sigma_{H_2} n_{[v,J]}(r,z)$, the optical depth of H_2 in ground state [v,J] is described as:

$$\tau_\lambda(r,z) = \sum_{z}^{z-H_p} z\kappa_\lambda(r,z)\,. \tag{2.8}$$

For every vertical and radial position in the disk atmosphere that I sample $\tau_\lambda(r,z)$, I calculate the amount of the Lyα radiation that will be available for absorption by the warm H_2. To correct for line absorption overlap of shared Lyα photons, I adopt an effective optical depth $\tau_\lambda^{'}(r,z)$ (Liu and Dalgarno 1996, Wolven et al. 1997), defined as

$$\tau_\lambda^{'}(r,z) = \tau_\lambda(r,z)\,\frac{\tau_\lambda(r,z)}{\tau_{\rm all}(T(r),N(r,z))}, \tag{2.9}$$

which corrects for the absorption, scattering, and shielding of Lyα photons. Figure 2.1 shows a schematic of $\tau_\lambda(r,z)$ for [v',J'] = [1,4] and outlines the radiative transfer process in the disk.

I model the emission line flux of each λ_{H_2} produced from the cascade of transitions from energy level [v',J'] as:

$$F_{\lambda_{H_2}} = \eta S_\lambda(r,z)\,B_{mn}\sum^{\tau_\lambda^{'}}\left(1-e^{-\tau_\lambda^{'}(r,z)}\right), \tag{2.10}$$

where η represents the coverage fraction of H_2 in the Lyα radiation field (Herczeg et al. 2004), B_{mn} is the branching ratio describing the fraction of H_2 decaying via a given transition to ground state [v'',J''] over the whole suite of transitions available from the progression, and the source function ($S_\lambda(r,z)$) is defined as the Lyα emission line flux with wavelength $\lambda_{Ly\alpha}$, $F_{\rm Ly\alpha}(r,z)$.

I calculate how $F_{\rm Ly\alpha}(r,z)$ changes as a function of radial position in the disk. Assuming that the accretion-generated Lyα flux originates at the stellar surface, the ratio of the original $F_{Ly\alpha,\star}$ to the flux the warm H_2 disk atmosphere receives at r can be expressed as

$$F_{Ly\alpha} = F_{\star,Ly\alpha}\frac{R_\star^2}{r^2}. \tag{2.11}$$

To correctly incorporate the Lyα radiation field, I use reconstructed protostellar Lyα profiles created by Schindhelm et al. (2012b) and France et al. (2014b), which describe the stellar Lyα flux

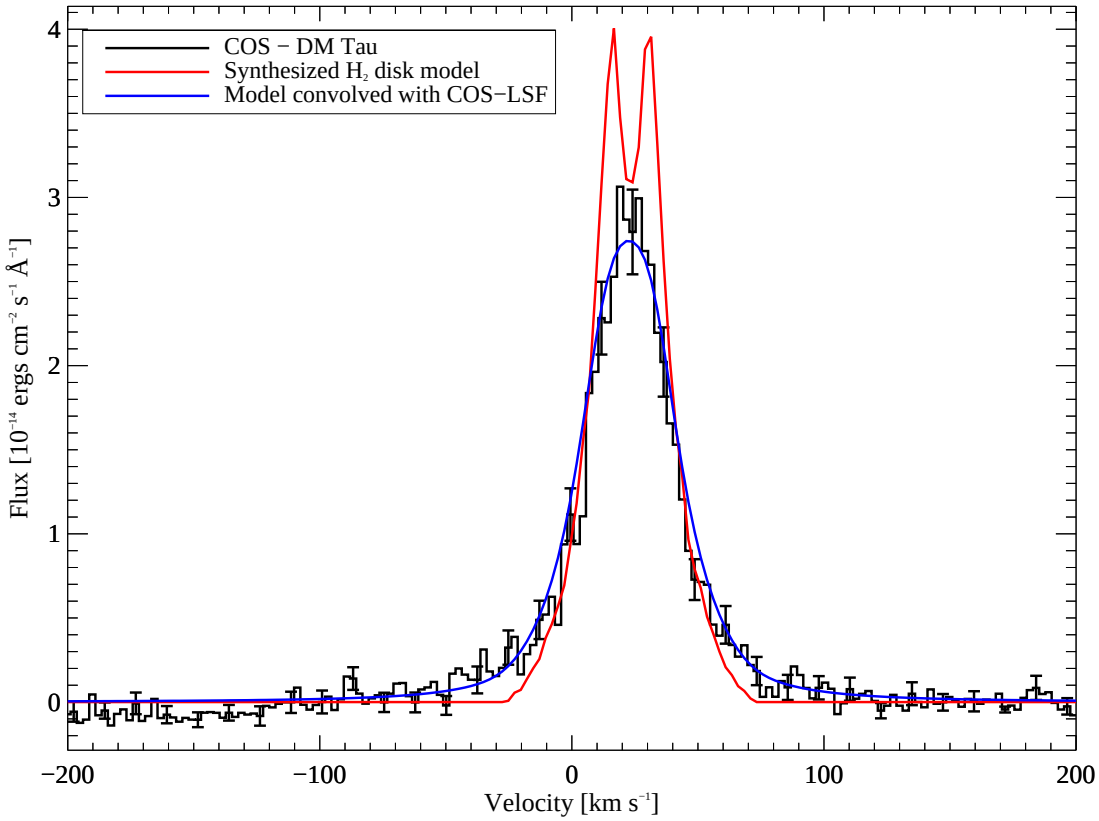

Figure 2.2 An example of a modeled emission line fit over a *HST*-COS emission line. The black line represents the observed H_2 fluorescent emission feature, including representative error bars. The red line shows the modeled emission, and the blue line is the convolution of the modeled emission line with the COS-LSF. The reduced-χ^2 statistic is calculated between the black (data) and blue (model) lines.

seen by the disk surface of each target. After calculating the FUV H_2 fluorescence flux at each disk grid point in our model, I radiate the H_2 emission isotropically, some fraction of which is intercepted by the observer. I calculate the distance of each gas parcel radiating in the disk from the observer $s(r, z)$, based on radial and angular positions of the disk gas parcel, distance to the target, and disk inclination angle. The final modeled emission line flux produced for a fluorescence transition of H_2 is expressed as:

$$F_{\lambda_{H_2}} = \eta F_{\star,Ly\alpha} \left(\frac{R_\star^2}{r^2}\right) \left(\frac{(d\cos i_{disk})^2}{s(r,z)^2}\right) \times B_{mn} \sum^{\tau_\lambda^{'}} \left(1 - e^{-\tau_\lambda^{'}(r,z)}\right) \tag{2.12}$$

Using a total of 6 parameters to represent the physical conditions of the warm, ground-state H_2 populations in the disk atmosphere ($z/r,\ \gamma, q, T_{1AU}, r_{char}, M_{H_2}$), Equation 2.12 characterizes the resulting emission line profiles from H_2 radiating from the disk. All free parameters were allowed to vary over a rough grid of controlled values to create a data cube representing the density distributions, temperature profiles, and radial radiation fields of inner disk H_2 around a given stellar target; see Table 2.3 for the full list of parameters explored in this study. The resulting models simulate the emission profiles produced for a given fluorescence transition λ_{H_2}, with emission flux as a function of orbital velocity. The radial velocity component of the emission line is determined by $v_\phi(r)$ of the emitting gas at a given radius in the disk, projected into the sight line of the observer. This model framework was used to describe the observed velocity field of single and binary systems, both close-in and extended. It is worth noting that the results of close-in binary systems (e.g. V4046 Sgr) may affect the inner disk velocity-radial relationship differently than a point mass. Therefore, the innermost H_2 modeled for these close-in binary systems may not be accurate, but the outer disk emission distributions is expect to remain unaffected.

Synthesized spectra of each H_2 emission line are compared to *HST* observations. Each model is convolved with either the *HST*-COS line spread function (LSF) (Kriss 2011) or a normalized Gaussian distribution with FWHM characterized by the STIS E140M mode spectral resolving power (R$\sim$25,000 for TW Hya; see Herczeg et al. 2006) prior to comparison with the observed emission line profiles. The FUV continuum level is estimated around each emission feature with a linear fit to

Table 2.3. Parametric Values Explored in Modeling Framework

Parameter	Values	Units
z/r	(2, 3, 4, 5, 6, 7) × H_p	
γ	0.0, 0.25, 0.5, 0.75, 1.25, 1.5, 1.75, 1.99	
q	-1.0, -0.5, -0.25, -0.1, -0.05, 0.0, +0.05, +0.1, +0.25, +0.5	
T_{1AU}	500, 1000, 1500, 2000, 2500, 3000, 3500, 4000, 4500, 5000	K
r_c	0.1, 0.5, 1.0, 3.0, 5.0, 7.5, 10.0, 20.0	AU
M_{H_2}	5×10^{-10}, 10^{-10}, 5×10^{-11}, 10^{-11}, 5×10^{-12}, 10^{-12}, 5×10^{-13}, 10^{-13}, 5×10^{-14}, 10^{-14}	$M_\odot$

the *HST*-COS data, which is subtracted from the observations before model-to-data comparisons are made. An example of an H_2 emission line, with native and convolved models laid over the *HST*-COS observed emission line, is shown in Figure 2.2.

2.5 Analysis

The goal of the model-to-data comparison is to find the combination of model parameters that best reproduce the observed fluorescent emission line profiles that cascade from the same excited state [v',J']. A reduced-χ^2 statistic is computed when comparing the observed FUV H_2 emission features to the entire data cube of models created for a target. I analyze the reduced-χ^2 statistic data cube for three cases when comparing the modeled emission lines to the observations: (1) fitting individual emission lines; (2) simultaneously fitting all H_2 emission lines fluorescing from the same excited energy level [v',J']; (3) fitting only the red wings of the emission lines. (1) was used to set the initial range of temperature and density model parameters of warm H_2 in each disk surface. (3) was explored to mitigate the potential influence of a warm molecular wind component that was unresolved at the spectral resolving power of *HST*-COS. The results of (3) proved inconclusive, finding no significant differences between the red and blue wing line shapes and suggesting that the models are not sensitive to an unresolved warm H_2 disk wind. I focus on the results of (2), which best describe the generalized behavior of the warm H_2 disk atmosphere populations. I simultaneously fit 3 observed fluorescent H_2 transitions for each progression as the most representative of the H_2 radiation distributions in each PPD.

Table 2.4 shows the minimum reduced-χ^2 statistics for all targets when simultaneously fitting the 3 progression emission lines from excited state [v',J']. Not all minimum reduced-χ^2 simultaneous progression fits for [0,1] and [0,2] were "good", however (i.e., some sources displayed reduced-χ^2 > 25). Many of the strongest lines from [0,1] and [0,2] share similar λ_{H_2}, which makes complex line profiles that depend on the shape of the stellar-Lyα profile illuminating the warm H_2 disk populations to these excited states. The [1,7] and [1,4] progressions are more reliable tracers of the warm H_2 disk atmosphere, and the brightest emission lines in our survey cascade from the [1,4]

Table 2.4. Minimum χ^2 Statistics for Each Progression Fit

Target	Progression [0,1]	[0,2]	[v',J'] [1,4]	[1,7]
AA Tau (2011)	5.37	6.48	5.52	1.25
AA Tau (2013)	1.78	5.29	4.24	1.62
BP Tau	2.82	51.75	5.28	2.97
CS Cha	4.56	5.14	4.19	2.62
DF Tau A	2.69	13.30	7.21	7.37
DM Tau	6.12	19.55	7.68	37.95
GM Aur	3.84	6.72	1.47	1.74
HN Tau A	41.71	63.16	13.52	35.81
LkCa15	111.03	103.30	14.14	151.65
RECX 11	2.40	9.48	1.09	0.93
RECX 15	42.45	90.01	13.98	63.32
SU Aur	25.73	39.31	13.24	21.07
TW Hya	2.64	3.29	3.63	2.15
UX Tau A	104.69	124.23	13.14	123.16
V4046 Sgr	12.82	13.09	5.93	2.86

[1]All model-to-data reduced-χ^2 statistics for simultaneous emission line fitting, transitioning from excited state [v',J']. Only the [1,4] progression show good fits for all targets ($\chi^2 < 15$).

progression. For the vast majority of the targets, the largest stellar Lyα fluxes pump the warm H_2 disk populations to the [1,4] energy level. This makes the line profile flux fitting more accurate for the [1,4] progression, providing the overall best model fits to the observe FUV emission.

Therefore, I focus on the results from the best-fit [1,4] progression for all targets. This progression has good reduced-χ^2 fits (≤ 15) and by-eye model-to-data comparisons for every target in our survey. Figure 2.3 shows an example of minimum reduced-χ^2 modeled progression lines to those observed with *HST*-COS for GM Aur, and all model fits for targets in this survey are presented in Appendix A. Figure 2.4 presents the resulting radial radiation distribution for each best-fit progression for GM Aur. While each progression peaks at somewhat different radii, the majority of the radiation distributions originate within similar annuli of the disk. This behavior is typical for all PPD targets that have good minimum reduced-χ^2 fits for all or most progressions.

2.5.1 Uncertainty Estimation and Parameter Degeneracies

Errors in each best-fit parameter per progression are determined after marginalizing the minimum reduced-χ^2 parameter fits over all free parameters. Uncertainties are measured as the range of values that encompass 68% of the distribution area, representing the 1-σ uncertainties for a Gaussian distribution. The modeled parameter space was crudely varied over a large range of values for each free variable, so a Gaussian distribution was fit over each marginalized best-fit parameter uncertainty space, and the FWHM of each Gaussian fit was calculated as the uncertainty in each model parameter.

Figure 2.5 displays the reduced-χ^2 marginalized parametric space for each variable in our modeling framework, with filled contours representing the 2-σ uncertainty in the parameter space. Since each parametrized uncertainty is taken within the 1-σ error contours of each marginalized distribution, the uncertainties outlined in red represent the 1-σ errors in the model parameters.

There are noticeable degeneracies amongst several of the parameters; for example, the total mass of emitting H_2 and vertical position of the disk atmosphere (M_{H_2}, z/r) show a trend that requires more mass contributing to the emission lines as the disk height above the disk mid plane

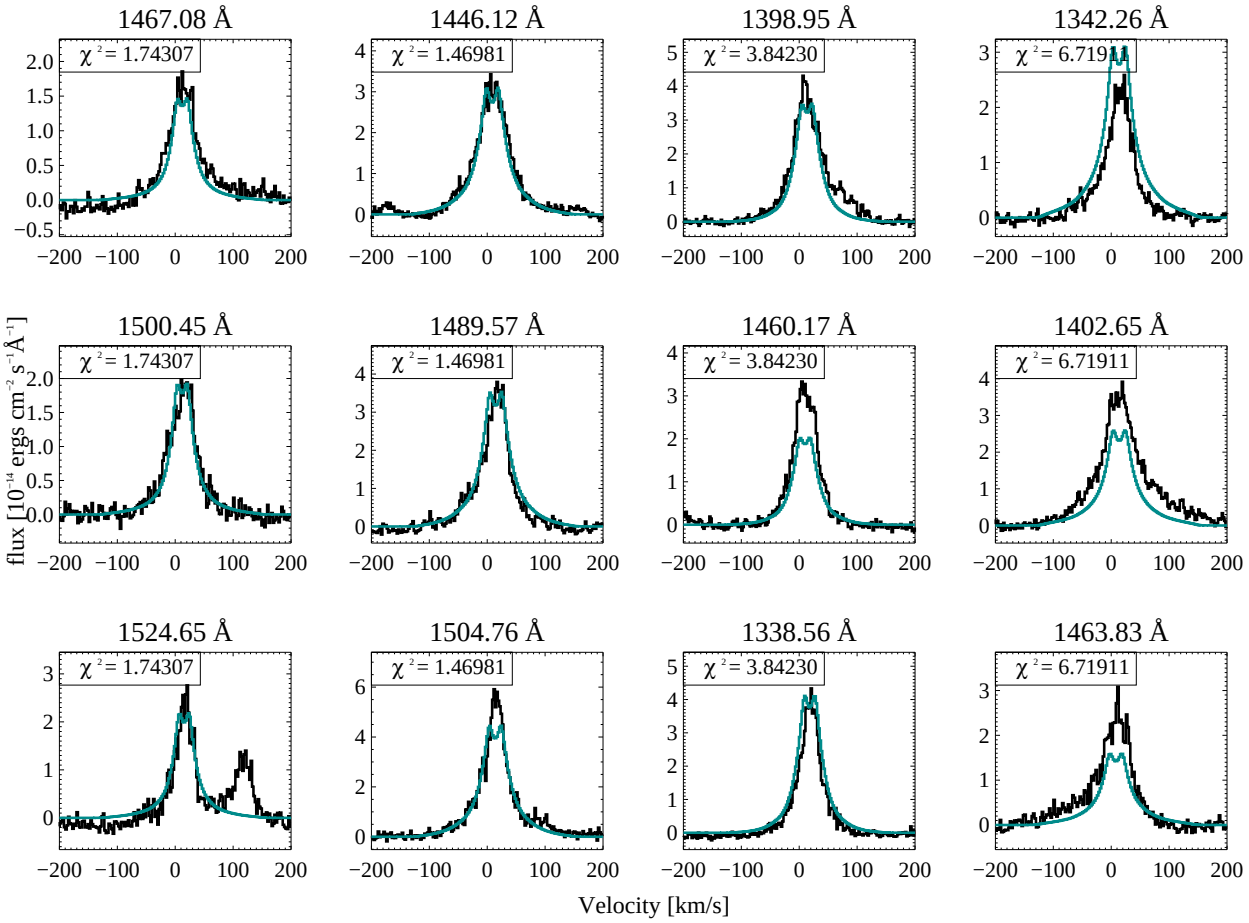

Figure 2.3 The resulting model and data fits of the minimum simultaneous progression χ^2 statistic for GM Aur. Each column represents transitions from a common excited energy level [v',J']. From left to right: the left column - [v',J'] = [1,7]; the middle-left column - [1,4]-; the middle-right column - [0,1]; the right column - [0,2]. The χ^2 shown in the top left of each emission line box represents the fitting of all emission lines from a given progression with one set of model parameters.

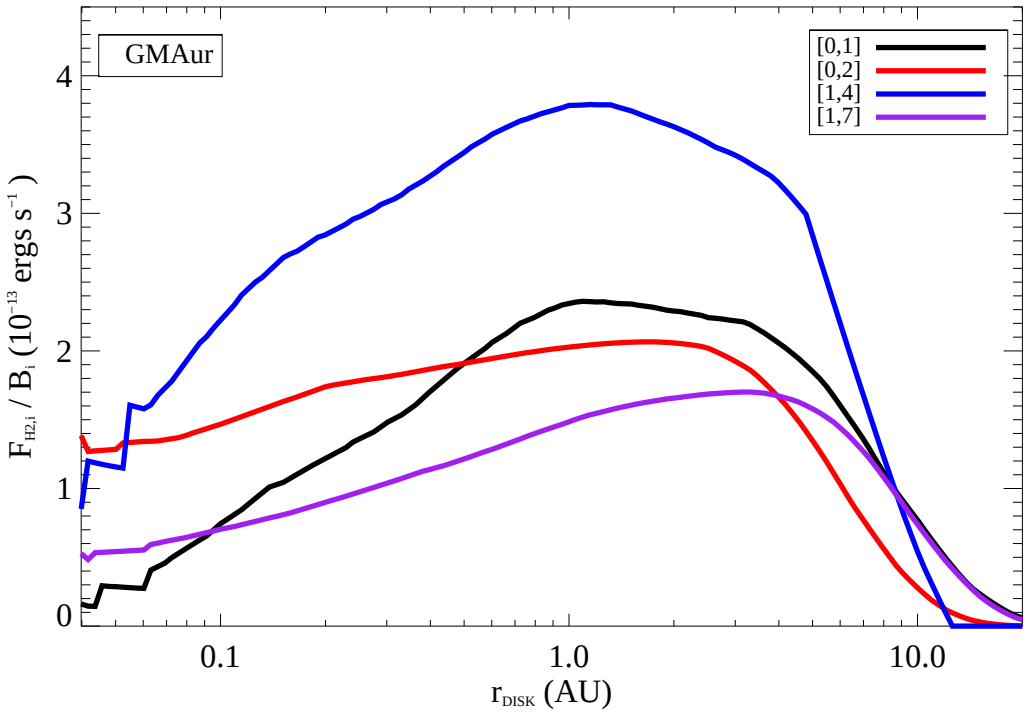

Figure 2.4 Using the best-fit progression model for GM Aur, I use Equation 2.12 to reproduce the observed spectrum. Each progression peaks at different radii, but the overall shape and radial extent of the distributions indicate that the bulk of the radiation for all progressions originates within similar disk annuli.

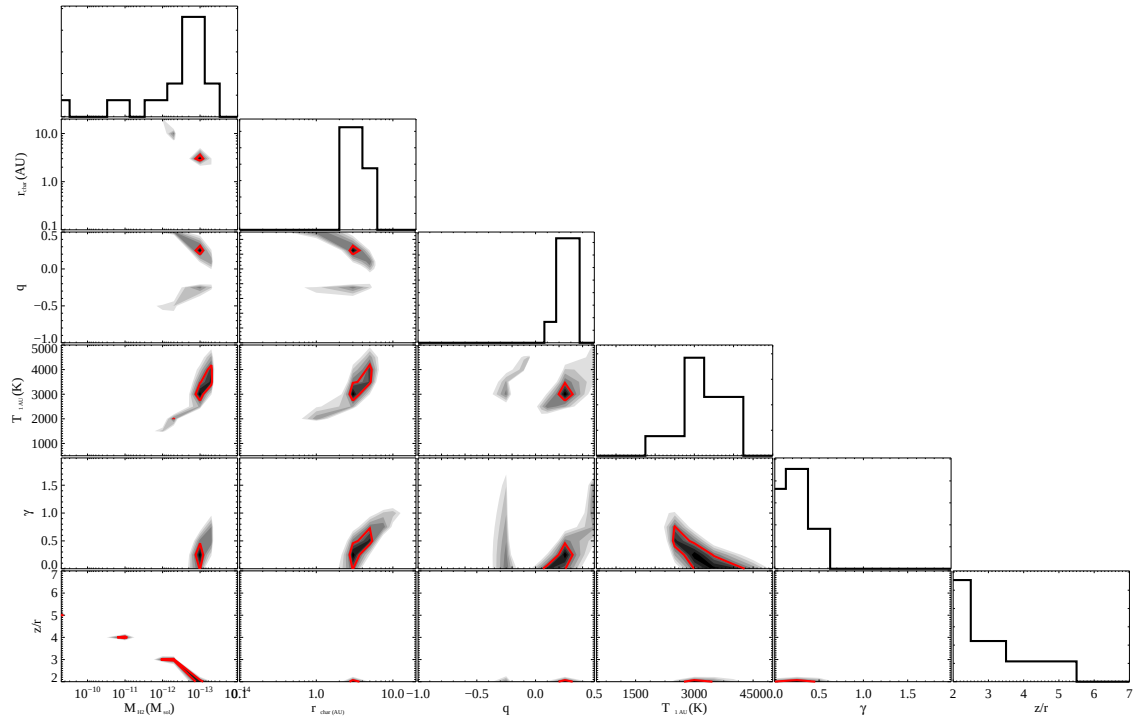

Figure 2.5 Marginalized distributions of the [1,4] progression reduced-χ^2 fits for RECX-11. The uncertainties in the best-fit model parameters are measured as the range of values that encompass 68% of the distribution area and are highlighted in red contour outlines. The posterior marginalized distributions for each parameter against all other model parameters are shown as the 2D plots at the top of each column.

increases. This trend makes sense - to produce the same amount of flux in the modeled emission lines, the total mass of H_2 contributing to the emission must increase as the density of H_2 decreases with vertical disk height above the mid plane. The optical depth of the disk atmosphere must remain the same to output the same observed emission line flux, and this relationship between the free parameters maintains the required optical depth. What is important to note is that the models produced are used as a means to describing the H_2 emission flux arising from the inner disk atmosphere. Despite the degeneracies in several parameter pairings relating to the total flux, the radiation distribution of H_2 emission is unaffected by these degeneracies.

2.5.2 The Radial Extent of H_2 Emission

Figure 2.4 represents an example of the radiation distributions of H_2 fluorescence flux produced in the disk for each progression explored in this study. The analysis from here focuses on results with the [1,4] radiation distributions for all targets, which are used to define inner and outer radial H_2 disk boundaries. These parameters describe where the bulk (90%) of the emitting H_2 atmosphere resides and fluoresces to produce the emission features observed with *HST*. I define the 90% emitting region as follows:

$$F_{H_2,obs} = \begin{cases} \frac{F(H_2,r)}{F_{tot}(H_2)} & \leq 0.95 \text{ for } r > r_{in} \\ \frac{F(H_2,r)}{F_{tot}(H_2)} & \leq 0.95 \text{ for } r < r_{out} \end{cases} \tag{2.13}$$

I use r_{in} and r_{out} to evaluate the evolutionary behavior of the H_2 radiation. Figure 2.6 presents a schematic of how the inner and outer radial boundaries encapsulate 90% of the total H_2 flux produced in the disk atmosphere. I analyze potential evolutionary characteristics of the molecular disk atmosphere by comparing the FUV H_2 radiation distributions to other dust and molecular disk observables.

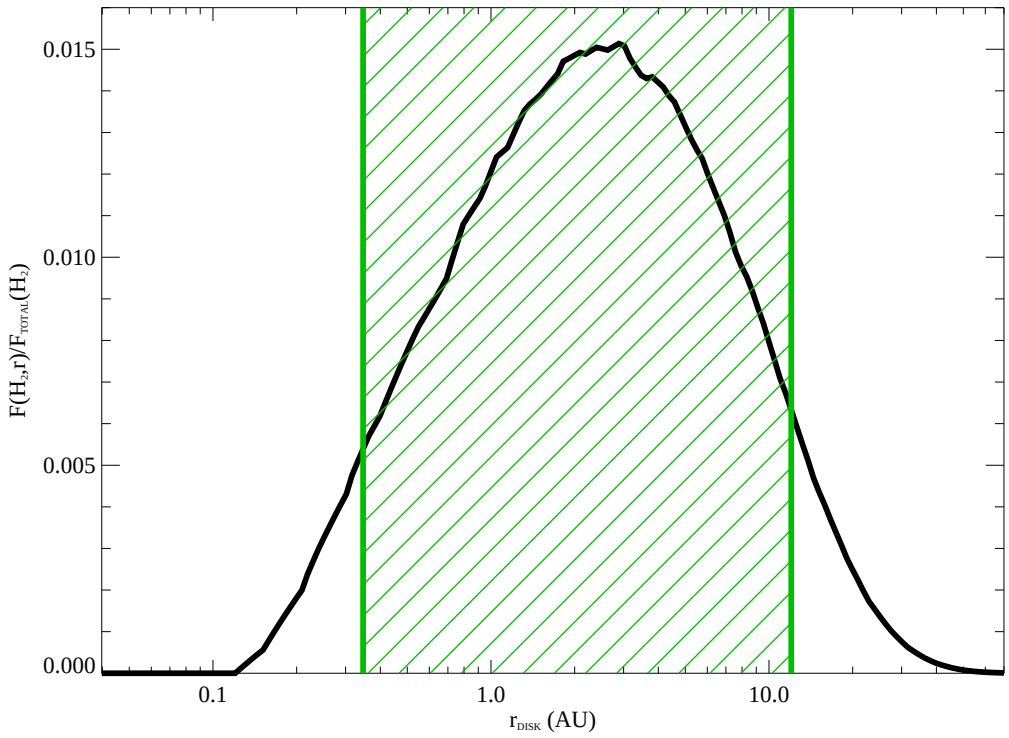

Figure 2.6 The inner and outer radial boundaries which define where 90% of the total radiation is arising from the disk. The black line represents the normalized radial distribution of the [1,4] progression emission for SU Aur. The green vertical lines show the radial boundaries that encapsulate 90% of the total emission.

2.5.3 Case Study: Model Robustness using AA Tau

I test the robustness of this modeling framework by comparing model outputs for two epochs of *HST*-COS data on AA Tau (2011 and 2013). The 2013 observations occur during a "dimming" event observed pan-chromatically (from X-ray through the near-IR). Based on the duration of the dimming, Bouvier et al. (2013) suggest an obscuration at r > 8 AU; this hypothesis is strengthened by the gas-to-dust ratio (N_H/A_v) of the absorber and the evolution of the FUV H_2 emission (Schneider et al. 2015). I utilize the line profile changes between AA Tau *HST*-COS FUV observing epochs to determine how those changes relate to radial H_2 radiation distributions in the disk.

There are noticeable differences between the observed FUV H_2 emission line profiles of the 2011 and 2013 AA Tau epochs. The 2013 emission lines are narrower with slightly larger peak fluxes than the same H_2 emission lines observed in 2011 (Schneider et al. 2015). This suggests that less flux is contributed from the innermost disk, but excess flux from warm H_2 further out in the disk could be contributing to the line profiles. The modeling results for the [1,4] progression are shown in Figure 2.7. Each AA Tau epoch was modeled independently, and the models reproduce the same rest wavelength emission lines. Figure 2.7 also shows the radiation distributions of [1,4] fluorescence for each epoch in the AA Tau disk. The 2011 emission includes a large contribution from material inside 1 AU ($r_{in,2011} = 0.08\pm0.01$ AU; $r_{peak,2011} = 0.75$ AU; $r_{out,2011} = 4.17\pm2.04$ AU), while the 2013 [1,4] emission "appears" to have shifted outward in the disk ($r_{in,2013} = 0.15\pm0.02$ AU; $r_{peak,2013} = 2.50$ AU; $r_{out,2013} = 7.59\pm2.75$ AU). My models indicate that the inner radius of detectable H_2 fluorescence from the [1,4] progression has moved outward radially in the disk as the "extra absorber" moved into the field of view in the AA Tau disk. Schneider et al. (2015), using an independent modeling technique to estimate the radial origins of H_2 fluorescence in the AA Tau disk, come to a similar conclusion: the observed 2013 H_2 emission within $\sim$ 1 AU is reduced compared to 2011.

The "extra absorber" obscures the inner disk H_2 fluorescence in the 2013 *HST*-COS FUV spectrum, making AA Tau appear as a disk with a deficit of inner disk emission - effectively, a

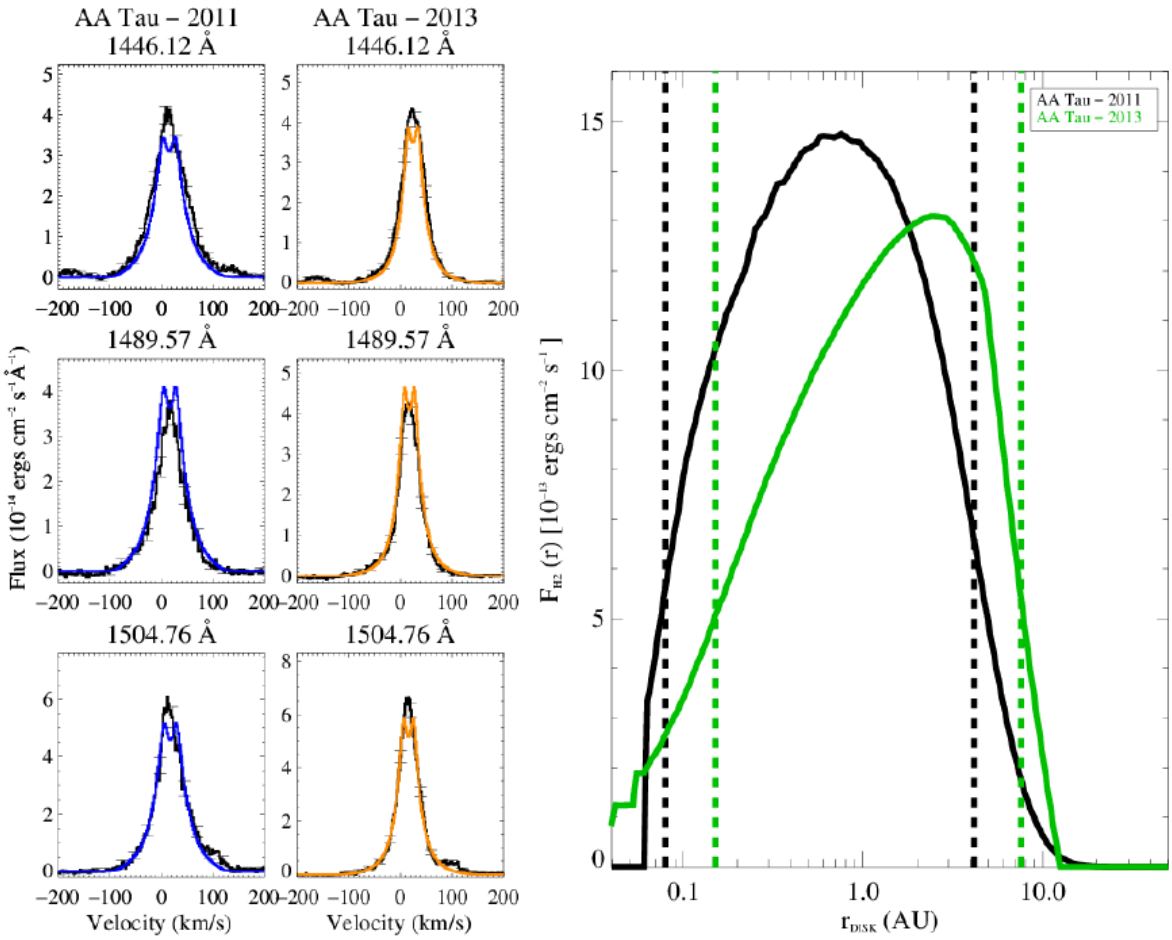

Figure 2.7 The comparison of the [1,4] progression observed with *HST*-COS for AA Tau, observed in 2011 and 2013. **Left:** The column under the 2011 label represent the 3 observed fluorescent emission line profiles cascading from the [1,4] excited state, with overlaid best-fit modeled emission lines in blue. The column to the right, labeled 2013, shows the observed [1,4] fluorescent emission lines, with modeled emission lines overlaid in orange. **Right:** The total [1,4] progression modeled flux radiating from the disk of AA Tau in the 2011 and 2013 observations.

pseudo-transition disk. My modeling framework was able to identify the changes in emission line profiles between the 2011 and 2013 AA Tau observations and found that the bulk of the 2013 AA Tau [1,4] radiation in the disk originated at larger radii than the 2011 H_2 fluorescence.

2.6 Discussion

I have created 2D radiative transfer models of warm fluorescent H_2 in PPDs to simulate observed *HST*-COS and -STIS FUV H_2 emission lines and understand where the majority of the FUV H_2 radiation arises from PPDs. I use the best-fit model results to define the inner and outer radii of warm H_2(r_{in}, r_{out}) and examine if and how the molecular distributions change as PPDs evolve. I compare r_{in} and r_{out} to other dust and molecular tracers that help describe the evolutionary state of the PPDs. Table 2.5 provides a detailed list of inner disk observables for each target, including dust cavity radius (r_{cavity}) and inner disk CO radius ($r_{in,CO}$). I also look at where the theoretical snow lines in the disks exist and how these radii relate to the H_2 disk emission.

2.6.1 Radiation Distribution of Modeled H_2 Fluorescent Emission

Figure 2.8 presents the normalized radial distributions of warm H_2 transitioning from excited state [1,4] for all targets. I modeled 6 primordial disks (AA Tau, BP Tau, DF Tau A, HN Tau A, RECX-11, and RECX-15) and 8 transition disks (CS Cha, DM Tau, GM Aur, LkCa 15, SU Aur, TW Hya, UX Tau A, and V4046 Sgr) to compare the radial distribution of warm H_2 in the disk atmospheres as the dust disk evolves. The H_2 radial distributions of the different dust disk stages appear qualitatively different. The primordial disk population (top plot in Figure 2.8) generally starts radiating significantly in the very inner disk ($r \lesssim 0.05$ AU), and the radiation only extends out to a few AU, consistent with the simple estimates of the average H_2 emitting radius presented by France et al. (2012c). The generalized transition disk radiation behavior (bottom plot) starts further out in the disk ($r \sim 0.1$ AU) and extend significantly further out into the disk ($r \sim 10$ AU). These different behaviors suggest structural changes in any of all of the following: the spatial distributions of warm H_2 in populations [v,J]; the degree of Lyα penetration into the disk

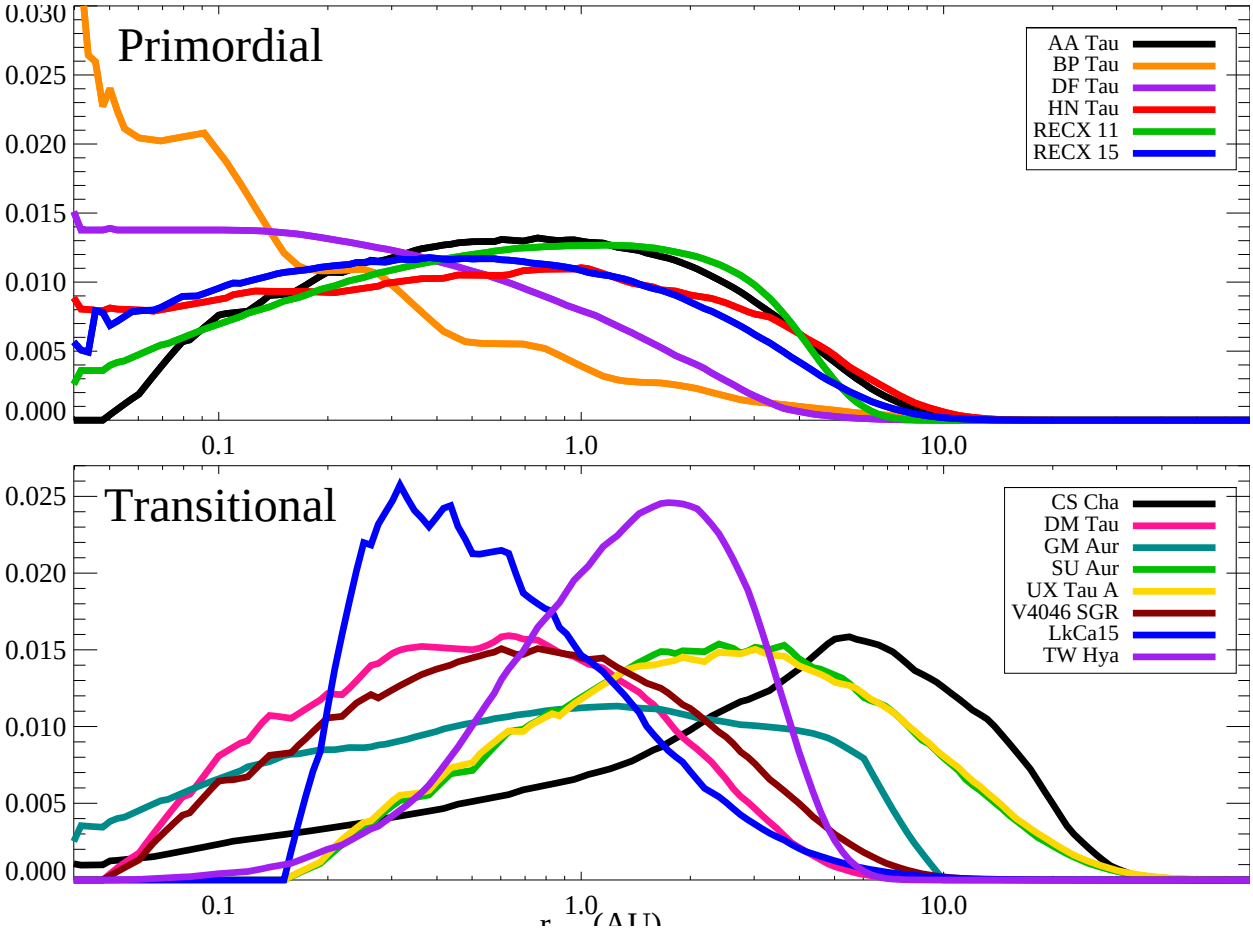

Figure 2.8 The normalized modeled radiation field distribution of H_2 fluorescence cascading from the $[v',J'] = [1,4]$ energy level for all targets. The top plot shows radiation distributions for all primordial disk targets, and the bottom plot shows the distributions for transition disks. The two disk evolution types appear to show an evolving H_2 FUV radiation field; primordial disks generally radiating more inward in the disk, with the bulk of the radiation occurring within r $\lesssim$ 1 AU, and transition disk H_2 radiation starting at larger radii (r $\sim$ 0.1 AU) extending to larger radii (r $\sim$ 10 AU).

by clearing H_2 from the inner disk atmosphere; or the evolution of the disk surface temperature distribution. This evolving radiation structure is also observable in the line profiles of the [1,4] progression, as seen in Figure 2.9. As the PPDs in our survey evolve from primordial to transition disks, the majority of the observed H_2 emission migrates to larger radii.

I compare estimates of r_{in} and r_{out} to investigate the idea that the radial distributions of fluorescing H_2 migrate outward in the disks as PPDs evolve. Figure 2.10 presents a comparison of r_{in} and r_{out}, which shows the annulus of H_2 emission extending further out into the disk as the inner disk radius moves outward. A line can be fit to represent the relationship between the inner and outer radiating disk radii for our survey targets:

$$\log_{10}(r_{out}(H_2)) = 0.79\ \log_{10}(r_{in}(H_2)) + 1.39, \tag{2.14}$$

where both $\log_{10}(r_{in}(H_2))$ and $\log_{10}(r_{out}(H_2))$ are in units of AU, and the coefficients [1.39 $\pm$ 0.22, 0.79 $\pm$ 0.21] are computed from a χ^2 minimization (χ^2_{min}=0.896) of a linear function between $\log_{10}(r_{in}(H_2))$ and $\log_{10}(r_{out}(H_2))$. The Spearman rank correlation coefficient between r_{in} and r_{out} indicates a statistically significant correlation between the variables ($\rho = 0.70$) with a small probability that the sample is randomized ($n = 5.5 \times 10^{-3}$), providing additional evidence that support the migration of the radial H_2 emission as PPD warm dust dissipates from the inner disk.

2.6.2 Comparison to Dust Evolution

I compare the results from the modeled H_2 [1,4] progression radial distributions with dust disk evolution diagnostics to gain insight into how the molecular inner disk environment of PPDs changes as dust grains clear. I identify PPD evolution using observed color-color changes in the near- to mid-IR SED slope of the disk, which provides an estimate of the degree of warm dust clearing (see Espaillat et al. 2014). The slope of each target SED is defined by the quantity n_{13-31} (Furlan et al. 2009):

$$n_{13-31} = \frac{log(\lambda_{31}F_{\lambda_{31}}) - log(\lambda_{13}F_{\lambda_{13}})}{log(\lambda_{31}) - log(\lambda_{13})}, \tag{2.15}$$

Table 2.5. Disk Parameters from Results & Literature

Target	n_{13-31}	$\dot{M}$[a] ($M_\odot$ yr^{-1})	r_{in,H_2} (AU)	r_{out,H_2} (AU)	$r_{in,CO}$ (AU)	r_{cavity} (AU)	T(H_2) K	ref.[b]
AA Tau	-0.51	1.5	0.08 ± 0.01	3.47 ± 0.54	0.10	...	4000^{+250}_{-1500}	2,11
BP Tau	-0.58	2.9	0.04 ± 0.01	0.87 ± 0.10	0.03	...	2000±300	1,2,11
CS Cha	2.89	5.3	0.23 ± 0.05	21.88 ± 4.68	...	40	2500±400	5
DF Tau A	-1.09	17.7	0.04 ± 0.01	1.26 ± 0.89	0.10	...	1500^{+1000}_{-100}	11
DM Tau	1.30	0.29	0.11 ± 0.01	2.19 ± 1.48	...	3	2000±500	3,4,10
GM Aur	1.76	0.96	0.10 ± 0.01	7.59 ± 2.75	0.20	20	3000±450	1,2,3,4,11
HN Tau A	-0.44	0.13	0.04 ± 0.01	3.80 ± 0.20	...	...	2500±750	
LkCa 15	0.62	0.31	0.20 ± 0.04	6.03 ± 2.45	0.10	46	1500^{+1250}_{-200}	1,3,6,10,11
RECX-11	-0.80[c]	0.03	0.07 ± 0.02	3.98 ± 2.00	...	...	3000^{+1000}_{-1250}	
RECX-15	-0.20[c]	0.10	0.05 ± 0.01	2.63 ± 1.62	...	7.5 ± 1.5	2500±350	12
SU Aur	0.74	0.45	0.35 ± 0.12	12.02 ± 3.47	...	...	1500^{+1250}_{-300}	
TW Hya	0.20[c]	0.02	0.38 ± 0.14	3.98 ± 1.0	$0.1^{+0.2}_{-0.04}$	4	2000^{+500}_{-150}	3,4,10
UX Tau A	1.83	1.00	0.25 ± 0.06	12.03 ± 3.46	0.30	25	1500^{+1000}_{-300}	3,6,11
V4046 Sgr	0.32[c]	1.30	0.11 ± 0.01	3.31 ± 1.82	...	14	2000±500	8,9

[a] All $\dot{M}$ values taken from Ingleby et al. (2013) and multiplied by 10^{-8}.

[b] (1) Akeson et al. (2005); (2) Andrews and Williams (2007); (3) Andrews et al. (2011); (4) Calvet et al. (2005); (5) Espaillat et al. (2007a); (6) Espaillat et al. (2007b); (7) France et al. (2012c); (8) Rapson et al. (2015); (9) Rosenfeld et al. (2013); (10) Salyk et al. (2009); (11) Salyk et al. (2011a); (12) Woitke et al. (2011)

[c] For $n_{13-31}\mu m$ values not listed in Furlan et al. (2009), we use Equation 2.15 to estimate the observable from known or modeled dust SED.

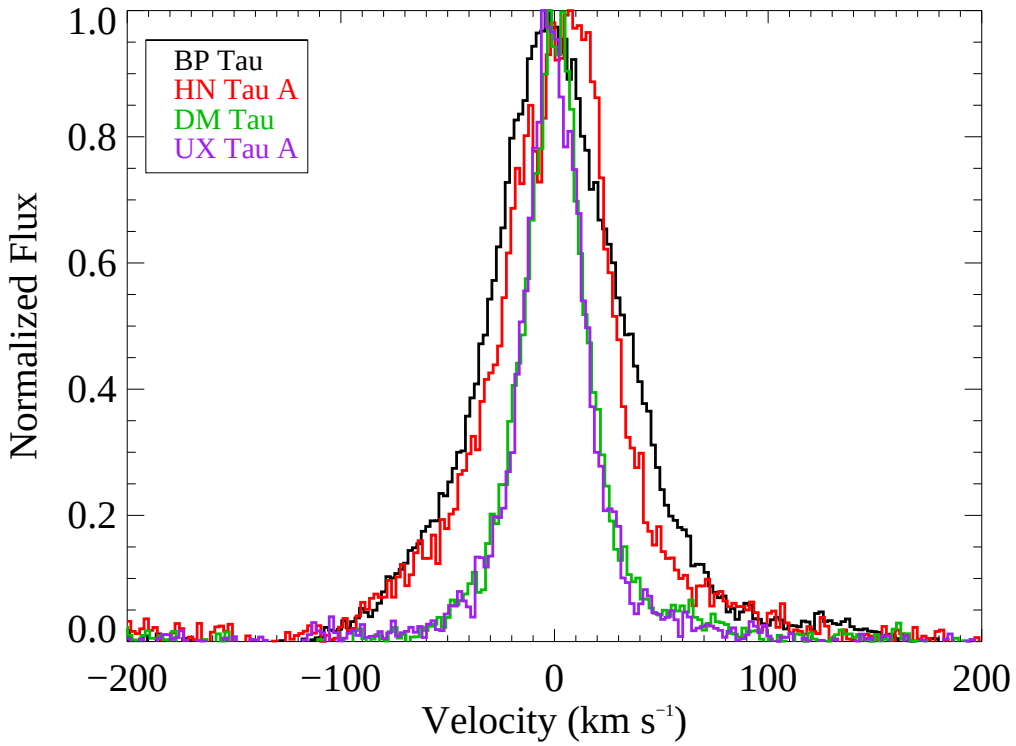

Figure 2.9 A comparison of observed [1,4] progression line profiles of targets with inclination angles between 30° and 40°. The two broadest line profiles, BP Tau and HN Tau A, are primordial disks. The two narrowest line profiles, DM Tau and UX Tau A, are transition disk targets.

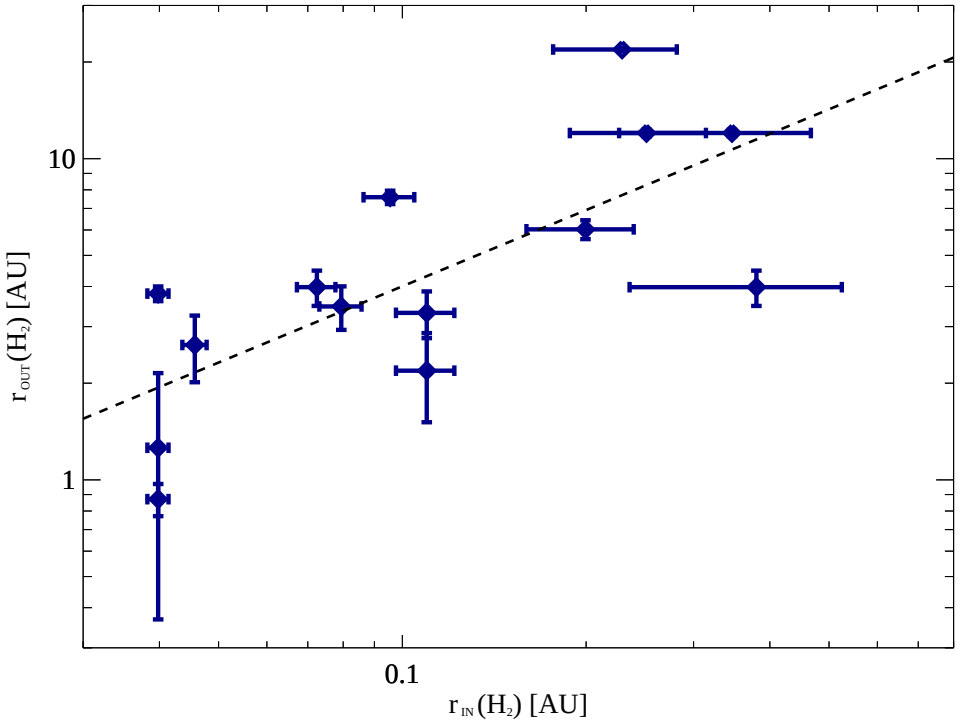

Figure 2.10 The relation between the estimated r_{in} and r_{out} quantities, determined from the best-fit modeled radiation distributions for all targets. The blue diamonds with error bars represent each modeled r_{in} and r_{out}, and the black dashed line represents a linear fit to the data.

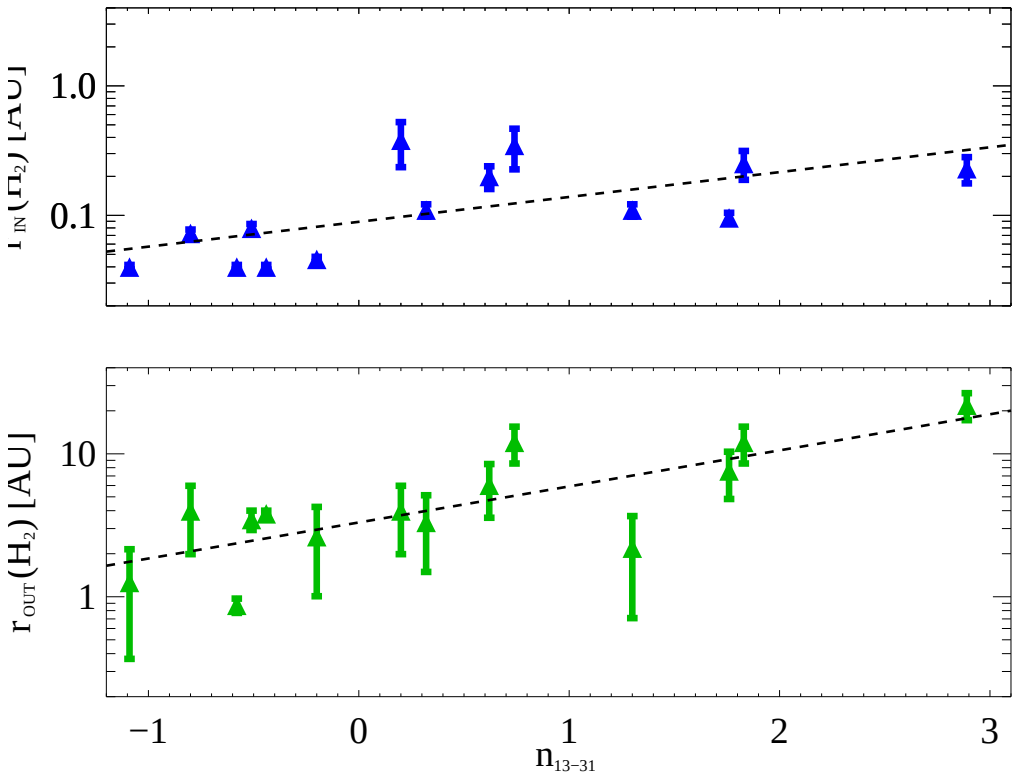

Figure 2.11 Comparison of r_{in} and r_{out} with an observable dust evolution diagnostic n_{13-31} (Furlan et al. 2009). **Top:** Each blue triangle with error bars represents a target point in our survey. The black dashed line represents the best-fit linear correlation between r_{in} and n_{13-31}. **Bottom:** Each green triangle with error bars represents a target point in our survey. The black dashed line represents the best-fit linear correlation between r_{out} and n_{13-31}. In both plots, a clear increasing trend is seen in the radial H_2 emission boundaries as the warm dust disk content evolves.

which is dominated by longer wavelength continuum emission from the optically-thick dust in the disk and is sensitive to the degree of dust settling towards the disk midplane (D'Alessio et al. 2006). For many targets in this work, n_{13-31} were available in Furlan et al. (2009), but for targets not included in the Furlan et al. (2009) survey, I calculated n_{13-31} with known or modeled disk SEDs (for example, an intricate model of V4046 Sgr SED was presented by Rosenfeld et al. 2013). The results of n_{13-31} are interpreted as follows: if $n_{13-31} < 0$, the inner dust disk is optically thick, essentially a primordial disk; if $n_{13-31} \geq 0$, the disk dust is optically thin, indicative of dust clearing or settling and evidence for PPD evolution into the transition state (Lada 1987, Strom et al. 1989, Andre and Montmerle 1994). Table 2.5 provides a list of n_{13-31} values for all targets in this survey.

A comparison of the [1,4] emission boundaries (r_{in}, r_{out}) to n_{13-31} is presented in Figure 2.11. The triangles in both plots represent each target in our survey, and the black dashed line in each plot shows the linear correlation between r_{in} versus n_{13-31} and r_{out} versus n_{13-31}. It is apparent that the molecular inner and outer disk emission radii show a positive correlation with the dust disk evolution: the Spearman rank correlation coefficient for r_{in} versus n_{13-31} is 0.72 (n = 4.0 x 10^{-3}), and $\rho = 0.69$ for r_{out} versus n_{13-31} (n = 6.9 x 10^{-3}). Both correlation coefficients suggest a strong increasing trend in the radial outward migration of the FUV H_2 radiation as the warm dust disk evolves in the disk samples. The linear correlation between r_{in} and n_{13-31} is expressed as:

$$\begin{aligned} \log_{10}(r_{in}(H_2)) =& (0.19 \pm 0.07) \times n_{13-31} \\ & - (1.05 \pm 0.08), \end{aligned} \tag{2.16}$$

and the linear correlation between r_{out} and n_{13-31} is expressed as:

$$\begin{aligned} \log_{10}(r_{out}(H_2)) =& (0.25 \pm 0.06) \times n_{13-31} \\ & + (0.52 \pm 0.07). \end{aligned} \tag{2.17}$$

Interestingly, for all transition disks in this study, r_{out} is found to be within the dust gap radius. One interpretation of this result, paired with the correlation between r_{in} and n_{13-31}, is that the H_2 FUV radiation observed from the inner PPD atmosphere lags behind the dust disk evolution.

This result does not automatically mean that the molecular content of the disk is clearing, and further evidence of evolution with other inner disk molecular tracers is needed before that distinction can be made. France et al. (2012c) outlined the conditions needed in the H_2 disk atmosphere to produce Lyα-pumped H_2 fluorescence. The opacity of absorbing H_2 in ground-state [v,J] must be large, with excitation temperatures $T_{exc} > 1500$K, and the mass accretion rate ($\dot{M}$) onto the proto-star must be large enough to produce enough Lyα photons to stimulate the molecules. The mass accretion rate implies there is a reservoir of material in the inner regions of PPDs that feeds onto the proto-star, and a decrease in $\dot{M}$ over time (e.g., Muzerolle et al. 2000) strongly suggests that the inner disk material is being depleted.

Figure 2.12 shows the relationship between $\dot{M}$ and $r_{in}(H_2)$, with purple points representing $r_{in}(H_2)$ and $\dot{M}$ for all targets except the RECX targets, which are represented at red diamonds. All mass accretion rates are taken from Ingleby et al. (2013). Figure 2.12 shows a negative correlation between $\dot{M}$ and $r_{in}(H_2)$, with Spearman rank correlation [ρ,n] = [-0.80, 1.9 x 10^{-3}] (not including the RECX targets), suggesting that the H_2 atmosphere may be physically thinned or in different ground-state populations not suitable for Lyα-pumping in the very inner disk regions of evolved PPDs. The outlier points in Figure 2.12, RECX-11 and RECX-15, appear to have abnormally low mass accretion rates given the evolutionary stage of the disks (Ingleby et al. 2011), and more targets of varying evolution may be needed to understand if this result is universal among a large sampling of PPDs. It is important to note that r_{in} is primarily dervied from the observed line widths of H_2 emission profiles, so determination of r_{in} is largely independent of the incident FUV flux.

The link between $\dot{M}$ and $r_{in}(H_2)$ suggests that the inner disk is clearing of material as the mass accretion rate declines. One explanation for this correlation is that the warm H_2 atmosphere dissipates with the small dust grains. Dust grains present in the disk atmospheres of primordial disks may give warm H_2 a formation site to replenish molecules lost to photo-dissociation and stellar accretion (see Augason 1970, Habart et al. 2004, Fleming et al. 2010). As the dust grains clear out and settle towards the disk midplane or evaporate from the inner disks of evolving PPDs,

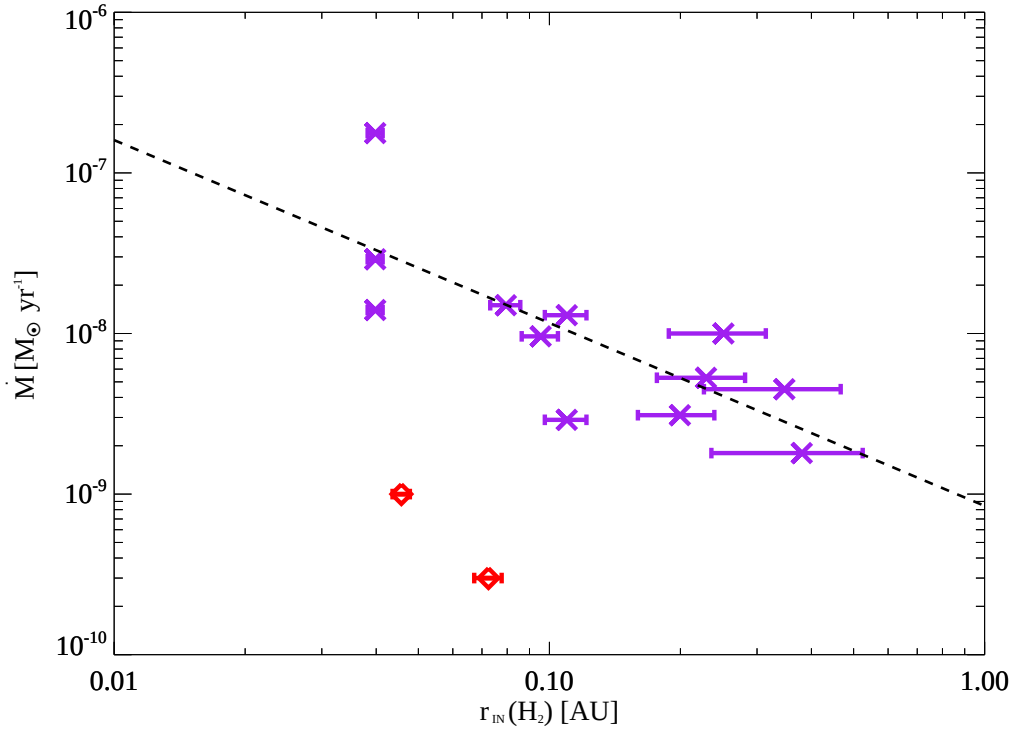

Figure 2.12 Comparison of the modeled inner H_2 emission radius to the mass accretion rate of the target (from Ingleby et al. 2013). The purple x-points represent all targets with mass accretion rates $> 10^{-9}$ $M_{\odot}$ yr^{-1}, while the red diamonds represent the RECX targets (which have known low mass accretion rates). The black line is a negative correlation fit through all the purple points, suggesting that the mass accretion rate decreases as r_{in} increases.

the warm H_2 atmosphere no longer has a formation site to maintain the molecular reservoir. Via accretion and photo-dissociative processes with FUV continuum photons between $\lambda\lambda$ 912 - 1120 Å, the leftover warm H_2 will continue to disperse, even as the accretion flux decreases. This leaves an optically thin ($N(H_2) \lesssim 10^{18} cm^{-2}$) path for stellar Ly$\alpha$ to reach the warm H_2 material at larger disk radii (r > 3 AU).

The migration of $r_{out}(H_2)$ with increasing n_{13-31} also suggests that neutral hydrogen (HI) is being cleared from the inner disks of transitional PPDs. Photo-excitation via stellar Lyα drives the H_2 fluorescence observed in the disk atmospheres, and as the emitting H_2 is observed further out in the disk, there must be new paths open for stellar UV radiation to reach the outer disk material. In primordial disks, HI re-processes and scatters incident stellar Lyα down into the inner disk (Fogel et al. 2011) while H_2 self-shields the radiation from penetrating to the outer disk, preventing the stellar Lyα from reaching the outer disk effectively. If H_2 and HI column densities in the inner disk become optically thin in transitional disks, more stellar Lyα can irradiate molecular material in the outer disk and may explain the observed correlation between $r_{out}(H_2)$ and n_{13-31}. This suggests that HI clearing from the inner disk may happen over a similar timescale as the characteristic dust dissipation (Wyatt 2008, Ribas et al. 2014) and mass accretion quenching (Fedele et al. 2010). This inner-to-outer disk dissipation is in agreement with the UV switch model, which describes the dispersal of inner disk gas cut off from the gas reservoir of the outer disk, due to selective photoevaporation of material out to r $\sim$ 5 - 10 AU (Clarke et al. 2001, Alexander et al. 2006). Observations of other outer-disk molecules photo-excited by Lyα radiation provide additional evidence for the loss of HI in the inner disks of transitional objects. For example, Schindhelm et al. (2012a) observe FUV-CO fluorescence, also powered by stellar Lyα-pumping, at $T_{exc} \sim$ 500K, in transitional phase objects with an average emission radius $R_{CO} \sim$ 1 - 5 AU. This indicates that less HI and H_2 column is present in the inner disk to shield the stellar Lyα flux from reaching the cooler CO material at intermediate radii in transition systems. UV heating of CO at larger disk radii is also suggested to explain near-IR CO emission observed from evolved PPDs samples by Banzatti and Pontoppidan (2015).

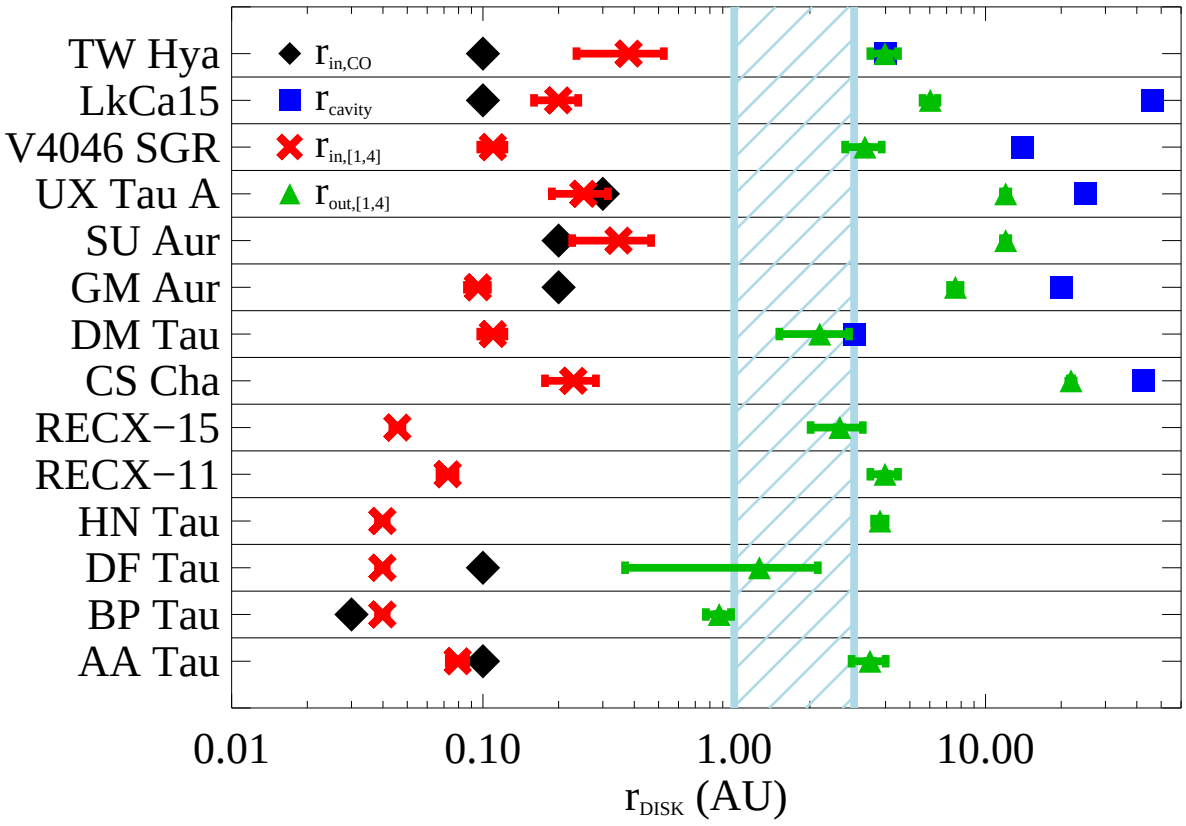

Figure 2.13 A radial comparison of the inner and outer extent of FUV H_2 emission (this work), the innermost radius of near-IR CO emission (Salyk et al. 2011a), and dust cavity locations in transition disk targets (see Table 2.5 for references). The light blue shaded area from 1 AU $\leq$ r_{DISK} $\leq$ 3 AU represents the theoretical water-ice snow line for the presence of water-ice at the midplane of primordial and transitional PPDs (Baillié et al. 2015).

Figure 2.13 shows a 1D radial comparison of dust and molecular tracers determined in this study and others. I present the locations of the outer radiation boundary for H_2 FUV emission, as determined from my models ($r_{out,[1,4]}$; green triangles), and the observed dust cavity walls of the transitional disk populations (r_{cavity}; blue squares). For all transitional disks, I find $r_{out,[1,4]}$ inward of r_{cavity}, meaning that the H_2 population observed in all transition PPDs radiates where the dust is optically thin. This suggests that the H_2 populations remain optically thick even after the dust grains have dissipated. Studies like van der Marel et al. (2015) also find a substantial depletion of the dust-to-gas ratio inside the dust cavities of well-studied transition disks, which is consistent with these findings.

2.6.3 Near-IR CO Emission and Comparison to Snow Line Radii

Figure 2.13 includes radial estimates of the inner radiation boundary for H_2 FUV emission ($r_{in,[1,4]}$; blue x's) and the inner radius of near-IR CO emission, determined from LTE models presented by Salyk et al. (2011a) ($r_{in,CO}$; black diamonds). The inner disk emission radii of FUV H_2 and near-IR CO appear to be roughly co-spatial, which is a result also found by France et al. (2012c) when comparing the observed FWHMs of FUV H_2 fluorescence emission and near-IR CO emission. An extensive study by Brown et al. (2013) and Banzatti and Pontoppidan (2015) concluded there is a correlation between the near-IR CO P(8) equivalent width and dust disk dispersal in transitional disks, suggestive of outer radial origins of the CO emission as PPD dust evolves. I have shown that $r_{in,[1,4]}$ increases with n_{13-31} and decreases with $\dot{M}$, providing further evidence that the inner gas disk environment becomes optically thin as disks evolve towards the transition stage.

The disk locations of possible theoretical snow lines in PPDs and the modeled H_2 fluorescence radii appears to coincide in Figure 2.13. As the disk evolves, it cools over time, so the snow line is expected to migrate inward in the disk as the protostellar system ages (Cassen 1994). Several independent studies (e.g. Meijerink et al. 2009, Mandell et al. 2012) conclude that the location of the water-ice snow line in PPDs are expected to be found within r $\sim$ 1 - 3 AU for all PPD

states. Baillié et al. (2015) shows that the evolution of the water-ice snow line at all stages of PPD evolution (from ages 10^6 - 10^7 yr) only varies by $\sim$ 0.5 AU. Observations of H_2O and OH (which is presented as a bi-product of H_2O dissociation) in the near- and mid-IR are also consistent with these condensation radii (Malfait et al. 1998, Carr et al. 2004, Mandell et al. 2008, Salyk et al. 2008). Figure 2.13 includes a shaded blue region that represents the assumed, generalized H_2O snow line radii in PPDs, located between r_{DISK} = 1 - 3 AU. With the exception of BP Tau and DF Tau A, all targets have outer H_2 emission radii that extend to within or outward of the water-ice snow line.

Chapter 3

The Behavior of Molecular Hydrogen in Protoplanetary Disk Environments

"A bottle of tequila in the shape of Texas. What more could you ask for?"
- Larry Conser, upon visiting the liquor store next to State Line BBQ.

3.1 Introduction & Scientific Motivation

The presence of significant amounts of gas in the disk is a defining quality of PPDs, where the earliest stages are assumed to have the canonical interstellar medium (ISM) gas-to-dust ratio $\sim$ 100:1 (e.g., Frisch et al. 1999, Tilling et al. 2012, Schneider et al. 2015). The gas content in PPDs controls essential processes tied to the formation and evolution of planetary systems, including dust grain growth (through the coupling of gas and dust dynamics), angular momentum transport, and thermal and chemical balance of the disk as it evolves (Weidenschilling 1977, Alexander and Armitage 2007, Woitke et al. 2009b, Youdin 2011, Levison et al. 2015a). However, over timescales of a few Myr, PPDs lose their massive gas disk, evolving to gas-sparse debris disks (with gas-to-dust ratios $\sim$0:1; Alexander et al. 2014, Gorti et al. 2015). The dispersal of the gas-rich disk is likely driven by a number of different physical processes throughout the PPD lifetime, ranging from photoevaporation of gas in a slow, molecular wind (see review by Alexander et al. 2014) or magnetohydrodynamic (MHD) wind (e.g. Ferreira et al. 2006, Bai 2016), to giant planet formation accreting and clearing gas remaining in a dust gap (Lin and Papaloizou 1986, Dodson-Robinson and Salyk 2011, Zhu et al. 2011, Dong et al. 2015, Owen 2016). Probing the physical mechanisms that drive the dispersal of gas from PPDs is critical for inferring when,

where, and how planet-forming disks lose their massive gas reservoir. In turn, these properties inform us of the physical and chemical environment in which planets form throughout the PPD lifetime.

Internal radiation from the protostellar source can play an important role in determining the chemical and physical state of the gas-rich PPD (Kamp and Dullemond 2004, Nomura 2004, Nomura et al. 2007, Öberg et al. 2010, Bethell and Bergin 2011). Ultraviolet (UV) and X-ray radiation, which are created by hot gas accretion onto and activity within the proto-star, can effectively create populations of high energy molecules and pathways to dissociate molecules in the disk atmosphere (e.g. Glassgold and Najita 2001, Bergin et al. 2004, Gorti and Hollenbach 2004, Glassgold et al. 2004, Kamp et al. 2005, Dullemond et al. 2007, Güdel et al. 2007, Kastner et al. 2016). High-energy radiation may also help heat and regulate chemical processes in the disk atmosphere, leading to the production of highly energetic by-products (e.g. Salyk et al. 2008, Walsh et al. 2015, Ádámkovics et al. 2016). Hot molecules can be swept up into the slow molecular wind over the disk lifetime (Alexander et al. 2006, Gorti and Hollenbach 2009, Owen et al. 2010, Owen 2016), leading to the dispersal of the disk from the inside-out.

Observations of molecular hydrogen (H_2) in PPDs are important because H_2 directly traces the bulk of the gaseous reservoir of the disks without assuming gas-to-dust or CO-to-H_2 ratios. Molecular hydrogen has been measured to be 10^4 times more abundant than any other molecule in the warm regions of PPDs (France et al. 2014a), and large quantities of H_2 in the disk allow the molecule to survive at hot temperatures ($T(H_2) \sim 1000 - 4500$ K; Williams and Murdin 2000) and shield against collisional- and photo-dissociation (Beckwith et al. 1978; 1983). The properties of H_2 make it a reliable diagnostic of the spatial and structural behavior of warm molecules probed in and around PPDs (Ardila et al. 2002, Herczeg et al. 2004), as it is expected to reliably trace even residual amounts of gas in disks throughout their evolution ($\Sigma_{H_2} \sim 10^{-6}$ g cm^{-2}; e.g., France et al. 2012c).

The far ultraviolet (FUV: λ 912 $-$ 1700 Å) offers the strongest transition probabilities for dipole-allowed electronic transitions of H_2 photo-excited by UV photons, specifically absorption

avenues incident with HI-Lyα (λ 1215.67 Å) photons, which are generated near the protostellar surface (France et al. 2012c, Schindhelm et al. 2012b) and make up $\sim$ 90% of the FUV flux in a typical T Tauri system (France et al. 2014b). Warm H_2 (T $\geq$ 1000 K) can absorb Lyα photons, exciting the molecule up to either the Lyman ($2p\sigma B\ ^1\Sigma_u^+$) or Werner ($2p\pi C\ ^1\Pi_u$) electronic bands. Because of the large, dipole-allowed transition probabilities ($A_{ul} \sim 10^8$ s^{-1}; Abgrall et al. 1993a;b), H_2 in these electronic states will decay instantaneously back to the ground state in a fluorescence cascade, having transition probabilities to decay to one of many different rovibrational levels of the ground electronic state ($X^1\Sigma_g^+$; Herczeg et al. 2002). Each fluorescence transition results in the discrete emission of a FUV photon, whose frequency depends on the electronic-to-ground state transition. We observed hundreds of these features throughout the FUV with the *Hubble Space Telescope* (*HST*) from $\lambda\lambda$ 1150 $-$ 1700 Å (see Herczeg et al. 2002, France et al. 2012c). This process predominantly favors regions where warm molecules reside in disks (Nomura and Millar 2005, Nomura et al. 2007, Ádámkovics et al. 2016). The characterization of H_2 emission from PPDs have provided complimentary results to high-resolution IR-CO surveys probing PPD evolution (e.g. Brown et al. 2013, Banzatti and Pontoppidan 2015).

Additionally, the excitation leg of the fluorescence process can be inferred by observing H_2 absorption lines imposed directly on the broad Lyα emission line in PPD systems. Several studies have looked to characterize and relate the H_2 absorption features observed within protostellar Lyα wings to fluorescent populations tied to the behavior of the inner disk material. Yang et al. (2011) detected the first signatures of Lyα-H_2 absorption in DF Tau and V4046 Sgr. They found that, for V4046 Sgr, which hosts a disk with a relatively face-on inclination angle ($i_{disk} \sim 35°$), the H_2 would have to be pumped near the accretion shock to explain how H_2 absorption features are detectable in the sightline. France et al. (2012b) performed an extensive study on warm molecules in the disk environment of AA Tau and were the first to empirically derive H_2 column densities from absorption features within the Lyα red stellar wing. The lower energy states of H_2 could be described by a warm thermal population ($T(H_2) \sim 2500$ K $\pm$ 1000 K) consistent with H_2 fluorescence emission from the inner disk. They noticed that, for high excitation temperature states of H_2 ($T_{exc} \geq 20{,}000$

K), column densities deviated significantly from thermal distributions, providing the first hint that there may be additional excitation mechanisms in the disk atmosphere pumping H_2 out of local thermodynamic equilibrium (LTE).

The behavior of these non-thermal states may provide clues about the mechanisms that drive molecules out of LTE and, potentially, the dispersal of gas from planet-forming disks. For this study, I perform a quantitative, empirical survey of H_2 absorption observed against the HI-Lyα stellar emission profiles of 22 PPD hosts observed with *HST*/STIS and *HST*/COS. My goal for the project was to characterize the physical state of the molecular gas in each sightline and learn how stellar and disk mechanisms (internal radiation and environmental effects) may contribute to or help explain the observed behavior of H_2 rovibration states.

3.2 Targets and Observations

The target list for this survey of H_2 absorption signatures is derived from McJunkin et al. (2014), who analyzed the reddening of the HI-Lyα profiles of 31 young stellar systems to create a comprehensive list of interstellar dust extinction estimates along each sight line. All of these observations have been described previously in studies of H_2 (e.g. France et al. 2012c, Hoadley et al. 2015), hot gas (e.g. Ardila et al. 2013), and UV radiation (e.g. France et al. 2014b). Several of the targets are known binaries or multiples (DF Tau: Ghez et al. 1993; HN Tau, RW Aur, and UX Tau: Correia et al. 2006; AK Sco and HD 104237 are spectroscopic binaries: Gómez de Castro 2009, Böhm et al. 2004; and V4046 Sgr is a short-period binary, which acts as a point source for most applications: Quast et al. 2000), and only the primary stellar component is observed within the aperture when applicable. The majority of the targets are either observed within the Taurus-Auriga, Chamaeleon I, or η Chamaeleontis star-forming regions, with distances ranging from 140, 160, and 97 pc, respectively. Young stars observed in these star-forming regions have ages ranging a few Myr, while field pre-main sequence stars (e.g. TW Hya, AK Sco, V4046 Sgr) have ages ranges between $10 - 30$ Myr. The majority of these targets have age ranges comparable to the depletion timescale of gas and circumstellar dust via accretion processes (Hernández et al. 2007, Fedele et al.

Table 3.1. Target Properties

Target	Spectral Type	Disk Type[a]	Distance (pc)	$L_\star$ ($L_\odot$)	$M_\star$* ($M_\odot$)	$\dot{M}$ ($M_\odot$ yr^{-1})	i_{disk} (°)	Ref.[b]
AA Tau	K7	P	140	0.71	0.80	0.33	75	2, 4, 7, 12, 16, 52, 53
AB Aur	A0	T	140	46.8	2.40	1.80	22	19, 39, 49, 50, 52, 53
AK Sco	F5	P	103	7.59	1.35	0.09	68	18, 20, 34, 57
BP Tau	K7	P	140	0.925	0.73	2.88	30	7, 12, 38, 52, 53
CS Cha	K6	T	160	1.32	1.05	1.20	60	21, 35, 40, 54
DE Tau	M0	T	140	0.87	0.59	2.64	35	7, 10, 12, 52, 53
DF Tau A	M2	P	140	1.97	0.19	17.70	85	7, 10, 52, 53
DM Tau	M1.5	T	140	0.24	0.50	0.29	35	16, 29, 32, 52, 53
GM Aur	K5.5	T	140	0.74	1.20	0.96	55	7, 16, 32, 52, 53
HD 104237	A7.5	T	116	34.7	2.50	3.50	18	19, 23, 31, 45
HD 135344B	F3	T	140	8.13	1.60	0.54	11	19, 22, 31, 42, 57
HN Tau A	K5	P	140	0.19	0.85	0.13	40	6, 7, 12, 52, 53
LkCa 15	K3	T	140	0.72	0.85	0.13	49	12, 29, 32, 52, 53
RECX-11	K4	P	97	0.59	0.80	0.03	70	13, 24, 47, 55
RECX-15	M2	P	97	0.08	0.40	0.10	60	13, 14, 15, 55
RU Lup	K7	T	121	0.42	0.80	3.00	24	25, 30, 36, 41, 56
RW Aur A	K4	P	140	2.3	1.40	3.16	77	5, 9, 11, 12, 17, 52, 53
SU Aur	G1	T	140	9.6	2.30	0.45	62	1, 3, 8, 11, 12, 52, 53
SZ 102	K0	T	200	0.01	0.75	0.08	90	26, 37, 43, 48
TW Hya	K6	T	54	0.17	0.60	0.02	4	27, 30, 42, 51, 56
UX Tau A	K2	T	140	3.5	1.30	1.00	35	12, 32, 52, 53
V4046 Sgr	K5	T	83	0.5+0.3	0.86+0.69	1.30	34	28, 33, 44, 46

[a]Disk Type is defined by the degree of dust settling observed in the dust spectral energy distribution (SED) between 13 μm and 31 μm: P = primordial ($n_{13-31} < 0$); T = transitional ($n_{13-31} > 0$)

[b]**References:** (1) Akeson et al. (2002), (2) Andrews and Williams (2007), (3) Bertout et al. (1988), (4) Bouvier et al. (1999), (5) Eisner et al. (2007), (6) France et al. (2011a), (7) Gullbring et al. (1998), (8) Gullbring et al. (2000), (9) Hartigan et al. (1995), (10) Johns-Krull and Valenti (2001), (11) Johns-Krull et al. (2000), (12) Kraus and Hillenbrand (2009), (13) Lawson et al. (2004), (14) Luhman (2004), (15) Ramsay Howat and Greaves (2007), (16) Ricci et al. (2010), (17) White and Ghez (2001), (18) van den Ancker et al. (1998), (19) van Boekel et al. (2005), (20) Alencar et al. (2003), (21) Lawson et al. (1996), (22) Lyo et al. (2011), (23) Feigelson et al. (2003), (24) Lawson et al. (2001), (25) Herczeg et al. (2005), (26) Comerón and Fernández (2010), (27) Webb et al. (1999), (28) Quast et al. (2000), (29) Hartmann et al. (1998), (30) Herczeg and Hillenbrand (2008), (31) Garcia Lopez et al. (2006), (32) Andrews et al. (2011), (33) France et al. (2012b), (34) Gómez de Castro (2009), (35) Espaillat et al. (2007a), (36) Stempels et al. (2007), (37) Comerón et al. (2003), (38) Simon et al. (2000), (39) Tang et al. (2012), (40) Espaillat et al. (2011), (41) Stempels and Piskunov (2002), (42) Pontoppidan et al. (2008), (43) Coffey et al. (2004), (44) Rodriguez et al. (2010), (45) Grady et al. (2004), (46) Rosenfeld et al. (2012a), (47) Ingleby et al. (2011), (48) Hughes et al. (1994), (49) Hashimoto et al. (2011), (50) Donehew and Brittain (2011), (51) Rosenfeld et al. (2012b), (52) Bertout et al. (1999), (53) Loinard et al. (2007), (54) Luhman (2004), (55) Mamajek et al. (1999), (56) van Leeuwen (2007), (57) Grady et al. (2009).

*Multiplied by 10^{-8}.

2010), making them ideal candidates for understanding the abundance and physical state of H_2 at a variety of PPD evolutionary stages. Table 3.1 presents relevant stellar and disk properties.

Table 3.2 presents information about the observations and properties of the Lyα wing emission. All observations of the stellar Lyα profiles were taken either with the Cosmic Origins Spectrograph (COS) or Space Telescope Imaging Spectrograph (STIS) aboard the *Hubble Space Telescope* (*HST*).

3.2.1 COS Observations

Each PPD spectrum collected with *HST*/COS was taken either during the Disk, Accretion, and Outflows (DAO) of Tau Guest Observing (GO) program (PID 11616; PI: G. Herczeg) or COS Guaranteed Time Observing (PIDs 11533 and 12036; PI: J. Green). Each spectrum was observed with the medium-resolution far-UV modes of the spectrograph (G130M and G160M ($\Delta v \approx 18$ km s^{-1} at Lyα); Green et al. 2012). Multiple central wavelength positions were included to minimize fixed-pattern noise. The COS data were processed using the COS calibration pipeline (CALCOS) and were aligned and co-added with the procedure described by Danforth et al. (2010). By design, COS is a slitless spectrograph, allowing the full 2.5″ field of view through the instrument. This means the instrument is exposed to strong contamination from geocoronal Lyα (Ly$\alpha_\oplus$). To mitigate this contamination, I mask the central ~ 2 Å of the Lyα spectra.

3.2.2 STIS Observations

Several targets either exceeded the COS bright-object limit or had archival STIS observations available with the desired far-UV bandpass and resolution (AB Aur, HD 104237, TW Hya). The archival data were obtained with the STIS medium-resolution grating mode (G140M ($\Delta v \approx 30$ km s^{-1} between $1150 - 1700$ Å): Kimble et al. (1998), Woodgate et al. (1998)), while the COS-bright objects were observed with the echelle medium-resolution mode (E140M ($\Delta v \approx 7$ km s^{-1} between $1150 - 1700$ Å)). The STIS echelle spectra were processed using echelle calibration software developed for the STIS StarCAT catalog (Ayres 2010). Unlike COS, STIS has a small slit aperture

Table 3.2. Target Observation and Lyα Profile Properties

Target	*HST* PID[a]	Flux$_{red}$[b]	$\langle$SNR$_{red}\rangle$[c]	Flux$_{blue}$[b]	$\langle$SNR$_{blue}\rangle$[c]
AA Tau	11616	1.1 ± 0.2	5.9	0.3 ± 0.1	7.6
AB Aur	8065 - S	114.5 ± 54.4	1.8	-	-
AK Sco	11616 - S	35.0 ± 14.9	1.6	8.1 ± 1.2	0.6
BP Tau	12036	9.6 ± 0.7	12.0	7.9 ± 0.7	10.8
CS Cha	11616	14.4 ± 1.2	9.5	20.9 ± 1.5	11.1
DE Tau	11616	0.6 ± 0.2	2.9	-	-
DF Tau A	11533	19.6 ± 0.9	17.0	-	-
DM Tau	11616	1.3 ± 0.3	7.6	3.4 ± 0.5	6.8
GM Aur	11616	5.0 ± 0.8	5.8	4.5 ± 0.8	5.1
HD 104237	11616 - S	4238.7 ± 143.6	26.6	102.4 ± 53.8	2.5
HD 135344B	11828	38.5 ± 1.8	17.1	21.1 ± 1.4	12.8
HN Tau A	11616	0.22 ± 0.08	2.6	-	-
LkCa15	11616	0.34 ± 0.09	2.6	0.4 ± 0.1	2.2
RECX 11	11616	10.5 ± 0.7	18.1	7.2 ± 0.7	9.0
RECX 15	11616	64.7 ± 1.6	23.7	2.9 ± 0.4	4.9
RU Lupi	12036	23.7 ± 2.0	7.9	1.5 ± 0.6	1.9
RW Aur A	11616	18.0 ± 1.6	9.8.	2.0 ± 0.6	2.7
SU Aur	11616	0.9 ± 0.4	2.0	-	-
SZ 102	11616	11.2 ± 1.4	6.5	-	-
TW Hya	8041 - S	5760.8 ± 196.3	19.6	1412.7 ± 123.2	10.2
UX Tau A	11616	0.3 ± 0.1	2.1	0.9 ± 0.3	2.6
V4046 Sgr	11616	454.2 ± 4.5	67.0	367.5 ± 4.3	60.1

[a]Program IDs. PIDs with - S are STIS observations.

[b]Fluxes are the integral of the observed Lyα flux ($\times$ 10^{-12} ergs cm^{-2} s^{-1}).

[c]The average signal-to-noise (SNR) per resolution element across the Lyα emission feature from 1216.8 - 1221 Å (red) and 1210 - 1214.6 Å (blue, when applicable).

($0.2'' \times 0.2''$), so the Ly$\alpha_{\oplus}$ signal is weaker; nonetheless, I remove the inner region of the Lyα profile ($\sim 0.5 - 2$ Å) for consistency among all the data.

3.3 Lyα Normalization and Absorption Line Spectroscopy

I identify absorption signatures of H_2 in each sightline by creating transmission spectra of the stellar Lyα profiles of each PPD host. I treat each Lyα profile as a "continuum" source and normalize the emission feature, such that $I_{Ly\alpha} \approx 1.0$. A grid of $5 - 10$ unique spectral bins is created from $\lambda\lambda$ 1216.5 − 1221.5 Å (or $\lambda\lambda$ 1210.0 − 1215.0 Å for the blue wing component), which are each selected by hand to avoid molecular absorption features. Each grid bin is defined over 0.35 Å, to both smooth the Lyα emission feature while avoiding H_2 absorption features and to sample flux elements within the spectral resolution of both COS and STIS. Within each grid, I measure the mean and standard deviation along the Lyα profile and store them in binned flux and error arrays. I smooth each flux array with a boxcar function of size 0.5 Å over the Lyα bandpass and normalize the Lyα profile with this smoothed grid. An example of the smoothed grid array over the Lyα profile for one of the survey targets is shown in Figure 3.1, and all Lyα profiles are presented in Appendix B.

Figure 3.2 presents the normalized Lyα spectra for 6 targets, shown in order of inclination angle (edge-on targets on the bottom, and face-on targets towards the top). The effective "continuum" levels of the normalized Lyα flux profiles are indicated by the gray, dashed lines of each spectrum, and relative flux minima with full width half maximum (FWHM) greater than the spectral resolution of the data are interpreted as absorption features. I highlight where H_2 absorption features are expected to reside in the spectrum with a solid pink line. For the edge-on targets (DF Tau, RECX-11, RW Aur), it is apparent that the absorption features appear systematically red-shifted from the rest wavelength of H_2. For face-on targets (V4046 Sgr and HD 104237), the position of the absorption features matches with the expected laboratory wavelength of H_2. The observed red-shift in H_2 absorption is expected to within corrections made for the radial velocity ($v \sin i_{disk}$) of each target and the uncertainty in the COS wavelength solution ($\Delta v \sim 15$ km s^{-1}).

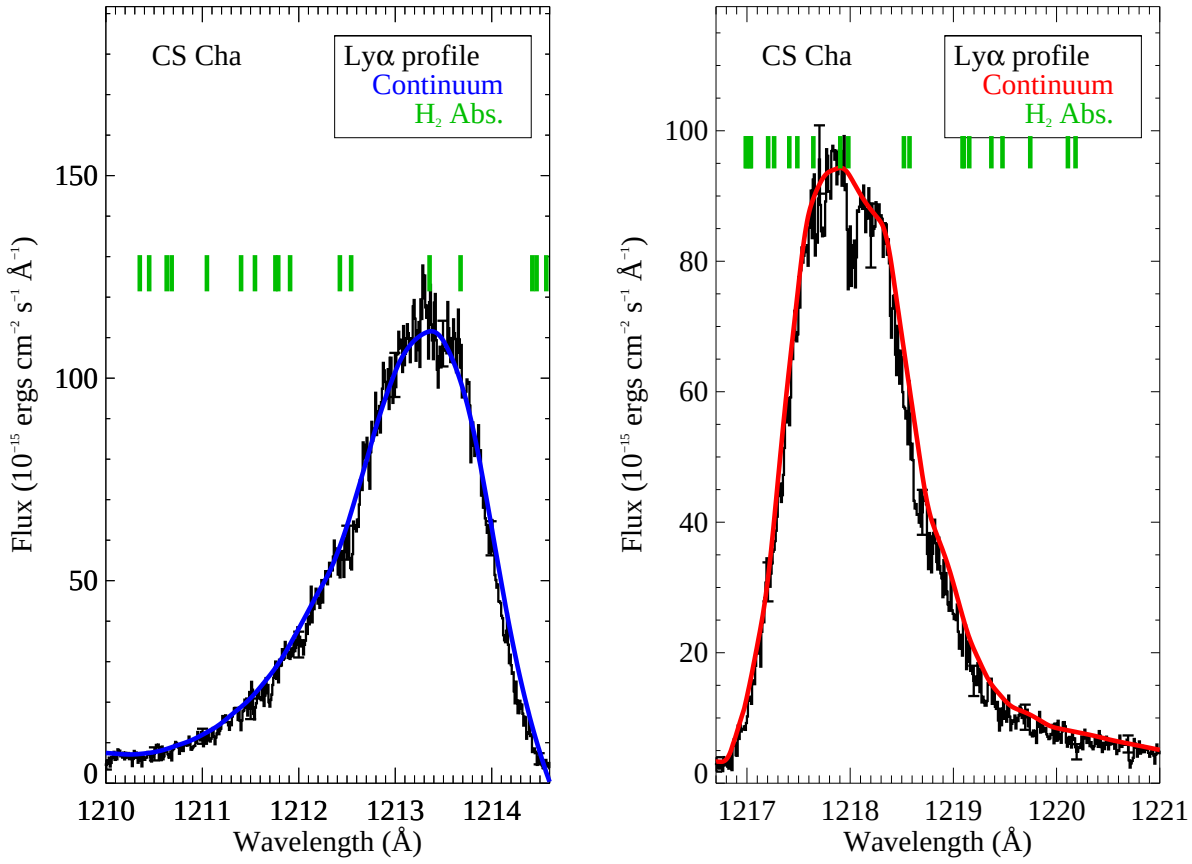

Figure 3.1 The stellar Lyα wings for one target (CS Cha) in our survey. Within the wings themselves, absorption signatures can be seen. The mean flux array over the Lyα profile is selected to minimize contamination from the absorption features and trace the shape of the Lyα wings. The mean flux array is smoothed (and shown in blue over the blue Lyα wing and red over the red Lyα wing), and the observed line profile is divided by the mean flux array to create relative absorption spectra across the Lyα profile. H_2 absorption transitions are identified with green hashes and properties about each transition are shown in Table 3.3.

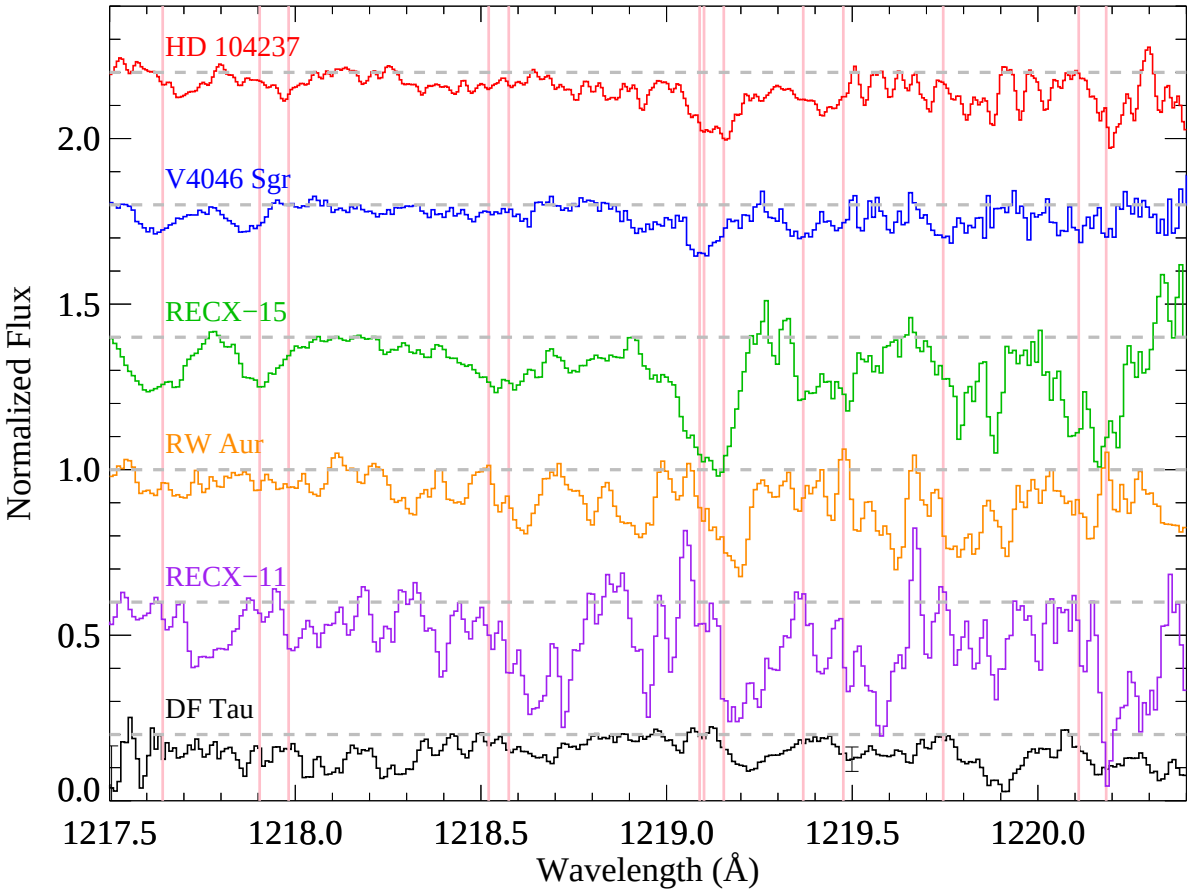

Figure 3.2 The normalized absorption spectra for 6 targets of this survey, ordered by increasing disk inclination angle (i_{disk}) from the top-down (11°, 34°, ∼60°, ∼70°, 77°, and 85°, respectively) from $\lambda\lambda$ 1217.5 − 1220.5 Å. Each target is shown in a different color and offset from $I_{Ly\alpha} \approx 1.0$, which is shown with the dashed gray horizontal line. The laboratory wavelengths of H_2 absorption features considered in this study are show with solid pink vertical lines. For each target, absorption profiles are expected to be red-shifted by $v \sin i_{disk} \approx 2$, 0, 10, 15, 19, and 16 km s^{-1}, respectively (Nguyen et al. 2012, Woitke et al. 2013, Quast et al. 2000), which correspond to $\Delta\lambda \sim 0.01$, 0.00, 0.04, 0.06, 0.08, and 0.07 Å.

Additionally, there are several absorption features seen in more than one target that do not coincide with marked H_2 features, most notably around 1218.35 Å, 1218.90 Å, and 1219.80 Å. Identification of these features will happen as a part of follow-up research pertaining to the results from this study, as outlined in Section 5.2.3.3.

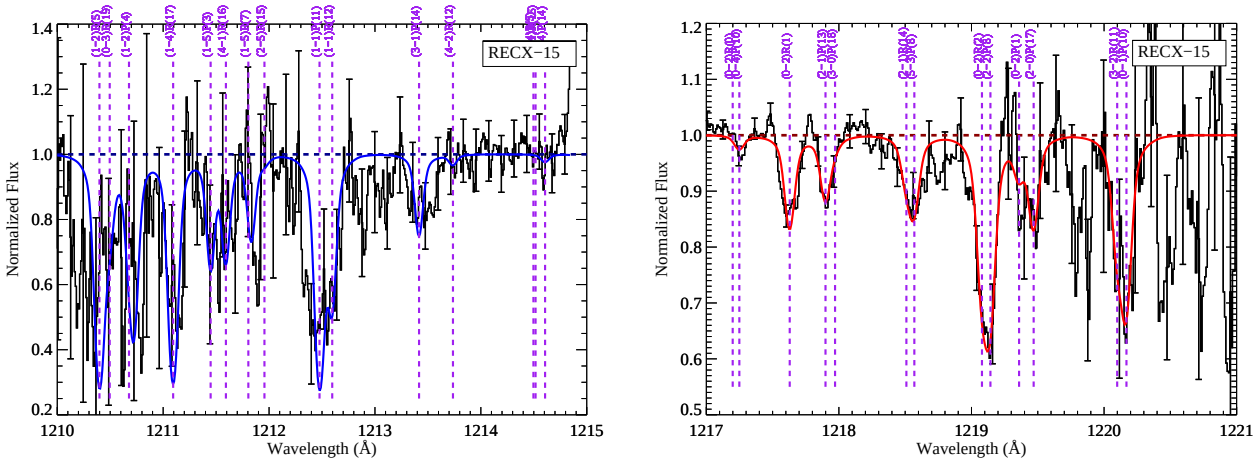

Figure 3.3 The best-fit H_2 absorption spectrum for RECX-15, assuming $b_{H_2} = 5$ km s^{-1} is shown in blue (**left**) and red (**right**) over the data (black). Prominent absorption features are labeled in each figure. Table 3.3 lists all H_2 features considered for the fit, and Table 3.4 presents best-fit thermal model parameters, given the distribution of rovibrational column densities derived from these absorption line fits.

I create a multi-component H_2 fitting routine to measure the column density in the absorption lines probed within the red and blue stellar wings of Lyα, pumped either into the Lyman ($2p\sigma B\ ^1\Sigma_u^+$) or Werner ($2p\pi C\ ^1\Pi_u$) electronic band system. Intrinsic line profiles of H_2 absorption are created from the molecular transition properties (listed in Table 3.3) to determine the column densities probed in each observed rovibrational [v,J] level. Each line profile is co-added in optical depth space, and a transmission curve is created, which is convolved with either the COS or STIS LSF (Kriss 2011), prior to comparison with the observed Lyα spectra. Each best-fit, multi-absorption H_2 spectrum H_2 is then determined using the `MPFIT` routine (Markwardt 2009). Initial conditions for each transmission curve were first determined by manually fitting each H_2 spectrum. To remove bias introduced by the choice of initial conditions, a grid of initial parameters was searched for all sampled absorption spectra. The only parameter allowed to float continuously for

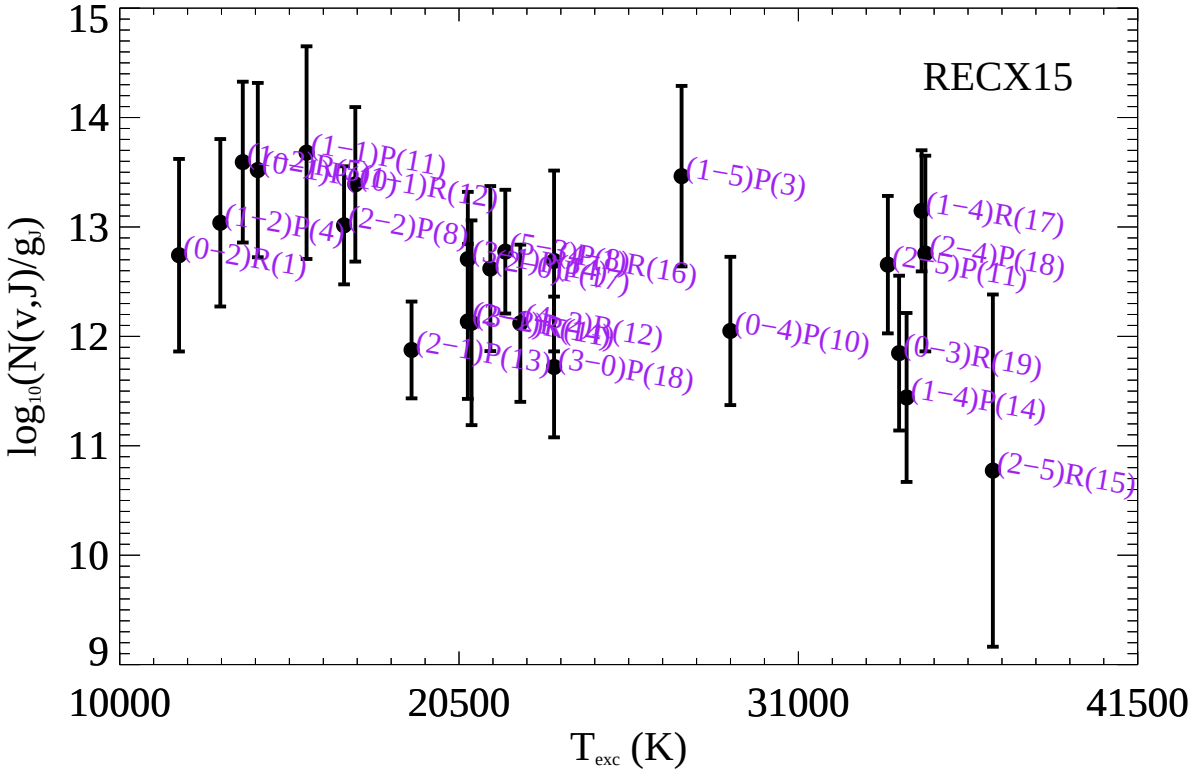

Figure 3.4 The rotation diagram produced for H_2 ground state rovibration levels probed in the protostellar Lyα profile of RECX-15. The column density in each rovibration state is determined from the H_2 absorption line fits shown in Figure 3.3.

all targets was the velocity shift of the line centers of the H_2 absorption features, v_r.

Figure 3.3 shows the normalized H_2 absorption profiles in the blue and red Lyα emission profiles of RECX-15, with the best-fit synthetic H_2 absorption profiles overlaid in blue (left) and red (right) and labeled with the H_2 transition ID. Figure 3.4 presents the resulting rotation diagram of H_2 ground state rovibrational in the sightline of RECX-15. All other synthetic H_2 absorption models are presented in Appendix C.1, while rotation diagrams are presented in Appendix D.2. The best-fit column densities and standard deviations are plotted in rotational diagrams against the rovibrational energy level (T_{exc} = E″/k_B). Each H_2 level is statistically-weighed to correct for ortho- and para-H_2 species, such that $g_J = (2S + 1)(2J + 1)$, for S = 0 (para-H_2) and S = 1 (ortho-H_2).

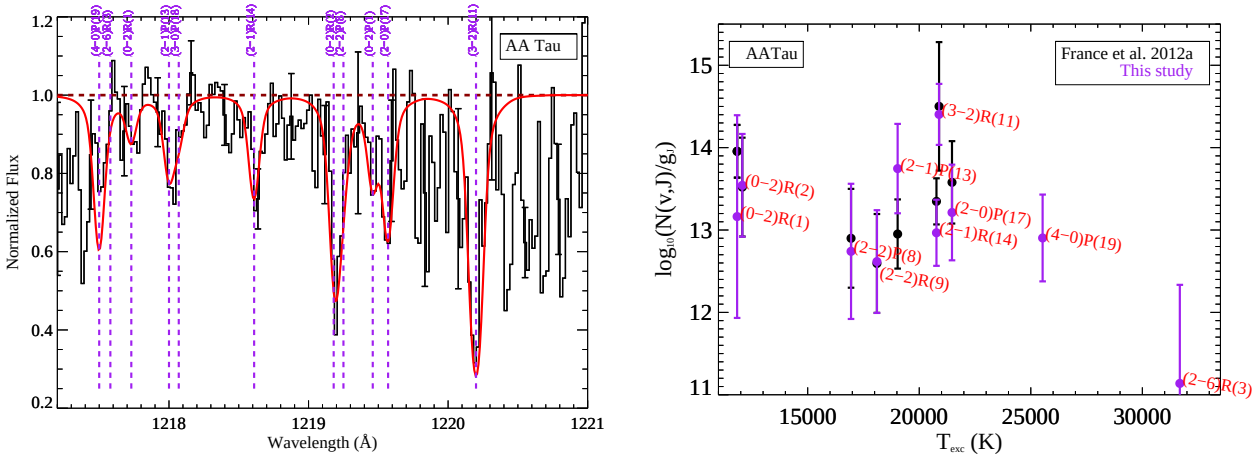

Figure 3.5 (a) **Left:** The best-fit synthetic H_2 absorption model (red) for AA Tau from 1217 − 1221 Å (black). Each transition is marked with dashed purple lines and identified with the progression ID. (b) **Right:** The rotation diagram of H_2 populations for features modeled from 1217 − 1221 Å (purple). I compare column density estimates from my procedure in this study to results from France et al. (2012b) (black). Both agree within the standard deviations determined from the absorption feature analysis.

My methodology is compared to results presented by France et al. (2012b), who performed the same procedure for the Lyα absorption spectrum of AA Tau. Figure 3.5 (left) shows the H_2 absorption spectrum for the red Lyα spectrum of AA Tau, as performed in this study. Additional details about the H_2 properties and initial conditions for each absorption model are provided in Appendix C. Figure 3.5 (right) shows the H_2 rotation diagram for AA Tau determined in this study

(purple) and France et al. (2012b) (black). The H_2 column densities in both studies agree within the error bars determined by the multi-component fit. Our study identified two additional H_2 absorption features not fit in France et al. (2012b) (H_2[0,19], pumped by λ1217.41 Å, and H_2[6,3], pumped by λ1217.49 Å).

3.4 Analysis & Results

The main goal of this study was to to characterize the behavior of the rovibrational H_2 populations identified in the PPD host Lyα spectra. From these H_2 states, an estimate of the total thermal and non-thermal column densities ($N(H_2)$ and $N(H_2)_{\rm nLTE}$) of H_2 in each sightline can be derived. In this section and the next, I will explain my methodology and results exploring the physical mechanisms of the protostellar environment which may identify key processes that correlate to these two main H_2 populations.

Figure 3.6 presents the rotation diagrams for all targets in this survey. I split the sampled sightlines by PPD evolution phase, which are defined by the behavior of excess infrared (dust) emission from $13 - 31$ μm (Furlan et al. 2009). Primordial PPDs are thought to be young disks with very little evidence of dust evolution and grain growth, meaning planet formation is either has not started or in very early stages. Transitional disks are viewed as older disks where proto-planets have formed and are evolving, since the observed infrared dust distributions point to the build-up of larger dust grains. Transition disks also (typically) harbor one or more large dust cavities that indicate significant evolution of the disk material (e.g., see Strom et al. 1989, Takeuchi and Artymowicz 2001, Calvet et al. 2002; 2005, Espaillat et al. 2007a). To explore the behavior of H_2 populations simultaneously in all PPD sightlines, I normalize each H_2 rotation diagram to the [v = 2,J = 1] level. I include thermal models of warm/hot distributions of H_2 populations, drawn through the normalization rovibrational level [v = 2,J = 1], which range from the expected thermal populations of fluorescent H_2 in PPDs (Herczeg et al. 2002; 2006, France et al. 2012c, Hoadley et al. 2015) to the dissociation limit of the molecule (red dashed line for $T_{diss} \approx 4500$ K; Shull and Beckwith 1982, Williams and Murdin 2000).

Table 3.3. Observed Lyα-Pumped H_2 Transitions: Intrinsic Properties

Blue Lyα Wing					Red Lyα Wing				
line ID[a]	λ_{pump} (Å)	f_{osc}[b] (10^{-3})	E″[c] (eV)	A_{ul} (10^8 s^{-1})	line ID[a]	λ_{pump} (Å)	f_{osc}[b] (10^{-3})	E″[c] (eV)	A_{ul} (10^8 s^{-1})
B(1-2)R(5)	1210.352	36.3	1.19	1.4	C(1-5)R(5)	1216.988	7.1	2.46	0.39
C(0-3)R(19)	1210.449	25.4	2.94	1.1	C(1-5)R(9)	1216.997	19.7	2.76	0.80
B(1-2)P(4)	1210.631	29.1	1.13	1.7	B(3-3)R(2)	1217.031	1.24	1.50	0.04
C(2-5)P(11)	1210.682	30.1	2.91	1.5	B(3-3)P(1)	1217.038	1.28	1.48	0.17
C(1-4)R(17)	1211.048	37.2	3.00	1.6	B(0-2)R(0)	1217.205	44.0	1.00	0.66
C(1-5)P(3)	1211.402	7.5	2.36	0.48	C(0-4)Q(10)	1217.263	10.0	2.49	0.45
B(4-1)R(16)	1211.546	25.7	2.02	1.1	B(4-0)P(19)	1217.410	9.28	2.20	0.44
C(1-5)R(7)	1211.758	24.2	2.57	0.97	C(2-6)R(3)	1217.488	36.4	2.73	1.30
C(2-4)P(18)	1211.787	15.2	3.01	0.73	B(0-2)R(1)	1217.643	28.9	1.02	0.78
C(2-5)R(15)	1211.910	32.8	3.19	1.4	B(2-1)P(13)	1217.904	19.2	1.64	0.93
B(1-1)P(11)	1212.426	13.3	1.36	0.66	B(3-0)P(18)	1217.982	6.64	2.02	0.32
B(1-1)R(12)	1212.543	10.9	1.49	0.46	B(2-1)R(14)	1218.521	18.1	1.79	0.76
B(3-1)P(14)	1213.356	20.6	1.79	1.00	B(5-3)P(8)	1218.575	12.9	1.89	0.66
B(4-2)R(12)	1213.677	9.33	1.93	0.39	B(0-2)R(2)	1219.089	25.5	1.04	0.82
C(3-6)R(13)	1214.421	5.17	2.07	0.29	B(2-2)R(9)	1219.101	31.8	1.56	1.30
B(3-1)R(15)	1214.465	23.6	1.94	1.00	B(2-2)P(8)	1219.154	21.4	1.46	1.10
C(1-4)P(14)	1214.566	28.3	2.96	1.40	B(0-2)P(1)	1219.368	14.9	1.02	2.00
B(4-3)P(5)	1214.781	9.90	1.65	0.55	B(2-0)P(17)	1219.476	3.98	1.85	0.19
					B(0-1)R(11)	1219.745	3.68	1.36	0.15
					B(3-2)R(11)	1220.110	21.3	1.80	0.88
					B(0-1)P(10)	1220.184	5.24	1.23	0.26

[a]Describes ground state-to-excited state transition, due to absorption of Lyα photon λ_{pump}. IDs beginning with "B" are excited to Lyman excitation level ($2p\sigma B^1\Sigma_u^+$), and IDs beginning with "C" are excited to Werner excitation state ($2p\pi C^1\Pi_u$).

[b]The oscillator strength of the transition.

[c]The energy level of ground state ($X^1\Sigma_g^+$) H_2 before photo-excitation.

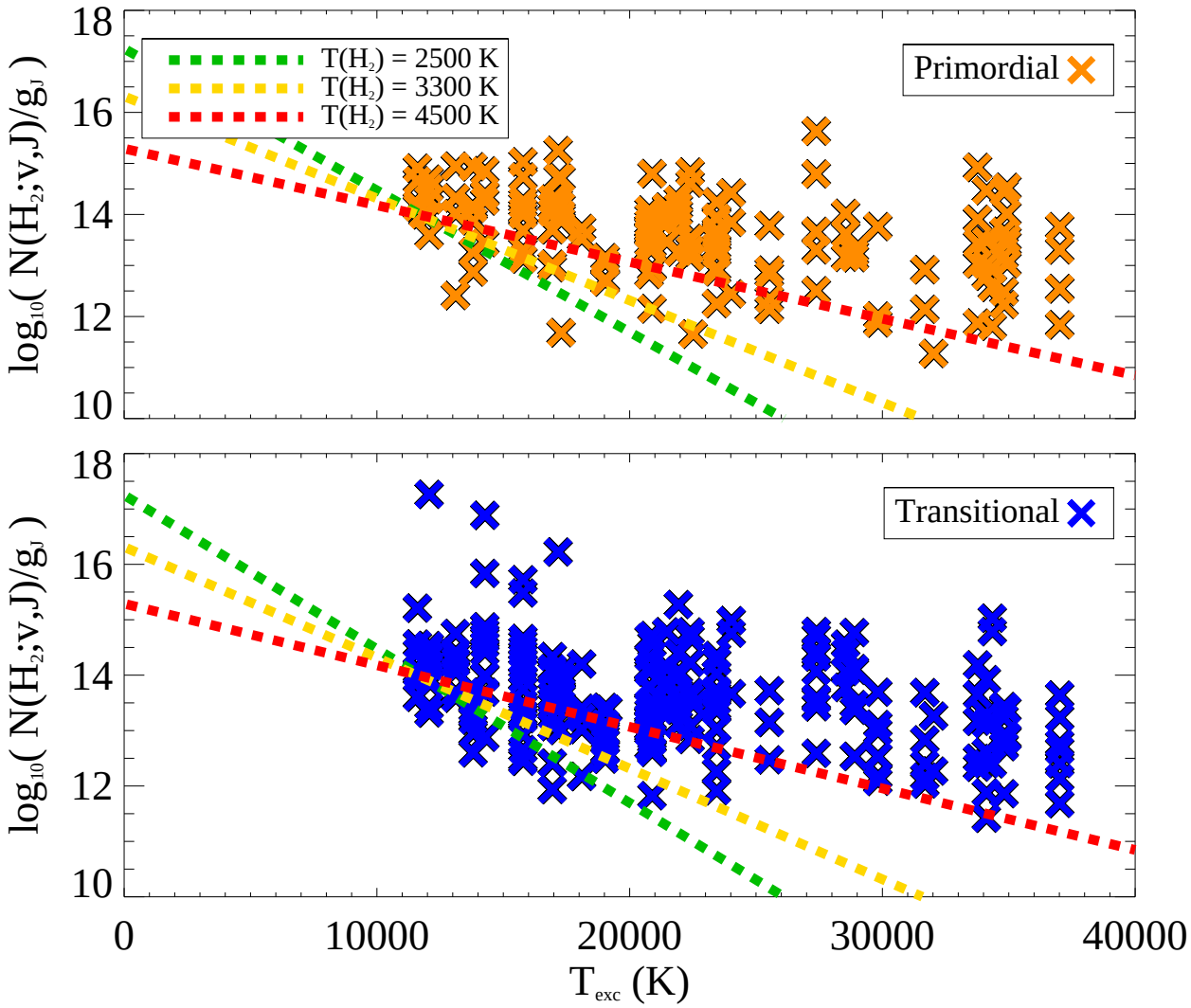

Figure 3.6 A relative comparison of H_2 rotation diagram behaviors. I normalize the rotation diagrams for H_2 distributions in all PPD sightlines to the [v = 2,J = 1] level and split these relative spectra by disk evolution, where primordial targets are shown at the top (orange) and transitional targets are shown at the bottom (blue). I fit thermally-distributed H_2 through the [v = 2,J = 1] level for warm ($T(H_2)$ = 2500 K; green) and hot ($T(H_2)$ = 3500 K and 4500 K; yellow and red) H_2 populations.

Despite the evolutionary differences in the dust distributions between the two PPD types, primordial and transitional PPD sightlines appear to show very similar H_2 rovibrational behaviors. Thermal distributions for $T(H_2) < 3300$ K do not appear to describe the behavior of H_2 rovibration levels for $T_{exc} > 23{,}000$ K, but a thermal distribution of H_2 at or near the dissociation limit of the molecule does appear to be consistent with the lowest column densities of rovibrational H_2 at $23{,}000\ \mathrm{K} < T_{exc} < 40{,}000$ K. Still, the majority of H_2 levels are significantly pumped, sometimes by as much as 4 dex, above the thermal distribution of H_2.

Additionally, there is a striking behavioral deviation away from thermal models for H_2 rovibrational levels with $T_{exc} > 20{,}000$ K. At $T_{exc} \sim 20{,}000$ K, there is an abrupt upturn, or "knee," away from the thermal distributions and an increase in rovibrational column density for higher excitation temperature states by $\gtrsim 1$ dex. This "knee" appears to repeat around $T_{exc} \sim 25{,}500$ K and 31,000-32,000 K. This behavior, specifically between the "knees" at $T_{exc} \sim 25{,}500$ and 32,000 K, may be a result of under-sampling the distribution of highly-energetic H_2 with ground state energies in this range.

Non-thermal pumping mechanisms include many complex processes, which are challenging and computationally-expensive to model simultaneously; Nomura et al. (2007) show how many mechanisms, such as chemical processes (resulting in the destruction and formation of H_2), FUV/X-ray pumping, and dust grain formation and size distributions in PPD atmospheres (Habart et al. 2004, Aikawa and Nomura 2006, Nomura and Nakagawa 2006, Fleming et al. 2010), affect the population ratios of H_2 and pump H_2 populations out of. However, Nomura and Millar (2005) also show that small changes in any of these processes can have dramatic effects on the final structure of H_2 rovibrational levels. Since the Lyα-pumped rovibration state of H_2 do not sample the full suite of $[v,J]$ ground states, specifically for $v < 2$, it is not beneficial to attempt to model multiple, non-thermal mechanisms in the hope of re-producing the observed behavior of H_2 rovibration levels.

Instead, I compare the observed rovibration level distributions to thermal H_2 models. While thermal models alone will not explain the distributions and behaviors of H_2 in PPD sightlines, exploring various thermal distribution realizations will help place limits on the total thermal column

density of H_2 in each PPD sightline.

I fit two thermal distributions to the rovibrational levels of each target:

(1) Model 1: I fit purely thermal distributions of H_2 to all observed rovibrational states, regardless of excitation temperature.

(2) Model 2: I fit purely thermal distributions of H_2 to only observed rovibrational states with $T_{exc} \leq 17{,}500$ K ($E'' \leq 1.5$ eV).

Further details regarding the molecular physics and energy equations used for Models 1 and 2 can be found in Appendix D. Each model is optimized to the rotation diagram of each target through a Markov Chain Monte Carlo (MCMC) routine, performed with the Python `emcee` package (Foreman-Mackey et al. 2013). The routine uses randomly-generated initial conditions and minimizes the likelihood function of the observed rovibrational column densities, given the range of model parameters. This process determines the best representative thermal model parameters ($N(H_2)$,$T(H_2)$) to the data. Further details about the MCMC and parameter fits are discussed in Appendix D.1.

3.4.1 Thermal and Non-Thermal H_2 Column Densities

Each set of best-fit thermal model parameters is shown in Table 3.4. Figure 3.7 shows the rovibrational levels and thermal model realizations for RW Aur. In this figure, data from this study are shown as black circles and lower excitation temperature states from France et al. (2014a) are shown as black stars. The lower excitation temperature states from France et al. (2014a) were detected against the FUV continuum between $\lambda\lambda$ 1092.5 − 1117 Å. RW Aur is the only target in this sample of PPDs with both sets of H_2 data and provides a great example for visualizing how higher excitation temperature ground states deviate from the warm, thermal states likely probing the denser, cooler portions of the disk atmosphere ($\log_{10}(N(H_2)) = 19.90$ cm^{-2} and $T(H_2) = 440$ K: magenta; France et al. 2014a). Higher energy rovibrational H_2 levels appears to scatter out of thermal equilibrium and are described by higher bulk temperatures, as predicted by

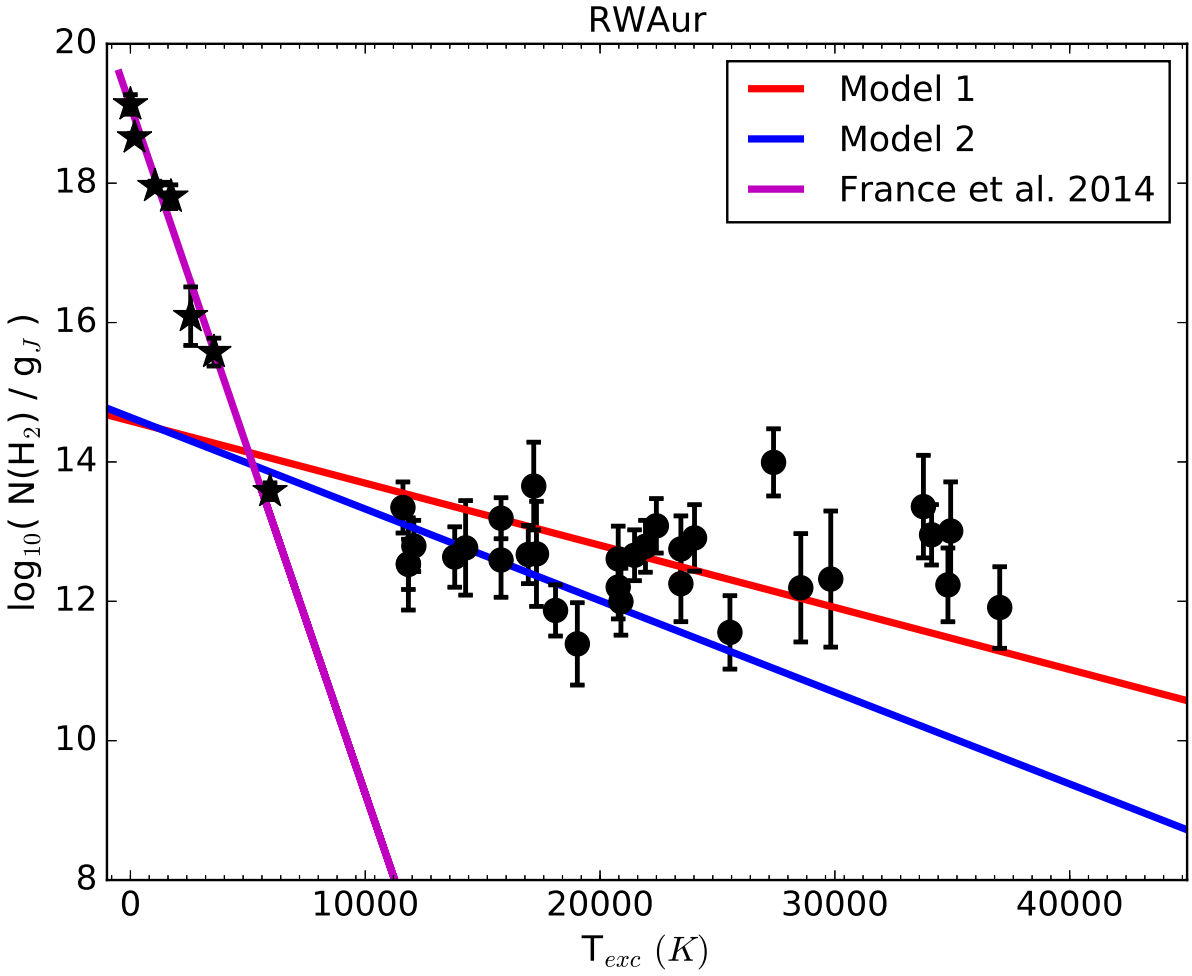

Figure 3.7 The rotation diagram for RW Aur, with rovibrational column densities derived in this study (black circles) and lower energy states calculated by France et al. (2014a) (black stars; $\lambda\lambda$ 1092.5 − 1117 Å). The red and blue solid lines represent thermal distributions of H_2 levels populated in Models 1 and 2, respectively. The magenta solid line shows the thermal distribution H_2 levels examined by France et al. (2014a), with $\log_{10}(\ N(H_2)\ ) = 19.90$ cm^{-2} and $T(H_2) = 440$ K.

Nomura and Millar (2005). H_2 rotation diagrams and thermal distributions for all targets explored in this survey are presented in Appendix D.2.

Table 3.3 lists the average S/N of each Lyα emission profile as observed by either *HST*/COS or *HST*/STIS. I compute a Spearman rank coefficient between the best-fit thermal model N(H_2) and the Lyα wing S/N and find significant trends for both Model 1 (ρ = -0.71, with a probability to exceed the null hypothesis that the data are drawn from random distributions (p)[1] = 7.0×10^{-3}) and Models 2 (ρ = -0.78, p = 5.6×10^{-2}). However, when I exclude one low S/N data point from the correlation (LkCa 15) and re-calculate the Spearman rank coefficient for both model realizations, a more randomly-distributed set of modeled column density estimates is found (Model 1: ρ = -0.22, p = 3.91×10^{-1} and Model 2: ρ = -0.27, p = 1.92×10^{-1}). Therefore, I elected to exclude resulted from LkCa 15 for the remainder of my analysis.

I use the results from Models 1 and 2 to estimate the total column density of thermally-distributed H_2 (N(H_2)) in each sight line. I choose to represent the thermal distributions of hot H_2 with the results from Model 2. T(H_2) from Model 2 represents a more realistic determination of the bulk temperature profiles of thermal H_2 (T(H_2) $\sim 2500 - 3500$ K) in each sightline, whereas Model 1 produces T(H_2) $\approx$ T_{diss}(H_2). In reality, there is very little difference between N(H_2) determined from Models 1 and 2; both model realizations predict similar N(H_2), though Model 2 results tend to under-predict N(H_2) when compared to Model 1 results, and thus provide a lower limit to the total thermal column density of hot H_2.

To approximate how much of the total observed H_2 column density is associated with excess H_2 populations in highly energetic (non-thermal) states, I define a metric for the total non-thermal column density of H_2 in highly excited levels (E$''$ > 1.75 eV, or T_{exc} > 20,000 K), which I refer to as N(H_2)$_{\rm nLTE}$. N(H_2)$_{\rm nLTE}$ is calculated by integrating the residual between observed H_2 rovibration levels with T_{exc} > 20,000 K and the predicted populations of H_2 at that same rovibration level from the modeled thermal distributions, or N(H_2)$_{\rm nLTE}$ = Σ(N($H_2[v,J]$)$_{\rm obs}$ - N($H_2[v,J]$)$_{\rm model}$). For

[1] I categorize the strength of p throughout this study as follows: p > 5% (5.0×10^{-2}) show little evidence of being correlated; 1% < p < 5% is a trend, but may or may not be correlated; 0.1% < p < 1% is a confident correlation, and p < 0.1% is strongly correlated

Table 3.4. Thermal H_2 Column Density & Temperature Results

	Model 1		Model 2			
Target	$N(H_2)^a$	$T(H_2)^b$	$N(H_2)^a$	$T(H_2)^b$	$N(H_2)_{nLTE}{}^a$	$N(H_2[5,18])^{a,c}$
AA Tau	$16.27^{+0.50}_{-0.34}$	4179^{+585}_{-887}	$15.85^{+0.11}_{-0.11}$	3578^{+282}_{-221}	$16.40^{+0.01}_{-0.01}$	10.35
AB Aur	$15.59^{+0.31}_{-0.20}$	4488^{+376}_{-704}	$15.34^{+0.34}_{-0.26}$	3628^{+744}_{-631}	$15.44^{+0.01}_{-0.01}$	-
AK Sco	$15.57^{+0.17}_{-0.16}$	4880^{+90}_{-190}	$15.52^{+0.51}_{-0.29}$	3661^{+872}_{-922}	$15.04^{+0.05}_{-0.01}$	-
BP Tau	$15.50^{+0.21}_{-0.19}$	4855^{+107}_{-220}	$15.11^{+0.55}_{-0.31}$	3693^{+868}_{-972}	$15.37^{+0.01}_{-0.02}$	10.72
CS Cha	$15.82^{+0.17}_{-0.16}$	4889^{+83}_{-174}	$15.27^{+0.57}_{-0.34}$	3536^{+954}_{-962}	$15.52^{+0.01}_{-0.02}$	9.92
DE Tau	$16.20^{+0.50}_{-0.32}$	4082^{+644}_{-927}	$16.08^{+0.86}_{-0.50}$	3466^{+1030}_{-1120}	$16.03^{+0.01}_{-0.01}$	-
DF Tau A	$15.13^{+0.29}_{-0.19}$	4375^{+443}_{-695}	$14.98^{+0.09}_{-0.09}$	3382^{+188}_{-159}	$14.74^{+0.01}_{-0.01}$	11.19
DM Tau	$16.02^{+0.20}_{-0.18}$	4810^{+140}_{-274}	$16.14^{+0.75}_{-0.54}$	2900^{+1170}_{-776}	$15.90^{+0.01}_{-0.02}$	10.23
GM Aur	$15.84^{+0.18}_{-0.17}$	4873^{+95}_{-200}	$15.67^{+0.68}_{-0.50}$	2966^{+1096}_{-762}	$15.51^{+0.01}_{-0.02}$	-
HD 104237	$15.95^{+0.27}_{-0.26}$	4831^{+126}_{-264}	$15.16^{+0.46}_{-0.28}$	3734^{+830}_{-906}	$16.47^{+0.01}_{-0.01}$	-
HD 135344 B	$15.60^{+0.18}_{-0.17}$	4886^{+86}_{-181}	$15.24^{+0.42}_{-0.29}$	3544^{+878}_{-770}	$15.26^{+0.01}_{-0.02}$	-
HN Tau A	$16.92^{+1.03}_{-0.64}$	3035^{+1193}_{-966}	$16.85^{+1.08}_{-0.72}$	2798^{+1305}_{-912}	$14.63^{+1.20}_{-0.20}$	-
LkCa15	$17.77^{+0.62}_{-0.51}$	4556^{+324}_{-611}	$17.35^{+0.11}_{-0.11}$	3516^{+260}_{-200}	$17.64^{+1.50}_{-0.20}$	10.01
RECX 11	$15.84^{+0.13}_{-0.13}$	4905^{+71}_{-147}	$15.55^{+0.24}_{-0.17}$	3939^{+629}_{-611}	$15.64^{+0.01}_{-0.01}$	9.98
RECX 15	$16.03^{+0.21}_{-0.20}$	4858^{+106}_{-219}	$15.47^{+0.47}_{-0.27}$	3944^{+729}_{-950}	$15.63^{+0.01}_{-0.02}$	9.48
RU Lupi	$16.03^{+0.21}_{-0.19}$	4765^{+174}_{-336}	$15.38^{+0.61}_{-0.34}$	3840^{+807}_{-1106}	$15.66^{+0.01}_{-0.02}$	-
RW Aur A	$16.23^{+0.29}_{-0.27}$	4822^{+133}_{-263}	$15.60^{+0.56}_{-0.33}$	3729^{+858}_{-1005}	$17.36^{+0.01}_{-0.01}$	-
SU Aur	$16.21^{+0.51}_{-0.38}$	4264^{+525}_{-802}	$16.51^{+3.48}_{-1.22}$	2574^{+1654}_{-1565}	$15.31^{+3.00}_{-0.20}$	-
SZ 102	$15.43^{+0.20}_{-0.15}$	4493^{+362}_{-530}	$15.83^{+0.32}_{-0.34}$	2785^{+588}_{-366}	$15.26^{+0.01}_{-0.01}$	-
TW Hya	$15.40^{+0.17}_{-0.16}$	4880^{+89}_{-192}	$15.08^{+0.54}_{-0.33}$	3483^{+954}_{-887}	$15.19^{+0.01}_{-0.02}$	11.31
UX Tau A	$16.76^{+0.38}_{-0.34}$	4668^{+244}_{-460}	$16.40^{+1.32}_{-0.56}$	3129^{+1283}_{-1383}	$16.38^{+2.60}_{-0.20}$	-
V4046 Sgr	$15.33^{+0.15}_{-0.14}$	4894^{+80}_{-164}	$15.05^{+0.40}_{-0.25}$	3900^{+740}_{-891}	$15.05^{+0.01}_{-0.01}$	10.27
Avg. Model Results	$15.97^{+1.80}_{-0.84}$	4604^{+301}_{-1570}	$15.70^{+1.65}_{-0.72}$	3442^{+500}_{-870}	$15.70^{+1.94}_{-1.07}$	10.35

[a]All column densities are to the power of 10 ($\log_{10}N(H_2)$).

[b]Thermal temperatures of the bulk H_2 populations ($T(H_2)$) are in Kelvin.

[c]Estimated from the formalism outlined in Rosenthal et al. (2000) (Equation 3.1). I assume the H_2[5,18] population is optically thin.

consistency, I calculate $N(H_2)_{nLTE}$ from all best-fit model realizations from both Models 1 and 2 and was able to produce approximately the same $N(H_2)_{nLTE}$ estimate from $N(H_2)$ of both Models 1 and 2. Associated error bars on $N(H_2)_{nLTE}$ are estimated as the minimum and maximum deviations away from the median $N(H_2)_{nLTE}$ for all Model 1 and Model 2 best-fit thermal parameters. Table 3.4 includes the estimates of $N(H_2)_{nLTE}$ for each target.

3.4.2 CIV-Pumped H_2 Fluorescence

Molecular hydrogen populations photo-excited by CIV photons (λ 1548.20, 1550.77 Å) are found in highly excited ground states ([3,25], [5,18], and [7,13]; $E'' \geq 3.8$ eV, $T_{exc} > 43{,}000$ K) that are difficult to explain with thermally-generated H_2 populations alone at temperatures probed in PPDs ($T(H_2) \sim 2000$ - 3000 K; Herczeg et al. (2006), France et al. (2012c), Hoadley et al. (2015), McJunkin et al. (2016)). These highly excited states are also unlikely to be directly populated by the fluorescence process. Electronic transitions are dipole-allowed, meaning $J'' = \pm 1$ between excited and ground state transitions. Therefore, the decay from excited electronic to ground states can easily increase the ground electronic vibrational levels, but will not substantially change the ground electronic quantum rotational levels (Herczeg et al. 2006). Therefore, other physical processes, such as collisional (Bergin et al. 2004) and chemical (Takahashi et al. 1999, Ádámkovics et al. 2016) processes, must be responsible for populating these highly energetic levels of H_2.

Since it is uncertain which processes dominate the pumping of H_2 into these highly energetic upper rotational levels, I use the emission from CIV-pumped H_2 as a proxy for a variety of non-thermal processes that may excite H_2 to highly non-thermal states. I estimate the column density of H_2 populating these energetic levels from the total fluorescent emission produced by CIV-pumped H_2, stipulating two conditions to verify whether the target exhibits CIV-pumped H_2 emission in the FUV spectrum: 1) each emission line must have an elevated flux level $\geq 1.5\sigma$ above the continuum floor, and 2) at least two emission lines from the same progression must be present. Figure 3.8 demonstrates this process. Only fluorescence from the B(0-5)P(18) 1548.15 Å transition meets this criteria for all targets in our survey. The two brightest transitions from the B(0-5)P(18) 1548.15

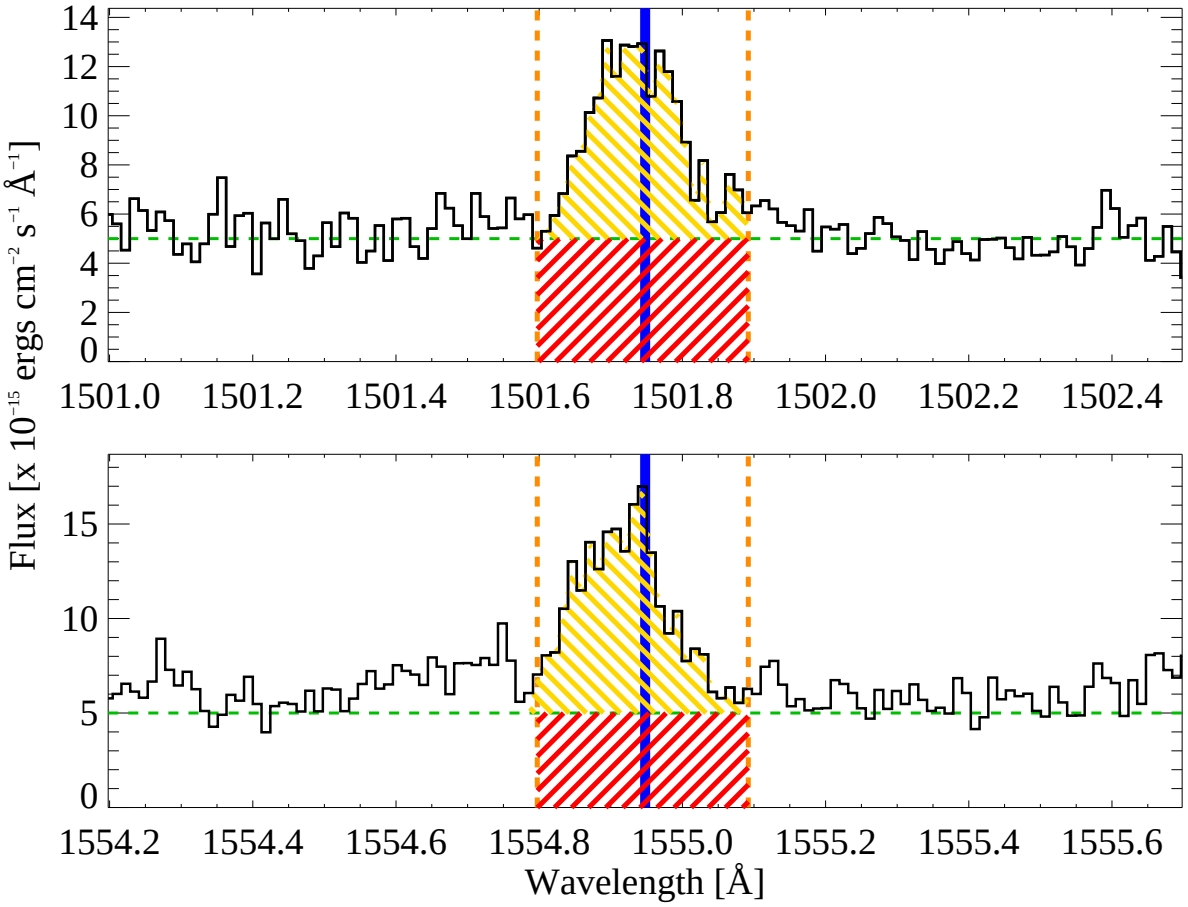

Figure 3.8 The presence of CIV-pumped H_2 emission from the B(0-5)P(18) progression, as shwon for BP Tau, for emission lines at 1501.75 Å (0-5R(16)) and 1554.95 Å (0-6R(16)), (rest wavelength indicated by the blue dotted lines). The green dashed line shows the continuum levels in each spectral region. The orange dashed lines mark off the region considered for each fluorescence line. The yellow hashed region represents the integrated flux F(CIV-H_2 within the orange region, while the red hashed region represents the integrated continuum flux in the same region.

Å cascade, λ 1501.75 Å and λ 1554.95 Å, are free of blending from other atomic or molecular contaminants (Herczeg et al. 2006). Therefore, emission features observed at these wavelengths are detected fluorescence transitions, originating from the highly non-thermal H_2 state [5,18]. Of the 22 targets, 10 show statistically significant emission lines from VIC-pumped H_2 fluorescence. Five of these 10 are in the primordial dust disk phase, while the other 5 are in the transition disk phase.

I estimate the column density of highly excited H_2 from the flux observed in the two brightest emission features at λ 1501.75 Å and λ 1554.95 Å (after subtracting the UV continuum). This column density estimate works under the assumption that the emitting gas is optically thin, which is suggested by previous studies (e.g., (Herczeg et al. 2002; 2006)). The total column density (N(CIV-H_2)), then, is calculated from the formalism outlined in Rosenthal et al. (2000),

$$N(CIV - H_2[v'', J'']) = \frac{4\pi\lambda}{hc} \frac{F(CIV - H_2)([v', J'] \rightarrow [v'', J''])}{A_{ul}([v', J'] \rightarrow [v'', J''])} \tag{3.1}$$

where N(CIV-H_2[v'',J'']) is the column density of CIV-pumped H_2 that decays to ground state [v'',J''], λ is the transition wavelength between electronic and ground states, F(CIV-H_2) is the integrated flux in the emission line produced by the transition between excited electronic level [v',J'] and ground level [v'',J''], and A_{ul} is the spontaneous decay coefficient for the transition. For each emission line, N(CIV-H_2) is calculated, and the average of the results from the two emission features provides the estimate of N(CIV-H_2). Error bars on N(CIV-H_2) are taken as the residual between the N(CIV-H_2) and the column density derived from each emission feature at λ 1501.75 Å and λ 1554.95 Å. Derived N(CIV-H_2) values are listed in Table 3.4. All column densities derived from the fluorescence emission from the B(0-5)P(18) progression are $\log_{10}$(N(CIV-H_2)) < 12.0, which is consistent with a thin layer of highly energetic H_2 (Herczeg et al. 2006).

3.5 Discussion

This study has focused on characterizing the column density of H_2 from observed distributions of rovibrational states derived from their respective absorption features embedded within the stellar Lyα wings of PPD hosts. Systematically, I empirically determined larger-than-expected col-

umn densities for higher excitation levels than would be expected in thermally-distributed, warm populations of H_2 alone. The behavior of the H_2 distributions of rovibrational states may therefore point to non-thermal mechanisms in or around the circumstellar environment that are affecting the equilibrium state of warm molecules in these sightlines. For this section, I explore the general behavior of thermal and non-thermal H_2 populations and column densities in PPD environments to stellar and circumstellar observables which may be responsible for creating large non-thermal H_2 densities.

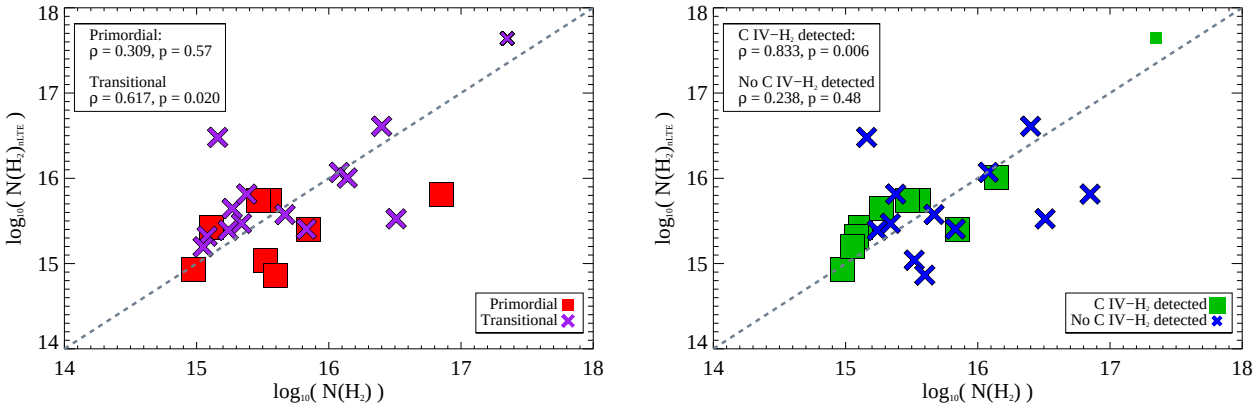

Figure 3.9 I compare model-derived $N(H_2)$ to $N(H_2)_{nLTE}$ and separate populations by disk evolutionary phase (**left**) and whether there is evidence of CIV-pumped H_2 fluorescence in the FUV spectrum (**right**). Transitional disk targets and targets with detected CIV-pumped H_2 fluorescence (AA Tau, BP Tau, CS Cha, DF Tau, DM Tau, LkCa 15, RECX 11, RECX 15, TW Hya, and V4046 Sgr) appear to have a strong correlation with $N(H_2) \sim N(H_2)_{nLTE}$.

First, I look for correlations between the modeled distributions of warm, thermal H_2 ($T(H_2) > 2500$ K) and the populations of non-thermal H_2 states for the sampled PPD sightlines. Figure 3.9 compares thermal, model-derived $N(H_2)$ to the sum of the residuals in highly-energetic H_2 states, $N(H_2)_{nLTE}$. Before noting the distributions of total column densities by categorization, the general trend between the distributions of $N(H_2)$ and $N(H_2)_{nLTE}$ appear roughly related, with a Spearman rank coefficient which agrees with this assessment ($\rho = +0.54$), but a PTE that suggests there is no strong indication of a trend between the two variables ($p = 1.17\times10^{-1}$). However, when I categorize targets by their disk evolution and whether CIV-pumped H_2 fluorescence is detected in their FUV spectra, much clearer trends point to target distributions which have correlated $N(H_2)$

and $N(H_2)_{nLTE}$ populations. Transitional disks appear to predominantly straddle the $N(H_2) = N(H_2)_{nLTE}$ equality line ($\rho = +0.62$, p = 2.00×10^{-2}), and targets which have detectable CIV-pumped H_2 fluorescence show the same behavior ($\rho = +0.83$, p = 6.03×10^{-3}). The observed presence of CIV-pumped H_2 fluorescence is suggestive of H_2 populations that should not be populated if the H_2 are thermal and are therefore attributed to populations in existence because of non-thermal processes, such as H_2 formation (Herczeg et al. 2002; 2006). Primordial disk targets appear to have more scattered distributions of $N(H_2)$ and $N(H_2)_{nLTE}$ ($\rho = +0.31$, p = 5.69×10^{-1}), as do targets with no detected CIV-pumped H_2 fluorescence ($\rho = +0.24$, p = 4.82×10^{-1}).

3.5.1 H_2 Column Densities & the Circumstellar Environment

Next, I explore possible connections between circumstellar radiation (from the protostar, accretion shock, and disk molecular fluorescence) and derived $N(H_2)$ and $N(H_2)_{nLTE}$ from our thermal H_2 models. The physical evolution of PPDs is thought to be primarily driven by internal irradiation from the host protostar and planet formation (Takahashi et al. 1999, Nomura et al. 2007, Dodson-Robinson and Salyk 2011, Zhu et al. 2011, Owen 2016). Nomura and Millar (2005) and Nomura et al. (2007) examined in great detail the expected effects of stellar UV and X-ray irradiation on the state of the molecular disk and discovered that excess UV/X-ray emission pumps H_2 to highly energetic, non-thermal ground levels. Consequently, similar behavior is observed in each empirical PPD H_2 rotation diagram developed through this study (e.g., Figure 3.6).

I compare $N(H_2)$ and $N(H_2)_{nLTE}$ to observables that may be linked to excitation processes favoring higher-energy rovibrational H_2 levels in the PPD environments, including X-ray, FUV, Lyα, CIV, H_2 fluorescence, and H_2 dissociation "bump" luminosities (L_X, L_{FUV}, $L_{Ly\alpha}$, L_{CIV}, L_{H_2}, and L_{Bump}); total flux from $\lambda\lambda$ 912 - 1150 Å ($F_{1110Å}$); and the column density of highly energetic H_2 pumped by stellar CIV ($N(CIV\text{-}H_2)$; see Section 3.4.2).

I first consider the role of excess FUV and X-ray emission on the modeled thermal and non-thermal total column densities of H_2, to explore if the distributions of observed H_2 levels match the behaviors observed in Nomura and Millar (2005) and Nomura et al. (2007). I split the var-

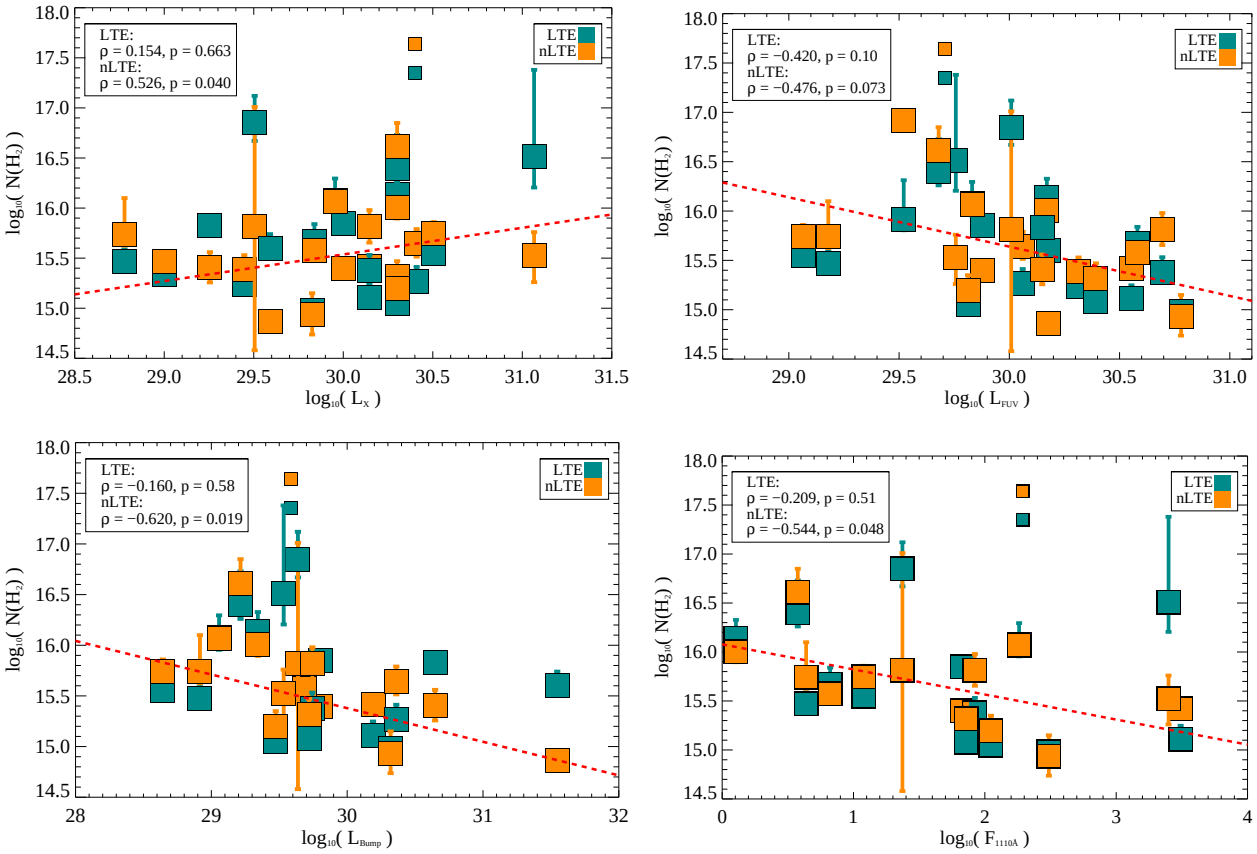

Figure 3.10 The total column densities of thermal and non-thermal H_2 are compared to the total X-ray luminosity (**top left**), the total FUV continuum luminosity (**top right**), the total H_2 dissociation "bump" luminosity around λ 1600 Å (**bottom left**), and the integrated, de-reddened flux from $\lambda\lambda$ 912 − 1150 Å (**bottom right**). $N(H_2)$ shows no significant correlations with any high-energy radiation observables, while $N(H_2)_{\rm nLTE}$ shows confident trends with L_X, L_{Bump}, and $F_{1110Å}$. Both total column densities show a very loose trend with L_{FUV}. Outside of log space, the column density variable have units of cm^{-2}, the luminosity variables have units of erg s^{-1}, and the flux variables have units of erg cm^{-2} s^{-1}.

ious excess emission into the following categories: the total X-ray luminosity (L_X; France et al. 2017 and references therein), the total FUV continuum luminosity (L_{FUV}: $\lambda\lambda$ 1490 − 1690 Å, excluding any discrete or extended emission features; France et al. 2014b), the total H_2 dissociation continuum around λ 1600 Å (L_{Bump}; France et al. 2017), and the total observed flux, corrected for ISM reddening, of FUV continuum+discrete emission features from $\lambda\lambda$ 912 − 1150 Å ($F_{1110Å}$; France et al. 2014b). Figure 3.10 shows the comparison of $N(H_2)$ and $N(H_2)_{nLTE}$ to these circumstellar observables. I find a correlation between L_X and $N(H_2)_{nLTE}$ (ρ = +0.53, p = 4.00×10^{-2}), but no correlation between $N(H_2)$ and L_X (ρ = +0.15, p = 6.62×10^{-1}). I find an anti-correlation between $N(H_2)_{nLTE}$ and L_{Bump} (ρ = -0.62, p = 1.90×10^{-2}), while no strong trend between $N(H_2)$ and L_{Bump} (ρ = -0.16, p = 5.83×10^{-1}). I also find an anti-correlation between $N(H_2)_{nLTE}$ and $F_{1110Å}$ (ρ = -0.54, p = 4.81×10^{-2}), yet no indication of a trend between $N(H_2)$ and $F_{1110Å}$ (ρ = -0.21, p = 5.14×10^{-1}). Finally, both $N(H_2)$ and $N(H_2)_{nLTE}$ show potential anti-correlations with L_{FUV}, but they are not statistically significant, as determined by the p-value ($N(H_2)$: ρ = -0.42, p = 1.02×10^{-1}; $N(H_2)_{nLTE}$: ρ = -0.48, p = 7.30×10^{-2}).

Then, I look at how discrete emission line features (from the protostar and accretion shock regions) and disk fluorescence processes may play a role on the total column densities of H_2 in PPD sightlines. I split the circumstellar parameters into the following categories: the total luminosity from stellar+shock-generated Lyα emission ($L_{Ly\alpha}$; ; France et al. 2014b), the total luminosity from stellar+shock-generated CIV emission (L_{CIV}; France et al. 2014b), the total H_2 fluorescence luminosity from Lyα-pumped H_2 predominantly produced in the disk atmosphere (L_{H_2}; France et al. 2014b), and the estimated total column density of H_2[5,18], derived from the statistically-determined CIV-pumped fluorescence features ($N(CIV\text{-}H_2)$, derived in Section 3.4.2). Figure 3.11 shows the comparison of $N(H_2)$ and $N(H_2)_{nLTE}$ to these circumstellar variables. I find no trends between the modeled column densities of H_2 and $L_{Ly\alpha}$ ($N(H_2)$: ρ = -0.31, p = 2.34×10^{-1}; $N(H_2)_{nLTE}$: ρ = -0.04, p = 7.86×10^{-1}), as well as L_{H_2} ($N(H_2)$: ρ = -0.25, p = 3.45×10^{-1}; $N(H_2)_{nLTE}$: ρ = -0.06, p = 7.54×10^{-1}). I do calculate a suggestive anti-correlation between L_{CIV} and $N(H_2)$ (ρ = -0.51, p = 4.52×10^{-2}), but no trend between $N(H_2)_{nLTE}$ and

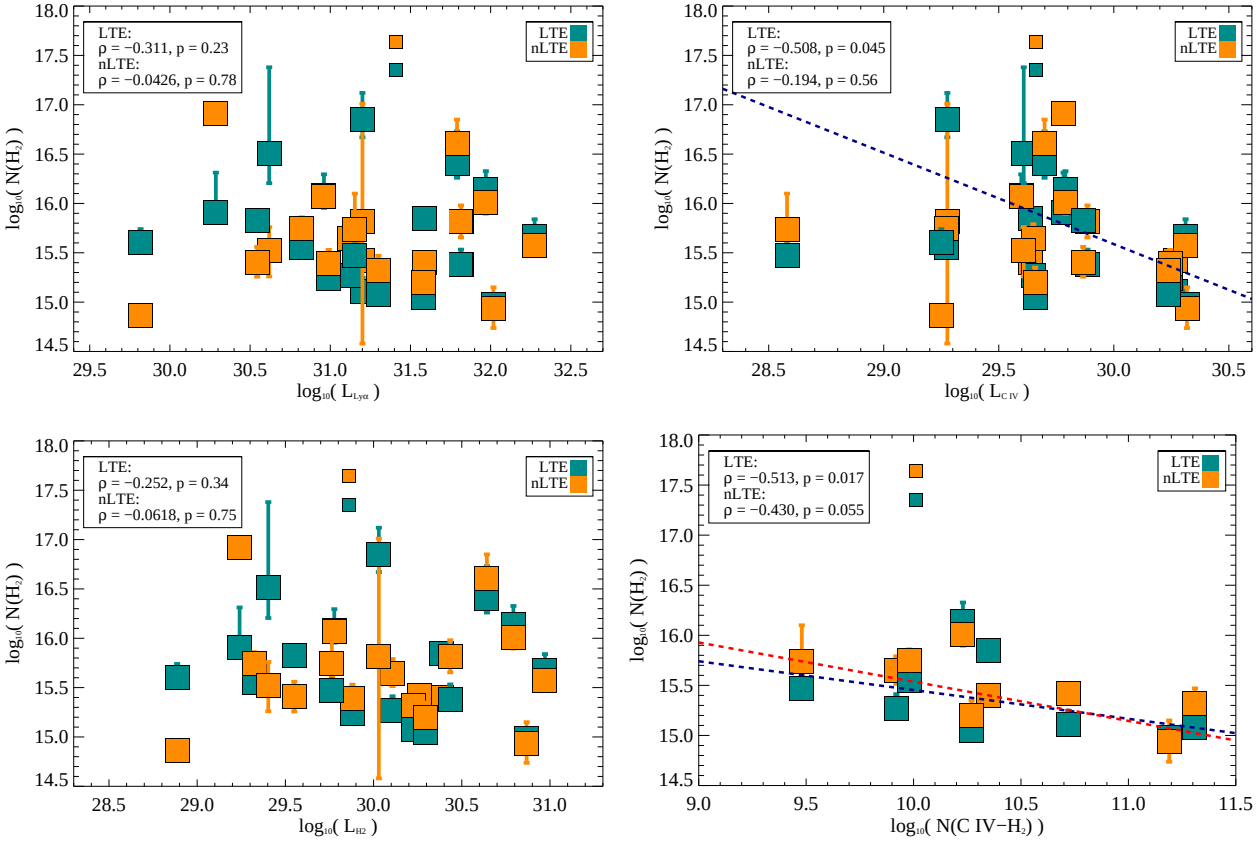

Figure 3.11 The total column densities of thermal and non-thermal H_2 are compared to the total Lyα luminosity (**top left**), the total CIV luminosity (**top right**), the total H_2 fluorescence luminosity (**bottom left**), and the total column density of H_2 found in H_2[5,18] (**bottom right**). N(H_2) shows confident trends with L_{CIV} and N(CIV-H_2), while N(H_2)$_{\rm nLTE}$ only displays a loose trend with N(CIV-H_2). I find no correlations between the modeled H_2 column densities and $L_{Ly\alpha}$ and L_{H_2}. Outside of log space, the column density variable have units of cm^{-2} and the luminosity variables have units of erg s^{-1}.

L_{CIV} (ρ = -0.19, p = 5.62×10^{-1}). Finally, I find an anti-correlated relation between both $N(H_2)$ and $N(H_2)_{nLTE}$ with N(CIV-H_2) ($N(H_2)$: ρ = -0.51, p = 1.71×10^{-2}; $N(H_2)_{nLTE}$: ρ = -0.43, p = 5.50×10^{-2}).

3.5.2 The Odd Behavior of Hot H_2

From the analysis performed so far, the non-thermal column densities of H_2 appear correlated to many non-thermal diagnostics of the circumstellar environment, such as internal radiation and H_2 dissociation tracers. For example, I find that $N(H_2)_{nLTE}$ increases with X-ray luminosity. It has been proposed that X-rays from protostars can create appreciable populations of non-thermal electrons, which, in turn, can excite H_2 into non-LTE populations (e.g., Walsh et al. 2012). This finding compliments the $N(H_2)_{nLTE}$-to-H_2 dissociation continuum luminosity correlation demonstrated in Figure 3.10; Bergin et al. (2004) suggest that the dissociation continuum of H_2 may be driven by non-thermal electrons in the hot layers of PPD atmospheres. Additionally, my results point to higher-energy (higher excitation temperature) H_2 being preferentially dissociated. Paired with the correlation found between $N(H_2)_{nLTE}$ and L_X, non-thermal electrons appear to play a significant role in dissociating H_2 in highly energetic rovibration levels.

I also find that $N(H_2)_{nLTE}$ decreases as the total flux between $\lambda\lambda$ 912 − 1110 Å increases, such that non-thermal populations may have higher dissociation probabilities when pumped by higher energy FUV photons (Stecher and Williams 1967, Shull and Beckwith 1982, Abgrall et al. 1993a;b). FUV photons, however, are not efficient at penetrating large densities of material. In the ISM, appreciable columns of dust and molecules can effectively "shield" FUV radiation from cooler, more dense material by either scattering the photons out of the line of sight or absorbing and re-emitting lower energy photons (e.g., see Draine 2011 and references therein). For $N(H_2)_{nLTE}$ to show such a correlation with the flux of higher energy FUV photons, the H_2 populations must be located somewhere in the circumstellar environment which does not shield or scatter FUV photons away from the H_2 populations.

Furthermore, I find that $N(H_2)$ and $N(H_2)_{nLTE}$ do not have correlations with $L_{Ly\alpha}$ or L_{H_2}.

The vast majority of H_2 fluorescence emission in the FUV spectra of PPD targets is attributed to H_2 rovibrational levels which predominantly absorb Lyα photons (Herczeg et al. 2002, France et al. 2012c), so one might expect that the observed H_2 absorption populations are associated with the observed fluorescence from each PPD sightline. However, estimates of the mass density of hot absorption H_2 population probed in the Lyα profiles in these sightlines show that the density of absorbing H_2 is two orders of magnitude below the threshold of H_2 mass density needed to produced fluorescence signatures ($\Sigma_{H_2,abs} \sim 10^{-8}$ g cm^{-2} versus $\Sigma_{H_2,min} \sim 5{\times}10^{-6}$ g cm^{-2}; France et al. 2012c). This suggests that the H_2 absorption populations are optically thin and not expected to contribute significant flux to the observed fluorescence signatures of warm-hot H_2 in PPD atmospheres, which have N(H_2) $\geq 10^{18}$ cm^{-2} (Herczeg et al. 2006, France et al. 2012b;c, Hoadley et al. 2015, McJunkin et al. 2016).

The empirical distributions of H_2 absorption populations appear to be located somewhere in the protostellar environment where 1) the H_2 can interact with an abundance of non-thermal electrons, and 2) the H_2 have access to protostellar radiation with $\lambda < 1110$ Å, and 3) the H_2 populations are optically-thin to Lyα radiation. Piecing all of these results together, I suspect that the observed H_2 populations against the protostellar Lyα wing provide are not associated with the H_2 that fluoresces in the disk and may, instead, arising from a hot, nebulous origin. Ádámkovics et al. (2016) explore the effects of FUV, X-ray, and Lyα radiation on stratified layers of molecular PPD atmospheres. In the presence of all three, FUV continuum and X-ray radiation create a hot, atomic layer along the uppermost disk surface, and Lyα radiation penetrates deeper into the disk via HI scattering. The penetration of Lyα into the molecular disk is found to photodissociate trace molecules like H_2O and OH, which, along with H_2 formation on dust grains, heat this region of the disk and create a warm molecular layer ($T_{gas} > 1500$ K). This warm layer is found to have an appreciable column of warm H_2 (N(H_2) $> 10^{19}$ cm^{-2}) in the appropriate temperature regime to reproduce fluorescent emission signatures in PPDs, though Ádámkovics et al. (2016) acknowledges that the distribution of H_2 rovibrational levels is not computed with their models.

The Ádámkovics et al. (2016) study produces a hot (T $\sim$ 5000 K) atomic layer in the upper-

most disk atmosphere, similar in nature to a photodissociation region (PDR; Hollenbach and Tielens 1999 and references therein) and is arises almost inconsequentially of luminosity or dust grain distribution parameters chosen for their models. This layer of hot atomic gas contains a minute abundance of H_2 ($x(H_2) \lesssim 10^{-5}$), with total column densities of hot H_2 similar to those found in this study ($N(H_2)_{hotlayer} \sim 10^{15}$ cm^{-2}; $\langle N(H_2)_{H_2abs} \rangle \sim 10^{15.5}$ cm^{-2}. This hot atomic layer is modeled above the warm molecular layer (where H_2 fluorescence may arise) and extends substantially further away from the disk midplane (Ádámkovics et al. 2016). What their study finds is that Lyα radiation is key to producing the warm molecular regions that may be associated with warm H_2 and CO populations, but the hot, atomic layer is driven by the FUV continuum and X-ray luminosities, which cannot penetrate (i.e., scatter) into the cooler disk like Lyα.

Connecting the findings from this work and the Ádámkovics et al. (2016) models, I propose that the observed H_2 absorption populations, probed in the wings of protostellar Lyα profiles, reside in this tenuous, hot atomic region of the circumstellar environment. The nature of the Lyα transition, being a powerful resonance line, allows Lyα radiation to scatter through both the PPD and the surrounding PDR-like environment. Rather than probing a discrete line source coming straight from the accretion shock near the protostellar surface, Lyα is scattered through the circumstellar environment by HI atoms before reaching the observer. The scattering of Lyα radiation by neutral hydrogen causes Doppler shifts away from the rest wavelength of Lyα, which is observed as a broadening of the emission line profile to several hundred km s^{-1} before leaving the hot atomic environment around the PPD (McJunkin et al. 2014). It appears that the H_2 probed in absorption against these observed Lyα wings may be tied to this optically-thin, hot haze surrounding the PPD, where optically-thin densities of H_2 absorb Lyα before it exits the system.

3.5.3 H_2 "Multiple Pumping" Versus Cooling

The scattering of Lyα radiation through the hot atomic regions surrounding PPDs may help explain the non-thermal behavior of H_2 associated with these environments. The odd behavior of the absorption rovibrational levels may be the result of "multiple pumping" happening with the

hot H_2, meaning that the excitation rate by UV photon absorption (in this case, specifically Lyα photons) is faster than the molecules can decay (cool) via rovibrational emission lines or collisions.

I perform a simple back-of-the-envelope comparison of the H_2 rovibrational emission and total collision rates required to counteract H_2 photo-excitation ("Lyα-pumping"), assuming the H_2 species are located in a hot atomic layer above the PPD. The hot atomic region is assumed to be a plane-parallel slab above the inner disk ($r < 1$ AU; Ádámkovics et al. 2016) with a thickness $a \sim 1$ AU. I assume the average Lyα luminosity for a typical PPD system $\langle L_{Ly\alpha} \rangle \sim 10^{31}$ erg s^{-1} (Schindhelm et al. 2012b, France et al. 2014b), which translates into an average photon rate $\langle \Gamma_{Ly\alpha} \rangle = \langle L_{Ly\alpha} \rangle$ / $E_{Ly\alpha} \sim 10^{42}$ photons s^{-1} incident on the hot H_2. Since H_2 is expected to only be a trace species in this region ($x(H_2) \sim 10^{-5}$; Ádámkovics et al. 2016), I include a "coverage factor" for the total Lyα luminosity on the H_2 populations. This leads to an estimation of the total photo-excitation rate of H_2 in the hot atomic layer, $\langle \Gamma_{Ly\alpha} \rangle \sim x(H_2) \times 10^{42}$ photons $s^{-1} \sim 10^{37}$ photons s^{-1}. Therefore, taking into account the geometry of the hot atomic layer, I calculate the average rate of incident Lyα photons on the H_2 populations in the PDR slab to be $\gamma_{Ly\alpha} \sim \langle \Gamma_{Ly\alpha} \rangle$ / $(\sigma(H_2) \times a^2) \approx 10^{-3}$ photon s^{-1}, where $\sigma(H_2)$ is the average Lyα line absorption cross-section of an individual molecules, given by

$$\sigma(H_2) = \frac{\sqrt{\pi} e^2}{m_e c b_{H_2}} \lambda_i f_i \tag{3.2}$$

(McCandliss 2003, Cartwright and Drapatz 1970), where λ_i is the absorption wavelength for a given transition in the Lyα profile (taken as 1215.67 Å for this example), f_i is the oscillator strength (the average assumed as ≈0.01), and b_{H_2} is the b-value of the line, assumed to match my models (b_{H_2} = 5 km s^{-1}), producing an average cross section for Lyα photon absorption $\sigma(H_2) \sim 10^{-14}$ cm^2.

I do not include additional losses of Lyα flux due to absorption from other atomic species, as it is assumed that the dominant constituent of the disk PDR is neutral hydrogen at an average T_{gas} ~ 3500 - 5000 K, which will scatter Lyα around the region. I quantify the ratio of the UV photo-excitation rate to the average transition probability for quadrupolar H_2 IR emission lines ($A_{quad} \sim 10^{-7}$ s^{-1}; Wolniewicz et al. 1998), $\gamma_{Ly\alpha}$ / $A_{quad} \sim 10^4$ photons, meaning that of order 10,000

Lyα photons are expected to be absorbed by hot H_2 for every one quadrupolar emission photon emitting. By this simple calculation, quadrupole emission is not an effective means of cooling the hoto-excited H_2 populations in these regions.

Next, I explore what the expected collisional rate between H_2 and other particles in the hot atomic slab must be to balance with the UV photo-excitation rate. First, I set the total collisional rate of all particle interactions with H_2 in this region to match the photo-excitation rate of H_2 in the hot atomic region, such that $\Sigma\alpha_{H_2,i} = \gamma_{Ly\alpha} \sim 10^{-3}$ collisions s^{-1}. Given $\langle N(H_2) \rangle$ from my empirical models, I estimate the total number density of H_2 in the hot atomic layer to be $n(H_2) \sim 10^3$ cm^{-3}. Finally, I estimate the total collisional rate with H_2 needed to match the photo-excitation rate of H_2 via Lyα-pumping, $\Sigma C_{H_2,i} \sim \Sigma\alpha_{H_2,i}$ / $n(H_2) \sim 10^{-6}$ cm^3 s^{-1}.

This result suggests that, at $T_{gas} \approx$ 3500 - 5000 K, interactions between H_2 and dominant particles in the hot atomic environment, like HI, protons (p^+), and electrons (e^-), are expected to occur at a total rate of $\sim 10^{-6}$ cm^3 s$-$1. Mandy and Martin (1993) and Roberge and Dalgarno (1982) find collisional rates between H_2 + HI to be of order $C_{H_2,HI} \sim 10^{-10}$ cm^3 s$-$1 for gas with $T_{gas} \approx$ 2000 - 4500 K (which is similar to interactions between H_2 + p^+; Black and Dalgarno 1977, Smith et al. 1982). The rate of collisions between H_2 + e^-, for gas with $T_{gas} \sim$ 3500 K, is found to be $C_{H_2,e^-} \sim 10^{-11}$ cm^3 s$-$1 (Prasad and Huntress 1980). Additionally, interactions between H_2 + H_2 are expected to occur much less frequently, with $C_{H_2,H_2} \sim 10^{-16}$ cm^3 s$-$1 for $T_{gas} \sim$ 3500 K (Mandy 2016).

I find that the integrated collision rate of H_2 in these environment, derived from literature values, is $\sim$ 4 dex lower than the photo-excitation rate of H_2 by Lyα radiation alone. When I quantify the ratio of the UV photo-excitation rate to the total collisional rate of particles with H_2 in this exercise (optimistically assuming $\Sigma C_{H_2,i} \sim 10^{-9}$ cm^3 s^{-1}), $\gamma_{Ly\alpha}$ / ($\Sigma C_{H_2,i} \times n(H_2)$) $\sim 10^3$ photons, or that $\sim$1,000 Lyα photons are absorbed for every one de-excitation collision of H_2.

It appears viable that "multiple pumping" may play a key role in re-distributing H_2 rovibrational states in this hot gas region of the circumstellar environment before collisions or rovibrational emission can cool the molecules. Indeed, my simple calculation compliments observed

behaviors of H_2 rovibration levels in ISM PDR environments (e.g., Draine and Bertoldi 1996, Hollenbach and Tielens 1999, and references therein). The critical density of most H_2 rovibration levels, or the ratio of the radiative lifetime of a given state (A_{ul}, in s^{-1}) to the collision rate for de-excitation out of the same state ($C_{H_2,i}$, in $cm^3\ s^{-1}$), is typically of order $10^4\ cm^{-3}$ for $T_{gas} >$ 2000 K (Mandy and Martin 1993). By my estimation, the density of H_2 is near this critical density, but is still under it, allowing "multiple pumping" to repopulate H_2 states by UV pumping before collisions de-excite the level populations (Draine and Bertoldi 1996, Hollenbach and Tielens 1999).

3.5.4 A Simple Model of Lyα-pumped H_2

What, then, is the expected distribution of H_2 rovibration levels if Lyα-pumping plays a significant role in regulating the ground states of the molecules? I create a simple model of H_2 photo-excitation, in the absence of cooling routes (i.e., rovibrational emission and collisional de-excitation), which monitors the column densities of individual H_2 rovibrational levels in the presence of an appreciable Lyα radiation field. This model tracks the fluorescence cascade of H_2 from excited electronic levels, pumped by photo-excitation, back to the ground electronic level until the column densities of rovibration states settles to a preferential distribution, (i.e. the states no longer significantly change due to the photo-excitation process). The framework of the model, which we will refer to as Model 3, is as followings:

(1) I start with a thermal distribution of hot H_2, where rovibrational levels are statistically defined by the total column density ($N(H_2)$) and temperature ($T(H_2)$) of the bulk molecular population.

(2) A constant, uniform radiation distribution of Lyα photons are generated and exposed to the initially-defined thermal population of H_2.

(3) H_2 in the correct $[v,J]$ ground level will have some cross-sectional probability to absorb Lyα photons incident on the H_2 populations. If the H_2 molecules absorb the photons, they are pumped to an excited electronic level, either in the Lyman or Werner bands. From

there, they immediately decay back to the ground state in one of multiple routes, or in a fluorescent cascade. The probability for a Lyα-pumped H_2 to decay back to a specific ground level is defined by the branching ratios (transition probabilities) from the excited electronic level [v',J'] to the ground electronic level [v'',J''].

(4) All rovibration levels of H_2 are followed simultaneously and allowed to redistribute themselves by transition probabilities after initially being photo-pumped out of their original ground electronic level, [v,J]. The model runs until the ground robvibration levels settle to a nearly constant distribution of levels in the presence of this unchanging Lyα radiation field.

The Lyα radiation distribution used in Model 3 is assumed to mimic the observed line width and shape on a target-by-target basis. The Lyα line shape is assumed to be Gaussian, with parameters describing the line shape adapted from McJunkin et al. (2014). The flux in the Lyα line, $F_{Ly\alpha}$, is allowed to float in each model run, as are N(H_2) and T(H_2), which set the initial conditions for each model iteration. For the duration of each model, the Lyα line emission is assumed to neither change in shape nor in peak flux, effectively providing the H_2 populations with a constant, uniform distribution of Lyα photons until the H_2 ground states relax to some preferential distribution. The basic mechanics of the model take advantage of $\sim$100 H_2 cross sections coincident with the Lyα emission profiles of typical PPD targets (i.e., Classic T Tauri stars; France et al. 2014b). These cross sections are calculated using intrinsic transition properties of H_2 with Lyα provided by Abgrall et al. (1993a) and Abgrall et al. (1993b). Based on the energy of a given Lyα photon, H_2 in a receptive rovibration level [v,J] will absorb the photon and be pumped to either the Lyman or Werner excited electronic band. The excited H_2 molecules will decay back to one of many potential ground electronic rovibration levels via branching ratio probabilities, again inferred from intrinsic molecular properties provided by Abgrall et al. (1993a) and Abgrall et al. (1993b). This process is repeated until the rovibration levels of H_2 relax to some distribution of states under the constant Lyα flux (i.e., no more significant change to in the column densities of rovibration levels

is detected, to within $\delta\log_{10}\mathrm{N}(\mathrm{H}_2[v,J]) \lesssim 0.1$ for all rovibration levels). See Appendix D.1.1 for more details about the models, including the iteration process used for Lyα-pumping, H_2 electronic fluorescence and further details regarding the MCMC and statistics of the process.

I present Model 3 results in Table 3.5. Figure 3.12 shows the observed rotation diagram of RW Aur A and the resulting modeled distribution of H_2 rovibration levels produced by Model 3. The Lyα photo-excitation models for all targets are presented in Appendix D.4. Green plus symbols represent all H_2 rovibrational states for $v \leq 15$, $J \leq 25$, while cyan "X"s represent modeled rovibration levels with the same rovibration level as those empirically measured in the stellar Lyα wings of the target. Model 3 for RW Aur finds a total column density of H_2, $\log_{10}(\ \mathrm{N}(\mathrm{H}_2)\ ) \approx 18.0$, which is $\sim$2 dex lower than results from France et al. (2014b), at a temperature $\mathrm{T}(\mathrm{H}_2) \approx 2500$ K (in France et al. (2014b), $\mathrm{T}(\mathrm{H}_2)_{warm} = 440$ K).

The total column density of thermal H_2 for RW Aur slightly larger than the average best-fit $\mathrm{N}(\mathrm{H}_2)$ for all targets ($\langle\log_{10}\mathrm{N}(\mathrm{H}_2)\rangle \sim 17.0$), with the smallest total column density $\log_{10}\mathrm{N}(\mathrm{H}_2) \approx 15.5$. Interestingly, for almost all samples in this survey, the derived total column density of thermal H_2 distributions is larger than those estimated by the purely thermal H_2 models (i.e., Models 1 and 2). For all targets, the derived thermal temperatures of H_2 from the Lyα-pumping model range from 1500 - 4000 K ($\langle\mathrm{T}(\mathrm{H}_2)\rangle \sim 2800$ K). Overall, the final results from the Lyα-pumping models slightly overestimate the total column density of H_2 for a hot atomic layer origin by $\sim$1-2 dex and underestimate the total column density of H_2 for a warm molecular layer origin by the same amount (Ádámkovics et al. 2016). Additionally, the temperature of thermal H_2 is found somewhere between the two layers.

Interestingly, the modeled H_2 rovibrational levels from Model 3 are redistributed in such a way that more highly thermal H_2 populations ($T_{exc} \gtrsim 30{,}000$ K) can be pumped to higher column densities than they are expected to be in thermal distributions. Rovibrational levels of H_2 most affected by the flux of Lyα (i.e., $v \geq 2$; $T_{exc} \sim 10{,}000$ K) first appear diminished in column density, relative to the native thermal distributions, but for rovibrational levels with $T_{exc} \gtrsim 30{,}000$ K, the relative column densities of highly energetic states appears to return back towards the level of the

Table 3.5. Lyα-pumped H_2 Column Density & Temperature Results

	Model 3			
Target	$N(H_2)^a$	$T(H_2)^b$	$F_{Ly\alpha}{}^c$	$\Delta N(H_2)^{a,d}$
AA Tau	$16.28^{+0.52}_{-0.33}$	3214^{+570}_{-810}	$-10.4^{+0.8}_{-0.7}$	14.13
AB Aur	$15.60^{+0.29}_{-0.16}$	3437^{+410}_{-691}	$-10.5^{+0.5}_{-0.6}$	13.44
AK Sco	$15.65^{+0.50}_{-0.27}$	3601^{+290}_{-522}	$-10.2^{+0.7}_{-0.3}$	13.35
BP Tau	$17.09^{+0.94}_{-0.58}$	2557^{+1113}_{-1339}	$-6.7^{+0.6}_{-0.5}$	13.09
CS Cha	$18.36^{+0.68}_{-1.17}$	1596^{+1700}_{-340}	$-6.9^{+0.3}_{-0.4}$	13.61
DE Tau	$16.21^{+0.45}_{-0.34}$	2982^{+693}_{-812}	$-9.4^{+0.7}_{-0.7}$	13.94
DF Tau A	$16.48^{+1.23}_{-1.38}$	2678^{+940}_{-1258}	$-6.9^{+0.4}_{-4.2}$	12.63
DM Tau	$16.30^{+0.80}_{-0.28}$	3670^{+232}_{-888}	$-8.7^{+1.0}_{-0.6}$	13.90
GM Aur	$16.15^{+0.32}_{-0.22}$	3469^{+376}_{-650}	$-7.5^{+0.3}_{-0.4}$	13.55
HD 104237	$17.87^{+0.57}_{-0.52}$	2200^{+1060}_{-766}	$-5.7^{+0.2}_{-0.3}$	13.25
HD 135344 B	$16.78^{+0.46}_{-0.31}$	3185^{+517}_{-1128}	$-6.4^{+0.3}_{-0.3}$	13.26
HN Tau A	$16.95^{+0.99}_{-0.64}$	2140^{+1088}_{-998}	$-8.9^{+1.5}_{-1.3}$	12.24
LkCa15	$18.09^{+1.00}_{-0.53}$	3456^{+394}_{-858}	$-8.9^{+2.1}_{-1.3}$	13.81
RECX 11	$16.72^{+0.32}_{-0.25}$	3087^{+593}_{-411}	$-6.7^{+0.3}_{-0.7}$	13.60
RECX 15	$17.13^{+0.55}_{-0.53}$	2679^{+933}_{-798}	$-5.9^{+0.2}_{-0.5}$	13.85
RU Lupi	$17.26^{+0.46}_{-0.47}$	2735^{+621}_{-976}	$-5.7^{+0.1}_{-0.4}$	13.95
RW Aur A	$18.03^{+0.68}_{-0.71}$	2504^{+1489}_{-627}	$-5.6^{+0.1}_{-0.2}$	14.25
SU Aur	$17.59^{+1.31}_{-1.20}$	2739^{+857}_{-1631}	$-6.1^{+0.4}_{-4.0}$	12.85
SZ 102	$16.97^{+1.31}_{-0.89}$	2662^{+940}_{-1435}	$-6.9^{+1.0}_{-2.3}$	13.16
TW Hya	$17.19^{+1.22}_{-0.61}$	1910^{+1514}_{-1029}	$-6.6^{+0.6}_{-0.3}$	13.03
UX Tau A	$17.54^{+1.40}_{-0.49}$	2734^{+880}_{-1789}	$-6.5^{+0.8}_{-1.2}$	13.75
V4046 Sgr	$16.24^{+1.05}_{-0.32}$	2803^{+771}_{-1309}	$-6.6^{+0.7}_{-1.1}$	12.76
Avg. Model Results	$16.93^{+1.40}_{-1.33}$	2820^{+850}_{-1224}	$-7.4^{+1.8}_{-3.1}$	13.43

[a]All column densities are to the power of 10 ($\log_{10}N(H_2)$).

[b]Temperatures of H_2 ($T(H_2)$) are in Kelvin.

[c]The integrated Lyα fluxes that pump H_2 populations out of thermal equilibrium are described by the sum of a narrow and broad Gaussian component, with FWHMs of each component adapted from McJunkin et al. (2014). Flux are to the power of 10 ($\log_{10}F(Ly\alpha)$). $F(Ly\alpha)$ has units of ergs cm^{-2} s^{-1}.

[d]The integrated residual between the observed column densities of H_2 in states $[v,J]$ to the model prediction of column density in the same rovibrational levels, $\Sigma|N(H_2[v,J])_{data} - N(H_2[v,J])_{model}|$.

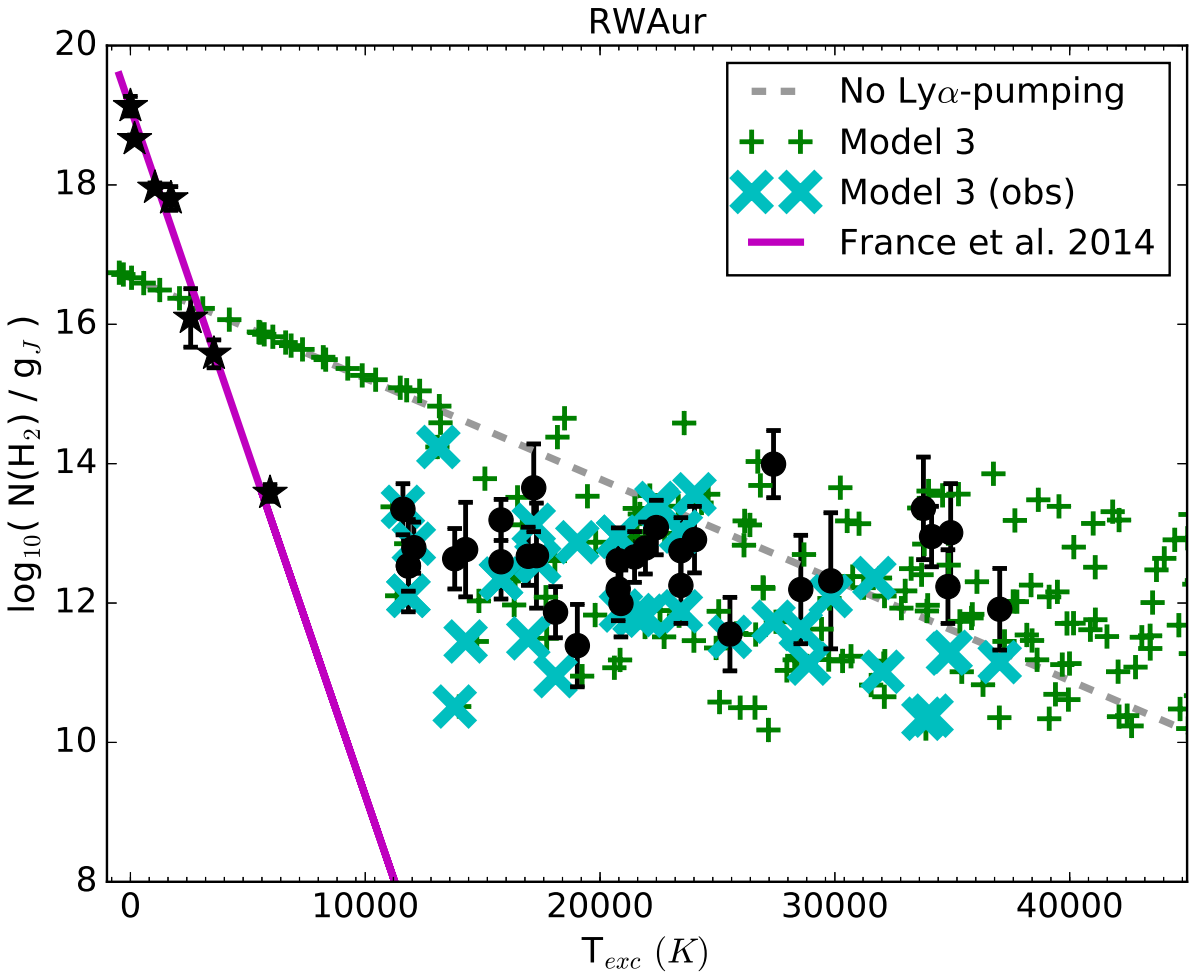

Figure 3.12 The rotation diagram for RW Aur, with rovibrational column densities derived in this study (black circles) and lower energy states calculated by France et al. (2014a) (black stars; $\lambda\lambda$ 1092.5 − 1117 Å). The magenta solid line shows the thermal distribution H_2 levels examined by France et al. (2014a), with $\log_{10}(\ N(H_2)\ ) = 19.90$ cm^{-2} and $T(H_2) = 440$ K. The green plus symbols represent the H_2 rovibrational levels output by the Lyα-pumping models (Model 3). The cyan "X"s mark rovibrational levels from Model 3 which match the observed H_2 levels, so the reader can directly compare the the data with the modeled states. The gray dashed line presents the initial thermal distribution of H_2 in the models (i.e., without Lyα pumping), which is described by $\log_{10}(\ N(H_2)\ ) = 18.03$ and $T(H_2) = 2504$ K.

thermal distribution, with many states being pumped by $\gtrsim$ 1 dex more than they would otherwise be in thermally-distributed states.

The re-distributed H_2 rovibrational levels also appear scattered, with the distributions appearing roughly consistent for rovibrational levels with $T_{exc} \gtrsim$ 10,000 K and a spread of $\sim$1 dex. This behavior roughly matches the characteristic distributions of empirically-derived H_2 rovibration levels measured against Lyα for most, if not all, of the PPD sightlines. The Lyα redistribution appears to scatter most H_2 states out of thermal equilibrium at $T_{exc} \gtrsim$ 10,000 K, suggesting that the H_2 absorption coincident on the Lyα wings do not probe thermal populations of H_2 in these sightline. The fact that this same peculiar H_2 population behavior is observed for all disks in our survey, regardless of orientation of the disk in the line of sight (i.e., i_{disk}) or disk evolutionary phase, suggests that the sampling of H_2 may not be co-spatial with the same H_2 populations observed in fluorescence from each disk. The models also suggest that, for rovibrational levels insensitive to Lyα radiation (i.e., $v < 2$), H_2 may still be thermally populated. Theoretically, if the rovibrational levels of the same H_2 populations could be observed (independent from those probed in the protostellar Lyα profiles), this hypothesis may be tested.

There is one case study - RW Aur - where this test is currently possible. The sightline to RW Aur probes both hot H_2 embedded in the Lyα profile of the protostar and warm H_2 detected against the protostellar FUV continuum ($\lambda\lambda$ 1090 - 1120 Å; France et al. 2014b). If the warm disk H_2 populations and the hot Lyα H_2 populations were co-spatial with one another, it is expected that signatures of the hot H_2 populations would be detected in the FUV-continuum (specifically for $v = 0$, $J = 4$, 5, 6; λ = 1100.2, 1104.1, 1104.5, 1109.3, 1109.9, 1115.5, 1116.0 Å, where the distributions of warm and hot H_2 populations overlap; Figure 3.12). From the Lyα-pumping model results for RW Aur, the column densities of hot H_2 are expected to be several dex higher than those in the warm H_2, as determined by France et al. (2014b). The FUV continuum is much less likely to scatter through the gas disk than Lyα, and therefore is expected to provide a better probe of the geometry through the disk material. The fact that the France et al. (2014b) study does not see clear deviations to either larger column densities found by Model 3 for hot $H_2[v = 0, J = 4, 5, 6]$

or excited H_2 populations associated with hotter H_2 distributions in the FUV continuum is further evidence supporting my original hypothesis: that the resonance nature of Lyα allows the radiation to scatter through a hot atomic haze or layer above the PPD, and the observed H_2 signatures observed in the protostellar Lyα wings probe residual H_2 in these environments, rather than H_2 in the planet-forming disk.

However, while the general behavior of rovibration levels matches the characteristic behavior of empirically-derived Lyα-H_2 absorption species, Model 3 does not perfectly replicate the observed level populations of H_2. I present the total residual H_2 densities unaccounted for by the models in Table 3.5, which are $\sim$4 dex lower than residuals found between purely thermal models (Models 1 and 2) and highly energetic H_2 states ($T_{exc} > 20{,}000$ K). The models I put forth for this experiment were simplified, and perhaps including more physical mechanisms to the simulations, such as additional UV-pumping throughout the FUV, H_2 dissociation and formation routes, rovibration emission, and collisional de-excitation, will better estimate the distribution of H_2 levels under all these processes simultaneously. Still, the Lyα-pumping models were successful in replicating the general behavior of hot H_2 rovibrational levels observed in PPD sightlines against the protostellar Lyα features. This result suggests that photo-excitation from HI-Lyα may be an effective process for re-distributing the ground electronic levels of the hot H_2 probed in the Lyα profiles. This has its limits, as demonstrated at the end of Section 3.5.3: Lyα photo-excitation may only be an effective means of re-distributing H_2 ground levels in optically-thin regimes (e.g., PDRs), or where rovibrational cooling and collisional de-excitation of H_2 occur much less frequently than photo-excitation, but otherwise likely does not have as strong a role in other astrophysical environments where these conditions do not hold true.

Chapter 4

CHESS: The Colorado High-resolution Echelle Stellar Spectrograph

"It's a rocket condom; I don't know how no one else sees it."

- Larry Conser, on the protective bagging placed over the payload for transport to the rail.

The Colorado High-Resolution Echelle Stellar Spectrograph (CHESS) is a far-ultraviolet (far-UV) sounding rocket payload designed to study the materials which will go into forming the next generations of stars and planets. As a significant portion of my Ph.D. thesis, I collaborated in the design, fabrication, testing, build, calibration, and flight of CHESS for two sound rocket launches. The first launch (NASA/CU 36.285 UG; CHESS-1) was on 24 May 24 2014 at 01:35 (MST) from White Sands Missile Range (WSMR) in New Mexico, and the second launch (NASA/CU 36.297 UG; CHESS-2) occurred on 21 February 2016 at 21:15 (MST) from WSMR. CHESS launched from a Black Brant IX missile stack (Terrier + Black Brant motor), allowing for $\sim$400 seconds of exposure time on target and an apogee of roughly 300 km. Both launches were comprehensively successful, with spectrograph and electronics components working as nominally designed and science data acquired. In this chapter, I describe the CHESS experiment, from design to component testing and novel alignment procedures to laboratory calibration techniques, and include results from the first two launches of CHESS.

4.1 The Scientific Motivations & Objectives of CHESS

4.1.1 Translucent Cloud Characteristics

Translucent clouds reside in the transition between the diffuse (traditionally defined as $A_V < 1$) and dense ($A_V > 3$) phases of the interstellar medium (ISM). It is in this regime where the ultraviolet portion of the average interstellar radiation field plays a critical role in the photochemistry of the gas and dust clouds that pervade the Milky Way galaxy. The most powerful technique for probing the chemical structure of translucent clouds is to combine measurements of H_2 with knowledge of the full carbon inventory (CI, CII, and CO) along a given line of sight. It has been argued that an analysis of the carbon budget should be the defining criterion for translucent clouds, rather than simple measurements of visual extinction (Snow and Jensen 2006). Moderate resolution spectra from FUSE (λ = 1000 - 1120 Å) higher-resolution data from HST/STIS ($\lambda >$ 1150 Å) have been used to show that many of these sightlines have $CO/H_2 > 10^{-6}$ and CO/CI $\sim$ 1, consistent with the existence of translucent material in the framework of current models of photodissociation regions in the ISM (Burgh et al. 2007; 2010).

The CHESS experiment is designed to study translucent clouds with its combination of broad bandpass and high spectral resolution. The FUV bandpass between λ = 1000 - 1600 Å contains a myriad of atomic and molecular features, most notably for this study, absorption features of H_2 ($\lambda\lambda$ 1000 - 1120 Å; we note that several H_2 complexes are expected to be blended with strong atomic features, such as HI-Lyβ at λ1026), CII (λ1036 and λ1335; however, we note that saturation effects can complicate the interpretation of these lines), CI (λ1158, λ1193, λ1277, λ1560 Å), and the $A - X$, $B - X$, $C - X$, and $E - X$ rovibrational bands of CO ($\lambda <$ 1510 Å). High resolution (R) > 100,000 is required to resolve the velocity structure of the CI lines and the rotational structure of CO and, therefore, is an essential aspect of this experiment to accurately determine the column densities of these species (Jenkins and Tripp 2001). The FUV also provides access to many absorption lines of ionic metals, such as FeII, MgII, SiII, SII, and NiII, allowing for an exploration of the depletion patterns through the ISM. CHESS, with its high-resolution and large bandpass covering

wavelengths inaccessible with IUE ($\lambda < 1150$ Å), is well-suited to the study of translucent clouds and will help create an observational base for models of the chemistry and physical conditions in interstellar clouds.

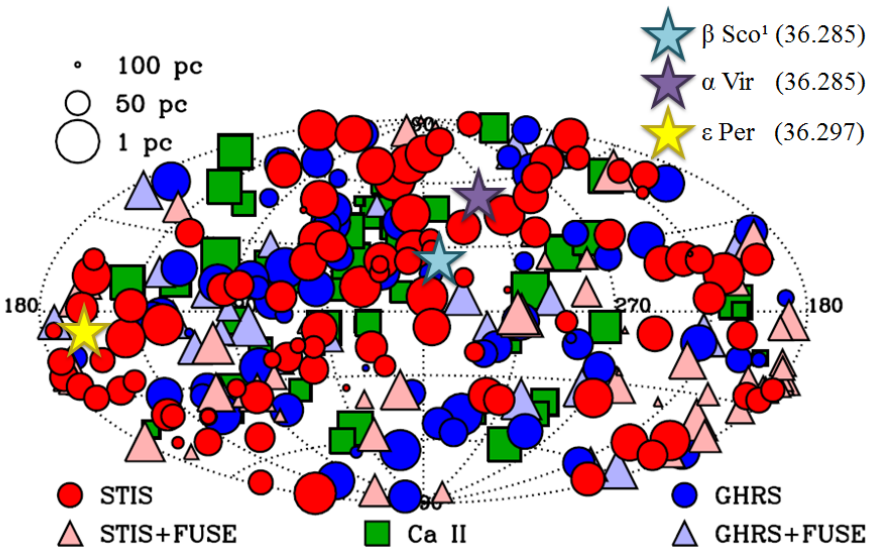

Figure 4.1 The observational database of FUV LISM sightlines within 100 pc. CHESS targets (NASA/CU missions 36.285UG and 36.297UG) are included to show how CHESS observations help fill in the sky coverage to create a more complete map of LISM properties (distribution of LISM sightlines adopted from Redfield 2009).

4.1.2 The Local Interstellar Medium

The CHESS experiment also provides a unique testbed to characterize the structure and thermal properties of the local interstellar medium (LISM). The LISM provides an opportunity to study general ISM phenomena up close and in three dimensions, including interactions of different phases of the ISM, cloud collisions, cloud evolution, ionization structure, thermal balance, turbulent motions, etc (Redfield 2006). Our immediate interstellar environment also determines the structure of the heliosphere, or the momentum balance of the solar wind and the surrounding ISM. Additionally, multiple launches of CHESS allows for multiple lines of sight through the LISM, making it possible to construct a three-dimensional morphological and physical model of the LISM. Several physical characteristics of the LISM are measurable, including the ionization structure.

Table 4.1. Stellar Target Parameters for CHESS-1 & CHESS-2 Launches

Stellar Object	Right Ascension	Declination	d (pc)	E(B-V)	$\log_{10}$ N(HI + H_2)[a]	F_λ(1150Å)[b] (erg cm^{-2} s^{-1} $Å^{-1}$)
β Sco[1]	16^h 05^m 26.2^s	-19° 48′ 19.6″	161	0.2	21.14	2.0×10^{-8}
ϵ Per	03^h 57^m 51.2^s	+40° 00′ 36.8″	307	0.1	20.50	2.5×10^{-8}
α Vir[c]	13^h 25^m 11.6^s	-11° 09′ 40.8″	43	0.03	< 19.0	1.0×10^{-7}
Object Sky Calibration	Right Ascension	Declination				
β Sco[1]	15^h 58^m 32.0^s	-19° 48′ 12.8″				
ϵ Per	03^h 48^m 10.6^s	+40° 00′ 32.0″				

[a]Savage et al. (1977)

[b]Flux taken from archival IUE spectra.

[c]Back-up target for CHESS-1, and no sky calibration coordinates were chosen for this target.

Since any clouds in the LISM are optically thin, the distribution of ionizing sources (i.e., hot stars) determines the three-dimensional ionization structure of the LISM.

Measurements of different ionization stages are required to probe the different ionization environments of the LISM. In addition to local ionization structure, local temperature and elemental depletion structure are also critical to understanding the three-dimensional morphology of the LISM. The temperature distribution of the LISM can place constraints on models of the evolution of the local solar neighborhood. Determining these temperatures requires high spectral resolution so that contributions from thermal and turbulent motions can be distinguished, a capability that is achievable with the high spectral resolution of CHESS.

4.1.3 CHESS Targets & Known Characteristics

For the first flight of the CHESS payload, CHESS examined the constituents of the local interstellar medium (LISM) with a detailed study of the interstellar material in the sightline of β Sco[1] (HD 144217). β Sco[1] is spectroscopic binary comprised of a B0.5V and a B1.5V spectral type star at distance of 161 pc with intermediate reddening (E(B-V) = 0.2, $A_V \sim 0.6$; log N(H_2) $\sim$ 19.8 cm^{-2} (Savage et al. 1977)). Because of concerns regarding the final performance of the CHESS experiment for first flight (see Section 4.3.2), the science team elected to define a back-up

target to move to if the signal-to-noise (S/N) of β Sco[1] was insufficient to produce a science-quality spectrum during the limited time of the flight. The back-up target, α Vir (HD 116658; "Spica"), is a spectroscopic binary, consisting of a B1III-IV star + B2V star at a distance of 43 pc (Hoffleit and Jaschek 1982), well within the Local Bubble (E(B-V) = 0.03, $A_V \sim 0.1$ (Savage et al. 1977)). While α Vir does not provide an interesting sightline for the science goals of CHESS, it outputs $4 - 5$ times more far-UV flux than β Sco[1] and could demonstrate the capabilities of the CHESS instrument, if the optical components of CHESS did not meet the outlined specifications for launch. For the second flight of CHESS, we observed the line of sight towards ϵ Per (HD 24760). ϵ Per is a B0.5III star at d $\approx$ 300 pc, with low−intermediate reddening (E(B-V) = 0.1, $A_V \sim 0.4$; log N(H_2) $\sim$ 19.5 cm^{-2} (Savage et al. 1977)), indicating that the sightline samples cool interstellar material.

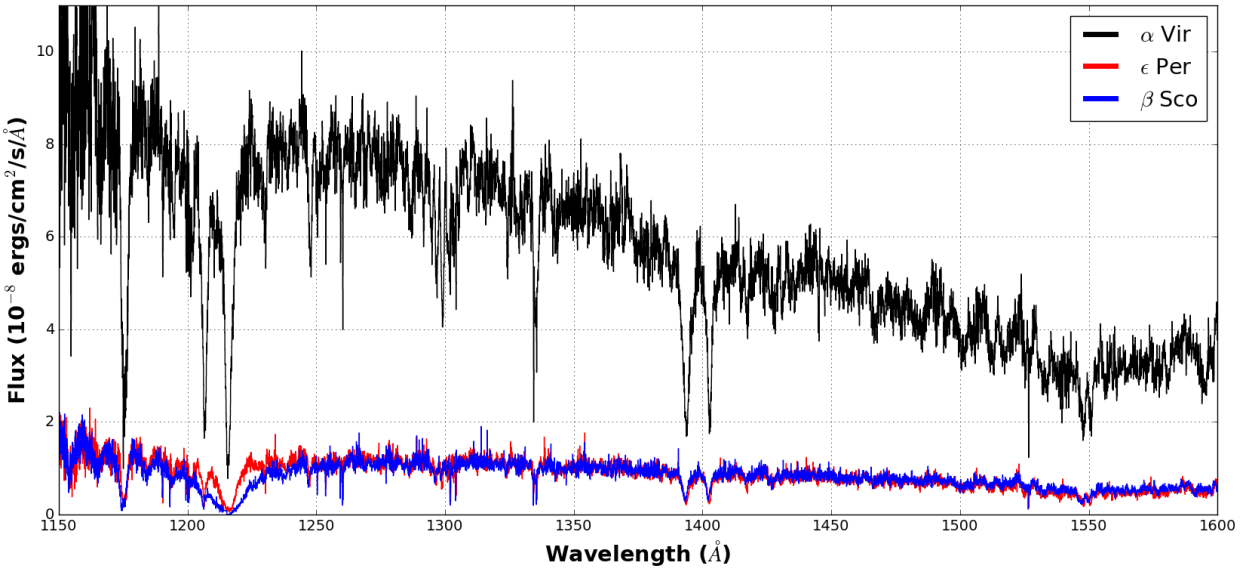

Figure 4.2 The far-UV spectrum (115- − 1600 Å) of each CHESS science target. β Sco[1] and α Vir were chosen for the first launch of the instrument and ϵ Per for the second.

Figure 4.2 shows all flux-calibrated data from the *International Ultraviolet Explorer* (IUE) for each CHESS target. Primary science targets for both flights of CHESS have very similar flux outputs, but to mitigate any unseen compromise to one or more experimental optical components in the CHESS payload, a brighter secondary target is chosen to address science goals related to the

LISM.

Both primary science targets of CHESS (β Sco^1 and ϵ Per), show traces of H_2, CI, and CO in their sightlines, as detected by Copernicus and IUE (e.g., Savage et al. 1977, Bohlin et al. 1978, Tarafdar and Krishna Swamy 1982); however, given instrumental limitations, higher sensitivity and spectral resolution are required for a complete analysis of both stellar sightlines (Federman et al. 1980). The β Sco^1 sightline has been used to study the physical and dynamical behaviors of molecular and atomic material in the Scorpius OB association in several Copernicus and IUE survey studies of interstellar absorption lines (Federman et al. 1980, Bohlin et al. 1983, van Steenberg and Shull 1988). Additionally, observations by Copernicus and IUE have been used to measure the velocity structure along the sightline to ϵ Per, and both have found at least three separate cloud structures described by different kinematic behavior and molecular abundances (Bohlin et al. 1983). Overall, the β Sco^1 sightline shows depletion of molecular material and ionized metal features, such as CO, FeII and MgII (Bohlin et al. 1983), consistent with the sightline to δ Sco^1 but inconsistent with other nearby hot stellar sightlines, such as ζ Oph (Morton 1975) and ρ Oph (Snow and Jenkins 1980). Abundances of such species in the ϵ Per sightline were found to be consistent with typical sightlines towards recent star-forming sites (Bohlin et al. 1983). Both CHESS experiments sought to perform the first high resolution (R > 100,000) observations of β Sco^1 and ϵ Per in the far-UV, to observe H_2, carbon budget species, and ionized metal lines simultaneously, thereby constraining the metal content, kinematic structure, and photo-dissociation processes of the nearby molecular material and warm ISM.

4.2 CHESS Instrument Design

CHESS is an objective echelle spectrograph with a slow focusing beam (f/12.4), allowing for a relatively large tolerance in spectrograph focal position. The instrument design includes the development of two novel gratings and detector (Beasley et al. 2010). The instrument is designed to achieve a high resolving powers (R $\geq$ 100,000 $\lambda/\Delta\lambda$) across a broad bandpass in the FUV ($\lambda\lambda$ 1000 - 1600 Å) (France et al. 2012a, Hoadley et al. 2014; 2016, France et al. 2016b). Light entering

the spectrograph section undergoes the following to produce the raw science product:

(1) A mechanical collimator, consisting of a 2-dimensional array of black anodized aluminum tubes, blocks stray and off-axis light from entering the spectrograph.

(2) A high-dispersion grating (echelle) intercepts and disperses on-axis FUV stellar light into higher diffraction terms.

(3) The dispersed starlight is directed to a cross-dispersing grating (cross disperser), which separates light with the same high-dispersion solutions. The cross disperser used in CHESS is also a powered optic, which focuses the echelle spectra.

(4) The detector reads in the focused, high-dispersion spectra from the cross disperser.

Because the echelle disperses light into high order terms and the cross disperser separates light sharing the same echelle diffraction order solutions, the final data product is a series of spectra, where each echelle spectra provides a small fraction of the total spectral coverage of the instrument. An example of a raw data product produced by CHESS in a laboratory setting is shown in Figure 4.3. At the same time, each spectral snippet in the full raw data is able to be sampled at high resolution. This is how CHESS is able to achieve both large wavelength coverage and high resolution. A more detailed description of each experimental optical component ((2) − (4)) is provided in Section 4.3.

Pointing towards the primary science target while on-target during flight was critical for the primary science objectives of CHESS and ensures both target acquisition and stability while collecting science data, the latter of which was crucial for the high spectral resolution capabilities of the experiment. Therefore, to track, acquire, and monitor the stellar target during flight, CHESS is equipped with a secondary optical system through the spectrograph section, which is used to align the spectrograph to the stellar target during calibrations and flight. The optical system is designed to track mis-alignments between the instrument optics by using a reference mirror directly mounted to the optical mount of the echelle grating, which reflects light to the cross dispersing

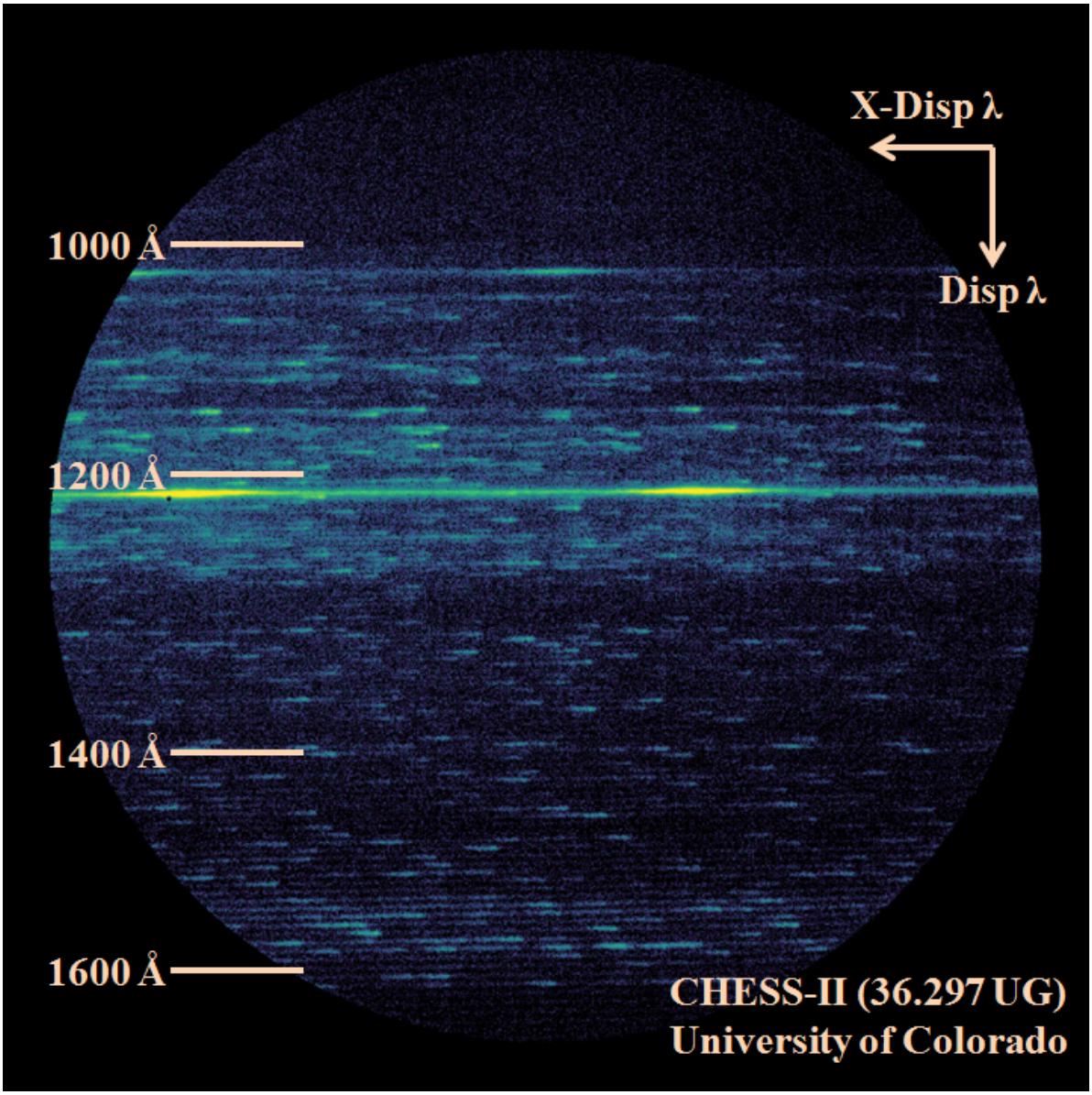

Figure 4.3 A false-color representation of the full-resolution (8192×8192 digital pixels) laboratory echellogram of CHESS after instrument alignment. The black/blue represents little to no counts in the binned pixel location, while green/yellow represent emission lines from hydrogen (Lyα λ1215.67 Å) and molecular hydrogen (H_2). Overlaid are arrows showing the direction of dispersion from the echelle ("Disp λ") and cross disperser ("X-Disp λ"), and the tick marks show the approximate location of different spectral regions. The final laboratory calibration image contains over 73 million photon counts.

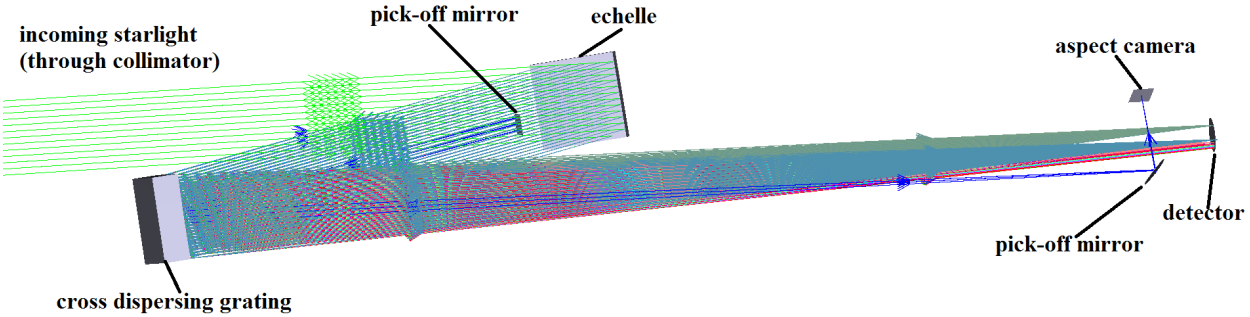

Figure 4.4 A Zemax rendition of CHESS, including the secondary aspect camera (star tracking) system. The mechanical collimator reduces stray light in the line of sight and feeds starlight to the echelle. The echelle disperses UV light into high-dispersion orders, which are spread and focused by the cross disperser onto the detector plane. The different colored lines (yellow, teal, pink, red) represent a series of wavelengths within the $\lambda\lambda$ 1000 - 1600 Å bandpass of CHESS. Light green entering the spectrograph represents white stellar light, and dark blue represents optical (visual) wavelengths feeding the aspect camera system.

grating. The zeroth-order solution off the cross dispersing grating is directed to another stand-alone mirror on the detector bulkhead, which directs the starlight to a stand-alone optical camera (the aspect camera). Figure 4.4 shows the raytrace for CHESS, illustrating the light path through the instrument to create the echellogram seen in Figure 4.3 and showing the secondary star-tracking system in relation to the UV spectrograph.

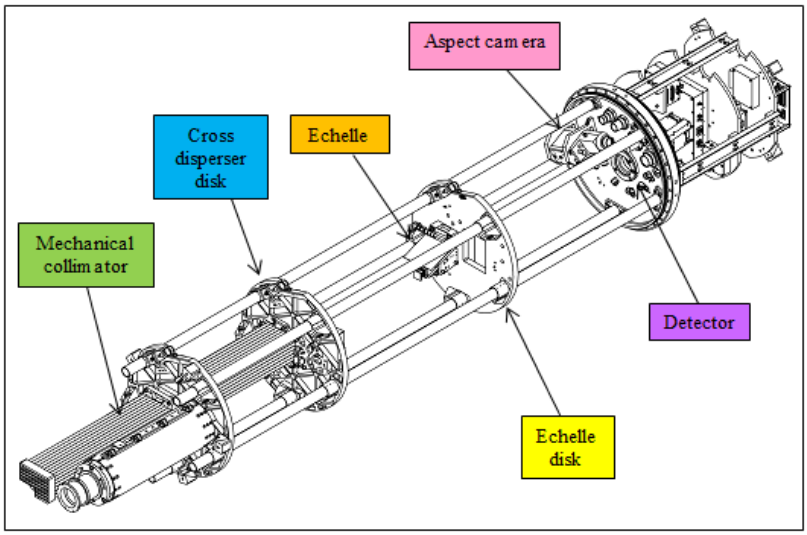

Figure 4.5 The Solidworks rendition of the entire CHESS experiments, including both the spectrograph and electronics sections. Omitted are the rocket skins, which surround both sections. Labeled are important components in the spectrograph section. Light enters the spectrograph through the mechanical collimator, at the bottom left of the schematic.

CHESS is an aft-looking payload that uses 17.26 inch-diameter rocket skins and is split into two sections: a vacuum (spectrograph) section and non-vacuum (electronics) section. The spectrograph section is kept under vacuum for three reasons: (1) the UV detector requires high voltage (V $>$ 3000 V), which can arch at pressures between partial atmospheric pressure and moderately high vacuum (100 - 10^{-4} Torr); (2) UV light ($\lambda\lambda$ 900 - 2000 Å) has high cross sections with air at atmospheric pressure, which absorbs and scatters light before it can be collected by the spectrograph; and (3) the UV reflection coatings on both spectrograph gratings and detector photocathode will degrade in the presence of water and oxygen, diminishing the reflection efficiency by a factor of 6 in the optical coatings (France et al. 2013a). The two sections are separated by a

hermetic bulkhead. The overall length of the spectrograph is 226.70 cm, while the length of the electronics section is 50.80 cm. The total weight of the payload (spectrograph+electronics) is 364.0 lbs. The shutter door is the only moving component during flight in the experiment section. The detector is mounted with a hermetic seal on the electronics section side of the vacuum bulkhead and faces into the spectrograph section.

The vacuum section uses two 113.35 cm-long rocket skins with hermetic joints. The only mechanical component on CHESS (other than the NASA Sounding Rockets Operations Contact (NSROC)-supplied shutter door) is a manual butterfly valve attached along the 180° roll-axis onto the aft skin. This allows for the evacuation of the experiment throughout development, integration and pre-flight activities, safeguarding the sensitive optical coatings. A carbon-fiber frame is attached to the aft side of the hermetic bulkhead and suspends the aspect camera, mechanical collimator, echelle grating and cross-disperser in place. The spectrograph mechanical frame is comprised of three aluminum disks attached to five 2.54 cm diameter × 182.88 cm long carbon fiber tubes, as shown in Figure 4.5.

4.3 CHESS Optical Components & Technology Development

The necessity for improved component performance in the UV - from reflection coatings, to grating scattered light suppression, to higher detector quantum efficiency (DQE) - has become relevant as the need for larger, space-based UV missions is becoming vital to the needs of the astrophysical community. However, with the current state of optical and detector component efficiencies in the Lyman-UV ($\lambda\lambda$ 912 - 1200 Å), it remains difficult to construct a worth-while space telescope for practical use. Sounding rocket experiments play a significant role in the development and demonstration of next-generation technology components for space applications. These components attempt to push the performance of optical and detector components currently available and dependable for astrophysical space missions. By testing advanced technology components on sounding rocket payloads and characterizing their behaviors in the space environment, future astrophysics missions can point to these demonstrations as relevant tests for better components to telescopes

and instruments. The CHESS experiment tested and flew three different advanced-technology UV optical/detector components for demonstration during its first two launches, and each technology component made up a vital part of the UV spectrograph. Below, I will describe the design of each CHESS optical component and how experimental technology developments attempted to replicate this design. I will discuss the final performance of each component in relation to the sensitivity achieved by CHESS.

4.3.1 Grating Measurements in the far-UV

All grating testing occurred in the Astrophysics Research Laboratory (ARL) on the CU-Boulder East Campus. I measured the efficiency and scattered light profiles of all research and development (R&D) echelle samples, final flight echelle gratings, and the flight cross dispersing grating for the first two launches of CHESS. All measurements took place in a large high-vacuum chamber (named the "Square Tank," $P_{vac} \approx 10^{-6}$ Torr) attached to a differentially pumped hollow-cathode arc lamp an externally supplied gas, primarily made up of hydrogen and argon (H/Ar 35/65 %). The differentially-pumped lamp is attached to a monochromatic system, which diffracts light produced by the lamp into discrete emission lines with a Rowland Circle grating, which can then enter the high-vacuum "Square Tank."

The measurement of groove efficiency happens in two steps. First, I must record the input count rate of discrete emission at a given wavelength λ without interference from any optical component in the "Square Tank." This is accomplished by recording the light beam entering the "Square Tank" with either a bare-plate (i.e., no photocathode) Quantar Raenicon microchannel plate (MCP) photon-counting detector (sensitive to far-UV light up to λ1300) or a Hamamatsu MgF_2-window photon multiplying tube (PMT) unit (sensitive from λ1150 through optical wavelengths). Second, I must record the count rate of light diffracted off of the grating being tested. The grating is placed in such a fashion as to intercept the light beam entering the "Square Tank" in the correct grating configuration, and the detector used is moved remotely to intercept the diffracted light and record the count rate of light dispersed by the grating. Figure 4.6 shows a top-down view

of the experimental set up of the vacuum chamber and points out each important component of the test.

I calculate the relative reflectivity of each grating order by dividing the grating λ dispersion count rate by the count rate of λ entering the "Square Tank". By knowing the material each grating is coated with and measuring the material reflectivity, I fold out the reflective properties of the coating to extract a total groove efficiency for each grating. In this way, I calculate the performance of each optical component in CHESS and use this information to determine the total sensitivity of the instrument. In the subsequent sections, I disclose the final performance of each optical component tested for flight in the CHESS experiment.

4.3.2 CHESS Echelle Grating

Echelle gratings are distinguishable by their course line densities (20 - 300 lines/mm) and use at steep facet angles (θ: 20° - 80°). Both qualities allow echelle gratings to theoretically achieve high dispersion, high efficiency at or near the Littrow configuration, or where the angle of incidence equals the diffraction angle ($\alpha = \beta = \theta$), and high resolution with low polarization effects. Figure 4.7 shows a schematic of how, in principle, a tradition echelle disperses light.

The CHESS echelle grating is designed as an R/2.35 echelle (angle of incidence: $alpha$ = 67°) with a low line density (69 grooves/mm). The combination of the CHESS echelle grating parameters gives high dispersion solutions to far-UV light (m = 266 - 166 for $\lambda\lambda$ 1000 - 1600 Å). Because echelle gratings work most efficiently in Littrow, the grating must be off-axis to direct the diffracted light to the next optical component in the spectrograph. This off-axis angle (γ) in CHESS is 6°, which both mitigates grating efficiency losses due to the off-axis configuration and confines the physical spectrograph size within the dimensions of the sounding rocket payload.

Unfortunately, the echelle parameters for CHESS are not commercially-available. Instead, as a part of the instrument design, the echelle was meant to be an experimental technology demonstration piece for two different grating fabrication processes: the first is a lithographic-ruling process, and the second is an electron-beam etching technique. For the lithographically-ruled echelle,

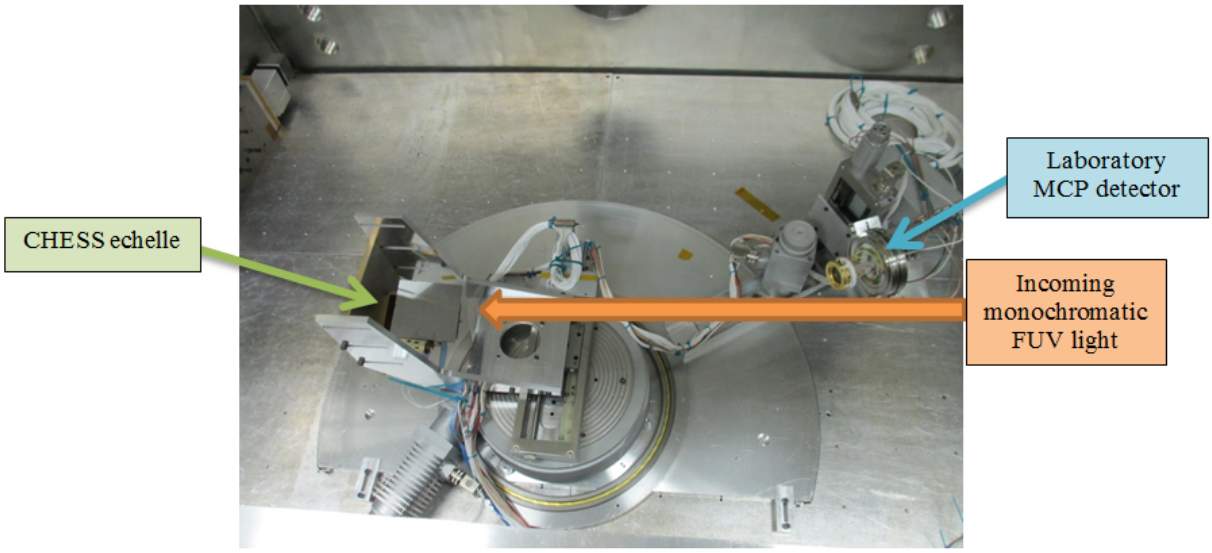

Figure 4.6 Measuring the efficiency of the CHESS optical components. Monochromatic light enters the vacuum chamber and strikes the center of the echelle (shown), located in the middle of the chamber on a rotation and left/right translation motor. To accurately simulate efficiency expectancies during flight, the grating is set to the flight offset angle (γ) = 6°. The Quantar Raenicon MCP detector unit is set up on a swing arm translation stage and an up/down stage, to measure the main order efficiencies, adjacent order efficiencies, and scatter light profile at each monochromatic wavelength sampled within the CHESS bandpass.

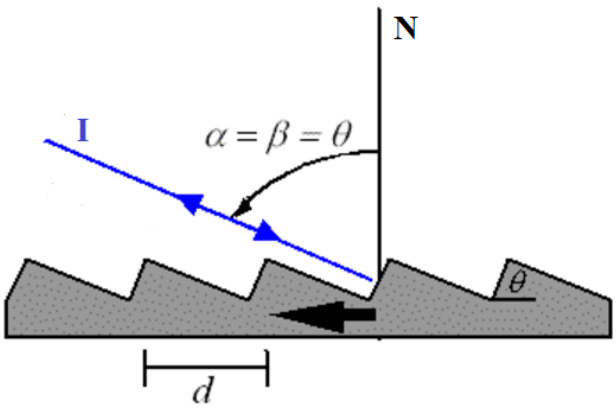

Figure 4.7 *Adapted from Richardson Gratings.* A simple schematic showing how an echelle grating works in practice. When used in Littrow for maximum groove efficiency, the incoming light (labeled "I") diffracts off the steep groove facet, which has an angle θ, back the way in entered. The groove density is derived as 1/d, where d is the length of one groove (in mm). "N" represents the normal axis of the grating. The arrow shows the direction to point the grating to intercept the incoming light.

LightSmyth, Inc. fabricated the flight echelle for CHESS-1, and I tested roughly ten fabrication samples, which helped the manufacturer hone their parameter space and attempt to create a high-efficiency, low scatter grating. The electron-beam etched echelle was created in collaboration with JPL, and I tested several fabrication samples on their behalf. Below, I outline the procedure for each experimental fabrication process, which highlights the advantages and difficulties of each technique.

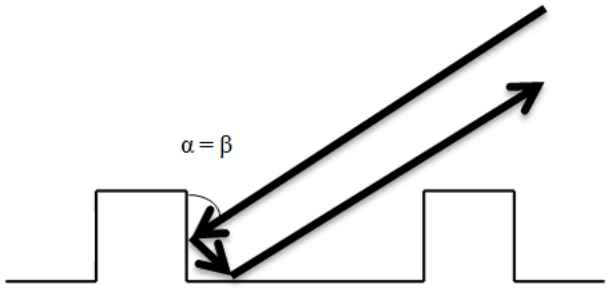

Figure 4.8 A simple schematic showing how a corner-cube echelle grating disperses light. When used in Littrow for maximum groove efficiency, the incoming light bounces off the groove wall and is directed towards the groove bottom. The light then reflects off the bottom and goes back out the way it came in. This design required two light reflections. The spacing between the grooves and wall height defines the incidence angle of the echelle.

4.3.2.1 Lithographic Ruling

The original design of CHESS relied heavily on lithographic fabrication, which would theoretically produce uniform line densities and controlled groove facet smoothness across the entire ruled area of the echelle. The lithography process starts with a substrate (silicon) with a thin oxidation layer, over which a photoresist and photomask with the desired groove pattern is overlaid. Using extreme-UV light to etch into the photoresist, the photomask is removed and the oxide layer is further etched via chemical agents that do not harm the photoresist. After removing the rest of the photoresist, the etched substrate is left with the desired groove density and thickness. This new manufacturing process allows low-scatter gratings at arbitrary groove densities with sub-100 nm surface deviations. The fabricated groove profiles would maximum echelle order efficiency while suppressing interorder scattered light, a significant issue seen with traditionally-ruled (mechani-

cally, typically with a diamond-tipped cutter) echelle gratings in modern UV instruments (e.g., *HST*/STIS).

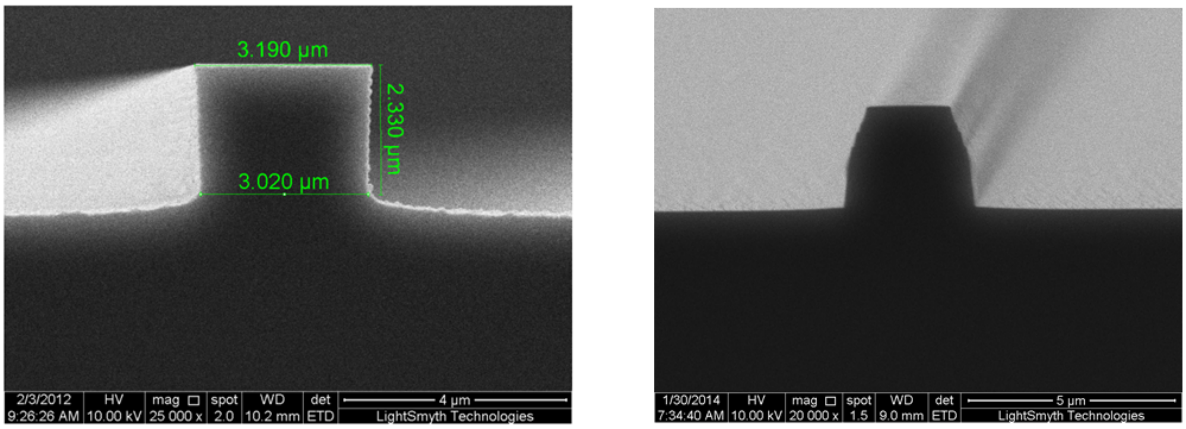

Figure 4.9 Two examples of lithographically-ruled echelle fabrication attempts by LightSmyth, with groove profiles revealed by a scanning electron microscope (SEM). *Left:* One of the first echelle gratings fabricated for testing. The groove walls and bottom are jagged, which greatly affects the scattered light performance of the grating. LightSmyth worked to smooth the wall profiles, but this resulted in sloped and angled wall profiles, as shown on the *Right*. The *Right* groove profile shows the profiles of the echelle flown in CHESS-1.

Because of the nature of the lithography process, etching the saw-tooth profiles of traditional gratings is difficult. Therefore, a corner-cube groove design was created to mimic the behavior of the traditional groove profile. Figure 4.8 demonstrates how this groove design theoretically works. Incoming light strikes the wall of the groove and it redirected to the groove bottom. The light then reflects off the groove bottom and is directed back towards the incidence light. This grating design works at maximum efficiency in the Littrow configuration, and the two-bounce requirement for dispersed light to exit the grating is designed to significantly diminish interorder scattered light. However, the design comes with serious disadvantages. UV reflective coatings, specifically for $\lambda < 1150$ Å, have notoriously low reflectivities, and some of the better reflective coatings known to date can be difficult to work with. The two-bounce requirement diminishes the already low reflectivity of the coating (R^2, rather than R), which results the total groove efficiency being reduced with the additional bounce that is not needed in traditional saw-tooth gratings. Additionally,light intercepting two surfaces places stringent restraints on the smoothness of two groove facets and the

geometry of the two surfaces with respect to one another. Figure 4.8 shows the ideal scenario for this fabrication process: the groove walls and bottom are perfectly smooth and perpendicular to one another. In practice, this is very difficult to achieve, as shown in Figure 4.9.

4.3.2.2 Electron-beam Etching

The echelle grating is a development project, in conjunction with the Microdevices Laboratory at the Jet Propulsion Laboratory (JPL), utilizing an electron-beam lithography process to better control scatter and the ruling profile of the grating surface. A focused beam of electrons scans across the surface of the optic, which is covered with an electron sensitive film. The electron beam changes the solubility of the resist, allowing for precise removal of the exposed regions of the resist by removing it in a solvent (McCord and Rooks 2000). This enables controlled line spacing on the grating and sub-10 nm surface deviations for low scatter grooves. The Microdevices Laboratory at JPL has a strong history of creating high efficiency, low scatter gratings for used in the visible and near-IR for space-based missions (e.g., the Compact Reconnaissance Imaging Spectrometer for Mars (CRISM) instrument on the NASA Mars Reconnaissance Orbiter; Wilson et al. 2003). The collaboration with JPL was to demonstrate that the same technologies that can create high efficiency, low scatter, high dispersion gratings in the optical to near-IR regimes can be applied to UV astrophysical applications.

The electron-beam etching process allows for the fabrication of traditional saw-tooth groove profiles, which eliminates the two-bounce diffraction requirement and increases the possibility for higher total groove efficiency. The electron beam also (theoretically) produces smaller surface deviations, which can create groove surface smoothness of order 1/10 λ (at λ 1000Å), which is important to minimize to suppress scattered light. Unfortunately, there were a few disadvantages with the electron-beam fabrication procedure. The beam can only etch a small square area of the total grated area at a time before moving to another region, and any small mis-alignments with the fabricated optic and the machine results in offset grooves locations, which has serious consequence resulting in interorder scattered light, reduced peak efficiency, and ghosting. Figure 4.10

shows a SEM view of this effect. The etching process also results in a secondary periodicity in the overall grating profile, which effectively creates "two gratings in one," with the same blaze angle but different groove densities, and confuses dispersion orders together near Littrow. Both disadvantages create serious problems for the echelle spectrograph as a whole, as confusion between orders, especially the introduction of ghost orders, or secondary diffraction patterns parallel to the primary diffraction axis, makes it very difficult, if not impossible, to fully and successfully separated overlapping echellograms.

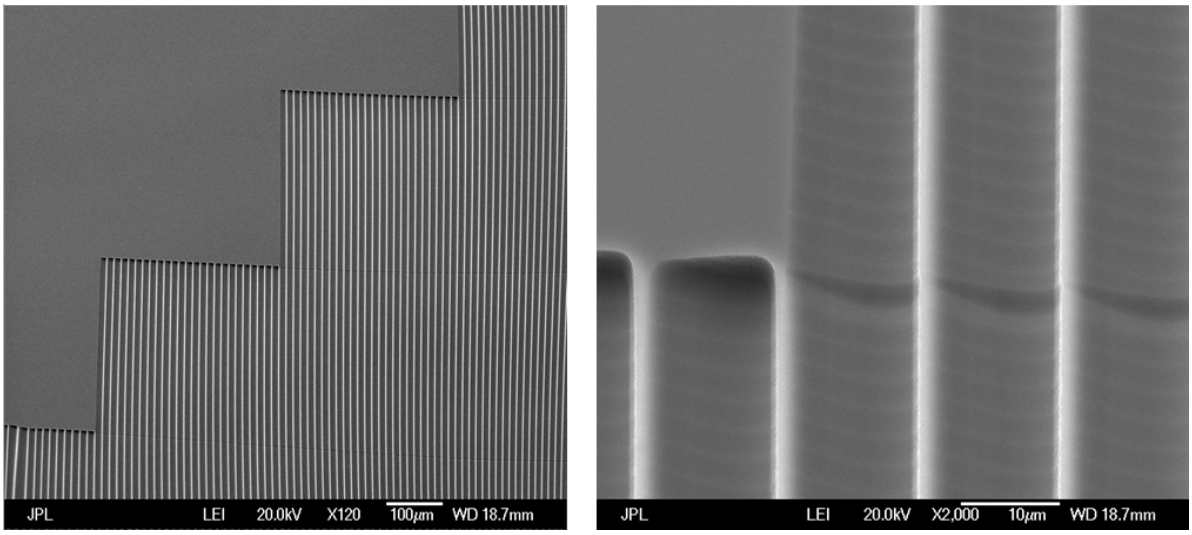

Figure 4.10 Two SEMs showing how the stitching fabrication of the electron-beam machine affects the final groove profile over the entire grating area. *Left:* A top view of the groove profiles for a sample echelle fabrication attempt by JPL, showing where each electron-beam etching patch occurred. *Right:* A zoom-in on the area between two electron-beam etching patches, which produces slight inconsistencies across the groove profile. These fabrication errors add up over the entire grated area, which result in efficiency losses, increased scattered light, and ghosting.

4.3.2.3 Echelle Groove Efficiencies

Figure 4.11 shows the groove efficiency of each CHESS echelle grating sample provided by LightSmyth and JPL to test the fabrication procedures of the lithography and electron-beam ruling techniques, respectively. For the lithographically-ruled gratings, no minimum groove efficiency specification was stated, and the goal of the project was to launch the best-performing echelle

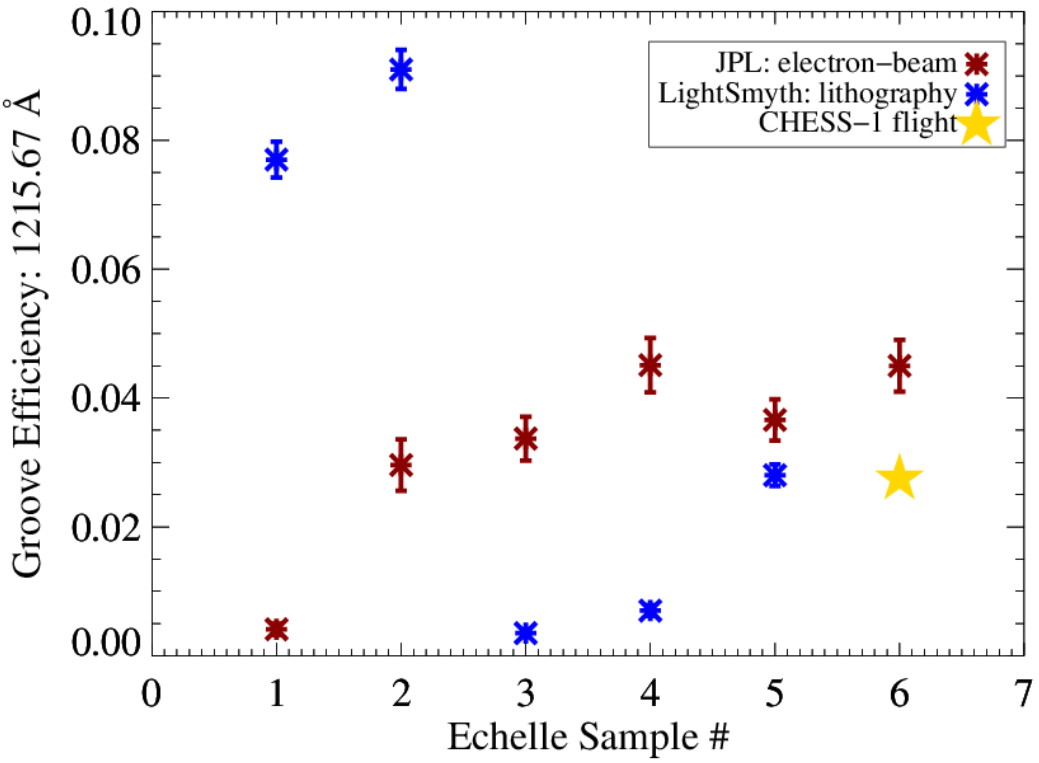

Figure 4.11 A comparison of the peak echelle order groove efficiency (1.0 = 100% efficient) of each R&D echelle sample measured at HI-Lyα (λ1215.67 Å). All samples performed well under 10% groove efficiency. For CHESS-1, one of the last echelle gratings fabricated by LightSmyth was flown, although it underperformed the first few sample provided by them by several factors. A threshold minimum efficiency was defined for the R&D collaboration with JPL (20% at λ1215.67 Å), which represented the minimum efficiency required of the echelle grating to observe the CHESS-2 target (ϵ Per) at a S/N $\sim$ 20 over a 250-second exposure time.

grating the manufacturer could produce, given the limitations of their lithographic ruling facilities. This resulted in very poor performing gratings, with the CHESS-1 flight echelle having only a peak order efficiency of $\sim$2% at HI-Lyα.

Applying lessons learned from this first R&D experience, a minimum groove efficiency threshold of 20% at HI-Lyα was set for the electron-beam etching program with JPL. This threshold represents the echelle groove efficiency required to observe the primary science target of CHESS-2 at a signal-to-noise ratio (S/N) = 20 for an exposure time of 250 seconds. It was agreed upon by both JPL and CU that this goal could be readily obtained, given a projected performance of 60% - 80% by JPL. However, as shown in Figure 4.11, all JPL electron-beam gratings failed to meet the specified target groove efficiency for the project. The most efficient gratings (Samples #4 and #6) were only 4.5% efficient at Lyα, which was comparable to the efficiency of the LightSmyth, Inc. echelle flown in CHESS-1 (Hoadley et al. 2014). We also saw significant ghosting effects from every echelle sample fabricated with the electron-beam technique in both optical and far-UV diffraction, where the ghosts had as much as 50% the power in the primary echelle diffraction orders.

For the second launch of CHESS, and not relying on a new R&D project to produce an echelle grating to meet the instrument specifications, I reconsidered the grating parameter space of the echelle needed to produce the desired echellogram, with high spectral resolution and coverage, and compared these new parameters with pre-fabricated gratings from manufacturers who have demonstrated moderate efficiency gratings in the UV. I ordered and measured the groove efficiencies of several mechanically-ruled echelle gratings from two vendors: Bach Research, Inc. and Richardson Gratings. Both manufacturers provided echelle gratings that greatly outperformed the experimental echelle products and met the CHESS-2 minimum efficiency threshold. Figure 4.12 presents the measured groove efficiency of the flight echelle from CHESS-1, the best-performing JPL echelle, and the mechanically-ruled echelle gratings from Bach Research and Richardson Gratings. While the Richardson Gratings echelle out-performed the Bach Research echelle, the long lead-time for the Richardson flight echelle prevented it from arriving before the second launch of CHESS. Instead, the Bach Research, Inc. echelle was flown on CHESS-2, and the Richardson grating will launch on

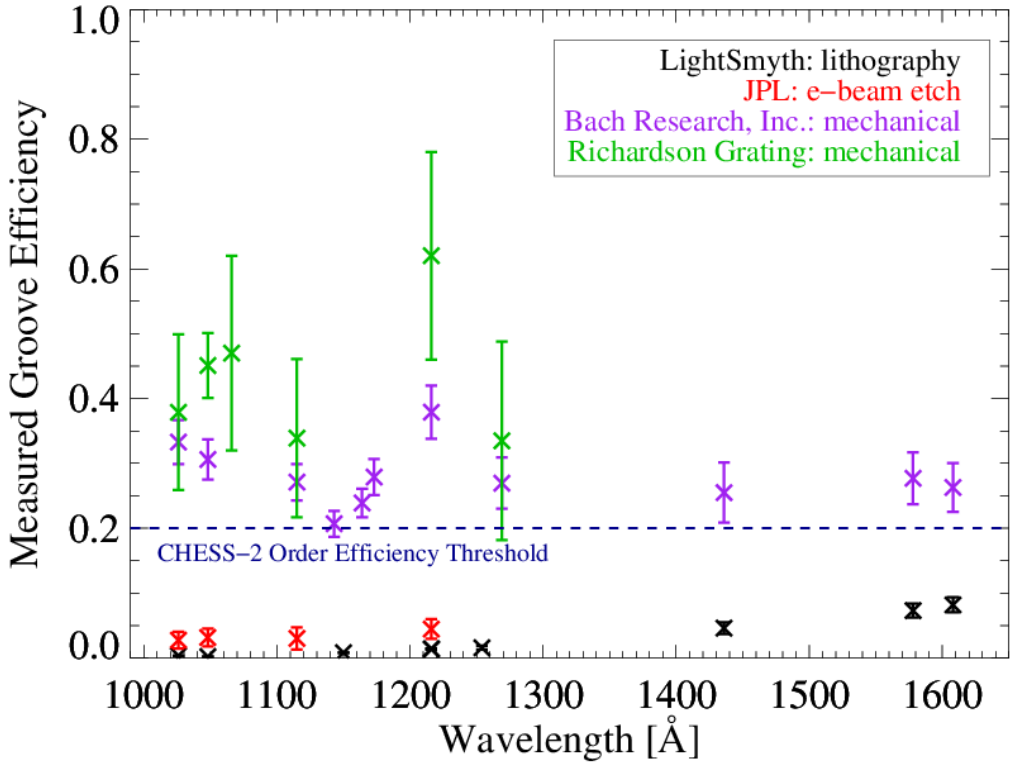

Figure 4.12 A comparison of echelle gratings tested for use in the CHESS instrument. We include the best-performing echelle gratings from the lithography etching R&D project undertaken by LightSmyth, Inc. (flown on CHESS-1), the electron-beam samples fabricated by JPL, and two mechanically-ruled replica gratings from Bach Research, Inc. and Richardson Gratings, respectively. Both mechanically-ruled gratings out-performed the R&D echelles and met the CHESS minimum order efficiency threshold.

the next two missions of CHESS.

The final flight echelle gratings used for both CHESS launches had different grating parameters than the original echelle design. The LightSmyth echelle, flown in CHESS-1, had a groove density of 71.66 grooves/mm and a blaze angle $\alpha = 73°$. This did not significantly affect the final echelle order solutions in the FUV, where solutions remained in the range m = 265 - 165. The Bach Research echelle grating, flown in CHESS-2, had a groove density of 53.85 grooves/mm and a blaze angle $\alpha = 64.3°$, which did significantly affect the final echelle order solutions in the FUV: m = 335 - 205. The final determination of the echelle parameters for CHESS-1 and CHESS-2 were determined during optical alignments, which are described in Section 4.4. For CHESS-3 and CHESS-4, I identified a manufactured echelle grating from Richardson gratings with echelle parameters (groove density: 87 grooves/mm, $\alpha = 63°$) that produce less order solutions in the FUV similar to those designed for CHESS (m = 205 - 125).

4.3.3 Cross Dispersing Grating

The CHESS cross disperser grating is a 100 mm × 100 mm × 30 mm fused silica optic with a toroidal surface profile. The toroidal surface shape separates the foci of the spatial and sagittal axes of the dispersed light. The optic works at f/12.4 to focus light spatially and sagittally on the detector, ensuring we do not interfere with focused light around the detector ion repeller or QE grids. The cross dispersing optic is a new type of imaging grating that represents a new family of holographic solutions and was fabricated by Horiba Jobin-Yvon (JY). The line densities are low (351 lines/mm, which is difficult to achieve with the ion etching process), and the holographic solution allows for more degrees of freedom than was previously available with off-axis parabolic cross dispersing optics. The holographic ruling corrects for aberrations that otherwise could not be corrected via mechanical ruling. The grating is developed under the formalism of toroidal variable line spacing gratings (Thomas 2003), corresponding to a holographic grating produced with an aberrated wavefront via deformable mirror technology. This results in a radial variability in the groove density and a traditional surface of concentric hyperboloids from holography, like those used

in the Imaging Spectrograph for Interstellar Shocks (Beasley et al. 2004) and the Cosmic Origins Spectrograph (Green et al. 2003).

The cross disperser was delivered in the summer of 2012, and order efficiencies around both the m = +1 and m = -1 orders were measured to be between 20% − 45% in the FUV (900 − 1700 Å) before and after the Al+LiF optical coating. Figure 4.13 shows the reflectivity (order efficiency × reflectivity of Al+LiF) of the cross dispersing optic for order m = -1, which is the dispersion order used in the CHESS instrument, for pre-36.285 field operations, post-36.285 launch, and pre-36.297 field operations. Overall, the performance of the cross disperser exceeded our initial expectations, with reflectivity $\sim 30\%$ at Lyα. The cross disperser is effective at dispersing most of the on-axis light into the m = ± 1 orders and suppressing the m = 0 order because of the characteristic sinusoidal groove profiles created via the ion-etching procedure at JY. Additionally, at optical wavelengths, the reflectivity of the m = 0 order becomes comparable to the m = ± 1 orders, which allows the secondary camera system to track the movements of our optical axis and target acquisition during flight.

4.3.4 Cross-Strip Anode Microchannel Plate Detector

The cross-strip MCP detector was built and optimized to meet the CHESS spectral resolution specifications at Sensor Sciences (Vallerga et al. 2010, Siegmund et al. 2009). The detector has a circular format and a diameter of 40 mm. The microchannel plates are lead silicate glass, containing an array of 10-micron diameter channels. They are coated with an opaque cesium iodide (CsI) photocathode, which provides QE = 15 − 35% at FUV wavelengths ($\lambda < 2000$ Å). When UV photons strike the photocathode to release photoelectrons, the photoelectrons are accelerated down the channels by an applied high voltage ($\sim$ 3100-3200 V). Along the way, they collide with the walls of the channels, which produces a large gain over the initial single photoelectron. There are two MCPs arranged in a "chevron" configuration. During flight, the detector achieved spatial resolution of 25 μm over an 8k x 8k pixel format. The QE estimate across the CHESS bandpass, measured by Sensor Sciences, is plotted in Figure 4.14 against the efficiency measurements of the flight echelle

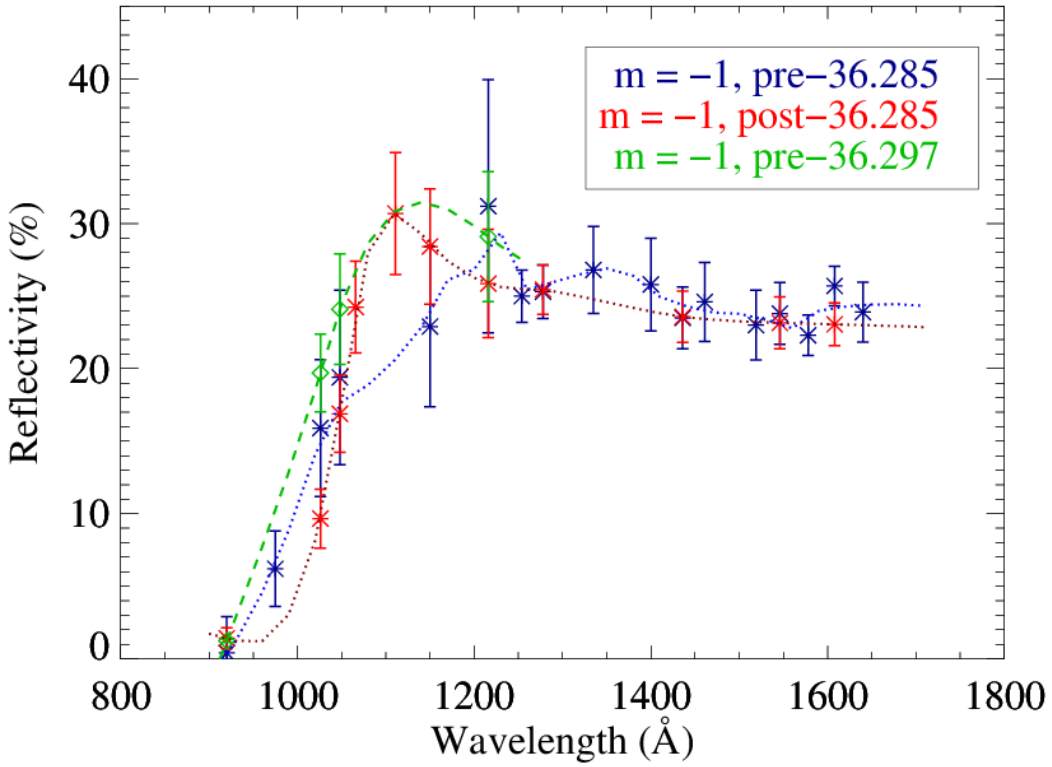

Figure 4.13 Measured reflectivity (order efficiency × reflectivity of Al+LiF) of the cross dispersing grating in CHESS, overplotted with spline curves to show the resemblance of each trial. We focus on the reflectivity of the m = -1 order, which is the dispersion order used in the CHESS instrument. Because the LiF coating can degrade when not stored properly, we measure how the order reflectivity changes between CHESS-1 and CHESS-2 without re-coating the optic. No significant degradation of the coating has been measured between the first assembly of CHESS (November 2013) and the build-up of CHESS-2 (November 2015).

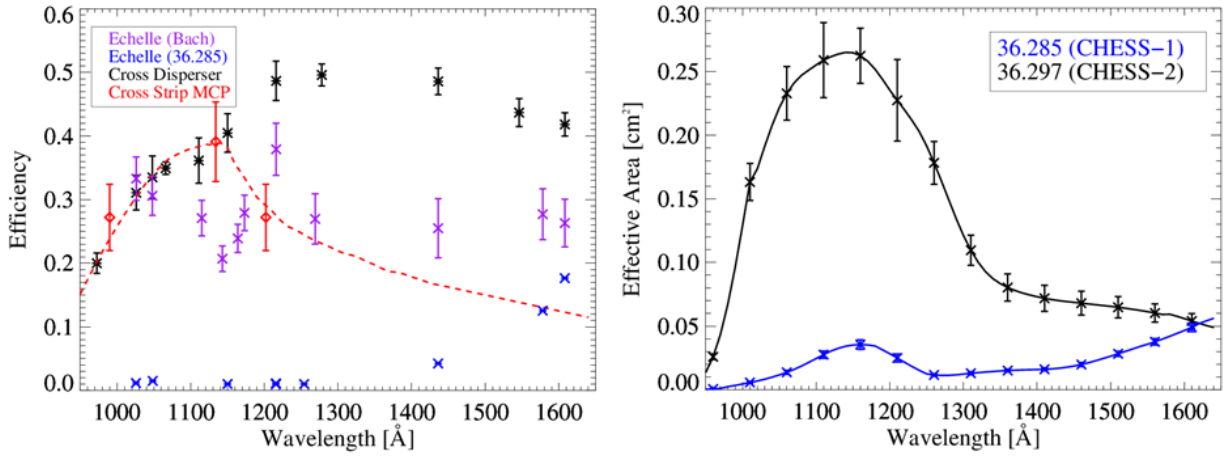

Figure 4.14 **Left:** Performance (for each grating: peak order efficiency, and for the detector: DQE) of all optical components of CHESS-1 and CHESS-2. The only component changed between flights was the echelle grating. **Right:** The Effective Area, including throughput loss from baffling, of CHESS-1 and CHESS-2. After 36.285, we sent the cross-strip anode MCP back to Sensor Sciences, Inc. to replace the CsI photocathode, which had begun to crystallize during field operations of CHESS-1. The total effective area of CHESS-2 is about an order of magnitude larger than that of CHESS-1 from $\lambda\lambda$ 1000 - 1300 Å, which is mainly ttributed to the large gain in echelle order efficiency in this wavelength region (Hoadley et al. 2014; 2016) (see Figure 4.12 for a comparison of the echelle performance).

Table 4.2. Instrument Specifications for the CHESS Sounding Rocket Payload

Mechanical Collimator		Spectrograph	
FOV: $18.5' \times 18.5'$ Dimensions (mm): $10.74 \times 10.74 \times 1000$ Collecting area (cm^2): 40.0		Bandpass (Å): 1000 - 1650 Resolving power: Theoretical R $\sim$ 120,000 Demonstrated R $\leq$ 10,000 $F\#$: $f/12.4$	
Echelle (CHESS-1)	**Echelle (CHESS-2)**	**Cross Disperser**	**Detector**
Vendor: LightSmyth Shape: Flat Blaze angle(°): 73.0 Groove density (gr/mm): 71.7 Ruling: Lithographic Coating: Al+LiF Dimensions (mm): $100 \times 100 \times 0.7$ Material: Silicon	Vendor: Bach Research Shape: Flat Blaze angle(°): 64.3 Groove density (gr/mm): 53.85 Ruling: Mechanical Coating: Al+LiF Dimensions (mm): $104 \times 104 \times 16$ Material: Zerodur	Vendor: HORIBA Jobin-Yvon Shape: Toroidal Radius (mm): 2500.25/2467.96 Groove density (gr/mm): 351 Ruling: Holographic Coating: Al+LiF Dimensions (mm): $100 \times 100 \times 30$ Material: Fused Silica	Vendor: Sensor Sciences Type: Open-face MCP Pixel format: 8k $\times$ 8k Spatial resolution (μm): 25 Anode: Cross-strip Photocathode: CsI Outer dimension (mm): 40 Global count rate (Hz): 10^6 Material (MCPs): Borosilicate

and cross disperser for CHESS-2.

The 2013 and 2015 NASA Cosmic Origins Program Annual Technology Reports emphasized that the technology readiness level (TRL) for large format, high count rate, and high QE MCP detectors needs to improve for future UV space missions. One of the goals of the CHESS instrument is to demonstrate the flight performance of the cross strip anode design to raise the TRL level to 6. In the laboratory setting, we demonstrated count rates of $\gtrsim$ 150,000 photons/second, which the MCP handled smoothly over the 8k $\times$ 8k digital readout.

A summary of all relevant instrument parameters are provided in Table 4.2.

4.4 CHESS Alignment & Calibration

4.4.1 Optical Alignment

To simplify instrument alignments while the instrument is in a vacuum system, I devised a plan to use optical light through the spectrograph to pre-align each grating to the fixed detector location in the payload. First, I verified analytically that both grating components in CHESS

produce diffraction solutions at optical wavelengths using the generalized grating equation:

$$\frac{m\lambda}{d} = (\sin\alpha + \sin\beta)\cos\gamma, \tag{4.1}$$

where m is the integer diffraction order we solve for, λ is the wavelength of light (in mm), d is the inverse of the groove density of the grating (in mm/grooves), α is the incident angle of light on the grating, β is the outgoing angle of diffracted light of order m off the grating, and γ is the off-axis angle of the grating with respect to the incident light. Knowing the angles of incidence of each grating, the offset angle of the echelle grating, and the ruled groove densities for each grating, I calculated order solutions when solved for discrete, optical light (ranging from 405, 532, and 632 nm, which were chosen for violet, green, and red laboratory laser solutions). Off of the CHESS echelle gratings, high order solutions existed for m = 40 65 (CHESS-1) and m = 50 - 85 (CHESS-2) for 632 - 405 nm wavelength solutions.

I simulated optical light off of each grating component in the payload using Zemax to mark fiducials (or markers) in the mechanical structure that would roughly align the echelle to the cross disperser, and the cross disperser to the detector plane in the FUV, given the designed grating parameters. I used the three lasers with different wavelength coverage - 405 nm (violet), 543 nm (green), and 632 nm (red) - to over-sample the optical solutions and fiducials to optimize the initial grating positions in the payload prior to working with FUV light under vacuum. Using laser light ensured we used roughly monochromatic light and provided a known beam diameter at each wavelength. This meant that the size of the optical fiducials for alignment could be small (4 mm-diameter circles), yet still oversize the beam diameter, ensuring that all laser dispersion solutions fell within the marked fiducials. The fiducials were designed for on-axis laser light dispersing from the center of the echelle; the size and number of fiducials for each laser provided room for small offsets of the laser-to-echelle center and small off-axis angles of the laser-to-echelle alignment. Figure 4.15 shows the echelle/cross disperser fiducials marked on the echelle disk. Since the cross disperser provides m = -1, 0 ,and +1 optical solutions for each echelle dispersion order, there were many more cross disperser fiducials to work with, which helped constrain the echelle-to-cross disperser

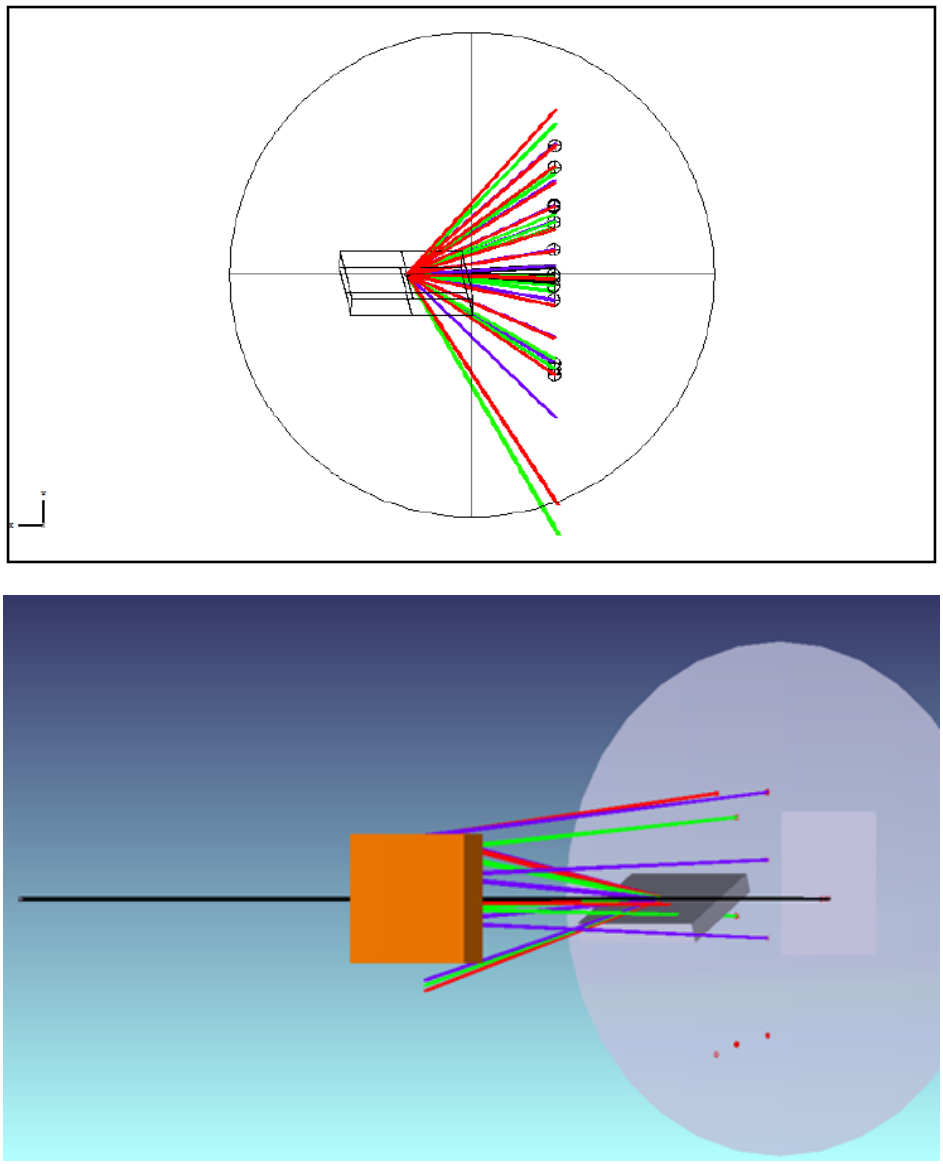

Figure 4.15 **Top:** A 2D Zemax ray trace of echelle high-order dispersion solutions for optical wavelengths (405, 532, and 632 nm), oriented such that the reader is looking stright at the echelle grating, and the disperser light is coming towards the reader. The solutions are marked at the cross disperser mechanical disk. **Bottom:** A Zemax 3D ray trace of optical laser solutions off of both instrument gratings. All light enters the system via the black ray, disperses into its color constituents off the echelle, and spreads in the (x,y) plane of the payload off the cross disperser. This image shows laser dispersion for m = -1 cross disperser solutions for each laser. Rays are color coded by their corresponding laser wavelength. The circle behind the echelle represents the echelle disk, and small red fiducials mark where laser light falls during optical alignments, to produce the desired UV alignment on the detector plane.

alignments.

The optical components were assembled in the payload for the first time in the following order: 1) the echelle grating; 2) the cross-dispersing grating; 3) the mechanical collimator; and 4) the secondary aspect camera system, including flat mirrors on the echelle flight mount and detector bulkhead. Figure 4.16 shows a series of photos taken during optical alignments, to illustrate the laser alignment set-up and how fiducials were used to roughly align each grating before fine-tuning the grating alignments in vacuum. For CHESS-2, the mechanical collimator stayed in place in the mechanical structure, so this alignment went first before the echelle.

Laser alignment: The alignment of the violet, green, and red lasers to the payload had to be done quantitatively, to measure mis-alignments between the two systems. First, two lasers were installed in separate laser holders, each with independent tip/tilt mount, onto one laboratory stand. The stand screwed into a theodolite stand, which was leveled and fixed with three stable feet, to avoid any mis-alignments due to stand movement. A large, flat laboratory mirror was used to retro-reflect the laser beams back into each laser entrance aperture. The payload mechanical structure was then placed between the laser system and flat mirror on a rocket cart with tip/tilt functionality. The payload has several flat mirrors bonded to the spectrograph structure to align the spectrograph to an independent system, such as the lasers. In this configuration, we assumed that the lasers were aligned to the optical axis of the instrument, and verified this alignment by retro-reflecting the laser light off of several payload flat mirrors.

Echelle: The echelle grating is installed first. Both the echelle grating and cross-dispersing grating were coated with Al+LiF to maximize reflectivity of the gratings at FUV wavelengths ($\lambda\lambda$ 1000 - 1150 Å). However, because the Al+LiF coating is sensitive to moisture in the air, the instrument structure was designed to include a nitrogen purge distributor. This fed in lines of Ultra-High Purity gaseous N_2 and evenly distributed a stream of gas across the surfaces of the echelle and cross disperser, keeping a layer of dry nitrogen gas between the optical coating and the air. I used each laser wavelength and the fiducials marked on the cross disperser disk to first optimize the AOI of the echelle, using a small, linear motor (actuator) affixed to the echelle flight

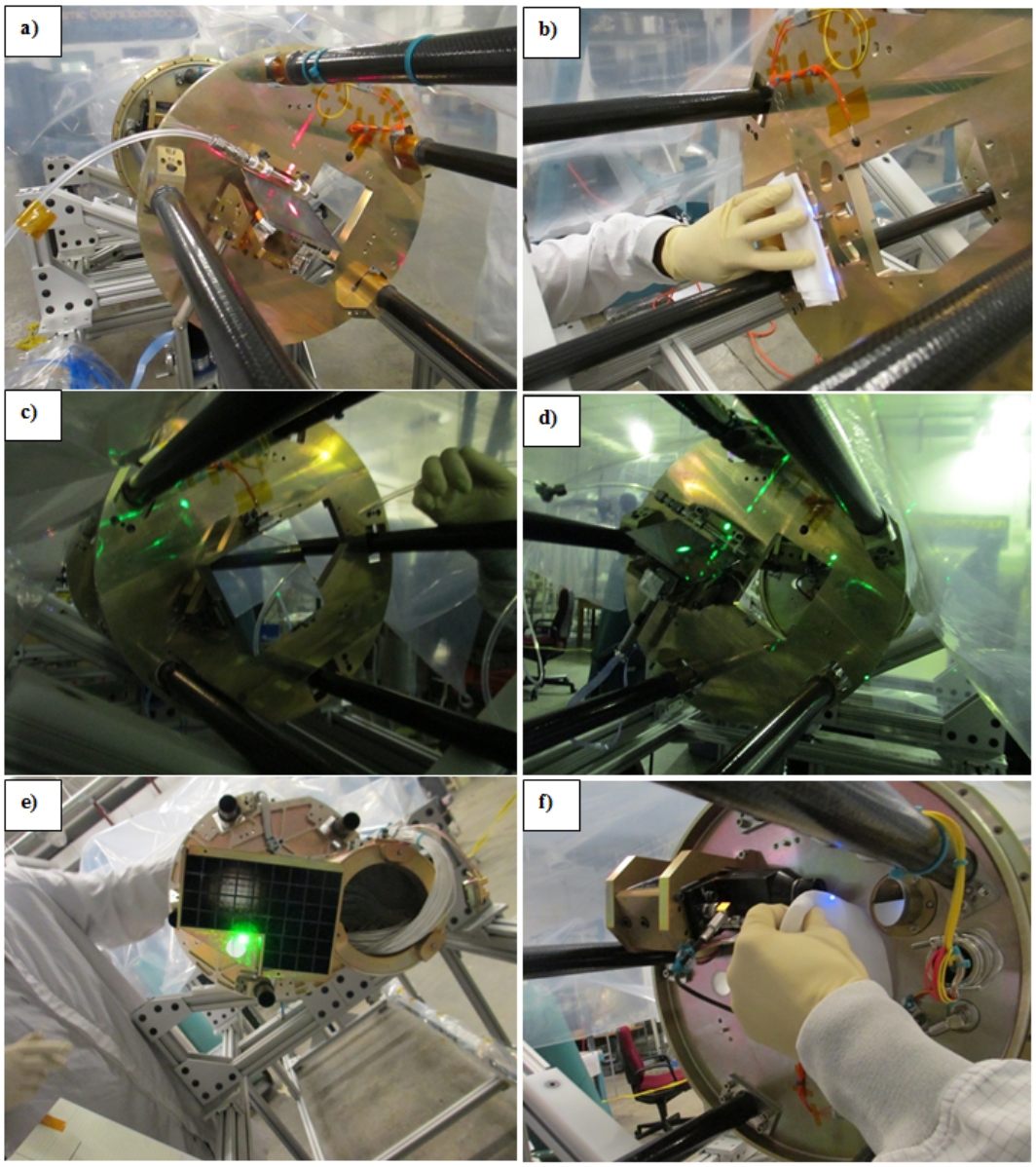

Figure 4.16 I show each step in the optical alignment procedure as photos taken during the build of CHESS-1. **a)** View of red laser light intercepting the echelle center during optical alignments. **b)** Checking that the violet laser dispersion pattern matches the fiducials marked on the disk. They did not; see reasoning in Sec. 3.1. **c)** Aligning the cross disperser with green laser dispersed light off the echelle. **d)** Image of the green laser intercepting the echelle, but also the dispersion pattern of the green light off the cross disperser back onto the echelle disk. **e)** Looking down the mechanical collimator and starting collimator alignments with green laser light. **f)** Verifying and tracing the optical alignment of the aspect camera system with the violet laser light.

mount. This motor, as well as three strategically placed behind the cross disperser flight mount, provides controlled movements of the mounts both at air and in vacuum.

At this stage, it was discovered that the echelle grating properties did not match the behavior of the designed echelle parameters, and our vendor did not inform us that the grating parameters would be different. However, I measured the distance between the marked fiducials and the actual locations of the dispersion spots on the cross disperser mechanical structure disk. Then, I simulated the new locations of the spots in Zemax and backed out the true grating parameters of the echelle on CHESS-1. Instead of an echelle groove density of 69 grooves/mm and blaze angle $\alpha = 67°$, I determined the echelle parameters in CHESS-1 were a groove density of 71.66 grooves/mm and a blaze angle $\alpha = 73°$. A similar problem was encountered with the echelle in CHESS-2; the vendor provided us with the wrong echelle parameters, specifically the groove density, which threw our original Zemax simulations for optical alignments 2 diffraction orders off. We found that, rather than a groove density of 52 grooves/mm provided by the vendor, the echelle in CHESS-2 had a groove density of 53.85 grooves/mm.

Cross disperser: The cross disperser was installed after the echelle parameters were verified for both CHESS-1 and CHESS-2. Because the echelle grating behavior was not what was planned for, this affected the location of the cross disperser fiducial locations marked in the payload. Instead, I mapped out the new fiducial locations for each laser by noting how offset from the marked fiducials the new spots should be off the cross disperser. Keeping the echelle at the optimized AOI, the cross disperser was tilted using vacuum actuators to disperse the laser solutions to their optimized positions on the echelle mechanical structure disk.

Mechanical collimator: We used a transparency cutout of a 1-to-1 outline of the collimator tube structure to guide laser light through the collimator tubes and recorded how far the laser light traveled in the (x,y) perpendicular plane through the instrument optical axis. The total travel distance was converted to an angular offset (in arc minutes) between the instrument optical axis and the collimator. Due to the limited capabilities of determining the absolute alignment between the lasers and instrument axis, the alignment of the mechanical collimator was good to within $\pm$

$2'$, using the known beam size of the violet laser. This was okay, given the field of view (FOV) of the collimator tubes being $0.6^\circ \times 0.4^\circ$, or $36' \times 24'$.

The mechanical collimator was then locked in place with two sets of fitted brackets one was made of aluminum, the other of Delrin.

Aspect Camera System: The secondary aspect camera system, used to track the UV spectrograph to starlight entering the payload, was aligned-by-eye with a green laser. A small, 25 mm flat mirror was mounted to a small tip/tilt flexure attached to the echelle mount, which reflected light to the center of the cross disperser. Using the zero-order solution off the cross disperser, a second flat mirror, located on the detector bulkhead and tilted at a 45° angle, intercepted the light and reflected it into the sensor of the aspect camera.

Baffling: Before the instrument entered the vacuum chamber for final alignments and focusing of the spectrum, an inspection of baffling, or obstacles to stop excess scattered light from contaminating the science spectrum of CHESS, was needed. This effort happened on two fronts: inspection of the payload through the detector mount on the detector bulkhead, to spot any stray light regions by-eye, and simulations in Zemax to point out areas where stray light can enter the spectrograph. Baffles were added at the following locations:

(1) At the echelle disk entrance, where light leaves the cross disperser to intercept the detector, a metal sheet, bonded with black kapton, was bonded onto the side of the entrance hole closest to the echelle grating. This baffle was necessary to black direct-light contamination coming through several collimator tubes, which would have been directly in the light of sight to the detector.

(2) Several rings of black kapton were placed between an ion repeller grid (which is located at the entrance to the hole to the detector and used to repel ions that can contribute significantly to noise during flight) and the detector, which cut down first-order scatter bounces near the detector.

(3) Any through-holes left open in the structural disks were blocked with black kapton.

Once the payload aluminum skins were installed around the spectrograph, we added additional baffling around the openings between the disks and skins, to limit grazing bounces off of the aluminum skins. Overall, the choice in baffling locations reduced on-axis stellar light by 25% on the blue end of the spectrum (λ 1000 Å) and 3% on the red end of the spectrum (λ 1650 Å). The effects of the baffling are included in the final CHESS Effective Area curves (Figure 4.14). However, the baffling was estimated to reduce scattered light contamination, specifically from geo-coronal Lyα and O I diffuse light, by $> 90\%$. I calculated all quantitative loses in light (for both on-axis and diffuse, scattered light) in Zemax simulations.

4.4.2 Vacuum Alignment

Vacuum alignments for CHESS were necessary to make final adjustments to the desired FUV bandpass onto the detector plane and to focus the echellogram onto the detector. Similar to previous CASA sounding rocket missions, UV alignments were performed in a long vacuum chamber ("Long Tank") at the CU-Boulder ARL location, which is large enough to accommodate the diameter and length of the payload (the tank has a 30" O.D. and is 23' long) and can pump to high vacuum with the help of a dedicated cryopump ($P_{tank} \lesssim 10^{-6}$ Torr). A discharge lamp source, the same as described in Section 4.3.1, feeds into the "Long Tank," which is then collimated by a 24" f/4 gold-coated Newtonian collimator, effectively producing simulated starlight at UV wavelengths. The instrument points at this collimated light, and data can be collected to complete alignments and characterization of the instrument in the laboratory. Unlike previous payloads, CHESS included the use of dedicated vacuum linear actuators at each optic, which manipulated the orientation of the two gratings while the payload system at high vacuum ($\lesssim 4\times10^{-6}$ Torr), which allowed for real-time spectral alignment modifications. This proved useful when aligning the desired echellogram in the view of the collecting detector area. Unfortunately, the payload electronics had no cooling source and would heat significantly over the course of ~ 30 minutes, so vacuum-cycling the system was generally required before moving the optics with the cross disperser actuators for focusing the spectrum.

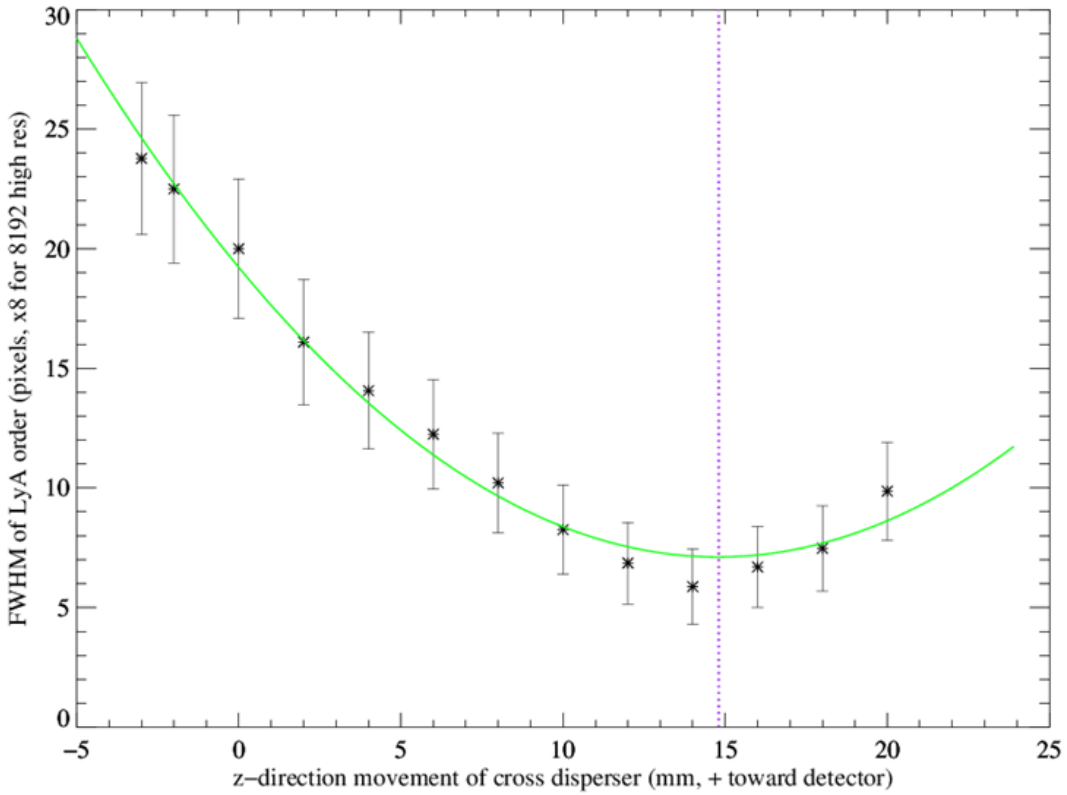

Figure 4.17 The focus curve of the FUV echelle order width (using Lyα as a proxy) versus the cross disperser position along the optical axis. A position z = 0 references the starting position of the cross disperser after optical alignments were complete. Order widths are defined as the full width at half maximum (FWHM) of a Gaussian fit through the integrated light produced in the order. The green curve is a best-fit quadratic function through the measured order widths at each cross disperser position, and the purple vertical line represents the best focus position of the instrument.

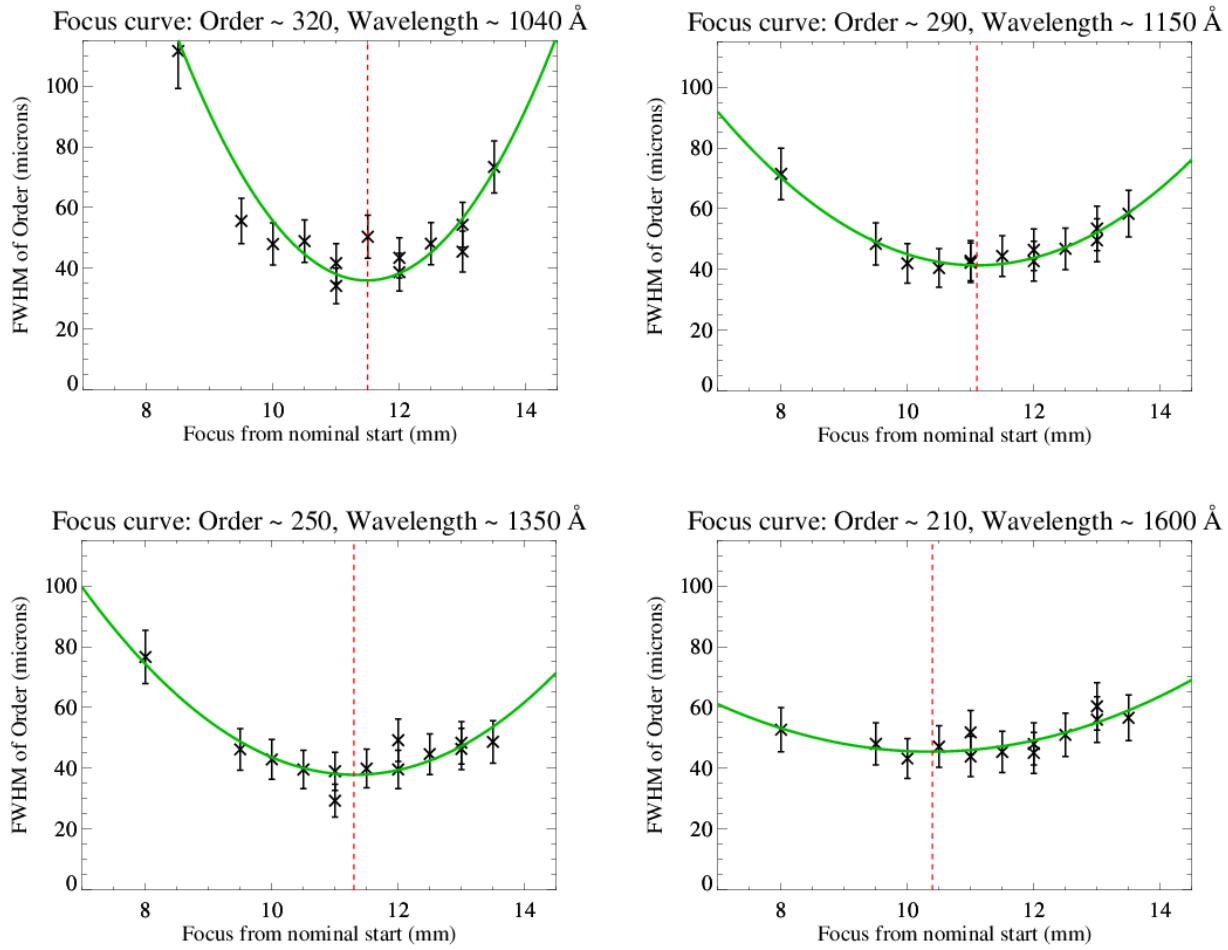

Figure 4.18 Focus curves for CHESS-2 echelle orders with λ = 1040 Å, 1150 Å, 1350 Å, and 1600 Å. The FWHM were taken as the width over which the entire order extends, not the spectral width of specific emission features within the order. We focused the echellogram closer to the minima of the 1040 Å and 1150 Å orders, at z = 11.2 mm from the original starting position of the cross disperser, because the separation of orders with wavelengths $\lambda < 1100$ Å was critical for the final data product.

The aspect camera was used to align the payload to the collimated light source of the "Long Tank". The light off the cross-disperser can be tracked as it comes into focus; before reaching focus, the illumination through the collimator tubes, where the "Long Tank" light source enters the instrument, was imaged. By maximizing the squareness and throughput of illumination from this image of the tubes, CHESS was aligned to the optical axis of the "Long Tank." Adjustments were made to the first aspect camera pick-off mirror on the echelle mount, such that the mirror directed the "Long Tank" simulated starlight to the center of the cross-dispersing grating. CHESS is then installed in the vacuum system, and first light images are taken to adjust the echellogram in the detector image. Once a position for the echellogram was chosen, the aspect camera flat mirrors were once more adjusted manually to direct light to the center of the aspect camera. Final adjustments of these mirrors were made only after all spectrograph optics have been locked in place at final alignment and focus positions.

The cross dispersing grating in CHESS is the only powered optic in the system, so the position of this grating, with respect to the detector, controls the focus of the echellogram. Linear vacuum actuators were positioned behind the cross dispersing optic to control the tip, tilt, and optical axis motions of the grating during vacuum alignments. Vacuum alignments were conducted using a combination of 65/35% hydrogen/argon (H/Ar) gas through an arc lamp system on the side the Long Tank. The lamp was run at high voltage (~ 300 400 V) and current (> 300 mA) and produced many observable electron-impact-excited H_2 emission features. Focus sweeps were taken at various positions of the cross disperser away from the detector, such that a "focus curve" could be created and optimized to quantitatively determine the final position of the cross-dispersing grating, based on the changing behavior of echellogram features (specifically the H_2 emission) with cross-disperser movement. The final focused position of the cross disperser was found to be 14.9 ± 0.9 mm from the starting position of the cross disperser for CHESS-1, and 11.2 ± 0.3 mm from the starting position of the cross disperser for CHESS -2. The starting position of the cross disperser was relative to where the cross disperser started in z-space from the detector after optical alignments. Figure 4.17 and 4.18 show the focus curves for CHESS-1 and CHESS-2; for CHESS-1, only one focus curve

was created, using one Lyα echelle order, but for CHESS-2, four different wavelength regimes were considered, representing four different portions of the echellogram, to better constrain the final, focused position of the cross disperser.

4.4.3 Calibration Results

After final alignment and focus positions of the echelle and cross disperser were determined, long exposures with a 65/35% hydrogen/argon (H/Ar) gas mixture fed through the "Long Tank" hollow-cathode lamp were taken for a complete sampling of H and H_2 emission lines in the CHESS bandpass. Deep, integrated images for pre-launch instrument characterizations were necessary to fully define the one-dimensional (1D) extracted spectrum, the wavelength solution, and the line spread functions (LSFs) of the spectral features throughout the CHESS bandpass.

Figure 4.19 shows the echellograms of CHESS-1 and CHESS-2 used for pre-launch calibrations. Both echellograms are co-additions of multiple exposures taken under vacuum to accumulate more than 60 million photon counts for a complete sampling of H and H_2 emission lines. Each exposure was defined by how long we could run the full instrument configuration in vacuum without over-heating the electronics section, which usually lasted around 30 minutes. Each exposure collected was typically between 3 - 6 million (CHESS-1) and 10 - 20 million (CHESS-2) photon counts.

The basic principle of an echellogram and how to interpret its spectral information is as follows: The echelle grating crudely disperses light into higher order with a wavelength range ($\Delta\lambda$), which are stacked vertically in these images, from short wavelength solutions at the top and longer wavelength solutions toward the bottom. The cross disperser spreads out the spectral information in each echelle order, which is presented as the horizontal features in the images. Each horizontal spectral line contains $\Delta\lambda$ from the echelle solutions and are summed over the echelle order width to create a 1D spectrum. The CHESS instrument products > 100 of these horizontal spectral lines, all of which contribute to building the spectral coverage of the instrument.

Extracting the 1D spectra from the CHESS echellogram was accomplished in several steps.

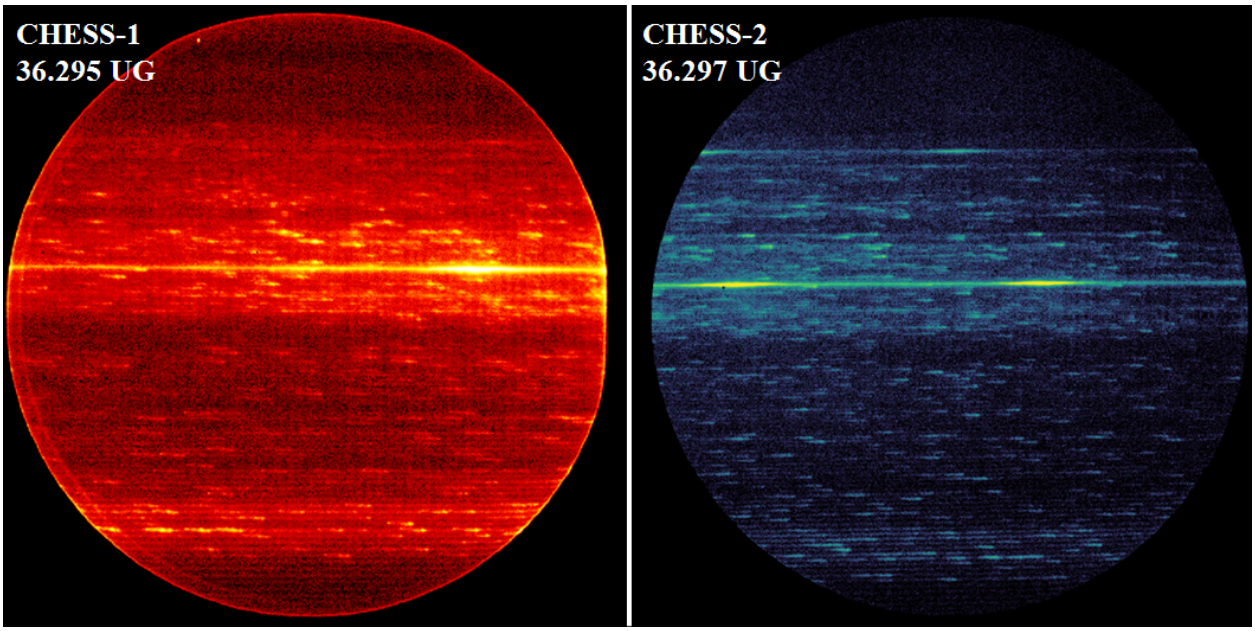

Figure 4.19 Presented are the raw images of the CHESS-1 (left) and CHESS-2 (right; edge effects have been cropped out) echellograms from pre-flight calibrations (March 2014 and December 2015) using an arc lamp flowing 65%/35% H/Ar gas. The brightest feature in both images is H I-Lyα (λ 1215.67 Å); the CHESS-1 echellogram only shows Lyα in one echelle order, while the CHESS-2 echellogram disperses Lyα photons into two adjacent echelle orders. The other broad feature(s) visible in the CHESS-2 echellogram are HI-Lyβ (1025.72 Å), about 1/4 of the way from the top of the image, and HI-Lyγ (97.25 Å), barely visible above the Lyβ features. The more discrete features dotted throughout the spectrum are H_2 emission from electron-impact fluorescence.

First, the echellogram had to be rotated very slightly ($\theta < 1^{\circ}$) to successfully extract the light in each order without contamination from light in adjacent orders. The location of each order was then determined by summing (collapsing) all photon counts along the x-axis (horizontally), which added all the light in each order together and created peaks where orders were present and troughs at inter-order pixels. This exercise also determined the width of each order, which ranged from 4 − 12 pixels wide in the final CHESS echellograms.

Once pixel locations and order widths were extracted, each horizontal spectral feature was collapsed along the y-axis (vertically), creating the 1D spectrum for each echelle order. We used the composition of air through the arc lamp to map out well-known atomic lines and their corresponding orders for both CHESS-1 and CHESS-2 echellograms. Once wavelengths and order locations were known for prominent emission lines of oxygen, carbon, and nitrogen, we used the H/Ar arc lamp echellogram, in conjunction with modeled electron-impact H_2 fluorescent lines, to extrapolate the pixel-to-wavelength conversion for the CHESS data over the entire FUV bandpass; an example of the pixel-to-wavelength extractions determined from H_2 emission features is shown in Figure 4.22 (CHESS-2).

Once wavelength solutions were known for 20 − 30 orders, we fit a 6^{th} order polynomial function to extrapolate the wavelength calibration over the entire 130 orders in the CHESS-2 echellogram. Figures 4.21 and 4.22 show the final wavelength calibration for pre-launch laboratory spectra from CHESS-1 and CHESS-2. In Figure 4.22, the different colored spectra represent separate orders extracted from the echellograms. The higher echelle order solutions of the Bach Research echelle grating resulted in overlap in wavelength coverage between adjacent orders throughout the bandpass of CHESS-2, which made it easier to stitch together the CHESS-2 1D spectrum by correlating spectral features. The steep AOI of the CHESS-1 grating, however, had the opposite effect on the spectral orders focused in the echellogram. The echelle orders were spread out past the edges of the detector, so no overlap in adjacent orders was recorded. This led to gaps in the wavelength coverage throughout the CHESS-1 bandpass.

After the wavelength solution was found for the pre-flight calibration echellogram, I deter-

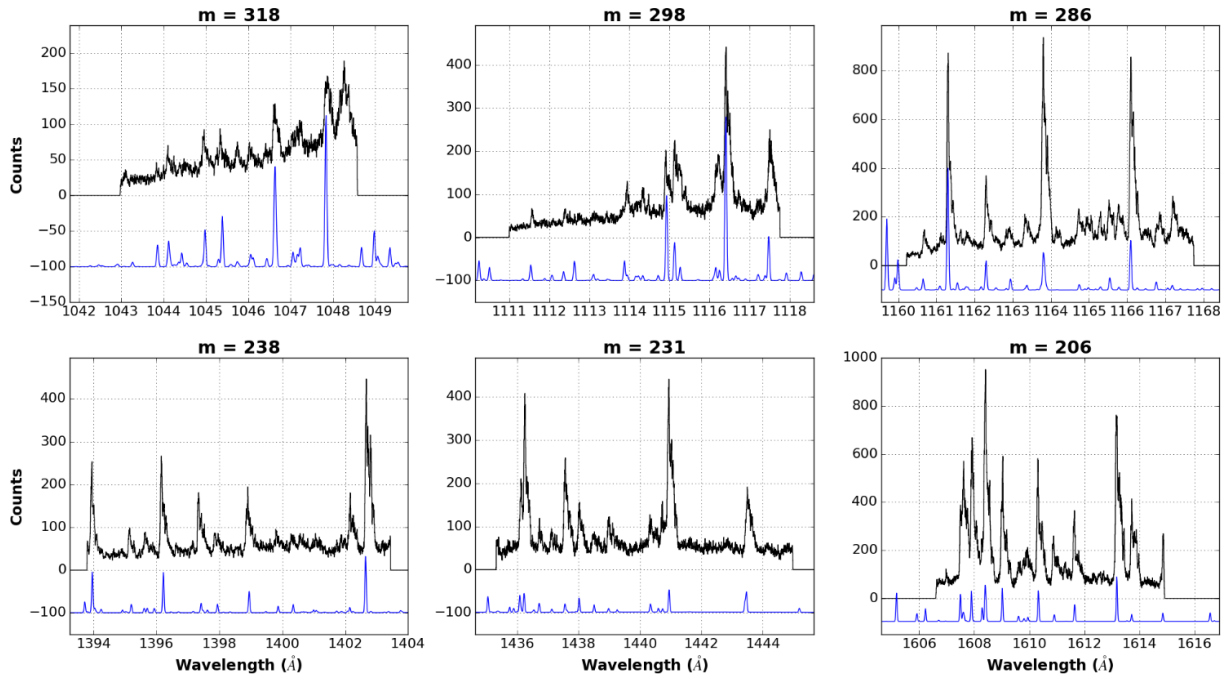

Figure 4.20 The extracted 1D spectra of six orders from the pre-launch calibration echellogram of CHESS-2. Black represents the CHESS-2 extracted spectrum over the order extent. The blue lines are modeled H_2 emission features, using estimated physical parameters of the conditions within the arc lamp, including the column density of H_2 molecules ($N(H_2) \sim 10^{19}$ cm^{-2}), effective temperature ($T_{eff} = 800$ K), and electron energy ($E_{elec} = 50$ eV).

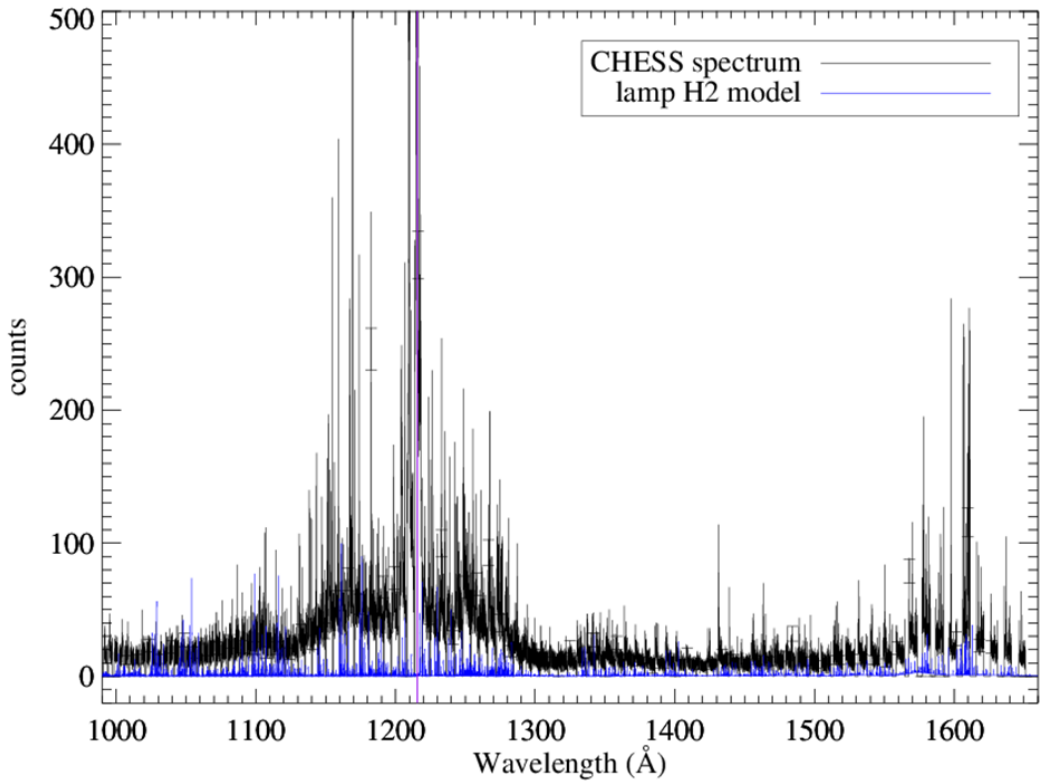

Figure 4.21 The complete first-order wavelength solution for the pre-launch CHESS-1 calibration spectrum from $\lambda\lambda$ 1000 - 1650 Å. The final wavelength solution using H_2 fluorescence emission features and and a functional extrapolation of the wavelength with a 6^{th}-order polynomial fit. Over-plotted in blue is a modeled electron-impact H_2 fluorescence spectrum producted within the discharge lam (T_{eff} = 400 K, N(H_2) = 10^{19} cm^{-2}, and $E_{electron}$ = 50 eV). The spectrum is scaled to the highest total counts of the H_2 features; otherwise, Lyα would dominate the spectrum and the H_2 features would be washed out.

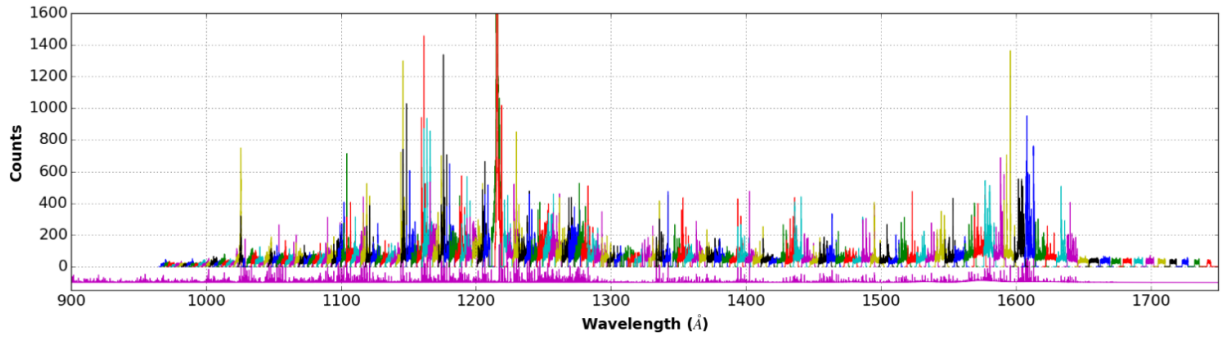

Figure 4.22 The complete first-order wavelength solution for the pre-launch CHESS-2 calibration spectra from $\lambda\lambda$ 900 - 1750 Å. The final wavelength solution was determined using H_2 fluorescence emission features and a functional extrapolation of the wavelength with a 6^{th}-order polynomial fit. Over-plotted in magenta is the model H_2 fluorescence inside the arc lamp (T_{eff} = 800 K, N(H_2) $\sim$ 10^{19} cm^{-2}, $E_{electron}$ = 50 eV). The spectrum is scaled to the highest total counts of the H_2 features; otherwise, Lyα would dominate the spectrum and the H_2 features would be washed out. To show how neighboring order spectra overlap and correlate to form the final 1D spectrum, individual order spectra have been plotted in different colors.

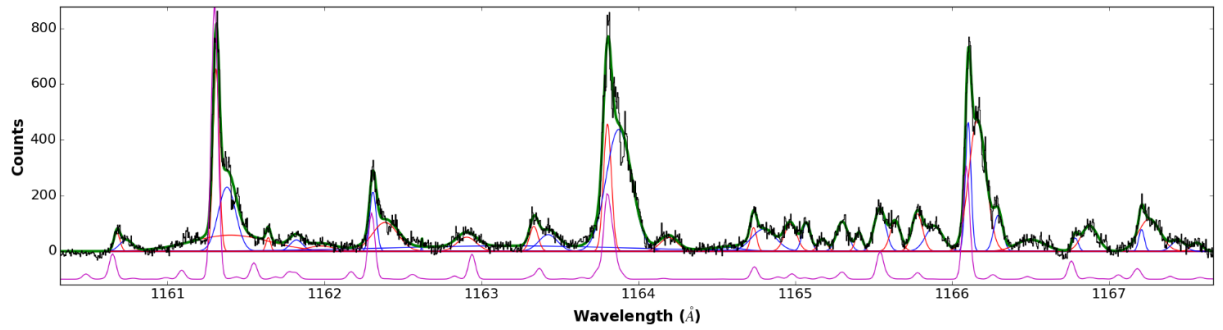

Figure 4.23 The line spread function (LSF) fits of H_2 emission features in one order of the pre-launch calibration spectrum of CHESS-2 (echelle order m = 286). The order spectrum is shown in black. Red and blue Gaussian line fits are shown for the narrow and board Gaussian fits for each line, respectively. The green line is the sum of all Gaussian components to reproduce the spectrum. A modeled H_2 fluorescence spectrum is shown in magenta.

mined the line spread function (LSF) and resolving power of the final, wavelength-calibrated 1D spectrum of CHESS, for the second flight only. I created a multi-Gaussian fitting routine, which fits to the line shapes of the emission features present in each echellogram order. I present an example of this fitting routine in Figure 4.23. At first glance, the emission lines produced by CHESS-2 are not symmetric; they have a sharp peak towards the left (shorter wavelength end) side of the emission line and a shallower slope back to the continuum level toward the right (longer wavelength end). I described this line shape with two separate Gaussian functions summed together, which results in a narrow- and broad-component LSF. Each echelle order spectrum showed very similar behavior in LSFs, specifically that the shorter (longer) wavelength end of each order has more power in the narrow (broad) Gaussian fit. The ratio of the Area(narrow)/Area(broad) of the emission features for shorter wavelengths in the echelle order is ~ 1, whereas emission features with longer wavelengths in the same echelle order have Area(narrow)/Area(broad) ~ 0.33. This indicates that the cross disperser may be tilted, resulting in a better focus at one end of the echellogram. For all emission lines, a peak (narrow) line fit was present, and I use this component of the LSF to estimate the maximum resolving power of CHESS. I also consistently measured narrow line component velocity widths (v_{narrow}) in the pre-launch CHESS-2 spectrum to be between $3 - 20$ km/s, and broad line velocity widths (v_{broad}) to range between $20 - 60$ km/s. For post-flight calibrations, I measured $v_{narrow} \sim 5 - 25$ km/s and $v_{broad} \sim 20 - 60$ km/s. All high S/N (> 100) emission LSFs across the CHESS-2 bandpass were saved to later convolve with CHESS-2 flight data, which would eliminate instrumental spectral line features present in the final science spectrum.

The FWHM of the narrow component of the CHESS LSFs are used to estimate the resolving power of the instrument, as a function of wavelength (Figures 4.24 and 4.25). Each orange spot represents a different emission line in the CHESS calibration data. In the CHESS-1 spectra, a clear trend towards better resolving powers is achieved as we probe lines with longer (redder) wavelengths. The different-colored dashed lines in Figure 4.24 in the CHESS-1 resolving power plots show the resulting resolving power as a function of FWHM and wavelength (magenta: R = 33,333; red: R = 50,000; green: R = 66,666; blue: R = 100,000). The resolving power for $\lambda <$

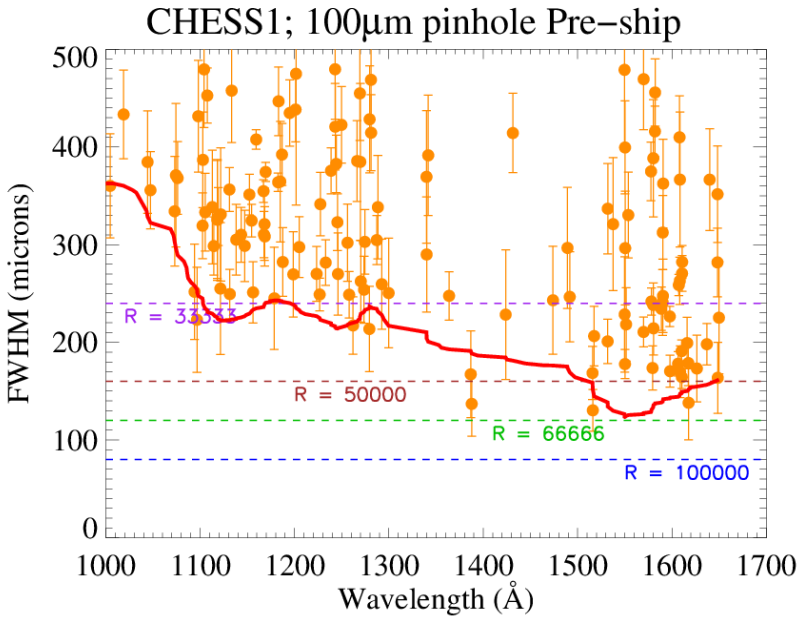

Figure 4.24 A scatter plot for CHESS-1 of measured resolution of individual electron-impact H_2 emission features in the pre-flight laboratory calibration spectrum. Orange spots are measured FWHM values of individual lines; the red line is a lower-limit resolution performance outline of the instrument, given the limitations of the external collimating system used to perform pre-flight calibrations; the dashed lines represent basic resolution cutoffs, based on the FWHM (in microns) of the emission line.

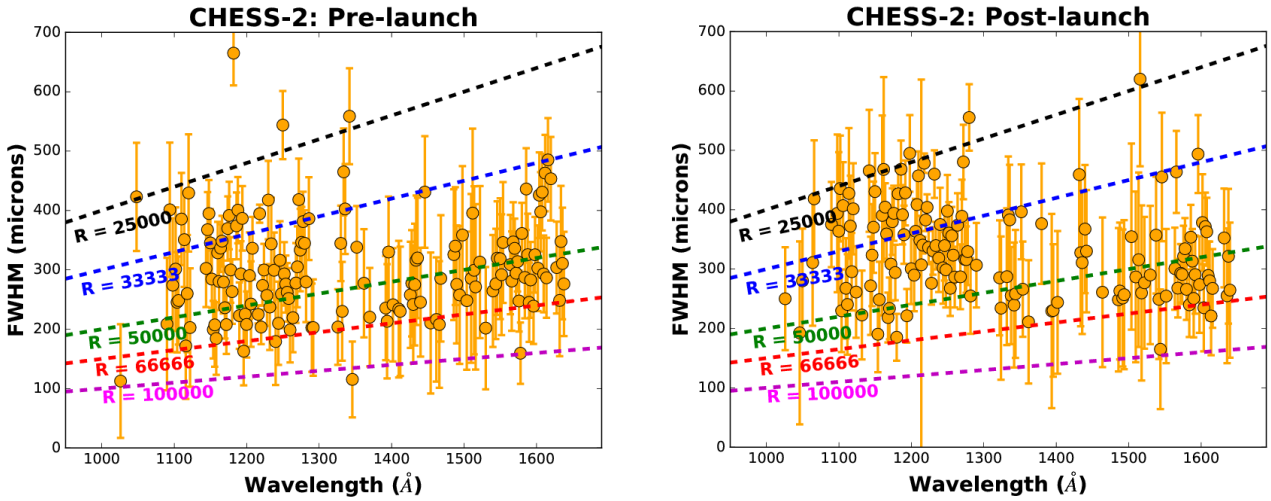

Figure 4.25 A scatter plot of the measured resolution (via FWHM measurements) of individual electron-impact H_2 emission features in the pre-flight calibration spectrum of CHESS. Orange spots are measured FWHM values of individual line peak cores, and the dashed lines represent resolution cutoffs, based on the FWHM (in microns) of the emission line as a function of wavelength. Both pre- and post-launch resolving powers seem to be concentrated around 25,000 − 70,000 over the bandpass of CHESS-2, but there is a noticeable concentration of lines at lower resolving powers (larger FWHM) at $\lambda < 1300$ Å for the post-launch calibration. Physical shifts in the optical alignment between pre- and post-launch calibrations affected the resolving power of the instrument. This may have been caused by tilting the cross disperser and subsequent echellogram, or by moving away from the instrument focus, or a combination of both.

1300 Å is measured to be R $\leq$ 33,333, and the resolution appears to get better by λ 1600 Å (R $\sim$ 70,000). A post-launch calibration image was not collected for CHESS-1 after launch because of an unidentified alignment slip between the echelle and cross dispersing grating, which resulted in no access to the CHESS-1 echellogram after launch. Only after deconstructing the instrument did we decide that the cross disperser mount was the most likely culprit to slip, which we adjusted for CHESS-2.

Figure 4.25 presents the revolving power of CHESS-2, pre- and post-launch, as a function of wavelength. The different-colored dashed lines in the CHESS-2 pre- and post-launch resolving power plots show the resulting resolving power as a function of FWHM and wavelength (black: R = 25,000; blue: R = 33,333; green: R = 50,000; red: R = 66,666; magenta: R = 100,000). The pre-launch calibration shows a concentration of resolving powers between R = 25,000 and 66,000, with an average resolution between R $\sim$ 33,000 $-$ 70,000 (velocity width between 9.0 $-$ 4.5 km/s) across the CHESS-2 bandpass.

While this is below our nominal resolving power goal of 100,000, it was originally thought that the measured resolving power of CHESS-2 using the laboratory calibration data may only represent a lower limit to the instrumental capabilities. The ray trace for CHESS requires an input on-axis light source with beam spread $< 1''$, but we have only been able to demonstrate constraining the spread to $2'' - 3''$ in our laboratory vacuum chamber. Additionally, the laboratory arc lamp may have pressure-broadening effects on the H_2 electron-impact emission, which would produce broader emission lines with than the resolving power of the instrument.

Post-launch calibration results showed a small shift from the average R $\sim$ 33,000 $-$ 70,000 to R $\sim$ 25,000 $-$ 60,000 (velocity width between 12.0 $-$ 5.0 km/s), indicating that either the instrument shifted slightly out of focus before, during, and/or after launch operations, or the shift in the echellogram affected the line shapes of the spectra. In either case, post-launch resolution of CHESS-2 is degraded slightly from pre-launch values. New LSFs were measured for the post-launch CHESS-2 calibration echellogram to better correct for instrument affects in the science (ϵ Per) spectrum.

For both CHESS-1 and CHESS-2, it was very difficult to demonstrate the designed resolving power of the instrument. For the first build of CHESS, it was originally thought that, with the combination of an imperfect calibration chamber and the experimental gratings being flown, the interesting spot shapes of the echellogram could be explained by those two unknowns. However, with the build of CHESS-2 and the re-introduction of the weird echellogram spot shapes (even when one of the experimental grating was replaced with a reliable replica grating), I began to suspect that something more significant was happening. The cross-dispersing grating in CHESS has an unusual surface curvature: it has two radii of curvature (toroidal surface shape), one to focus in the spatial axis of the spectrum and the other to correct along the sagittal plane. The ruling of the cross disperser had to happen along the the spatial radii of curvature, or the solutions off the cross disperser would not work in CHESS. Because the same spot shapes were seen in both CHESS-1 and CHESS-2 builds, I simulated in Zemax what the expected spot shapes might look like, if the cross disperser was ruled along the wrong radius of curvature. The simulations replicated the spot features almost perfectly, pointing to the cross disperser being ruled wrong. (Note: After the de-construction of CHESS-2, the cross disperser was physically measured in the lab to match the focii with the spatial plane of the grating, and it was experimentally determined that the cross disperser was, in fact, ruled along the wrong axis.)

This had serious implications for the expected instrument performance, the most serious being a severely degraded resolving power across the bandpass ($R_{max} \approx 15{,}000$). The narrow-component of the CHESS LSFs are actually re-produced by tilting the cross disperser off-axis by a small amount, which also explains why the shorter wavelength end of the echelle orders consistently showed "peakier" narrow components than the longer wavelength ends. In reality, the measured resolving power of CHESS-1 and CHESS-2 should have been measured by the broad-component of the emission line features, which consistently displayed velocity widths of 20 - 60 km s^{-1} (resulting in $R \sim 5{,}000 - 15{,}000$). For the CHESS-2 science spectrum, the shape of the broad component Gaussian LSF and resulting resolving power from those features are used to analyze the data.

4.5 CHESS Launches and Flight Results

4.5.1 CHESS-1

The first flight of CHESS (CHESS-1) was launched aboard NASA/CU mission 36.285 UG from WSMR on 24 May 2014 at 01:35 am using a two-stage Terrier/Black Brant IX vehicle. Overall, the mission was a comprehensive success and achieved all the goals it aimed to meet. The instrument successfully collected data over the allotted ∼400 seconds of observing time. When the instrument centered on the primary science target (β Sco[1]), the count rate from the target was $\sim 5\times$ lower than expected, and there was no clear indication of an echellogram after $\sim$ 30 seconds. To ensure some science spectrum was collected, if the components in CHESS stayed aligned through launch, the instrument was moved to the chosen back-up calibration target, α Vir, and stayed on this target for the remainder of the flight. The count rate at α Vir was also lower than expected, but it did increase on α Vir, and the appearance of stellar absorption features in the CHESS echellogram after $\sim$ 45 seconds on target made it clear that the α Vir stellar spectrum was being collected.

The total S/N of the flight data $\sim$ 2 over the entire bandpass, which makes the data difficult to work with and successfully extract features from the stellar continuum and noise. I extracted echelle orders from the flight data and created a rough 1D spectrum from the resulting echellogram, which I show in Figure 4.26. No more significant science analysis can be drawn from 1D spectrum, with the exception of analysis of some broad features seen in the echellogram.

4.5.2 CHESS-2

For CHESS-2, more careful monitoring of alignment shifts during field operations was taken to ensure the second build of CHESS produced a better-quality flight science spectrum.

CHESS-2 was brought to White Sands Missile Range (WSMR) in late January 2016 for field operations in preparation for launch. CHESS-2 underwent various tests, including vibration, which required a means of determining alignment shifts before launch. We fitted a Bayard-Alpert tube (ionization gauge)McCandliss et al. (2000) with a small, collimating mirror and pinhole (20 μm) to

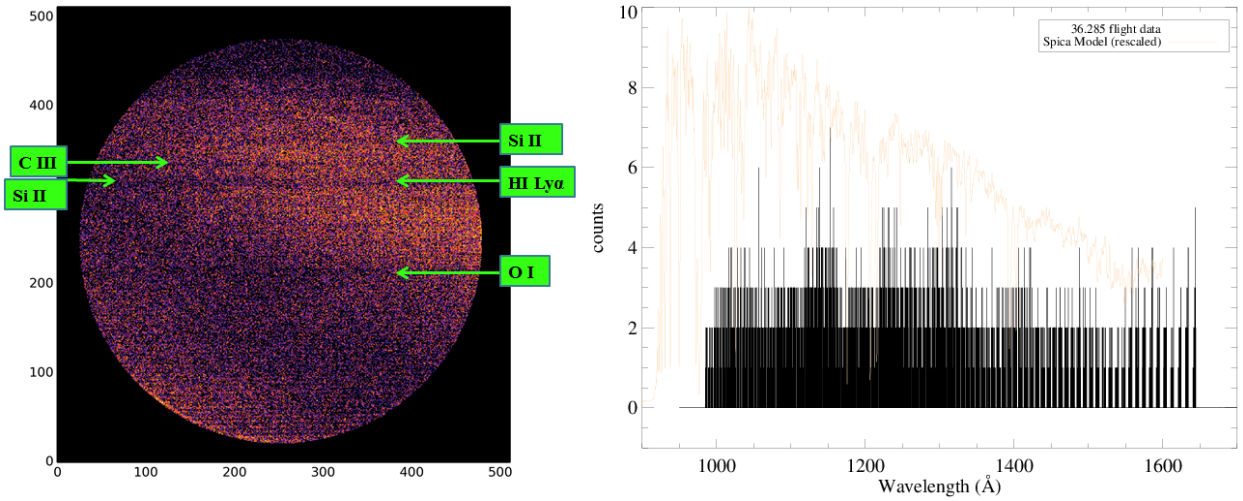

Figure 4.26 **Left:** The False-color representation of the flight echellogram from CHESS-1, taken on 24 May 2014, of α Vir. The purple/black regions represent areas with lower concentrations of photon counts, and blue/green pixels represent pixels with higher concentrations of photons collected. Marked with green arrows and labeled are the most prominent features in the echellogram. Because of the low S/N of the flight data, the echellogram has been binned to 512×512, to show absorption features in the image. **Right:** The flight spectrum (black) and the modeled spectrum for α Vir, given the expected amount of ISM materials (H I, H_2) in the sightline. Unfortunately, due to the very low quality of the flight data and the high background in the echellogram, we were unable to perform further analysis of the α Vir data.

the shutter door, which produced an echellogram with air spectral features (C, N, O, H). We used these images to measure the centroid pixel location (in both x and y axes) of N I and O I emission features. Comparing the new centroid location of $3 - 4$ emission lines to reference pixel locations measured at CU, we use the plate scale of the instrument (plate scale = $206265''/1236.834$ mm = $166.77\ ''$/mm) to estimate alignment shifts before launch. The largest centroid shift measured pre-launch was 105 pixels (over 2k $\times$ 2k pixels), which corresponded to a physical shift of 1176 μm (1.176 mm), or $3.27'$ ($196.12''$). Given the large FOV of the instrument (0.67°, or $40.2'$), the success criteria specification for the on-target acquisition ($5'$), and the ability to demonstrate that the instrument can still collect a science echellogram, this alignment shift was acceptable to continue with launch of the instrument.

CHESS-2 was launched aboard NASA mission 36.297 UG from White Sands Missile Range (WSMR) on 21 February 2016 at 09:15pm MST using a two-stage Terrier/Black Brant IX vehicle. The mission was deemed a comprehensive success. The instrument successfully collected data over the allotted ~ 400 seconds of observing time, with > 200 seconds without up-link maneuvers. When the instrument centered on-target (ϵ Per), the count rate was lower than expected by a factor of 2 ($\sim$ 25,000 counts/second, instead of 50,000 counts/second), and an estimated 10,000 counts/second was attributed to geo-coronal (diffuse) scattered light.

From the first few seconds of integration on target, the CHESS echellogram displayed signs of photospheric and interstellar absorption features, the most prominent features being Lyα, C III, Si IV, and O I. Once the ϵ Per integration reached $t_{exp} \sim 100$ seconds, more interesting interstellar features started to appear, including Si II, Si III, N I, C I, C III, and H_2 complexes. Figure 4.27 shows the raw flight data (echellogram; left) after ~ 200 seconds on-target. The fully-calibrated (scattered light-subtracted, order cross-correlated, wavelength solution implemented, and flux corrected) 1D spectrum of ϵ Per, from the 200 second integration on CHESS-2, is show on the right in Figure 4.27. We estimate that the final data quality of the CHESS-2 ϵ Per spectrum has S/N $\gtrsim 5$ across the bandpass.

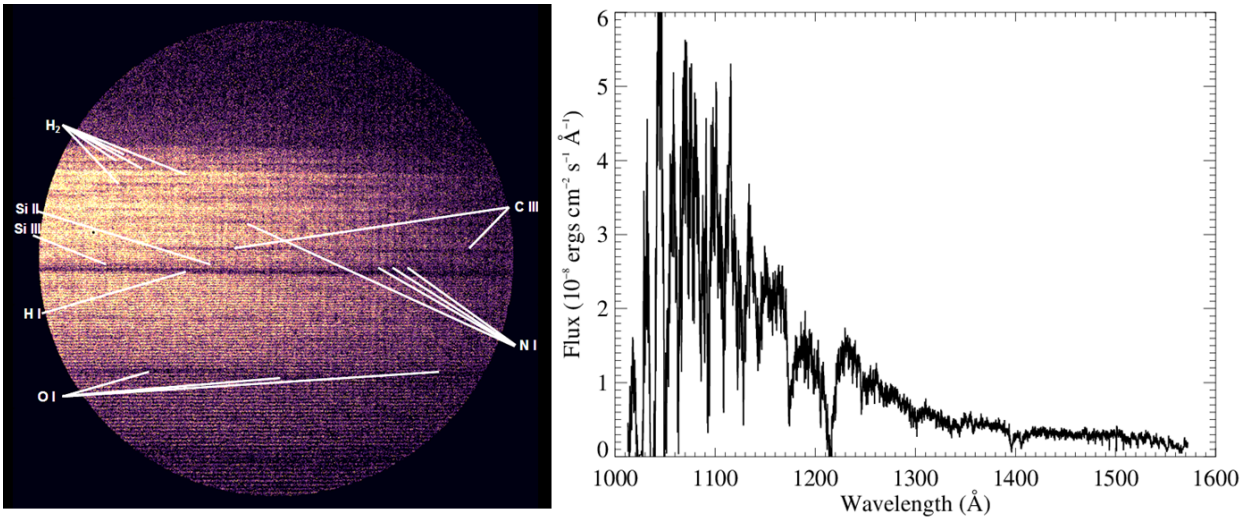

Figure 4.27 The flight data from 36.297 UG (CHESS-2). **Left:** The science echellogram of ϵ Per after an exposure time of $\sim$ 200 seconds. The echelle orders are stacked horizontally in the image, with order spectra easily distinguishable in the bottom half of the echellogram. Because the echelle used in CHESS-2 disperses the starlight into very high orders for $\lambda < 1200$ Å (m > 280), shorter wavelength orders are more difficult to distinguish and required scattered light subtraction and echellogram collapsing along the order axis of the image. I label important ISM and stellar absorption features in the echellogram, which are much more pronounced than in the CHESS-1 science echellogram. **Right:** The flux-calibrated 1D spectrum, with wavelength solutions incorporated, for ϵ Per from CHESS-2. Many prominent absorption features are observed in this spectrum, which covers the full CHESS bandpass from $\lambda\lambda$ 1000 - 1600 Å. Molecular hydrogen is prominent for $\lambda < 1110$ Å. Important interstellar and photospheric absorption species, such as C I, C II,C III, N I, Si II, Si IV, O I, and Fe II are easily distinguishable against the FUV continuum of ϵ Per,

4.5.3 H_2 Absorption Profile Fitting and Rotation Diagrams

The flux-calibrated CHESS spectrum of ϵ Per provides a unique data set to characterize the column of cool material in the sightline via the rotational behavior of molecular hydrogen. Present within the CHESS spectrum are 7 H_2 spectral bands, ranging from $\lambda\lambda$ 1020 - 1115 Å. At least three of the seven bands are relatively uncontaminated by other stellar and/or interstellar features: (4 - 0), (1 - 0), and (0 - 0) (λ_0 = 1049.4 Å, 1092.2 Å, and 1108.1 Å, respectively), which are used to model the column densities and Doppler velocity structure of the rotational levels of H_2, ranging from J'' = 0 - 7 in all bands.

This analysis is performed with a synthetic absorption profile fitting routine, similar to those performed by France et al. 2013b. I construct a multi-component H_2 absorption line fitting routine combining the `H2ools` optical depth templates (McCandliss 2003) and the `MPFIT` least-squares minimization routine in IDL (Markwardt 2009). This method takes the theoretical line shape of each H_2 rotational level at a given column density and Doppler-b value, convolves the synthetic spectrum with the line spread function (LSF) of the instrument, and simultaneously varies all parameters until a best-fit value is found. A single-component H_2 sightline is employed in this fitting, since a single molecular component is known to dominate each diffuse/translucent ISM sightline (Spitzer et al. 1974, Morton 1975). The fits are restricted to b-values over fits of H_2 rotational levels most sensitive to changes in b, J = 2 - 6, and found a best-fit b-value of 3.6 km s^{-1} for the lines in the H_2 progressions fit, consistent with typical b-values for H_2 in the local ISM (Lehner et al. 2003, France et al. 2013b) and previous curve-of-growth measurements of H_2 on the ϵ Per sightline (e.g., Stecher and Williams 1967, Carruthers 1971). The single b-value approximation may introduce systematic errors in our determination of N(J'') because it has been shown that, along certain sightlines, the higher rotational levels ($J'' \approx$ 4 - 6) are better fit with b-values of $\sim$ larger than J'' = 2 (e.g., see Lacour et al. 2005 and references therein). The final determined total column density of H_2, however, is not affected by the choice of b-value because the low-J'' lines that dominate the total column are highly damped and, thus, insensitive to b.

The flux-calibrated CHESS ϵ Per spectrum is normalized around the H_2 progressions of choices for profile fitting. I first fit profiles to the H_2 (1 - 0) (λ_0 1092.2 Å) and (0 - 0) (λ_0 1108.1 Å) for low-to-intermediate rotational levels ($J'' = 0$ - 7), as these bands are relatively uncontaminated by other stellar and interstellar absorption features and have the highest S/N of all H_2 bands in the CHESS bandpass. To check the solutions derived from the simultaneous H_2 profile fit of the (1 - 0) and (0 - 0) bands, I fit the calculated column densities of rotational states to the (4 - 0) H_2 band (λ_0 1049.4 Å), as that band is also clear of stellar and interstellar contaminants, but has lower S/N than the (1 - 0) and (0 - 0) bands. Other H_2 bands in the sightline are contaminated with one or more stellar and/or interstellar feature(s):

- $v' = 6$ (λ_0 1024.4 Å) is contaminated by stellar+interstellar HI-Lyβ,
- $v' = 5$ (λ_0 1036.5 Å) is contaminated with interstellar CII $\lambda\lambda$ 1036, 1037,
- $v' = 3$ (λ_0 1062.9 Å) is contaminated by stellar lines and interstellar ArI λ 1066, and

The normalization process places uncertainties on the total column density derived from the H_2 absorption features. I estimate that the uncertainty in the continuum placement of ± 3% for the (1 - 0) and (0 - 0) bands, and an uncertainty in the continuum placement of the (4 - 0) band of ± 5%. Both continuum placement uncertainties introduce errors less than the profile fitting errors introduced for $J'' = 0$ - 2. Underestimating the continuum level can result in large uncertainties in N($J'' = 3$ - 5), of order $\sim$ 1 dex, which has been accounted for in the errors of the final results.

The total H_2 column density in the sightline to ϵ Per is presented in Table 3.1. The normalized spectra and best-fit models for the $(4-0)$ and $(1-0)$+$(0-0)$ H_2 bands of ϵ Per are shown in Figure 4.28. I measure a total H_2 column density $\log_{10}N(H_2) = 19.72 \pm 0.35$ cm^{-2}. Following the same synthetic absorption profile fitting procedure used to find the column densities of $H_2[v'' = 0]$ rotational levels, I determine the total column density of neutral hydrogen (HI) from the Lyα absorption feature (λ 1216 Å) to be $\log_{10}N(\mathrm{HI}) = 20.33 \pm 0.19$. We find this to be in good agreement with the total column density of neutral hydrogen derived in previous studies (e.g.,

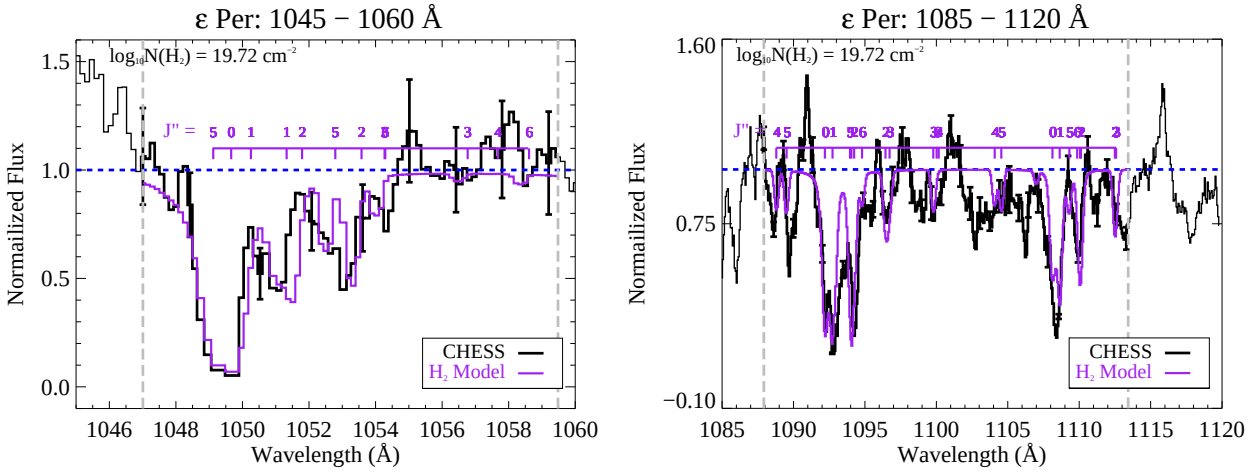

Figure 4.28 Synthetic H_2 profile fits for the $(4-0)$ band (*left*) and $(1-0)$ and $(0-0)$ bands (*right*), shown in purpler, are overlaid on top of the ϵ Per spectra taken with CHESS. Molecular rotational levels are labeled with purple dashes. The best-fit Doppler velocities for all three spectral band fits is $b = 3.6$ km s^{-1}.

Diplas and Savage 1994), and we use N(HI) and $N(H_2)$ to calculate the molecular fraction,

$$f(H_2) = \frac{2N(H_2)}{N(HI) + 2N(H_2)}, \tag{4.2}$$

to be $f(H_2) = 0.33 \pm 0.09$ in the sightline to ϵ Per. Our results agrees with previous *Copernicus* studies, which determine molecular fractions $f(H_2) \sim$ 0.2-0.3 (Spitzer et al. 1973, Savage et al. 1977).

Assuming that the column density of neutral hydrogen is mainly constituted of interstellar hydrogen (Diplas and Savage 1994) and represents the average HI density over the sightline, we estimate the average number density of neutral hydrogen to be n(HI) = 0.23 $\pm$ 0.07 cm^{-3}. The molecular column of hydrogen, however, is expected to lie beyond the boundary of the local bubble, which extends $d \approx 100$ pc in the sightline to ϵ Per. If the molecular column of hydrogen is averaged over the distance outside of the local bubble boundary, $n(H_2) = 0.08 \pm 0.03$ cm^{-3}. These estimates are in good agreement with previous studies (e.g., n(HI+H_2) = 0.34 cm^{-3}; Savage et al. 1977).

Due to the homonuclear nature of the hydrogen molecule, radiative transitions from $J'' = 1 \rightarrow J'' = 0$ are forbidden, while quadrupole transitions from $J'' = 2 \rightarrow J'' = 0$ are allowed, but very slow ($A_{2\rightarrow0} \approx 3 \times 10^{-11}$ s^{-1}; Wolniewicz et al. 1998). At the number densities in the diffuse/translucent clouds towards sightlines like ϵ Per, collisions are expected to control the level populations of the $J'' = 0$, 1, and 2 states. The *kinetic* temperature, T_{01}, of the H_2 in the sightline can be derived from the ratio of column densities in these levels,

$$N(J''=1)/N(J''=0) = \frac{g_1}{g_0} e^{(-E_{01}/kT_{01})} = 9e^{(-171K/T_{01})} \tag{4.3}$$

where $g_{J''}$ is the statistical weight. Using this formula, I find T_{01} along the ϵ Per sightline to be 95 $\pm$ 2 K. The temperature of the higher rotational levels are characterized by creating H_2 rotation (excitation) diagrams, as shown in Figure 4.29. The higher rotational levels ($J'' > 3$) of ϵ Per can be fit with an *excitation* temperature, T_{exc}, by determining the slope of the excitation diagram between the higher rotational states. A least-squares linear fitting routine was used to determine $T_{exc} = 500 \pm 150$ K for the H_2 sightline towards ϵ Per.

Table 4.3. CHESS-2 Stellar Parameters & Results

Target	Spec. Type [a]	d [a] (pc)	T_{exp} (s)	$\log_{10}$(N(HI))[b] (cm^{-2})	$\log_{10}$($N(H_2)$)[b] (cm^{-2})	$T(H_2)$[b] (K)
ϵ Per	B0.5 III	307	245	20.33 ± 0.19	19.72 ± 0.35	$T_{01} = 95 \pm 2$ $T_{exc} = 500 \pm 150$
ϵ Per					$N(J''=0) = 19.20^{+0.31}_{-0.02}$ $N(J''=1) = 19.56^{+0.42}_{-0.85}$ $N(J''=2) = 17.35 \pm 0.41$ $N(J''=3) = 15.47^{+0.81}_{-0.32}$ $N(J''=4) = 14.75^{+2.10}_{-1.58}$ $N(J''=5) = 14.91^{+0.63}_{-0.48}$ $N(J''=6) = 13.12^{+0.75}_{-0.42}$ $N(J''=7) < 13.51$	

[a]Diplas and Savage (1994)

[b]This work.

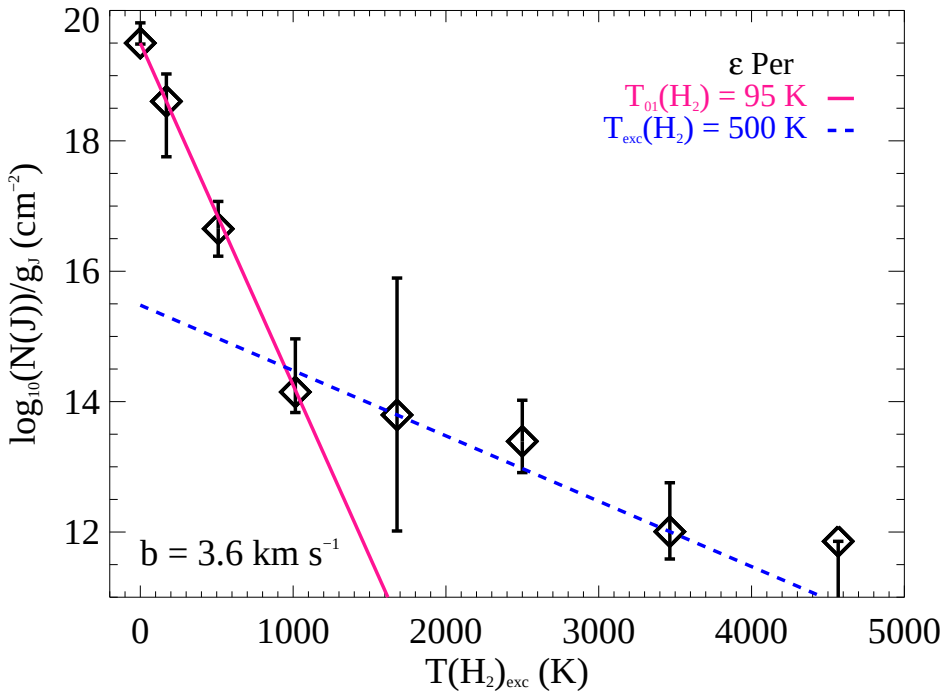

Figure 4.29 The rotation (excitation) diagram for ϵ Per, which demonstrates that two temperature populations of H_2 appears to exist in this sightline. The kinetic temperature is described by T_{01} (pink), while the excitation temperature of intermediate-rotational levels is described by T_{exc} (blue).

Chapter 5

Conclusions & Future Work

"Oh, he would be king down in Mexico. For $100, he could get a lot. At least until they rob him. And take his shoes."

- Larry Conser, discussing a hypothetical scenario where Bobby Kane visits Mexico.

5.1 The Molecular Sightline Towards ϵ Persei: CHESS-2 Results

5.1.1 Comparison to Previous Measurements & Physical Cloud Conditions

The interstellar sightline towards ϵ Per has been studied extensively aboard sounding rocket instruments (e.g., Carruthers 1970, Morton et al. 1972) and observations with *Copernicus* and *IUE* (e.g., Spitzer et al. 1973, Jura 1975b, Martin and York 1982, Vidal-Madjar et al. 1982; 1983). Sounding rocket experiments in the late 1960's through the 1970's found the sightline towards ϵ Per to be very similar to observations made towards α Vir, with the exception of noticeably stronger absorption features at molecular hydrogen transition wavelengths (e.g., Carruthers 1971). In the advent of *Copernicus*, characterization of the molecular sightline of ϵ Per was performed, where Spitzer et al. (1973) found $\log_{10}N(H_2) = 19.88$ and $f(H_2) \sim 0.3$, while Savage et al. (1977) found $\log_{10}N(H_2) = 19.53$ and $f(H_2) \sim 0.21$. Both studies are consistent with the results extrapolated from the CHESS-2 data. Spitzer et al. (1974) determined the Doppler velocity, kinetic, and excitation temperatures of H_2 in the ϵ Per sightline to be 2.9 km s^{-1}, 74 K, and 180 K, respectively; while the b-value found in the CHESS-2 data is on-par with Spitzer et al. (1974), the kinetic and excitation temperatures are 20 K and $\sim$ 300 K higher than found by *Copernicus*. However, T_{01}

from Savage et al. (1977) compare with the kinetic temperature estimated from the CHESS-2 observation. Therefore, molecular hydrogen results are consistent with previous studies of the ϵ Per interstellar sightline, and I use the CHESS-2 observations to infer molecular cloud characteristics along the sightline.

Assuming a plane-parallel interstellar cloud model of one cloud in the line of sight at a constant (uniform) density (Jura 1974; 1975b), I estimate the physical properties of the molecular cloud along the ϵ Per sightline using the observations from CHESS-2. With these assumptions, the product of the H_2 formation rate on dust grains (R_{form}) and the total particle density (n_H), $R_{form}n_H$, can be related to the ratio of H_2 column density in the $J'' = 4$ level to the neutral hydrogen column density (Jura 1975a), which can be written as

$$R_{form}n_H = \frac{N(H_2[v'' = 0, J'' = 4])}{N(HI)} \frac{A_{4\rightarrow 2}}{0.19 + 3.8p_{4,0}} \tag{5.1}$$

where $p_{4,0}$ is the radiative redistribution probability calculated by Jura (1975b), $A_{J'\rightarrow J''}$ is the spontaneous transition probability for the mid-IR rotational $\Delta J = 4 \rightarrow 2$ emission feature (Wolniewicz et al. 1998), and $N(HI)$ is the interstellar neutral hydrogen column density, which is derived from the Lyα absorption feature in the CHESS observation. A similar equation can be constructed using the $J'' = 5$ level, which is written as

$$R_{form}n_H = \frac{N(H_2[v'' = 0, J'' = 5])}{N(HI)} \frac{A_{5\rightarrow 3}}{0.44 + 5.3p_{5,1}}. \tag{5.2}$$

Both equations assume that $J'' = 4$ and 5 are dominantly populated by a combination of grain growth and radiative pumping. I use Equations 5.1 and 5.2 to verify the estimate of $R_{form}n_H$ from my CHESS H_2 analysis. I find $R_{form}n_H = 2.1 \times 10^{-15}$ s^{-1} for $J'' = 4$ and $R_{form}n_H = 2.7 \times 10^{-15}$ s^{-1} for $J'' = 5$, with an average $R_{form}n_H = 2.4 \times 10^{-15}$ s^{-1} for the molecular interstellar cloud in the sightline towards ϵ Per.

The product of the H_2 formation rate and cloud particle density can be used to estimate the total photoabsorption rate (β) in the Lyman and Werner electronic bands of H_2. This sets the

balance for the excitation and dissociation of molecules in typical diffuse/translucent interstellar clouds. Using the formalism outlined in Jura (1975b), I estimate $\beta(J'' = 0) = 7.1 \times 10^{-11}$ s^{-1} and $\beta(J'' = 1) = 3.5 \times 10^{-11}$ s^{-1}. Given the canonical H_2 photoabsorption rate in the diffuse ISM, $\beta_0 \approx 5 \times 10^{-10}$ s^{-1}, the rate in the sightline of ϵ Per is $\sim$ 1 dex lower. This suggests that some degree of shielding of molecular material is happening along the sightline, though the shielding does not appear to be as heavy as other diffuse/translucent H_2 cloud sightlines (e.g. δ Sco and ζ Oph; France et al. 2013b).

If the typical rate of H_2 formation in diffuse interstellar clouds is assumed accurate for the ϵ Per cloud, $R_{form} \approx 3 \times 10^{-17}$ cm^3 s^{-1} (Jura 1975b, Gry et al. 2002), then the average particle density in the H_2 cloud towards ϵ Per is $n_H = 80$ cm^{-3}. Under the assumption of a plane-parallel, uniform density slab, this constrains the molecular interstellar cloud in the sightline to $\Delta d \approx 0.2$ pc. My estimate of the total particle density in the ϵ Per molecular cloud is of the same order as those found from studies using *Copernicus*, although the CHESS observations produce larger particle densities in the cloud by a few factors ($\sim$ 2 - 6 (Jura 1974; 1975b)).

My evaluation of the physical cloud conditions in the ϵ Per sightline utilizes out-of-date analytic equations with uncertain assumptions about the interstellar environment. Rather, I use the inferred rates and density values as a generalized analysis of the diffuse/translucent cloud in the sightline. When compared to values inferred from previous sounding rocket and *Copernicus* studies, the CHESS-2 observed profiles of H_2 and Lyα are sound. However, for a publicized journal article, I plan to perform a more rigorous analysis of the ϵ Per sightline, as observed with CHESS-2, with up-to-date analytic equations and assumptions about the environment, such as those outlined in Habart et al. (2004). For now, this analysis acted as a good check to make sure the details about the molecular abundances in the ϵ Per sightline, as observed by CHESS-2, agreed well with previous studies.

5.1.2 Future CHESS Flights, Technology Demonstrations, and Observations

The Colorado High-resolution Echelle Stellar Spectrograph is scheduled to launch aboard two NASA/CU sounding rocket missions over the next two years. CHESS-3 (NASA/CU 36.323 UG) is currently on-schedule to launch from WSMR on 14 June 2017 at 00:01 MST, while CHESS-4 (NASA/CU 36.333 UG) is scheduled to launch from the Kwajalein Missile Range on 14 April 2018 at 03:00 MHT. CHESS-3 will observe β^1 Sco, which was not achieved during CHESS-1, and CHESS-4 will take advantage of access to the Southern Hemisphere sky and observe γ Ara, a B1I star known to display variable, enhanced stellar wind signatures (Prinja et al. 1997), which displays diagnostics of shock processes in the molecular hydrogen populations and can be used to provide insight into the chemical evolution of diffuse and translucent cloud material in the presence of strong ionizing radiation and particle fluxes.

CHESS-3 will re-fly the holographically-ruled toroidal cross dispersing grating and the cross-strip MCP, both of which were flown aboard CHESS-1 and CHESS-2. The Bach Research, Inc. grating will be replaced with a higher-efficiency grating ruled by Richardson Gratings. The echelle change will nearly double the effective area of the instrument from $\lambda\lambda$ 1050 - 1300 Å. CHESS-4 has the potential to test two new UV technologies: the δ-doped charged-couple device (CCD) for far-UV application, and an electron beam-etching echelle grating, fabricated by colleagues at Pennsylvania State University. The δ-doped CCD is currently being prepared for flight by a collaboration between JPL and Arizona State University. The CCD is designed to provide improved sensitivity at longer wavelengths in the CHESS bandpass than can be achieved with the CsI-coated MCP detector ($\sim 2\times$ higher QE at $\lambda > 1400$ Å). Additionally, the fixed pixels of the CCD chip allow for more-efficient flat-fielding, thereby supporting higher S/N observations of the bright targets CHESS observes. CHESS-4 is scheduled to demonstrate one of these δ-doped CCD focal plane arrays, which can be used in larger future space missions in larger arrays, thereby covering a larger collecting area and achieving higher resolution.

5.2 Characterization of Warm Gas in Protoplanetary Disks

5.2.1 Evolution of Warm Molecules from the Innermost Disk Radii

I have created two-dimensional radiative transfer models of far-UV H_2 fluorescence emission in protoplanetary disks (PPDs) and compared them with observations made with *HST*-COS and STIS. I have analyzed the radial distribution of H_2 emission produced by parametrized models, which are chosen using a reduced-χ^2 statistic, to understand how the emitting H_2 regions change as PPD dust disks evolve. Below, I list my findings and interpretations about the evolution of the molecular disk atmosphere as the inner dust disk dissipates:

(1) The modeled H_2 radial distributions differ between primordial and transitional disks. Primordial disks have the majority of the total H_2 flux arising from the innermost disk radii and less produced outside $\sim$ 1 AU. For transitional disks, the total H_2 flux migrates to larger disk radii, producing less flux in the innermost disk and more out to r $\sim$ 10 AU.

(2) A positive correlation arises between the resulting inner and outer emission radii of FUV H_2 (r_{in} and r_{out}), which supports the result described in conclusion 1. This can be interpreted in one or more ways: a) the physical structure (i.e., temperature) of the warm molecular disk atmosphere changes as PPDs evolve, b) the warm ground levels of H_2 populations [v,J] change, resulting in evolving regions of the disks where the warm H_2 atmosphere will reprocess the stellar Lyα radiation field, and/or c) H_2 is being destroyed in the inner disk and not re-formed, owing to the lack of dust grains. The latter argument allows stellar Lyα to penetrate to larger r_{out}.

(3) I also find positive correlations between r_{in}, r_{out}, and n_{13-31}, suggesting that r_{in} corresponds with the loss of warm, small dust grains in the innermost disk. There appears to be a negative correlation between r_{in} and $\dot{M}$, which provides additional evidence that the warm H_2 inner disk atmosphere may be physically thinned or cleared as the PPDs evolve, possibly by the loss of a molecular formation site as the dust grains dissipate from the atmosphere.

Using the observed dust cavity radii of the transitional disk targets, I compare r_{out} to r_{cavity} and find that, for all transition disk targets, r_{out} is found inward of r_{cavity}. This indicates that the warm H_2 disk (for $r > r_{in}$) remains optically-thick where the warm dust grains are optically-thin in the disks. This suggests that the physical mechanism that clears or settles the inner disk dust either does not have the same effect on the molecular disk atmosphere, or there is a time lag for the gas disk to respond to the changes observed in the dust distribution.

(4) I examine the origins of emitting H_2 in relation to warm CO and the theoretical location of water-ice snow lines. Inner disk CO is roughly co-spatial with r_{in} for all targets, which could point to the dispersal of the warm molecular disk atmospheres of evolving disk systems. With the exception of a few primordial disk targets, all targets have emitting H_2 regions that encapsulate the theoretical water-ice snow line. If disk clearing mechanisms, such as disk photoevaporation via EUV/X-ray photons, are primarily responsible for the final dispersal of the gas disk at the end of the PPD lifetime, it is important to examine late-type PPDs to monitor molecular disk clearing as transitional disks evolve to debris disks.

Studies of high-resolution warm CO in protoplanetary disks have uncovered very similar results regarding the loss of molecular gas from the innermost disk as disks evolve. Recently, Banzatti and Pontoppidan (2015) used a large survey of planet-forming disks observed with VLT/ CRIRES to deconvolve the IR-CO features into two emission components - a narrow and broad component. They determine that more evolved systems tend to have only a narrow component present in their emission features, suggesting depletion of CO from the inner disk. Additionally, when exploring the excitation temperature of CO as a function of disk age and emitting radius, they discovered that, for evolved disks with only a narrow-line CO feature, the excitation temperature of CO increases, even as the emission radius of CO in the disk increases. This suggests that warm CO, which may be thermally-populated in the innermost disk of early-stage PPDs, appears to transition to non-thermal populations as disks evolve and lose gas in the innermost disk. These

non-thermally-populated states could potentially be photo-excited by UV and/or X-ray emission from the protostar. One indication that this may be true is that warm CO absorption is seen in the far-UV in primarily transition disk objects (Schindhelm et al. 2012b), and the absorption radius of CO in these disks is roughly consistent with the emission radius found in Banzatti and Pontoppidan (2015). While the overlap in shared targets is limited, this points to a convenient overlap of panchromatic space, which explores the generic evolving nature of molecules in planet-forming disks.

5.2.2 The Behavior of Hot H_2 in Protoplanetary Disk Environments

I perform the first empirical survey of H_2 rovibrational absorption observed against the stellar Lyα emission profiles of 22 PPD hosts. The aim of this study was to identify thermal and non-thermal H_2 species in each sightline and investigate excitation mechanisms responsible for the distributions of non-thermal H_2 populations. I normalize each Lyα profile with a smoothing kernel and create optical depth models to simultaneously synthesize H_2 absorption features observed across the normalized Lyα spectra. Each optical depth model estimates the column density of H_2 in ground states [v,J] from the absorption depth in the Lyα wings, and I have presented the H_2 rotation diagrams of all samples in this survey, which examine the behavior of the H_2 rovibrational populations in all sightlines. Below, I list highlights and conclusions from this study:

(1) Thermally-distributed H_2 models alone cannot reproduce observed rovibration levels. When exploring the general behavior of all PPD hosts, there appears to be a repeating pattern, where highly-energetic states are "pumped" when compared with lower energy rovibrational states. This appears to happen at "knee" junctures, which are consistently found at T_{exc} = 20,000 K, 25,000-26,000 K, and 31,000-32,000 K.

(2) I find roughly-equivalent total column densities of thermal and non-thermal H_2 populations in transitional disk samples and samples with detectable CIV-pumped H_2 fluorescence. Interestingly, primordial disk targets have more spread in this relation and show more

samples with larger total column densities of thermal H_2 than non-thermal H_2 populations.

(3) High energy continuum radiation, produced primarily by accretion processes onto the host protostar, appear to play an important role in regulating the total density of non-thermal H_2 in the circumstellar environment. High energy FUV photons (912 Å $< \lambda <$ 1110 Å) and X-rays are effective at both grain heating and creating of free electrons, which can excite molecules to non-thermal states (Bergin et al. 2004), and I find correlations between both the X-ray and FUV luminosities and $N(H_2)_{\rm nLTE}$. I find little evidence that line emission from protostellar accretion processes play a significant role in regulating the total column densities of thermal and non-thermal H_2 states, except CIV, which appears to be anti-correlated with the total thermal column densities of H_2.

(4) There is a clear anti-correlation between $N(H_2)_{\rm nLTE}$ and H_2 dissociation continuum, suggesting that photo-excitation may be more effective at dissociating H_2 already in highly energized levels than lower energy thermal states.

(5) From one target that has access to cooler H_2 populations observed against the FUV continuum (RW Aur A; France et al. 2014b), I see a significant discrepancy between warm H_2 populations and the hot Lyα absorption populations. The total column of warm H_2 is several dex higher than the total column of hot H_2 in the Lyα wings. There is a crossing point between the warm and hot populations of H_2, where signatures of hot H_2 in the FUV continuum ($T_{exc} \approx$ 3,000 K) should be detected; however, observationally, this does not appear to be the case, as is shown in France et al. (2014b). HI-Lyα is a strong resonance, and a small amount of residual HI in the protostellar environment will scatter Lyα around the system many times before it escapes. It appears that the H_2 populations probed in the protostellar Lyα wings are not associated with the disk, but rather found in this tenuous haze of hot gas around the disk, since the hot H_2 populations are not seen in absorption against the FUV continuum (which will not scatter out of the line of sight as Lyα will and is a more likely tracer of the disk at a given observed geometry). The hot H_2 also probe much lower

column densities ($\langle N(H_2) \rangle \sim 10^{16}$ cm^{-2}) of H_2 than is required to produce the observe fluorescence in these same PPD samples ($N(H_2)_{fluor} \sim 10^{19}$ cm^{-2}; Herczeg et al. 2002, France et al. 2012c, Hoadley et al. 2015, McJunkin et al. 2016, Ádámkovics et al. 2016), strongly suggesting that absorption and fluorescence H_2 populations are not co-spatial.

5.2.3 Future Work

5.2.3.1 Temporal Evolution of Protoplanetary Disks: AA Tau

As shown in Chapter 2, AA Tau underwent a noticeable panchromatic dimming event at the end of 2011 (Figure 5.1). Luckily, data was obtained for AA Tau by *HST*/COS before and after the dimming event, which provided a natural testing bed to prove the concept of my Keplerian rotation models. Indeed, my models predicted AA Tau to have more H_2 emission from the outer disk, or material associated with the dimming obscuration. However, my models provided more information about the obscuration than I previously extracted.

The obscuration has been studied extensively to understand the nature and composition of material blocking the sightline to AA Tau (Zhang et al. 2015, Schneider et al. 2015). Schneider et al. (2015) and Hoadley et al. (2015) found that at least a portion of the H_2 emission coming from the AA Tau sightline in 2013 (dimming) must come from the obscuration, suggesting that the edge of the mass facing the protostar is being heated as it is exposed to the strong protostellar+accretion radiation field; Figure 5.2 shows how, while the obscuration blocks some of the H_2 flux coming from the innermost disk, the peak flux in all the lines has increased from the non-dim state (2011). Zhang et al. (2015) studied the changing emission profile of IR-CO at high resolution to determine the origin and behavior of the obscuration and found that the obscuration, as of 2012 - 2015, appeared to be located at $a \sim 8$ AU in the disk and moving towards the protostar at 8 km s^{-1}. While high-resolution data were necessary to determine the velocity of the obscuration, my Keplerian rotation models determined that the peak radius of H_2 emission in the obscured AA Tau dataset was $a \sim 3$ AU. When coupled with the red-shifted velocity of the material towards the protostar,

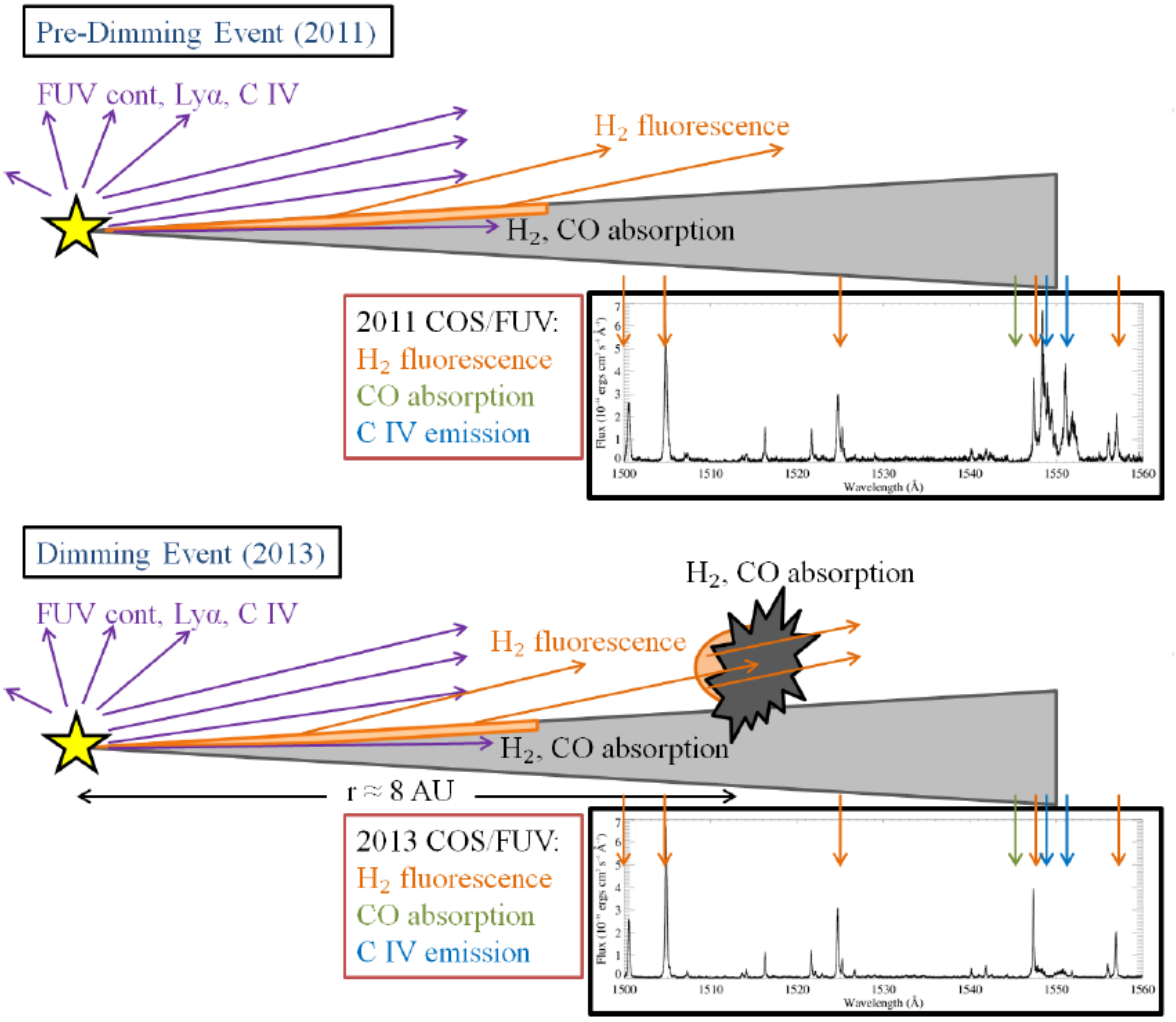

Figure 5.1 An illustration of observable stellar disk properties in AA Tau in 2011 and 2013. Included are spectra of interest during each COS/FUV epoch of AA Tau, which demonstrate how different emission and absorption features are affected by the presence of the "extra absorber." *Top figure:* An illustration of the emission, absorption, and continuum flux observed from AA Tau before the "extra absorber" occulted the view to the inner disk and protostar. H_2 fluorescence (in orange) is produced in the inner disk atmosphere irradiated by stellar Lyα photons. H_2 and CO absorption features are observed against stellar FUV photons penetrating the disk atmosphere. *Bottom figure:* All processes described above still take place in the AA Tau system, except now there is an "extra absorber" in the line of sight. The 'extra absorber" attenuates the FUV continuum and emission lines produced near the protostar. H_2 fluorescence line shapes change and extra flux is being produced in the cores of the lines for some H_2 ground states, meaning the "extra absorber" is not only blocking some of the emission from the inner disk molecules, but is also the site of additional fluorescence. H_2 and CO absorption should now be observed through the "extra absorber," placing important constraints of the H_2-to-CO and gas-to-dust ratios of the material.

my models also find that the H_2 emission from the obscuration appears to come from $a \sim 8$ AU.

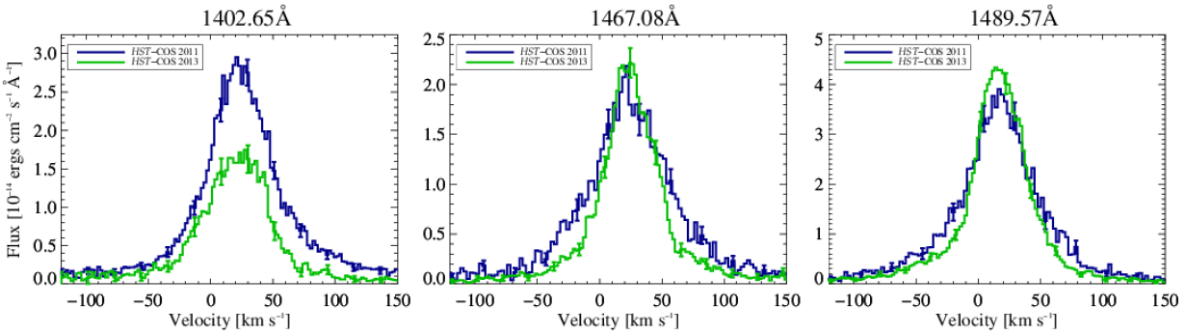

Figure 5.2 A direct comparison of H_2 emission lines from COS data of AA Tau taken in 2011 (pre-dimming; blue line) and 2013 (during dimming; green line). Comparing the evolution of the line shapes of H_2 in each progression will provide insights into the chemical evolution taking place in the mass as it travels closer to the the protostar, exposing it to stronger EUV/FUV radiation fields.

Continued monitoring of this obscuration is critical for helping in our current understanding of PPD mass transport and angular momentum exchange, and AA Tau, being well-studied before the dimming event, provides a natural astrophysical laboratory to explore and study these phenomena. I plan to continue monitoring the behavior of the H_2 fluorescence from this system as it remains in a dimming state with *HST*/COS in the GO Cycle 25 program. I am proposing to use the behavior of H_2 emission as a proxy to study the behavior and column density of H_2 in the obscuration. Assuming the emitting distribution of H_2 in the innermost disk stay roughly the same, the flux from the obscuration alone may be extrapolated from existing models of AA Tau pre-dimming. Using this information, I can assess whether the obscuring mass appears optically thin or thick in H_2, which will place important constraints on the density of the obscurer. Additionally, both the shape and absorption features in the AA Tau Lyα profile provide a means of probing the nature and composition of the obscurer, where I may be able to place additional constraints on the column density of HI and verify the inferred density of H_2 in the excess material.

5.2.3.2 Probing the Warm Molecular Disk Reservoir with *HST* & *JWST*

In my H_2 fluorescence study, I found that H_2 clears from the innermost disk as a function of warm dust dissipation. Assuming that the dusty disk evolves out of the innermost disk first, either by sublimating, settling out of the disk atmosphere and into the disk midplane, and/or growing into larger rubble, I speculated that H_2 evolves out of the system because the grain growth reformation site for H_2 is lost with the loss of small dust. Still, it remains unclear which physical mechanism(s) dominate the dissipation of gas from these systems and if the evolution of dust in planet-forming disks is a tell-tale sign of one or more of these mechanisms.

What, then, drives the dispersal of gas from these disks? There are two main mechanisms that may explain the fast dissipation of gas from the innermost planet-forming disk: photoevaporation and planet formation. In my H_2 study, the planet-formation scenario provides a convenient explanation for the loss of molecular gas from the inner disk. In Banzatti and Pontoppidan (2015), they relate the observed radii of IR-CO emission to observed semi-major axes of "hot Jupiter" exoplanets to explore how the evolution of gas from the inner disk may affect the architecture of planetary systems.

The overlap of UV-H_2 and IR-CO as separate diagnostics of molecular disk evolution in PPDs has provided a means of better interpreting the evolving nature of disks at different evolutionary phases. As a member of a *Hubble Space Telescope* Guest Observing Program for Cycle 24, I am a part of a small team looking to exploit the common characteristics of UV-H_2 and IR-CO in these systems to explore whether photoevaporation or planet formation dominate the dispersal of gas from these systems. Photoevaporative and planet formation mechanisms are expected to leave signature imprints on the density structure of planet-forming disks, as shown in Figure 5.3. Coincidentally, my Keplerian rotation models produce surface density and temperature maps of emitting H_2 fluorescence in the disk. While the physical structure of the disk was not meaningful to my analysis in Hoadley et al. (2015), I can re-define normalization factors to generalize the behavior of gas in the atmospheres of protoplanetary disks. In turn, this will provide at least a

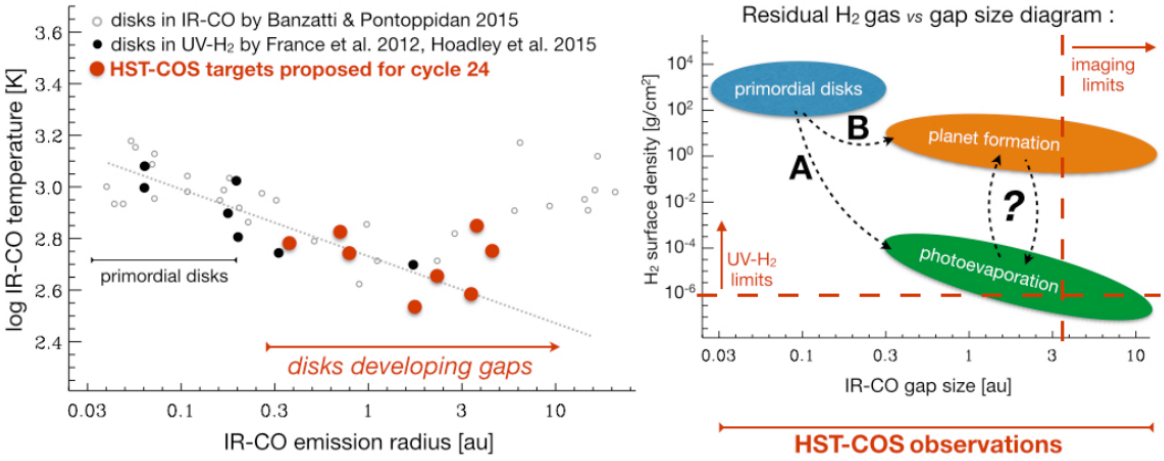

Figure 5.3 *Left:* A survey of IR-CO gas gaps measured in protoplanetary disks (Banzatti and Pontoppidan 2015). Disks shared from UV-H_2 studies are marked with solid black dots (France et al. 2012c, Hoadley et al. 2015). Disks whose IR-CO shows significant behavioral changes and will be investigated with UV-H_2 during the *HST* Cycle 24 GO Program are marked with solid red dots. *Right:* A diagram of measured residual gas vs. the gap size, where residual gas will be measured by UV-H_2. Distinguishing between the two disk dissipation paths is critical for understanding the evolutionary pathways of protoplanetary disks. The planet formation scenario favors pile-ups of Jupiter-mass planets with $a > 1$ AU (Alexander and Pascucci 2012) and in-situ formation of rocky planets as a function of decreasing gas-to-dust ratio (Gorti et al. 2015). The photoevaporation scenario provides gas to help sustain gas-rich protoplanetary atmospheres and encourages gas-drive migration of Jupiter-mass planets into the innermost disk (Masset and Papaloizou 2003, D'Angelo and Lubow 2008). (credit: A. Banzatti)

means of extracting the behavior of the physical structure of the disk gas, which will be helpful in pointing to which dissipation mechanism(s) are working to evaporate the gas from evolved PPDs.

Additionally, my Keplerian models can be modified to analyze emission profiles from other molecular tracers of the warm, inner planet-forming disk. With the commissioning of *JWST* in 2018, a powerful facility will be available to observe many rovibrational and band transitions of H_2, CO, water, and organic molecules with four orders of magnitude more sensitivity than *Spitzer* Houck et al. (2004), Martínez-Galarza et al. (2010). The medium-resolution mode of the *JWST*/Mid-Infrared Instrument (MIRI) will observe the terrestrial planet forming regions of PPDs, which I can use my Keplerian disk models to characterize the density distributions of gas from spectra taken with *HST* and *JWST* (for example, as illustrated for warm water diagnostics in Figure 5.4). The synthesis of UV and IR spectral diagnostics of warm molecules in PPDs will allow for analysis of the coupled behavior of the massive gas disk, traced with H_2 and CO, to the abundance of water at planet-forming radii. Understanding the structure and composition of multiple molecular diagnostics in the innermost PPD is critical to assess the formation and accretion of the first atmospheric constituents of planetary atmospheres.

5.2.3.3 The Origins of Non-thermal Molecular Hydrogen in Planet-forming Disk Environments

While my study of H_2 absorption signatures embedded in the stellar profiles of Lyα emission was extensive, I looked primarily at the column densities and behaviors of rovibrational levels of H_2 in each PPD sightline. Given the non-intuitive results from the study, a natural follow-up question remains: Where is this H_2 located in these circumstellar environments?

There are several empirical diagnostics I plan to explore to address the origins of H_2-Lyα absorption in these systems. The information from their velocity profiles - both in dispersion and relative offset to nearby H_2 emission features in wavelength space - may provide important clues about the turbulent/thermal structure in each sightline. When paired with disk parameters, such as the inclination angle, I may begin to address correlations which suggest certain origins of H_2 in

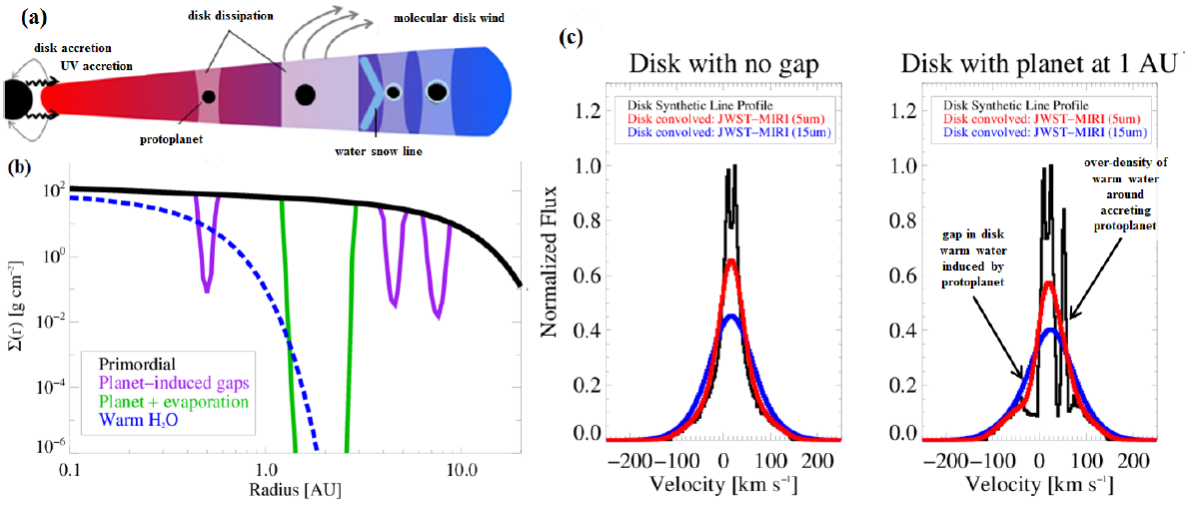

Figure 5.4 **(a)** Schematic of how planet formation is expected to affect the density of gas in PPDs Zhu et al. (2011). **(b)** Protoplanets create surface density gaps in the molecular disk that are several orders of magnitude lower than the unperturbed disk (black) Zhu et al. (2011). **(c)** My disk models show how protoplanets affect the synthetic emission features of molecules. Disks without planets (left) create smooth line profiles, while disks with a protoplanet (right) can show several signposts pointing to the presence of the planet. A gap can be carved out in the molecular disk around the planet, which creates a symmetric depletion of molecular emission in the line profile. Additionally, warm molecules can surround the planet in high densities as it accretes material, resulting in an asymmetric excess emission in the line profile where the planet is observed in the disk. Both features can be observed with the medium-resolution capabilities of *JWST*/MIRI.

the PPD environment. Additionally, using a "mirroring" technique, developed by Pascucci et al. (2011), of isolated H_2 absorption features, I can explore asymmetries in absorption profiles which may point to over-densities of absorbing H_2 in the circumstellar environment and identify possible disk locations the extra absorption arises from (e.g., accretion funnel onto the protostar). Furthermore, the distributions of H_2 populations in PPD environments determined in Chapter 3 point to very hot molecules at relatively low column densities. Using the thermal and radiatively-pumped distributions of H_2 developed for Chapter 3, I will look for traces of H_2 in the far-UV continuum of high S/N PPDs from $\lambda\lambda$ 1150 - 1200 Å. If evidence of H_2 absorption lies in the far-UV continuum of these sources, I have clues that may point to the hot H_2 being associated with disk material. If no evidence is found, the result points to hot H_2 probed by the resonant scattering of Lyα through a nebulous halo surrounding the protostar and planet-forming disk.

Finally, while seemingly unrelated, there are unidentified absorption signatures shared between PPD sightlines that I plan to identify and characterize. The species and inferred column densities of these signatures may help place important constraints on additional material in the sightline, such as whether they are of interstellar origin or if these atomic/molecular species are co-spatial with the observed H_2 absorption populations. If the latter, I may begin to explore what this means in the circumstellar environment, in terms of composition, density structure, and possible evolution through the lifetime of planet-forming disks.

5.3 A Full Molecular Inventory Through Terrestrial Planet-forming Regions with LUVOIR

Observations of planet-forming disks in the far-UV with the *Hubble Space Telescope* has revealed a wealth of knowledge about the warm gas reservoir, in both composition and evolution. Access to H_2 fluorescence tracers (e.g., Herczeg et al. 2002, France et al. 2012c, and this work) and the detection of warm (T $\sim$ 400 K) CO populations (e.g., France et al. 2011a; 2012b, Schindhelm et al. 2012a, McJunkin et al. 2013) have revolutionized our view of the complex structure and behavior of terrestrial planet-forming regions ($a < 10$ AU) that cannot be directly probed

(e.g., ALMA, VLT). However, these revelations have pushed *Hubble* to the limit of its capabilities and have required clever observational techniques to slowly break new ground (e.g., the *HST*/COS G130M λ1222 mode, allowing for detection down to λ 1065 Å (Penton et al. 2012; 2013)).

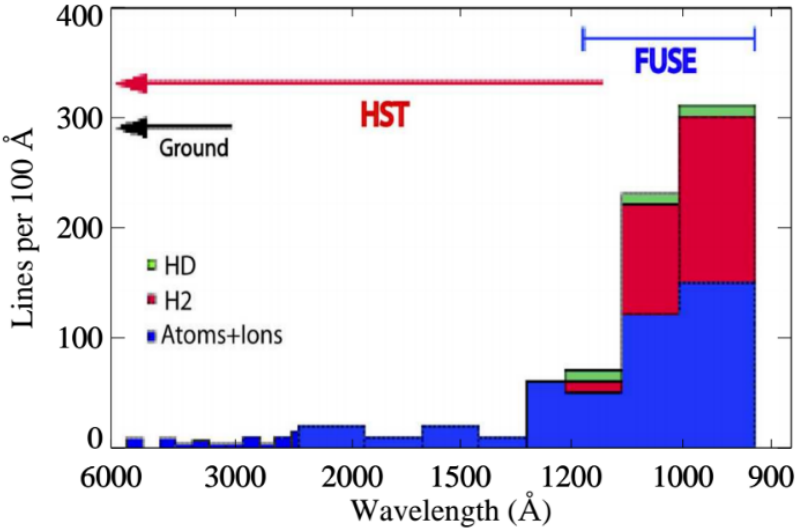

Figure 5.5 A histogram showing the density of spectral lines as a function of wavelengths (bin size $\approx$ 50 Å). The figure focuses on one molecular tracer - H_2 - but demonstrates the wealth of spectral features available at wavelengths currently difficult to observe or not observable with *HST*. (credit: *FUSE* website, Fleming et al. 2015)

There are a few major drawbacks about *Hubble* that halt further advancement in probing the full molecular inventory in terrestrial planet-forming regions of PPDs. First, *HST* was designed to detect light down to λ 1150 Å, a limit defined by the mirror coatings (Al+MgF_2) on the telescope. However, the "Lyman" UV ($\lambda\lambda$ 912 - 1216 Å) provides one of the richest bandpasses in the UV/Vis/IR regime, with hundreds of atomic, ionic, and molecular signatures (see Figure 5.5, adapted from the *FUSE* website and Fleming et al. 2015). By limiting the detection of molecular gas in PPDs to $\lambda > 1150$ Å, many important molecular tracers, like cool H_2 ($\lambda\lambda$ 900 - 1200 Å), water (H_2O: $\lambda > 1000$ Å) and methane (CH_4: $\lambda > 900$ Å), are excluded from the full inventory of molecular abundances and behavior in the innermost planet-forming disk. While detection down to λ 912 Å with *HST*/COS has been demonstrated, the sensitivity of the telescope diminishes significantly (McCandliss et al. 2010), making this mode insufficient to probe important molecular

constituents in PPDs. France et al. (2014a) demonstrated that the far-UV continuum of PPDs is detectable to $\lambda \sim 1060$ Å but were only able to analyze meaningful molecular signatures of $H_2(v'' = 0)$ from the region between $\lambda\lambda$ 1060 - 1150 Å for one PPD at a high inclination angle (edge-on orientation).

Additionally, the need for increased sensitivity for $\lambda < 1150$ Å must be paired with higher resolution to fully characterize the warm molecular reservoirs of PPDs. Molecular rovibrational bands have discrete electronic transitions, yet the energy difference between adjacent rotation states can be very small, which blends bands at lower resolution. Figure 5.6 demonstrates the absorption depths of several important molecular species in PPDs and how each molecular absorption structure appears throughout the far-UV. To successfully characterize the column densities and structure of warm molecular species in PPDs, high-resolution spectra are required to separate rotational states within a given band. However, the limiting factor for this drawback is the availability of high efficiency optical components, coatings, and detectors in the "Lyman" UV to create high sensitivity instruments. High-efficiency UV components are difficult to fabricate, and many technology development routes are being investigated to address this issue. One important role that sounding rocket instruments, like CHESS, play is the demonstration of these developing components in a space environment. Indeed, CHESS flew new UV gratings (the echelle and cross dispersing gratings) and a new far-UV detector technology (the cross-strip anode read-out) to demonstrate their performance in a space environment, in the hopes that the new, higher-efficiency UV components can be used in larger, future astronomical missions. Still, UV optics, coatings, and detectors have room to improve to efficiencies seen at $\lambda > 1150$ Å.

With a large enough space-based platform, however, even a moderate-performance UV instrument can gain enough sensitivity to properly explore the molecular inventory of warm gas in terrestrial planet-forming regions of PPDs from $\lambda\lambda$ 900 - 1200 Å. One of four major flagship mission concepts to be proposed to the Nation Academy of Sciences of the 2020 Astronomy and Astrophysics Decadal Survey is the Large UV/Optical/IR Surveyor (LUVOIR), which will provide a 9 - 16 meter-diameter space-based observatory for UV/Vis/IR astrophysics. Currently, there are 3 - 5

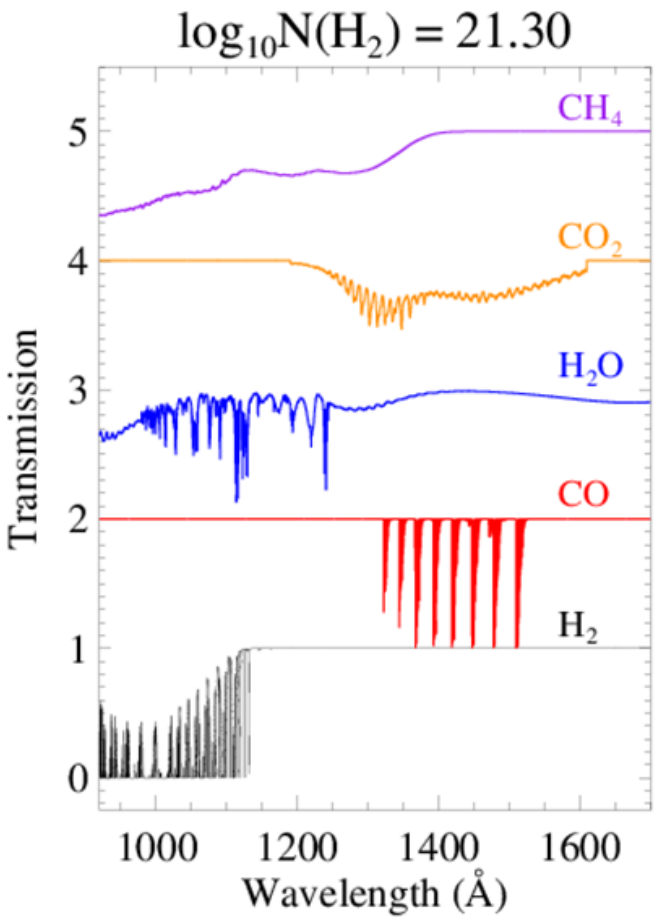

Figure 5.6 The absorption structure of trace molecules in planet-forming disks, assuming each is of fractional abundance to the total H_2 column density (defined as $\log_{10}N(H_2) = 21.3$). The fine structure of rovibrational bands is important to resolve to accurately estimate the column density of individual levels in the sightline, and most features can adequately be resolved with a spectrograph capable of R $\geq$ 120,000. (credit: K. France)

instruments being proposed for such a mission, with one being a dedicated UV multi-obect spectrograph/imager from $\lambda\lambda$ 1000 (stretch goal: 900) - 4000 Å (LUMOS, formerly CHISL; France et al. 2016a). The LUMOS instrument dedicates one channel to a CHESS-like high-resolution echelle spectrograph, which uses similar optical components to those demonstrated on sounding rocket experiments, like CHESS (for example, the toroidal-shaped cross dispersing grating and the cross-strip anode MCP detector read-out). I developed a first-draft preliminary design of the CHISL/LUMOS UV high-resolution mode from $\lambda\lambda$ 900 - 2000 Å with an average resolving power $\langle R(\lambda) \rangle \sim 120{,}000$.

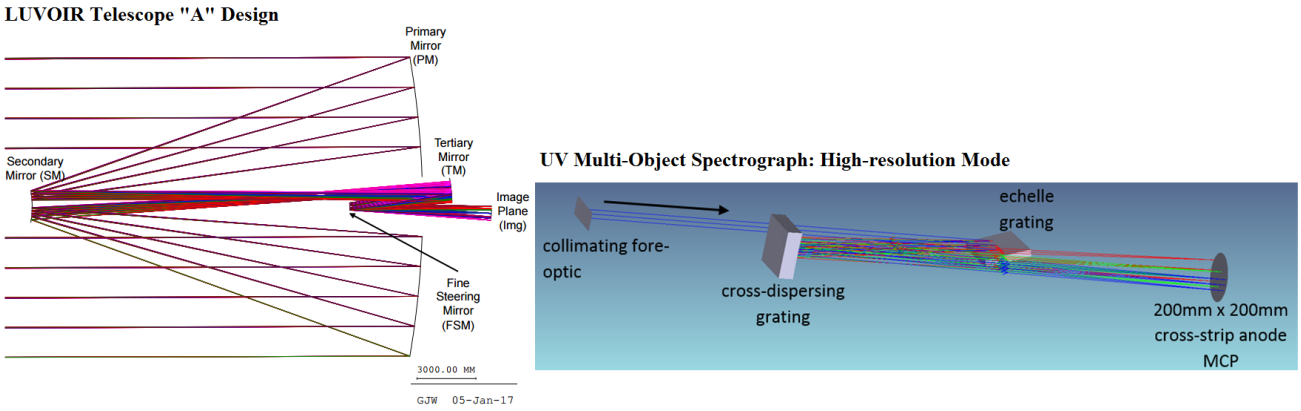

Figure 5.7 Raytraces of the current LUVOIR telescope design (for 16-m diameter primary; Bolcar, Feb. 2017, LUVOIR STDT) and the preliminary high-resolution channel of CHISL/LUMOS (France et al. 2016a).

The LUVOIR observatory is currently designed to have four telescope optics: the 16-meter primary (segmented) mirror, a secondary, tertiary, and flat pick-off mirror to direct light to individual instruments (raytrace is shown in Figure 5.7). The current orbital plan for LUVOIR is similar to *Hubble*, allowing for possible improvements and repairs to the telescope and instruments over the lifetime of the observatory. However, this limits on-target times to orbital revolution rates, which would be $t_{orb} \sim 90$ minutes. Given time required to move the telescope and settle on a given target, an exposure time estimate per orbit $t_{exp} \sim 40$ minutes $= 2400$ seconds. The LUMOS high-resolution spectrograph is currently designed as two grating elements (one high-dispersion (echelle) grating and one cross-dispersing grating) and a UV detector, as shown on the right in Figure 5.7. LUMOS is fed in light from LUVOIR by the fourth optical pick-off flat in the LUVOIR design. If the LU-

MOS high-resolution spectrograph has two grating elements and a detector with assumed uniform (over bandpass) efficiencies that reflect the best average performance optical elements measured to date ($E_{ech} \sim 50\%$, $E_{xdisp} \sim 50\%$, $DQE \sim 30\%$ for $\lambda\lambda$ 950 - 1200 Å) and all optical surfaces of LUMOS are coated with state-of-the-art UV coatings (e.g., "enhanced" Al+eLiF; Fleming et al. 2015), then the effective area ($A_{eff}(\lambda)$) of the high-resolution UV instrument on LUVOIR can be estimated as

$$\begin{aligned} A_{eff}(\lambda) &= \int_{\lambda} G(\lambda')d\lambda' \\ &= A_{geom} \times R(\lambda)^4 \times (E_{ech} \times R_{eLiF}(\lambda)) \times (E_{xdisp} \times R_{eLiF}(\lambda)) \times DQE \end{aligned} \tag{5.3}$$

where $G(\lambda')$ is the total efficiency (efficiency × reflectivity) of each optical component in the spectrograph pipeline, A_{geom} is the total effective collecting area of the primary mirror on LUVOIR, $R(\lambda)$ is the reflectivity of the telescope optics, which depends on the coating chosen, and $R_{eLiF}(\lambda)$ is the wavelength-dependent reflectivity of the "enhanced" Al+LiF UV coating.

Table 5.1 shows the properties of the current far-UV *HST* spectroscopic capabilities with COS and STIS, and includes the theoretical performance of different LUVOIR designs paired with the designed properties of the high-resolution channel of LUMOS. While the UV coating Al+eLiF is one of the best candidates for good UV performance on LUVOIR, the LUVOIR telescope itself is a multi-faceted facility, with 2 - 3 other instrument concepts to be included in the telescope (similar to the *HST* observatory). Therefore, coating the mirrors of LUVOIR with Al+eLiF may not be beneficial to other instruments and science goals of the observatory. To mitigate this contingency, I assume two case studies moving forward: 1. the LUVOIR telescope is coated with the same Al+MgF_2 as *HST*, to provide adequate reflectivity to UV science instruments and high reflectivity for $\lambda > 1150$ Å; and 2. the LUVOIR telescope is coated with the UV coating Al+eLiF to gain in UV reflectivity down to λ 1000 Å, resulting in $\lambda > 1150$ Å taking a few percent decrease in reflectivity, relative to Al+MgF_2.

I consider the scenario that I wish to characterize the molecular abundance in an arbitrary PPD candidate with an average observed far-UV continuum flux of $F_\lambda \sim 10^{-16}$ erg cm^{-2} s^{-1} Å^{-1}

Table 5.1. *HST* & LUVOIR UV Spectrographs: Specifications & Comparisons

Telescope:	Hubble Space Telescope[a]		LUVOIR[b]	
Primary Dia. (m)	2.4		9	16
Collection area (10^4 cm^2)	4.52		50.24[c]	135[c]
F#:	$f/24$		$f/20$[b]	$f/20$[b]
Spectral range:	1150 Å - 1.5 μm		1000 Å - 2.5 μm	
Stretch spectral range:[c]	(900 Å)		(900 Å - 5 μm)	
Spectrograph:	COS[a]	STIS[a]	LUMOS[b]	
Mode	FUV; G130M	FUV; E140H	FUV; H	
$\lambda\lambda$ (Å)	900 - 1775	1150 - 1700	(900)[d]1000 - 2000	
R ($\lambda/\Delta\lambda$)	13,000 - 17,000	114,000	$\geq$ 100,000	
⟨Spectral Thru-put⟩	4.5%	0.6%	3.7%[e]	
A_{eff} (cm^2):				
950 Å	20	–	15 / 30[f]	40 / 75[f]
1050 Å	40	–	360 / 9900[f]	1000 / 26,600[f]
1150 Å	1050	<20	17,900 / 14,200[f]	48,000 / 38,200[f]
1300 Å	3000	<140	15,800 / 9900[f]	43,500 / 26,600[f]

[a]Values taken from: STScI Spectrograph Handbooks and *HST* Spectrograph overviews: http://www.stsci.edu/hst.

[b]LUVOIR Telescope Properties: Bolcar, 2017, LUVOIR STDT. LUMOS properties: France et al. 2016a; AAS 229 COPAG SIG on LUMOS & HDI for LUVOIR.

[a]The LUVOIR collecting area estimates are not the total collecting area, assuming an unobscured primary mirror ($A_{coll} = 4\pi\left(\frac{d}{2}\right)^2$), but the *effective* collecting area of the primary mirrors (Bolcar, 2017, LUVOIR STDT). The effective collecting area takes into account the shape of the primary, segmentation of the aperture, and center obscuration for the secondary telescopic mirror.

[d]Stretch short wavelength goal for LUMOS.

[e]Calculated assuming spectrograph is made up for two grating + detector; average grating efficiency for both optics $\sim$ 50%, average UV coating reflectivity on the gratings $\sim$ 70%, and average detector DQE $\sim$ 30%.

[f]The total effective area of the LUMOS high-resolution channel was calculated assuming two scenarios: 1. (*left*) the main LUVOIR telescope assembly is coated with Al+MgF_2, while LUMOS optics are coated with the "enhanced" Al+LiF UV coating; 2. (*right*) every optical component (telescope + spectrograph) is coated with the "enhanced" Al+LiF UV coating.

from 950 - 1600 Å. If I desire to observe this object at high resolution (R $\geq$ 100,000 over the bandpass 950 - 1300 Å) and aim for a signal-to-noise (S/N) ratio of 10, what exposure time on-target do I need to achieve this over the "Lyman" UV, assuming the observed noise is dominated by photon noise? Another approach to this problem is: if I know how valuable observing time on LUVOIR will be and want to limit total exposure time to be favorable for selection (e.g., I want to keep my total exposure time to within 3 orbits of LUVOIR observing), then what is my expected S/N across the "Lyman" UV? The first two sections (1 and 2) of Table 5.2 present the expected exposure time (in number of orbits) and S/N of the observation, given the different telescope designs of LUVOIR and possible reflective coatings on the telescope. A couple of important observations can be made about the results from this simple exposure time calculation:

(1) Even with the UV-enhanced coating, λ 950 Å is still going to be difficult to observe with adequate S/N in a reasonable amount of time. This addresses the "stretch" goal of LUVOIR and LUMOS down to λ 900 Å; significant improvement in UV coatings and technology will be necessary to meet this goal.

(2) At λ 1050 Å, depending on the size of the LUVOIR primary mirror and the coating of the telescope, reasonable S/N or exposure time on target can be achieved to perform the science goals of the observation.

(3) For $\lambda > 1150$ Å with the smaller LUVOIR aperture, comparable S/N to what can currently be done with *HST*/COS is seen, except with a target flux 10$\times$ less than the sensitivity of COS and at higher spectral resolution ($R_{LUMOS} \sim$ 100,000 vs. $R_{COS} \sim$ 15,000; see Table 5.1).

It is clear that, even with the large aperture of LUVOIR, observing wavelengths of interest below λ 1000 Å will remain challenging. Currently, development of state-of-the-art fluoride UV protective coatings over aluminum have demonstrated a steep cut-off of optical reflectivity when approaching λ 1000 Å (e.g., Quijada et al. 2014, Fleming et al. 2015). Still, the current concept of

Table 5.2. Exposure Time and S/N Calculator for LUMOS (FUV; H) Observations[a]

	LUVOIR, 9-m Primary*		LUVOIR, 16-m Primary*	
	(Al+MgF_2)	(Al+eLiF)	(Al+MgF_2)	(Al+eLiF)
1. t_{exp} for S/N = 10 and $F_\lambda = 10^{-16}$ erg cm^{-2} s^{-1} Å^{-1}				
λ (Å)	t_{exp}[b]	t_{exp}[b]	t_{exp}[b]	t_{exp}[b]
950	6140	3070	2300	1230
1050	210	7.5	75	3.0
1150	3.5	4.5	1.5	1.5
1300	3.0	5.0	1.0	2.0
2. S/N for t_{exp} = 3 orbits and $F_\lambda = 10^{-16}$ erg cm^{-2} s^{-1} Å^{-1}				
λ (Å)	S/N[c]	S/N[c]	S/N[c]	S/N[c]
950	0.005	0.010	0.013	0.024
1050	0.14	3.9	0.40	10.6
1150	8.7	6.9	23.4	18.6
1300	9.9	6.2	27.1	16.6
3. $F_{\lambda,min}$ for t_{exp} = 3 orbits and $(S/N)_{min}$ = 10				
λ (Å)	F_{min}[d]	F_{min}[d]	F_{min}[d]	F_{min}[d]
950	2.0E-13	1.0E-13	7.7E-14	4.1E-14
1050	7.0E-15	2.5E-16	2.5E-15	9.5E-17
1150	1.2E-16	1.5E-16	4.3E-17	5.4E-17
1300	1.0E-16	1.6E-16	3.7E-17	6.0E-17

[a]All exposure time and S/N calculation assume the following: a) LUVOIR has a similar orbital configuration as *HST*, allowing for t_{max} per orbit = 45 min. Assuming orientation, maneuvers, etc., I assume that the exposure time on target t(1 orbit) = 40 min = 2400 sec. b) LUMOS is being used in high-resolution mode for all exposure calculations, such that R = 100,000 for all wavelengths considered.

[b]t_{exp} is quoted in units of orbits, such that 1 orbit = 2400 seconds of exposure time on target, and one full day includes 16 orbits.

[c]The expect S/N at λ, given the provided total exposure time and flux of the target at λ.

[d]The minimum F_λ to achieve S/N = 10 at the quoted exposure time on target. Units are in erg cm^{-2} s^{-1} Å^{-1}.

*Exposure time calculations were determined for the LUVOIR main telescope coated with: 1. Al+MgF_2, like *HST*, and 2. Al+eLiF, a good UV coating for $\lambda\lambda$ 1000 - 1150 Å, but under-performs Al+MgF_2 at longer wavelengths.

LUMOS and performance of optical coatings out to λ 1000 Å show great bounds in performance over what can be achieved with *HST*.

I performed one final calculation to better gauge the sensitivity limits of LUVOIR/LUMOS. If I want to look at a target to achieve a minimum S/N = 10 over a short exposure time (3 orbits), what does the flux of the target, as a function of wavelength, have to be to achieve this? This calculation provides an estimate of the minimum flux sensitivity of LUMOS as a function of wavelength, and is provided as the last section (3) of Table 5.2. These calculations, again, assume that LUMOS is being used in high-resolution mode, with R = 100,000 across the bandpass. Given the poor performance of UV coatings below λ 1000 Å, the sensitivity at λ 950 Å is comparable to the average sensitivity of, say, the *HST*/SITS FUV echelle modes. For $\lambda > 1000$ Å, it becomes apparent how powerful a tool the LUMOS spectrograph is compared with current UV facilities. Important molecular tracers from $\lambda\lambda$ 1000 - 1150 Å can be probed at the far-UV continuum flux level of typical PPDs in the Taurus-Auriga star forming region ($d \sim 120$ pc), where continuum fluxes are of order 10^{-15} erg cm^{-2} s^{-1} Å^{-1}.

Such a high-resolution, high-sensitivity instrument on LUVOIR has the capability to revolutionize our current understanding of the warm molecular PPD environment, including surveys of many disks over different evolutionary phases and orientations (inclination angles), which would infer the statistical abundances of important molecules through the lifetime of PPDs. Probing different regions of planet-forming disks, in particular different scale heights of gas above the disk mid-plane, is crucial to understand the physical processes leading to the evolution of molecules out of the disk and whether these processes remain throughout the lifetime of the disk or appear to turn "on" or "off" at critical phases in the disk, i.e. major accretion events, photoevaporation, or giant planet formation. By far, molecules have their strongest transitions in the UV, and photo-pumping of molecules to electronic states reveals not just which molecular species are in the PPD environment, but different populations of the same molecular species throughout different regions in and around the disk (e.g., cool/warm/hot H_2 from $\lambda\lambda$ 900 - 1120 Å, 1120 - 1600 Å, 1210 - 1220 Å (Lyα)). Access to multiple molecular species, particularly in absorption, for any

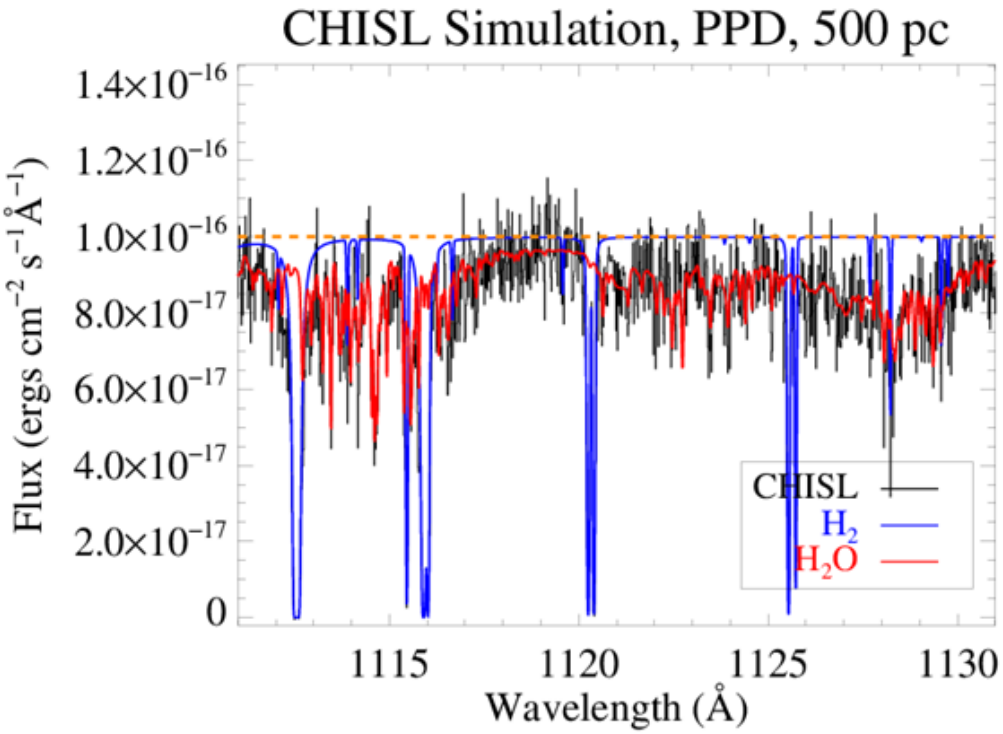

Figure 5.8 A simulation of the structure of the spectral sightline to an arbitrary PPD target, which shows abundances of both H_2 and H_2O over a small bandpass of the instrument. The flux continuum of the target is assumed to be $\sim 10^{-16}$ erg cm^{-2} s^{-1} Å^{-1}. With either design of LUVOIR (9-m or 16-m primary) and any choice of telescope coating, Table 5.2 shows that adequate S/N on such a target (S/N > 5) can be achieved over the course of 3 orbital exposure times on this target. Probing absorption signatures of trace molecules through different regions of planet-forming disks is critical for building up a statistical abundance measure of important molecules through the lifetime of PPDs, and a space observatory like LUVOIR (with LUMOS) has the potential to create this database. (credit: France et al. 2016a)

given PPD provides an immediate inventory and relative abundance fraction of important molecular constituents throughout the planet-forming disk; for example, H_2, H_2O, CO, CO_2, and CH_4 all have far-UV absorption signatures from $\lambda\lambda$ 900 - 1700 Å, and detection of each of these molecules against the protostellar far-UV continuum provides a means of determining the column density, and thus abundance, of the molecule in the disk environment. An example of such spectral overlap is shown in Figure 5.8 with H_2 and H_2O absorption signatures. While all of these molecules will be studied as emission tracers by *JWST* (via rovibrational transitions in the near- to mid-IR), these detections probe the disk atmosphere these lines form in. With LUVOIR, probing each molecular species in absorption for different disk orientations provides more information about different stratified layers in the planet-forming disk, which will place important constraints on the density, distribution, structure, and behavior of the molecular reservoirs throughout the disk lifetime and planet formation processes.

Bibliography

H. Abgrall, E. Roueff, F. Launay, J. Y. Roncin, and J. L. Subtil. Table of the Lyman Band System of Molecular Hydrogen. A&A, 101:273, October 1993a.

H. Abgrall, E. Roueff, F. Launay, J. Y. Roncin, and J. L. Subtil. Table of the Werner Band System of Molecular Hydrogen. A&A, 101:323, October 1993b.

M. Ádámkovics, J. R. Najita, and A. E. Glassgold. FUV Irradiated Disk Atmospheres: Lyα and the Origin of Hot H_2 Emission. ApJ, 817:82, January 2016. doi: 10.3847/0004-637X/817/1/82.

M. Agúndez, J. Cernicharo, and J. R. Goicoechea. Formation of simple organic molecules in inner T Tauri disks. A&A, 483:831–837, June 2008. doi: 10.1051/0004-6361:20077927.

Y. Aikawa and H. Nomura. Physical and Chemical Structure of Protoplanetary Disks with Grain Growth. ApJ, 642:1152–1162, May 2006. doi: 10.1086/501114.

R. L. Akeson, D. R. Ciardi, G. T. van Belle, and M. J. Creech-Eakman. Constraints on Circumstellar Disk Parameters from Multiwavelength Observations: T Tauri and SU Aurigae. ApJ, 566:1124–1131, February 2002. doi: 10.1086/338229.

R. L. Akeson, A. F. Boden, J. D. Monnier, R. Millan-Gabet, C. Beichman, J. Beletic, N. Calvet, L. Hartmann, L. Hillenbrand, C. Koresko, A. Sargent, and A. Tannirkulam. Keck Interferometer Observations of Classical and Weak-line T Tauri Stars. ApJ, 635:1173–1181, December 2005. doi: 10.1086/497436.

S. H. P. Alencar, C. H. F. Melo, C. P. Dullemond, J. Andersen, C. Batalha, L. P. R. Vaz, and R. D. Mathieu. The pre-main sequence spectroscopic binary AK Scorpii revisited. A&A, 409: 1037–1053, October 2003. doi: 10.1051/0004-6361:20031229.

D. R. Alexander, R. L. Rypma, and H. R. Johnson. Effect of molecules and grains on Rosseland mean opacities. ApJ, 272:773–780, September 1983. doi: 10.1086/161339.

R. Alexander, I. Pascucci, S. Andrews, P. Armitage, and L. Cieza. The Dispersal of Protoplanetary Disks. Protostars and Planets VI, pages 475–496, 2014. doi: 10.2458/azu_uapress_9780816531240-ch021.

R. D. Alexander and P. J. Armitage. Dust dynamics during protoplanetary disc clearing. MNRAS, 375:500–512, February 2007. doi: 10.1111/j.1365-2966.2006.11341.x.

R. D. Alexander and I. Pascucci. Deserts and pile-ups in the distribution of exoplanets due to photoevaporative disc clearing. MNRAS, 422:L82–L86, May 2012. doi: 10.1111/j.1745-3933.2012.01243.x.

R. D. Alexander, C. J. Clarke, and J. E. Pringle. Photoevaporation of protoplanetary discs - II. Evolutionary models and observable properties. MNRAS, 369:229–239, June 2006. doi: 10.1111/j.1365-2966.2006.10294.x.

ALMA Partnership. The 2014 ALMA Long Baseline Campaign: First Results from High Angular Resolution Observations toward the HL Tau Region. ApJL, 808:L3, July 2015. doi: 10.1088/2041-8205/808/1/L3.

P. Andre and T. Montmerle. From T Tauri stars to protostars: Circumstellar material and young stellar objects in the rho Ophiuchi cloud. ApJ, 420:837–862, January 1994. doi: 10.1086/173608.

S. M. Andrews and J. P. Williams. A Submillimeter View of Circumstellar Dust Disks in ρ Ophiuchi. ApJ, 671:1800–1812, December 2007. doi: 10.1086/522885.

S. M. Andrews, D. J. Wilner, C. Espaillat, A. M. Hughes, C. P. Dullemond, M. K. McClure, C. Qi, and J. M. Brown. Resolved Images of Large Cavities in Protoplanetary Transition Disks. ApJ, 732:42, May 2011. doi: 10.1088/0004-637X/732/1/42.

S. M. Andrews, K. A. Rosenfeld, A. L. Kraus, and D. J. Wilner. The Mass Dependence between Protoplanetary Disks and their Stellar Hosts. ApJ, 771:129, July 2013. doi: 10.1088/0004-637X/771/2/129.

S. M. Andrews, D. J. Wilner, Z. Zhu, T. Birnstiel, J. M. Carpenter, L. M. Pérez, X.-N. Bai, K. I. Öberg, A. M. Hughes, A. Isella, and L. Ricci. Ringed Substructure and a Gap at 1 au in the Nearest Protoplanetary Disk. ApJL, 820:L40, April 2016. doi: 10.3847/2041-8205/820/2/L40.

D. R. Ardila, G. Basri, F. M. Walter, J. A. Valenti, and C. M. Johns-Krull. Observations of T Tauri Stars using Hubble Space Telescope GHRS. I. Far-Ultraviolet Emission Lines. ApJ, 566:1100–1123, February 2002. doi: 10.1086/338223.

D. R. Ardila, G. J. Herczeg, S. G. Gregory, L. Ingleby, K. France, A. Brown, S. Edwards, C. Johns-Krull, J. L. Linsky, H. Yang, J. A. Valenti, H. Abgrall, R. D. Alexander, E. Bergin, T. Bethell, J. M. Brown, N. Calvet, C. Espaillat, L. A. Hillenbrand, G. Hussain, E. Roueff, E. R. Schindhelm, and F. M. Walter. Hot Gas Lines in T Tauri Stars. ApJS, 207:1, July 2013. doi: 10.1088/0067-0049/207/1/1.

P. J. Armitage, C. J. Clarke, and F. Palla. Dispersion in the lifetime and accretion rate of T Tauri discs. MNRAS, 342:1139–1146, July 2003. doi: 10.1046/j.1365-8711.2003.06604.x.

G. C. Augason. The Formation of Interstellar Molecular Hydrogen by Physical Adsorption on Grains. ApJ, 162:463, November 1970. doi: 10.1086/150679.

B. A. Ayliffe and M. R. Bate. Planet migration: self-gravitating radiation hydrodynamical models of protoplanets with surfaces. MNRAS, 408:876–896, October 2010. doi: 10.1111/j.1365-2966.2010.17221.x.

T. R. Ayres. VizieR Online Data Catalog: StarCAT: STIS UV echelle spectra of stars (Ayres, 2010). VizieR Online Data Catalog, 218, April 2010.

X.-N. Bai. Towards a Global Evolutionary Model of Protoplanetary Disks. ApJ, 821:80, April 2016. doi: 10.3847/0004-637X/821/2/80.

K. Baillié, S. Charnoz, and É. Pantin. Time evolution of snow regions and planet traps in an evolving protoplanetary disk. ArXiv e-prints, March 2015.

J. Bally, W. D. Langer, A. A. Stark, and R. W. Wilson. Filamentary structure in the Orion molecular cloud. ApJL, 312:L45–L49, January 1987. doi: 10.1086/184817.

A. Banzatti and K. M. Pontoppidan. An Empirical Sequence of Disk Gap Opening Revealed by Rovibrational CO. ApJ, 809:167, August 2015. doi: 10.1088/0004-637X/809/2/167.

P. J. Barnes, A. K. Hernandez, S. N. O'Dougherty, W. J. Schap, III, and E. Muller. The Galactic Census of High- and Medium-mass Protostars. III ^{12}CO Maps and Physical Properties of Dense Clump Envelopes and their Embedding GMCs. ArXiv e-prints, September 2016.

M. Beasley, C. Boone, N. Cunningham, J. Green, and E. Wilkinson. Imaging Spectrograph for Interstellar Shocks: A Narrowband Imaging Payload for the Far Ultraviolet. Applied Optics, 43: 4633–4642, August 2004.

M. Beasley, E. Burgh, and K. France. Colorado High-resolution Echelle Stellar Spectrograph (CHESS). In Space Telescopes and Instrumentation 2010: Ultraviolet to Gamma Ray, volume 7732 of Proc. SPIE, page 773206, July 2010.

T. L. Beck, J. S. Bary, A. Dutrey, V. Piétu, S. Guilloteau, S. H. Lubow, and M. Simon. Circumbinary Gas Accretion onto a Central Binary: Infrared Molecular Hydrogen Emission from GG Tau A. ApJ, 754:72, July 2012. doi: 10.1088/0004-637X/754/1/72.

S. Beckwith and B. Zuckerman. Molecular hydrogen emission from W51. ApJ, 255:536–540, April 1982. doi: 10.1086/159854.

S. Beckwith, I. Gatley, K. Matthews, and G. Neugebauer. Molecular hydrogen emission from T Tauri stars. ApJL, 223:L41–L43, July 1978. doi: 10.1086/182723.

S. Beckwith, N. J. Evans, II, I. Gatley, G. Gull, and R. W. Russell. Observations of the extinction and excitation of the molecular hydrogen emission in Orion. ApJ, 264:152–160, January 1983. doi: 10.1086/160583.

E. Bergin, N. Calvet, M. L. Sitko, H. Abgrall, P. D'Alessio, G. J. Herczeg, E. Roueff, C. Qi, D. K. Lynch, R. W. Russell, S. M. Brafford, and R. B. Perry. A New Probe of the Planet-forming Region in T Tauri Disks. ApJL, 614:L133–L136, October 2004. doi: 10.1086/425865.

E. A. Bergin, F. Du, L. I. Cleeves, G. A. Blake, K. Schwarz, R. Visser, and K. Zhang. Hydrocarbon Emission Rings in Protoplanetary Disks Induced by Dust Evolution. ApJ, 831:101, November 2016. doi: 10.3847/0004-637X/831/1/101.

C. Bertout, G. Basri, and J. Bouvier. Accretion disks around T Tauri stars. ApJ, 330:350–373, July 1988. doi: 10.1086/166476.

C. Bertout, N. Robichon, and F. Arenou. Revisiting Hipparcos data for pre-main sequence stars. A&A, 352:574–586, December 1999.

T. J. Bethell and E. A. Bergin. The Propagation of Lyα in Evolving Protoplanetary Disks. ApJ, 739:78, October 2011. doi: 10.1088/0004-637X/739/2/78.

R. Bieri, Y. Dubois, J. Silk, and G. A. Mamon. Playing with Positive Feedback: External Pressure-triggering of a Star-forming Disk Galaxy. ApJL, 812:L36, October 2015. doi: 10.1088/2041-8205/812/2/L36.

F. Bigiel, A. Leroy, F. Walter, E. Brinks, W. J. G. de Blok, B. Madore, and M. D. Thornley. The Star Formation Law in Nearby Galaxies on Sub-Kpc Scales. AJ, 136:2846–2871, December 2008. doi: 10.1088/0004-6256/136/6/2846.

J. H. Black and A. Dalgarno. Models of interstellar clouds. I - The Zeta Ophiuchi cloud. ApJ, 34: 405–423, July 1977. doi: 10.1086/190455.

J. H. Black and S. P. Willner. Interstellar absorption lines in the infrared spectrum of NGC 2024 IRS 2. ApJ, 279:673–678, April 1984. doi: 10.1086/161930.

J. H. Black, E. F. van Dishoeck, S. P. Willner, and R. C. Woods. Interstellar absorption lines toward NGC 2264 and AFGL 2591 - Abundances of H2, H3(+), and CO. ApJ, 358:459–467, August 1990. doi: 10.1086/168999.

J. Blum. Grain Growth and Coagulation. In A. N. Witt, G. C. Clayton, and B. T. Draine, editors, Astrophysics of Dust, volume 309 of Astronomical Society of the Pacific Conference Series, page 369, May 2004.

J. Blum and G. Wurm. Experiments on Sticking, Restructuring, and Fragmentation of Preplanetary Dust Aggregates. Icarus, 143:138–146, January 2000. doi: 10.1006/icar.1999.6234.

J. Blum, R. Schräpler, B. J. R. Davidsson, and J. M. Trigo-Rodríguez. The Physics of Protoplanetesimal Dust Agglomerates. I. Mechanical Properties and Relations to Primitive Bodies in the Solar System. ApJ, 652:1768–1781, December 2006. doi: 10.1086/508017.

P. Bodenheimer and A. Sweigart. Dynamic Collapse of the Isothermal Sphere. ApJ, 152:515, May 1968. doi: 10.1086/149568.

R. C. Bohlin, B. D. Savage, and J. F. Drake. A survey of interstellar H I from L-alpha absorption measurements. II. ApJ, 224:132–142, August 1978. doi: 10.1086/156357.

R. C. Bohlin, E. B. Jenkins, L. Spitzer, Jr., D. G. York, J. K. Hill, B. D. Savage, and T. P. Snow, Jr. A survey of ultraviolet interstellar absorption lines. ApJS, 51:277–308, March 1983.

T. Böhm, C. Catala, L. Balona, and B. Carter. Spectroscopic monitoring of the Herbig Ae star HD 104237. I. Multiperiodic stellar oscillations. A&A, 427:907–922, December 2004. doi: 10.1051/0004-6361:20041227.

S. Boissier, N. Prantzos, A. Boselli, and G. Gavazzi. The star formation rate in disc galaxies: thresholds and dependence on gas amount. MNRAS, 346:1215–1230, December 2003. doi: 10.1111/j.1365-2966.2003.07170.x.

J. S. Bolton and M. G. Haehnelt. The observed ionization rate of the intergalactic medium and the ionizing emissivity at z >= 5: evidence for a photon-starved and extended epoch of reionization. 382:325–341, November 2007. doi: 10.1111/j.1365-2966.2007.12372.x.

W. F. Bottke, R. J. Walker, J. M. D. Day, D. Nesvorny, and L. Elkins-Tanton. Stochastic Late Accretion to Earth, the Moon, and Mars. Science, 330:1527, December 2010. doi: 10.1126/science.1196874.

J. Bouvier. Rotation in T Tauri stars. II - Clues for magnetic activity. AJ, 99:946–964, March 1990. doi: 10.1086/115386.

J. Bouvier, A. Chelli, S. Allain, L. Carrasco, R. Costero, I. Cruz-Gonzalez, C. Dougados, M. Fernández, E. L. Martín, F. Ménard, C. Mennessier, R. Mujica, E. Recillas, L. Salas, G. Schmidt, and R. Wichmann. Magnetospheric accretion onto the T Tauri star AA Tauri. I. Constraints from multisite spectrophotometric monitoring. A&A, 349:619–635, September 1999.

J. Bouvier, K. Grankin, L. E. Ellerbroek, H. Bouy, and D. Barrado. AA Tauri's sudden and long-lasting deepening: enhanced extinction by its circumstellar disk. A&A, 557:A77, September 2013. doi: 10.1051/0004-6361/201321389.

J. C. Brown, J. P. Cassinelli, and M. Maheswaran. Magnetically Fed Hot Star Keplerian Disks with Slow Outflow. ApJ, 688:1320–1325, December 2008. doi: 10.1086/592558.

J. M. Brown, G. A. Blake, C. Qi, C. P. Dullemond, D. J. Wilner, and J. P. Williams. Evidence for Dust Clearing Through Resolved Submillimeter Imaging. ApJ, 704:496–502, October 2009. doi: 10.1088/0004-637X/704/1/496.

J. M. Brown, K. M. Pontoppidan, E. F. van Dishoeck, G. J. Herczeg, G. A. Blake, and A. Smette. VLT-CRIRES Survey of Rovibrational CO Emission from Protoplanetary Disks. ApJ, 770:94, June 2013. doi: 10.1088/0004-637X/770/2/94.

E. B. Burgh, K. France, and S. R. McCandliss. Direct Measurement of the Ratio of Carbon Monoxide to Molecular Hydrogen in the Diffuse Interstellar Medium. ApJ, 658:446–454, March 2007. doi: 10.1086/511259.

E. B. Burgh, K. France, and E. B. Jenkins. Atomic and Molecular Carbon as a Tracer of Translucent Clouds. ApJ, 708:334–341, January 2010. doi: 10.1088/0004-637X/708/1/334.

K. J. Burleigh, J. H. Bieging, A. Chromey, C. Kulesa, and W. L. Peters. The Arizona Radio Observatory CO Mapping Survey of Galactic Molecular Clouds. III. The Serpens Cloud in CO J = 2-1 and ^{13}CO J = 2-1 Emission. ApJ, 209:39, December 2013. doi: 10.1088/0067-0049/209/2/39.

N. Calvet, P. D'Alessio, L. Hartmann, D. Wilner, A. Walsh, and M. Sitko. Evidence for a Developing Gap in a 10 Myr Old Protoplanetary Disk. ApJ, 568:1008–1016, April 2002. doi: 10.1086/339061.

N. Calvet, P. D'Alessio, D. M. Watson, R. Franco-Hernández, E. Furlan, J. Green, P. M. Sutter, W. J. Forrest, L. Hartmann, K. I. Uchida, L. D. Keller, B. Sargent, J. Najita, T. L. Herter, D. J. Barry, and P. Hall. Disks in Transition in the Taurus Population: Spitzer IRS Spectra of GM Aurigae and DM Tauri. ApJL, 630:L185–L188, September 2005. doi: 10.1086/491652.

J. S. Carr and J. R. Najita. Organic Molecules and Water in the Planet Formation Region of Young Circumstellar Disks. Science, 319:1504–, March 2008. doi: 10.1126/science.1153807.

J. S. Carr and J. R. Najita. Organic Molecules and Water in the Inner Disks of T Tauri Stars. ApJ, 733:102, June 2011. doi: 10.1088/0004-637X/733/2/102.

J. S. Carr, A. T. Tokunaga, and J. Najita. Hot H_2O Emission and Evidence for Turbulence in the Disk of a Young Star. ApJ, 603:213–220, March 2004. doi: 10.1086/381356.

G. R. Carruthers. Rocket Observation of Interstellar Molecular Hydrogen. ApJL, 161:L81, August 1970. doi: 10.1086/180575.

G. R. Carruthers. Far-Ultraviolet Spectra and Photometry of Perseus Stars. ApJ, 166:349, June 1971. doi: 10.1086/150964.

D. C. Cartwright and S. Drapatz. Equivalent widths and optimum regions of space for the detection of interstellar H_2^+. A&A, 4:443–451, March 1970.

P. Cassen. Utilitarian models of the solar nebula. Icarus, 112:405–429, December 1994. doi: 10.1006/icar.1994.1195.

S. Cazaux and A. G. G. M. Tielens. H_2 Formation on Grain Surfaces. ApJ, 604:222–237, March 2004. doi: 10.1086/381775.

P. C. Clark and S. C. O. Glover. On column density thresholds and the star formation rate. MNRAS, 444:2396–2414, November 2014. doi: 10.1093/mnras/stu1589.

C. J. Clarke, A. Gendrin, and M. Sotomayor. The dispersal of circumstellar discs: the role of the ultraviolet switch. MNRAS, 328:485–491, December 2001. doi: 10.1046/j.1365-8711.2001.04891.x.

B. Clément, J.-G. Cuby, F. Courbin, A. Fontana, W. Freudling, J. Fynbo, J. Gallego, P. Hibon, J.-P. Kneib, O. Le Fèvre, C. Lidman, R. McMahon, B. Milvang-Jensen, P. Moller, A. Moorwood, K. K. Nilsson, L. Pentericci, B. Venemans, V. Villar, and J. Willis. Evolution of the observed Lyα luminosity function from z = 6.5 to z = 7.7: evidence for the epoch of reionization? 538: A66, February 2012. doi: 10.1051/0004-6361/201117312.

D. Coffey, F. Bacciotti, J. Woitas, T. P. Ray, and J. Eislöffel. Rotation of Jets from Young Stars: New Clues from the Hubble Space Telescope Imaging Spectrograph. ApJ, 604:758–765, April 2004. doi: 10.1086/382019.

F. Comerón and M. Fernández. High-resolution visible spectroscopy of the jet-driving star Th 28. A&A, 511:A10, February 2010. doi: 10.1051/0004-6361/200912959.

F. Comerón, M. Fernández, I. Baraffe, R. Neuhäuser, and A. A. Kaas. New low-mass members of the Lupus 3 dark cloud: Further indications of pre-main-sequence evolution strongly affected by accretion. A&A, 406:1001–1017, August 2003. doi: 10.1051/0004-6361:20030848.

S. Correia, H. Zinnecker, T. Ratzka, and M. F. Sterzik. A VLT/NACO survey for triple and quadruple systems among visual pre-main sequence binaries. A&A, 459:909–926, December 2006. doi: 10.1051/0004-6361:20065545.

J. N. Cuzzi, R. C. Hogan, J. M. Paque, and A. R. Dobrovolskis. Size-selective Concentration of Chondrules and Other Small Particles in Protoplanetary Nebula Turbulence. ApJ, 546:496–508, January 2001. doi: 10.1086/318233.

E. Daddi, H. Dannerbauer, D. Liu, M. Aravena, F. Bournaud, F. Walter, D. Riechers, G. Magdis, M. Sargent, M. Béthermin, C. Carilli, A. Cibinel, M. Dickinson, D. Elbaz, Y. Gao, R. Gobat, J. Hodge, and M. Krips. CO excitation of normal star-forming galaxies out to z = 1.5 as regulated by the properties of their interstellar medium. A&A, 577:A46, May 2015. doi: 10.1051/0004-6361/201425043.

J. E. Dale, B. Ercolano, and I. A. Bonnell. Ionization-induced star formation - IV. Triggering in bound clusters. MNRAS, 427:2852–2865, December 2012. doi: 10.1111/j.1365-2966.2012.22104.x.

P. D'Alessio, N. Calvet, L. Hartmann, S. Lizano, and J. Cantó. Accretion Disks around Young Objects. II. Tests of Well-mixed Models with ISM Dust. ApJ, 527:893–909, December 1999. doi: 10.1086/308103.

P. D'Alessio, N. Calvet, L. Hartmann, R. Franco-Hernández, and H. Servín. Effects of Dust Growth and Settling in T Tauri Disks. ApJ, 638:314–335, February 2006. doi: 10.1086/498861.

A. Dalgarno and W. G. Roberge. Collision-induced dissociation of interstellar molecules. ApJL, 233:L25–L27, October 1979. doi: 10.1086/183069.

A. Dalgarno and T. L. Stephens. Discrete Absorption and Photodissociation of Molecular Hydrogen. ApJL, 160:L107, May 1970. doi: 10.1086/180539.

T. M. Dame, D. Hartmann, and P. Thaddeus. The Milky Way in Molecular Clouds: A New Complete CO Survey. ApJ, 547:792–813, February 2001. doi: 10.1086/318388.

C. W. Danforth, J. T. Stocke, and J. M. Shull. Broad H I Absorbers as Metallicity-independent Tracers of the Warm-Hot Intergalactic Medium. ApJ, 710:613–633, February 2010. doi: 10.1088/0004-637X/710/1/613.

G. D'Angelo and S. H. Lubow. Evolution of Migrating Planets Undergoing Gas Accretion. ApJ, 685:560-583, September 2008. doi: 10.1086/590904.

A. Diplas and B. D. Savage. An IUE survey of interstellar H I LY alpha absorption. 1: Column densities. ApJ, 93:211–228, July 1994. doi: 10.1086/192052.

S. E. Dodson-Robinson and C. Salyk. Transitional Disks as Signposts of Young, Multiplanet Systems. ApJ, 738:131, September 2011. doi: 10.1088/0004-637X/738/2/131.

C. Dominik and A. G. G. M. Tielens. The Physics of Dust Coagulation and the Structure of Dust Aggregates in Space. ApJ, 480:647–673, May 1997. doi: 10.1086/303996.

B. Donehew and S. Brittain. Measuring the Stellar Accretion Rates of Herbig Ae/Be Stars. AJ, 141:46, February 2011. doi: 10.1088/0004-6256/141/2/46.

R. Dong, Z. Zhu, and B. Whitney. Observational Signatures of Planets in Protoplanetary Disks I. Gaps Opened by Single and Multiple Young Planets in Disks. ApJ, 809:93, August 2015. doi: 10.1088/0004-637X/809/1/93.

J. Donovan Meyer, J. Koda, R. Momose, M. Fukuhara, T. Mooney, S. Towers, F. Egusa, R. Kennicutt, N. Kuno, M. Carty, T. Sawada, and N. Scoville. Resolved Measurements of X $_{CO}$ in NGC 6946. ApJ, 744:42, January 2012. doi: 10.1088/0004-637X/744/1/42.

B. T. Draine. Physics of the Interstellar and Intergalactic Medium. 2011.

B. T. Draine and F. Bertoldi. Structure of Stationary Photodissociation Fronts. ApJ, 468:269, September 1996. doi: 10.1086/177689.

C. P. Dullemond and J. D. Monnier. The Inner Regions of Protoplanetary Disks. ARA&A, 48: 205–239, September 2010. doi: 10.1146/annurev-astro-081309-130932.

C. P. Dullemond, D. Hollenbach, I. Kamp, and P. D'Alessio. Models of the Structure and Evolution of Protoplanetary Disks. Protostars and Planets V, pages 555–572, 2007.

R. H. Durisen, K. Cai, A. C. Mejía, and M. K. Pickett. A hybrid scenario for gas giant planet formation in rings. Icarus, 173:417–424, February 2005. doi: 10.1016/j.icarus.2004.08.003.

D. J. Eden, T. J. T. Moore, J. S. Urquhart, D. Elia, R. Plume, A. J. Rigby, and M. A. Thompson. Star formation scales and efficiency in Galactic spiral arms. MNRAS, 452:289–300, September 2015. doi: 10.1093/mnras/stv1323.

J. A. Eisner, L. A. Hillenbrand, R. J. White, J. S. Bloom, R. L. Akeson, and C. H. Blake. Near-Infrared Interferometric, Spectroscopic, and Photometric Monitoring of T Tauri Inner Disks. ApJ, 669:1072–1084, November 2007. doi: 10.1086/521874.

B. G. Elmegreen. On the Rapid Collapse and Evolution of Molecular Clouds. ApJ, 668:1064–1082, October 2007. doi: 10.1086/521327.

P. J. Encrenaz, E. Falgarone, and R. Lucas. CO, dust and H2 in the molecular cloud near rho Ophiuchi. A&A, 44:73–80, November 1975.

C. Espaillat, N. Calvet, P. D'Alessio, E. Bergin, L. Hartmann, D. Watson, E. Furlan, J. Najita, W. Forrest, M. McClure, B. Sargent, C. Bohac, and S. T. Harrold. Probing the Dust and Gas in the Transitional Disk of CS Cha with Spitzer. ApJL, 664:L111–L114, August 2007a. doi: 10.1086/520879.

C. Espaillat, N. Calvet, P. D'Alessio, J. Hernández, C. Qi, L. Hartmann, E. Furlan, and D. M. Watson. On the Diversity of the Taurus Transitional Disks: UX Tauri A and LkCa 15. ApJL, 670:L135–L138, December 2007b. doi: 10.1086/524360.

C. Espaillat, E. Furlan, P. D'Alessio, B. Sargent, E. Nagel, N. Calvet, D. M. Watson, and J. Muzerolle. A Spitzer IRS Study of Infrared Variability in Transitional and Pre-transitional Disks Around T Tauri Stars. ApJ, 728:49, February 2011. doi: 10.1088/0004-637X/728/1/49.

C. Espaillat, J. Muzerolle, J. Najita, S. Andrews, Z. Zhu, N. Calvet, S. Kraus, J. Hashimoto, A. Kraus, and P. D'Alessio. An Observational Perspective of Transitional Disks. Protostars and Planets VI, pages 497–520, 2014. doi: 10.2458/azu_uapress_9780816531240-ch022.

D. Fedele, M. E. van den Ancker, T. Henning, R. Jayawardhana, and J. M. Oliveira. Timescale of mass accretion in pre-main-sequence stars. A&A, 510:A72, February 2010. doi: 10.1051/0004-6361/200912810.

S. R. Federman, A. E. Glassgold, E. B. Jenkins, and E. J. Shaya. The abundance of CO in diffuse interstellar clouds - an ultraviolet survey. ApJ, 242:545–559, December 1980.

E. D. Feigelson, W. A. Lawson, and G. P. Garmire. The ϵ Chamaeleontis Young Stellar Group and the Characterization of Sparse Stellar Clusters. ApJ, 599:1207–1222, December 2003. doi: 10.1086/379365.

J. Ferreira, C. Dougados, and S. Cabrit. Which jet launching mechanism(s) in T Tauri stars? A&A, 453:785–796, July 2006. doi: 10.1051/0004-6361:20054231.

G. B. Field, W. B. Somerville, and K. Dressler. Hydrogen Molecules in Astronomy. ARA&A, 4: 207, 1966. doi: 10.1146/annurev.aa.04.090166.001231.

B. Fleming, K. France, R. E. Lupu, and S. R. McCandliss. Spitzer Mapping of Polycyclic Aromatic Hydrocarbon and H_2 Features in Photodissociation Regions. ApJ, 725:159–172, December 2010. doi: 10.1088/0004-637X/725/1/159.

B. T. Fleming, M. A. Quijada, K. France, K. Hoadley, J. Del Hoyo, and N. Kruczek. New UV instrumentation enabled by enhanced broadband reflectivity lithium fluoride coatings. In UV, X-Ray, and Gamma-Ray Space Instrumentation for Astronomy XIX, volume 9601 of Proc. SPIE, page 96010R, August 2015. doi: 10.1117/12.2190556.

D. R. Flower and G. J. Harris. Three-body recombination of hydrogen during primordial star formation. MNRAS, 377:705–710, May 2007. doi: 10.1111/j.1365-2966.2007.11632.x.

J. K. J. Fogel, T. J. Bethell, E. A. Bergin, N. Calvet, and D. Semenov. Chemistry of a Protoplanetary Disk with Grain Settling and Lyα Radiation. ApJ, 726:29, January 2011. doi: 10.1088/0004-637X/726/1/29.

D. Foreman-Mackey, D. W. Hogg, D. Lang, and J. Goodman. emcee: The MCMC Hammer. PASP, 125:306–312, March 2013. doi: 10.1086/670067.

K. France and S. R. McCandliss. Molecular Hydrogen in Orion as Observed by the Far Ultraviolet Spectroscopic Explorer. ApJL, 629:L97–L100, August 2005. doi: 10.1086/462404.

K. France, A. Roberge, R. E. Lupu, S. Redfield, and P. D. Feldman. A Low-Mass H_2 Component to the AU Microscopii Circumstellar Disk. ApJ, 668:1174–1181, October 2007. doi: 10.1086/521348.

K. France, E. Schindhelm, E. B. Burgh, G. J. Herczeg, G. M. Harper, A. Brown, J. C. Green, J. L. Linsky, H. Yang, H. Abgrall, D. R. Ardila, E. Bergin, T. Bethell, J. M. Brown, N. Calvet, C. Espaillat, S. G. Gregory, L. A. Hillenbrand, G. Hussain, L. Ingleby, C. M. Johns-Krull, E. Roueff, J. A. Valenti, and F. M. Walter. The Far-ultraviolet "Continuum" in Protoplanetary Disk Systems. II. Carbon Monoxide Fourth Positive Emission and Absorption. ApJ, 734:31, June 2011a. doi: 10.1088/0004-637X/734/1/31.

K. France, H. Yang, and J. L. Linsky. The Far-ultraviolet "Continuum" in Protoplanetary Disk Systems. I. Electron-impact H_2 and Accretion Shocks. ApJ, 729:7, March 2011b. doi: 10.1088/0004-637X/729/1/7.

K. France, M. Beasley, R. Kane, N. Nell, E. B. Burgh, and J. C. Green. Development of the Colorado High-resolution Echelle Stellar Spectrograph (CHESS). In Space Telescopes and Instrumentation 2012: Ultraviolet to Gamma Ray, volume 8443 of Proc. SPIE, page 844305, September 2012a.

K. France, E. B. Burgh, G. J. Herczeg, E. Schindhelm, H. Yang, H. Abgrall, E. Roueff, A. Brown, J. M. Brown, and J. L. Linsky. CO and H_2 Absorption in the AA Tauri Circumstellar Disk. ApJ, 744:22, January 2012b. doi: 10.1088/0004-637X/744/1/22.

K. France, E. Schindhelm, G. J. Herczeg, A. Brown, H. Abgrall, R. D. Alexander, E. A. Bergin, J. M. Brown, J. L. Linsky, E. Roueff, and H. Yang. A Hubble Space Telescope Survey of H_2 Emission in the Circumstellar Environments of Young Stars. ApJ, 756:171, September 2012c. doi: 10.1088/0004-637X/756/2/171.

K. France, N. Nell, K. Hoadley, R. Kane, E. B. Burgh, M. Beasley, R. Bushinksy, T. B. Schultz, M. Kaiser, C. Moore, J. Kulow, and J. C. Green. Flight performance and first results from the sub-orbital local interstellar cloud experiment (SLICE). In UV, X-Ray, and Gamma-Ray Space Instrumentation for Astronomy XVIII, volume 8859 of Proc. SPIE, page 885910, September 2013a.

K. France, N. Nell, R. Kane, E. B. Burgh, M. Beasley, and J. C. Green. H_2 Excitation Structure on the Sightlines to δ Scorpii and ζ Ophiuci: First Results from the Sub-orbital Local Interstellar Cloud Experiment. ApJL, 772:L9, July 2013b.

K. France, G. J. Herczeg, M. McJunkin, and S. V. Penton. CO/H_2 Abundance Ratio $\approx 10^{-4}$ in a Protoplanetary Disk. ApJ, 794:160, October 2014a. doi: 10.1088/0004-637X/794/2/160.

K. France, E. Schindhelm, E. A. Bergin, E. Roueff, and H. Abgrall. High-resolution Ultraviolet Radiation Fields of Classical T Tauri Stars. ApJ, 784:127, April 2014b. doi: 10.1088/0004-637X/784/2/127.

K. France, B. Fleming, and K. Hoadley. CHISL: the combined high-resolution and imaging spectrograph for the LUVOIR surveyor. In Society of Photo-Optical Instrumentation Engineers (SPIE) Conference Series, volume 9905 of Proc. SPIE, page 990506, July 2016a. doi: 10.1117/12.2231080.

K. France, K. Hoadley, B. T. Fleming, R. Kane, N. Nell, M. Beasley, and J. C. Green. The SLICE, CHESS, and SISTINE Ultraviolet Spectrographs: Rocket-Borne Instrumentation Supporting Future Astrophysics Missions. Journal of Astronomical Instrumentation, 5:1640001, March 2016b. doi: 10.1142/S2251171716400018.

K. France, E. Roueff, and H. Abgrall. Spectral Signature of H_2O Dissociation in Protoplanetary Disks. ApJ, *In Preparation*, 2017.

P. C. Frisch, J. M. Dorschner, J. Geiss, J. M. Greenberg, E. Grün, M. Landgraf, P. Hoppe, A. P. Jones, W. Krätschmer, T. J. Linde, G. E. Morfill, W. Reach, J. D. Slavin, J. Svestka, A. N. Witt, and G. P. Zank. Dust in the Local Interstellar Wind. ApJ, 525:492–516, November 1999. doi: 10.1086/307869.

E. Furlan, D. M. Watson, M. K. McClure, P. Manoj, C. Espaillat, P. D'Alessio, N. Calvet, K. H. Kim, B. A. Sargent, W. J. Forrest, and L. Hartmann. Disk Evolution in the Three Nearby Star-forming Regions of Taurus, Chamaeleon, and Ophiuchus. ApJ, 703:1964–1983, October 2009. doi: 10.1088/0004-637X/703/2/1964.

E. Furlan, K. L. Luhman, C. Espaillat, P. D'Alessio, L. Adame, P. Manoj, K. H. Kim, D. M. Watson, W. J. Forrest, M. K. McClure, N. Calvet, B. A. Sargent, J. D. Green, and W. J. Fischer. The Spitzer Infrared Spectrograph Survey of T Tauri Stars in Taurus. ApJS, 195:3, July 2011. doi: 10.1088/0067-0049/195/1/3.

R. Garcia Lopez, A. Natta, L. Testi, and E. Habart. Accretion rates in Herbig Ae stars. A&A, 459:837–842, December 2006. doi: 10.1051/0004-6361:20065575.

J. E. Gaustad. The Opacity of Diffuse Cosmic Matter and the Early Stages of Star Formation. ApJ, 138:1050, November 1963. doi: 10.1086/147705.

A. M. Ghez, G. Neugebauer, and K. Matthews. The multiplicity of T Tauri stars in the star forming regions Taurus-Auriga and Ophiuchus-Scorpius: A 2.2 micron speckle imaging survey. AJ, 106: 2005–2023, November 1993. doi: 10.1086/116782.

A. E. Glassgold and J. R. Najita. The Effects of X-Rays on the Diffuse Gas in Protoplanetary Disks. In R. Jayawardhana and T. Greene, editors, Young Stars Near Earth: Progress and Prospects, volume 244 of Astronomical Society of the Pacific Conference Series, page 251, 2001.

A. E. Glassgold, J. Najita, and J. Igea. Heating Protoplanetary Disk Atmospheres. ApJ, 615: 972–990, November 2004. doi: 10.1086/424509.

S. C. O. Glover and P. C. Clark. Is molecular gas necessary for star formation? MNRAS, 421: 9–19, March 2012a. doi: 10.1111/j.1365-2966.2011.19648.x.

S. C. O. Glover and P. C. Clark. Approximations for modelling CO chemistry in giant molecular clouds: a comparison of approaches. MNRAS, 421:116–131, March 2012b. doi: 10.1111/j.1365-2966.2011.20260.x.

S. C. O. Glover and P. C. Clark. Molecular cooling in the diffuse interstellar medium. MNRAS, 437:9–20, January 2014. doi: 10.1093/mnras/stt1809.

P. Goldreich, Y. Lithwick, and R. Sari. Final Stages of Planet Formation. ApJ, 614:497–507, October 2004. doi: 10.1086/423612.

A. I. Gómez de Castro. AK Sco, First Detection of a Highly Disturbed Atmosphere in a Pre-Main-Sequence Close Binary. ApJL, 698:L108–L111, June 2009. doi: 10.1088/0004-637X/698/2/L108.

U. Gorti and D. Hollenbach. Models of Chemistry, Thermal Balance, and Infrared Spectra from Intermediate-Aged Disks around G and K Stars. ApJ, 613:424–447, September 2004. doi: 10.1086/422406.

U. Gorti and D. Hollenbach. Photoevaporation of Circumstellar Disks By Far-Ultraviolet, Extreme-Ultraviolet and X-Ray Radiation from the Central Star. ApJ, 690:1539–1552, January 2009. doi: 10.1088/0004-637X/690/2/1539.

U. Gorti, C. P. Dullemond, and D. Hollenbach. Time Evolution of Viscous Circumstellar Disks due to Photoevaporation by Far-Ultraviolet, Extreme-Ultraviolet, and X-ray Radiation from the Central Star. ApJ, 705:1237–1251, November 2009. doi: 10.1088/0004-637X/705/2/1237.

U. Gorti, D. Hollenbach, and C. P. Dullemond. The Impact of Dust Evolution and Photoevaporation on Disk Dispersal. ApJ, 804:29, May 2015. doi: 10.1088/0004-637X/804/1/29.

C. A. Grady, B. Woodgate, C. A. O. Torres, T. Henning, D. Apai, J. Rodmann, H. Wang, B. Stecklum, H. Linz, G. M. Williger, A. Brown, E. Wilkinson, G. M. Harper, G. J. Herczeg, A. Danks, G. L. Vieira, E. Malumuth, N. R. Collins, and R. S. Hill. The Environment of the Optically Brightest Herbig Ae Star, HD 104237. ApJ, 608:809–830, June 2004. doi: 10.1086/420763.

C. A. Grady, G. Schneider, M. L. Sitko, G. M. Williger, K. Hamaguchi, S. D. Brittain, K. Ablordeppey, D. Apai, L. Beerman, W. J. Carpenter, K. A. Collins, M. Fukagawa, H. B. Hammel, T. Henning, D. Hines, R. Kimes, D. K. Lynch, F. Ménard, R. Pearson, R. W. Russell, M. Silverstone, P. S. Smith, M. Troutman, D. Wilner, B. Woodgate, and M. Clampin. Revealing the Structure of a Pre-Transitional Disk: The Case of the Herbig F Star SAO 206462 (HD 135344B). ApJ, 699:1822–1842, July 2009. doi: 10.1088/0004-637X/699/2/1822.

J. C. Green, E. Wilkinson, and J. A. Morse. The Cosmic Origins Spectrograph. In Future EUV/UV and Visible Space Astrophysics Missions and Instrumentation., 2003.

J. C. Green, C. S. Froning, S. Osterman, D. Ebbets, S. H. Heap, C. Leitherer, J. L. Linsky, B. D. Savage, K. Sembach, J. M. Shull, O. H. W. Siegmund, T. P. Snow, J. Spencer, S. A. Stern, J. Stocke, B. Welsh, S. Béland, E. B. Burgh, C. Danforth, K. France, B. Keeney, J. McPhate, S. V. Penton, J. Andrews, K. Brownsberger, J. Morse, and E. Wilkinson. The Cosmic Origins Spectrograph. ApJ, 744:60, January 2012. doi: 10.1088/0004-637X/744/1/60.

C. Gry, F. Boulanger, C. Nehmé, G. Pineau des Forêts, E. Habart, and E. Falgarone. H_2 formation and excitation in the diffuse interstellar medium. A&A, 391:675–680, August 2002. doi: 10.1051/0004-6361:20020691.

M. Güdel, S. L. Skinner, S. Y. Mel'Nikov, M. Audard, A. Telleschi, and K. R. Briggs. X-rays from T Tauri: a test case for accreting T Tauri stars. A&A, 468:529–540, June 2007. doi: 10.1051/0004-6361:20066318.

S. B. Gudennavar, S. G. Bubbly, K. Preethi, and J. Murthy. A Compilation of Interstellar Column Densities. ApJ, 199:8, March 2012. doi: 10.1088/0067-0049/199/1/8.

G. Guidi, M. Tazzari, L. Testi, I. de Gregorio-Monsalvo, C. J. Chandler, L. Pérez, A. Isella, A. Natta, S. Ortolani, T. Henning, S. Corder, H. Linz, S. Andrews, D. Wilner, L. Ricci, J. Carpenter, A. Sargent, L. Mundy, S. Storm, N. Calvet, C. Dullemond, J. Greaves, J. Lazio, A. Deller, and W. Kwon. Dust properties across the CO snowline in the HD 163296 disk from ALMA and VLA observations. A&A, 588:A112, April 2016. doi: 10.1051/0004-6361/201527516.

E. Gullbring, L. Hartmann, C. Briceño, and N. Calvet. Disk Accretion Rates for T Tauri Stars. ApJ, 492:323–341, January 1998. doi: 10.1086/305032.

E. Gullbring, N. Calvet, J. Muzerolle, and L. Hartmann. The Structure and Emission of the Accretion Shock in T Tauri Stars. II. The Ultraviolet-Continuum Emission. ApJ, 544:927–932, December 2000. doi: 10.1086/317253.

E. Habart, F. Boulanger, L. Verstraete, C. M. Walmsley, and G. Pineau des Forêts. Some empirical estimates of the H_2 formation rate in photon-dominated regions. A&A, 414:531–544, February 2004. doi: 10.1051/0004-6361:20031659.

K. E. Haisch, Jr., E. A. Lada, and C. J. Lada. Disk Frequencies and Lifetimes in Young Clusters. ApJL, 553:L153–L156, June 2001. doi: 10.1086/320685.

P. Hartigan, S. Edwards, and L. Ghandour. Disk Accretion and Mass Loss from Young Stars. ApJ, 452:736, October 1995. doi: 10.1086/176344.

L. Hartmann and K. B. MacGregor. Protostellar mass and angular momentum loss. ApJ, 259:180–192, August 1982. doi: 10.1086/160158.

L. Hartmann and J. R. Stauffer. Additional measurements of pre-main-sequence stellar rotation. AJ, 97:873–880, March 1989. doi: 10.1086/115033.

L. Hartmann, N. Calvet, E. Gullbring, and P. D'Alessio. Accretion and the Evolution of T Tauri Disks. ApJ, 495:385–400, March 1998. doi: 10.1086/305277.

L. W. Hartmann, D. R. Soderblom, and J. R. Stauffer. Rotation and kinematics of the premain-sequence stars in Taurus-Auriga with CA II emission. AJ, 93:907–912, April 1987. doi: 10.1086/114376.

J. Hashimoto, M. Tamura, T. Muto, T. Kudo, M. Fukagawa, T. Fukue, M. Goto, C. A. Grady, T. Henning, K. Hodapp, M. Honda, S. Inutsuka, E. Kokubo, G. Knapp, M. W. McElwain, M. Momose, N. Ohashi, Y. K. Okamoto, M. Takami, E. L. Turner, J. Wisniewski, M. Janson, L. Abe, W. Brandner, J. Carson, S. Egner, M. Feldt, T. Golota, O. Guyon, Y. Hayano, M. Hayashi, S. Hayashi, M. Ishii, R. Kandori, N. Kusakabe, T. Matsuo, S. Mayama, S. Miyama, J.-I. Morino, A. Moro-Martin, T. Nishimura, T.-S. Pyo, H. Suto, R. Suzuki, N. Takato, H. Terada, C. Thalmann, D. Tomono, M. Watanabe, T. Yamada, H. Takami, and T. Usuda. Direct Imaging of Fine Structures in Giant Planet-forming Regions of the Protoplanetary Disk Around AB Aurigae. ApJL, 729:L17, March 2011. doi: 10.1088/2041-8205/729/2/L17.

C. Hayashi. Evolution of Protostars. ARAA, 4:171, 1966. doi: 10.1146/annurev.aa.04.090166.001131.

M. Hayashi. Pre-Main-Sequence Stages of Stars. PASJ, 17:177, 1965.

D. Heinzeller, H. Nomura, C. Walsh, and T. J. Millar. Chemical Evolution of Protoplanetary Disks − The Effects of Viscous Accretion, Turbulent Mixing, and Disk Winds. ApJ, 731:115, April 2011. doi: 10.1088/0004-637X/731/2/115.

D. Heißelmann, J. Blum, and H. J. Fraser. Experimental Studies on the Aggregation Properties of Ice and Dust in Planet-Forming Regions. In Proc. 58th Int. Astronautical Congress 2007 (Paris: Int. Astronautical Federation), IAC-07-A2.1.02, September 2007.

G. J. Herczeg and L. A. Hillenbrand. UV Excess Measures of Accretion onto Young Very Low Mass Stars and Brown Dwarfs. ApJ, 681:594–625, July 2008. doi: 10.1086/586728.

G. J. Herczeg, J. L. Linsky, J. A. Valenti, C. M. Johns-Krull, and B. E. Wood. The Far-Ultraviolet Spectrum of TW Hydrae. I. Observations of H_2 Fluorescence. ApJ, 572:310–325, June 2002. doi: 10.1086/339731.

G. J. Herczeg, B. E. Wood, J. L. Linsky, J. A. Valenti, and C. M. Johns-Krull. The Far-Ultraviolet Spectra of TW Hydrae. II. Models of H_2 Fluorescence in a Disk. ApJ, 607:369–383, May 2004. doi: 10.1086/383340.

G. J. Herczeg, F. M. Walter, J. L. Linsky, G. F. Gahm, D. R. Ardila, A. Brown, C. M. Johns-Krull, M. Simon, and J. A. Valenti. The Loopy Ultraviolet Line Profiles of RU Lupi: Accretion, Outflows, and Fluorescence. AJ, 129:2777–2791, June 2005. doi: 10.1086/430075.

G. J. Herczeg, J. L. Linsky, F. M. Walter, G. F. Gahm, and C. M. Johns-Krull. The Origins of Fluorescent H_2 Emission From T Tauri Stars. ApJS, 165:256–282, July 2006. doi: 10.1086/503558.

J. Hernández, N. Calvet, C. Briceño, L. Hartmann, A. K. Vivas, J. Muzerolle, J. Downes, L. Allen, and R. Gutermuth. Spitzer Observations of the Orion OB1 Association: Disk Census in the Low-Mass Stars. ApJ, 671:1784–1799, December 2007. doi: 10.1086/522882.

G. Herzberg. Molecular spectra and molecular structure. Vol.1: Spectra of diatomic molecules. 1950.

K. Hoadley, K. France, N. Nell, R. Kane, T. Schultz, M. Beasley, J. Green, J. Kulow, E. Kersgaard, and B. Fleming. The assembly, calibration, and preliminary results from the Colorado high-resolution Echelle stellar spectrograph (CHESS). In Space Telescopes and Instrumentation 2014: Ultraviolet to Gamma Ray, volume 9144 of Proc. SPIE, page 914406, July 2014.

K. Hoadley, K. France, R. D. Alexander, M. McJunkin, and P. C. Schneider. The Evolution of Inner Disk Gas in Transition Disks. ApJ, 812:41, October 2015. doi: 10.1088/0004-637X/812/1/41.

K. Hoadley, K. France, N. Kruczek, B. Fleming, N. Nell, R. Kane, J. Swanson, J. Green, N. Erickson, and J. Wilson. The re-flight of the Colorado high-resolution Echelle stellar spectrograph (CHESS): improvements, calibrations, and post-flight results. In Society of Photo-Optical Instrumentation Engineers (SPIE) Conference Series, volume 9905 of Proc. SPIE, page 99052V, July 2016. doi: 10.1117/12.2232242.

D. Hoffleit and C. Jaschek. The Bright Star Catalogue. Fourth revised edition. 1982.

D. Hollenbach and E. E. Salpeter. Molecular Hydrogen Formation on Grains in H I Regions. In Bulletin of the American Astronomical Society, volume 1 of Bulletin of the American Astronomical Society, page 244, June 1969.

D. Hollenbach, D. Johnstone, S. Lizano, and F. Shu. Photoevaporation of disks around massive stars and application to ultracompact H II regions. ApJ, 428:654–669, June 1994. doi: 10.1086/174276.

D. J. Hollenbach and A. G. G. M. Tielens. Dense Photodissociation Regions (PDRs). ARA&A, 35:179–216, 1997. doi: 10.1146/annurev.astro.35.1.179.

D. J. Hollenbach and A. G. G. M. Tielens. Photodissociation regions in the interstellar medium of galaxies. Reviews of Modern Physics, 71:173–230, January 1999. doi: 10.1103/RevModPhys.71.173.

D. J. Hollenbach, M. W. Werner, and E. E. Salpeter. Molecular Hydrogen in H i Regions. ApJ, 163:165, January 1971. doi: 10.1086/150755.

J. R. Houck, T. L. Roellig, J. Van Cleve, W. J. Forrest, T. L. Herter, C. R. Lawrence, K. Matthews, H. J. Reitsema, B. T. Soifer, D. M. Watson, D. Weedman, M. Huisjen, J. R. Troeltzsch, D. J. Barry, J. Bernard-Salas, C. Blacken, B. R. Brandl, V. Charmandaris, D. Devost, G. E. Gull, P. Hall, C. P. Henderson, S. J. U. Higdon, B. E. Pirger, J. Schoenwald, G. C. Sloan, K. I. Uchida, P. N. Appleton, L. Armus, M. J. Burgdorf, S. B. Fajardo-Acosta, C. J. Grillmair, J. G. Ingalls, P. W. Morris, and H. I. Teplitz. The infrared spectrograph on the Spitzer Space Telescope. In J. C. Mather, editor, Optical, Infrared, and Millimeter Space Telescopes, volume 5487 of Society of Photo-Optical Instrumentation Engineers (SPIE) Conference Series, pages 62–76, October 2004. doi: 10.1117/12.550517.

K. P. Huber and G Herzberg. Molecular Spectra and Molecular Structure IV: Constants of Diatomic Molecules. 1979.

J. Hughes, P. Hartigan, J. Krautter, and J. Kelemen. The stellar population of the Lupus clouds. AJ, 108:1071–1090, September 1994. doi: 10.1086/117135.

L. Ingleby, N. Calvet, E. Bergin, G. Herczeg, A. Brown, R. Alexander, S. Edwards, C. Espaillat, K. France, S. G. Gregory, L. Hillenbrand, E. Roueff, J. Valenti, F. Walter, C. Johns-Krull, J. Brown, J. Linsky, M. McClure, D. Ardila, H. Abgrall, T. Bethell, G. Hussain, and H. Yang. Near-ultraviolet Excess in Slowly Accreting T Tauri Stars: Limits Imposed by Chromospheric Emission. ApJ, 743:105, December 2011. doi: 10.1088/0004-637X/743/2/105.

L. Ingleby, N. Calvet, G. Herczeg, A. Blaty, F. Walter, D. Ardila, R. Alexander, S. Edwards, C. Espaillat, S. G. Gregory, L. Hillenbrand, and A. Brown. Accretion Rates for T Tauri Stars Using Nearly Simultaneous Ultraviolet and Optical Spectra. ApJ, 767:112, April 2013. doi: 10.1088/0004-637X/767/2/112.

J. H. Jeans. The Stability of a Spherical Nebula. Philosophical Transactions of the Royal Society of London Series A, 199:1–53, 1902. doi: 10.1098/rsta.1902.0012.

E. B. Jenkins and T. M. Tripp. The Distribution of Thermal Pressures in the Interstellar Medium from a Survey of C I Fine-Structure Excitation. ApJS, 137:297–340, December 2001.

D. E. Jennings, S. L. Bragg, and J. W. Brault. The V = 0 - 0 spectrum of H2. ApJL, 282:L85–L88, July 1984. doi: 10.1086/184311.

A. Johansen, J. S. Oishi, M.-M. Mac Low, H. Klahr, T. Henning, and A. Youdin. Rapid planetesimal formation in turbulent circumstellar disks. Nature, 448:1022–1025, August 2007. doi: 10.1038/nature06086.

C. M. Johns-Krull and J. A. Valenti. New Infrared Veiling Measurements and Constraints on Accretion Disk Models for Classical T Tauri Stars. ApJ, 561:1060–1073, November 2001. doi: 10.1086/323257.

C. M. Johns-Krull, J. A. Valenti, and J. L. Linsky. An IUE Atlas of Pre-Main-Sequence Stars. II. Far-Ultraviolet Accretion Diagnostics in T Tauri Stars. ApJ, 539:815–833, August 2000. doi: 10.1086/309259.

M. Joos, P. Hennebelle, and A. Ciardi. Protostellar disk formation and transport of angular momentum during magnetized core collapse. A&A, 543:A128, July 2012. doi: 10.1051/0004-6361/201118730.

M. Jura. Formation and destruction rates of interstellar H_2. ApJ, 191:375–379, July 1974. doi: 10.1086/152975.

M. Jura. Interstellar clouds containing optically thin H2. ApJ, 197:575–580, May 1975a. doi: 10.1086/153545.

M. Jura. Interstellar clouds containing optically thick H2. ApJ, 197:581–586, May 1975b. doi: 10.1086/153546.

I. Kamp and C. P. Dullemond. The Gas Temperature in the Surface Layers of Protoplanetary Disks. ApJ, 615:991–999, November 2004. doi: 10.1086/424703.

I. Kamp, C. P. Dullemond, M. Hogerheijde, and J. E. Enriquez. Chemistry and Line Emission of Outer Protoplanetary Disks. In D. C. Lis, G. A. Blake, and E. Herbst, editors, Astrochemistry: Recent Successes and Current Challenges, volume 231 of IAU Symposium, pages 377–386, 2005. doi: 10.1017/S1743921306007393.

J. H. Kastner, D. A. Principe, K. Punzi, B. Stelzer, U. Gorti, I. Pascucci, and C. Argiroffi. M Stars in the TW Hya Association: Stellar X-Rays and Disk Dissipation. AJ, 152:3, July 2016. doi: 10.3847/0004-6256/152/1/3.

K. K. Kelley. Selected Values of Thermodynamic Properties of Elements. 1973.

R. C. Kennicutt, Jr. The Global Schmidt Law in Star-forming Galaxies. ApJ, 498:541–552, May 1998. doi: 10.1086/305588.

R. C. Kennicutt, Jr., D. Calzetti, F. Walter, G. Helou, D. J. Hollenbach, L. Armus, G. Bendo, D. A. Dale, B. T. Draine, C. W. Engelbracht, K. D. Gordon, M. K. M. Prescott, M. W. Regan, M. D. Thornley, C. Bot, E. Brinks, E. de Blok, D. de Mello, M. Meyer, J. Moustakas, E. J. Murphy, K. Sheth, and J. D. T. Smith. Star Formation in NGC 5194 (M51a). II. The Spatially Resolved Star Formation Law. ApJ, 671:333–348, December 2007. doi: 10.1086/522300.

S. J. Kenyon, L. Hartmann, R. Hewett, L. Carrasco, I. Cruz-Gonzalez, E. Recillas, L. Salas, A. Serrano, K. M. Strom, S. E. Strom, and G. Newton. The hot SPOT in DR Tauri. AJ, 107:2153–2163, June 1994. doi: 10.1086/117026.

R. A. Kimble, B. E. Woodgate, C. W. Bowers, S. B. Kraemer, M. E. Kaiser, T. R. Gull, S. R. Heap, A. C. Danks, A. Boggess, R. F. Green, J. B. Hutchings, E. B. Jenkins, C. L. Joseph, J. L. Linsky, S. P. Maran, H. W. Moos, F. Roesler, J. G. Timothy, D. E. Weistrop, J. F. Grady, J. J. Loiacono, L. W. Brown, M. D. Brumfield, D. A. Content, L. D. Feinberg, M. N. Isaacs, C. A. Krebs, V. L. Krueger, R. W. Melcher, F. J. Rebar, H. D. Vitagliano, J. J. Yagelowich, W. W. Meyer, D. F. Hood, V. S. Argabright, S. I. Becker, M. Bottema, R. R. Breyer, R. L. Bybee, P. R. Christon, A. W. Delamere, D. A. Dorn, S. Downey, P. A. Driggers, D. C. Ebbets, J. S. Gallegos, H. Garner, J. C. Hetlinger, R. L. Lettieri, C. W. Ludtke, D. Michika, R. Nyquist, D. M. Rose, R. B. Stocker, J. F. Sullivan, C. N. Van Houten, R. A. Woodruff, S. A. Baum, G. F. Hartig, V. Balzano, C. Biagetti, J. C. Blades, R. C. Bohlin, M. Clampin, R. Doxsey, H. C. Ferguson, P. Goudfrooij, S. J. Hulbert, R. Kutina, M. McGrath, D. J. Lindler, T. L. Beck, J. K. Feggans, P. C. Plait, J. L. Sandoval, R. S. Hill, N. R. Collins, R. H. Cornett, W. B. Fowler, R. J. Hill, W. B. Landsman, E. M. Malumuth, C. Standley, M. Blouke, A. Grusczak, R. Reed, R. D. Robinson, J. A. Valenti, and T. Wolfe. The On-Orbit Performance of the Space Telescope Imaging Spectrograph. ApJL, 492:L83–L93, January 1998. doi: 10.1086/311102.

H. Kimura, I. Mann, and E. K. Jessberger. Elemental Abundances and Mass Densities of Dust and Gas in the Local Interstellar Cloud. ApJ, 582:846–858, January 2003. doi: 10.1086/344691.

J. Kominami and S. Ida. Formation of terrestrial planets in a dissipating gas disk. In E. Kokubo, T. Ito, and H. Arakida, editors, 33rd Symposium on Celestial Mechanics, Dedicated to Donald Saari for his 60th Birthday, pages 152–161, 2002.

A. L. Kraus and L. A. Hillenbrand. The Coevality of Young Binary Systems. ApJ, 704:531–547, October 2009. doi: 10.1088/0004-637X/704/1/531.

K. A. Kretke and H. F. Levison. Challenges in Forming the Solar System's Giant Planet Cores via Pebble Accretion. AJ, 148:109, December 2014. doi: 10.1088/0004-6256/148/6/109.

G. A. Kriss. Improved Medium Resolution Line Spread Functions for COS FUV Spectra. Technical report, March 2011.

Nicholas Kruczek, Kevin France, William Evonosky, R.O. Parke Lyod, Allision Youngblood, Aki Roberge, Robert A. Wittenmyer, John T. Stocke, Brian Fleming, and Keri Hoadley. H_2 Fluorescence in M Dwarf Systems: A Stellar Origin. ApJ, Submitted.

M. R. Krumholz and C. F. McKee. A General Theory of Turbulence-regulated Star Formation, from Spirals to Ultraluminous Infrared Galaxies. ApJ, 630:250–268, September 2005. doi: 10.1086/431734.

M. R. Krumholz, C. F. McKee, and J. Tumlinson. The Star Formation Law in Atomic and Molecular Gas. ApJ, 699:850–856, July 2009. doi: 10.1088/0004-637X/699/1/850.

J. H. Kwan, I. Gatley, K. M. Merrill, R. Probst, and D. A. Weintraub. On the molecular hydrogen emission at the Orion Nebula. ApJ, 216:713–723, September 1977. doi: 10.1086/155514.

S. Lacour, V. Ziskin, G. Hébrard, C. Oliveira, M. K. André, R. Ferlet, and A. Vidal-Madjar. Velocity Dispersion of the High Rotational Levels of H_2. ApJ, 627:251–262, July 2005. doi: 10.1086/430291.

J. H. Lacy, R. Knacke, T. R. Geballe, and A. T. Tokunaga. Detection of absorption by H2 in molecular clouds: A direct measurement of the H2:CO ratio. ApJL, 428:L69–L72, June 1994. doi: 10.1086/187395.

C. J. Lada. Star formation - From OB associations to protostars. In M. Peimbert and J. Jugaku, editors, Star Forming Regions, volume 115 of IAU Symposium, pages 1–17, 1987.

M. Lambrechts and A. Johansen. Rapid growth of gas-giant cores by pebble accretion. A&A, 544:A32, August 2012. doi: 10.1051/0004-6361/201219127.

M. Lambrechts and A. Johansen. Forming the cores of giant planets from the radial pebble flux in protoplanetary discs. A&A, 572:A107, December 2014. doi: 10.1051/0004-6361/201424343.

R. B. Larson. Numerical calculations of the dynamics of collapsing proto-star. MNRAS, 145:271, 1969. doi: 10.1093/mnras/145.3.271.

R. B. Larson. Angular Momentum and Protostellar Disks. RMxAA, 7:219, August 1983.

W. A. Lawson, E. D. Feigelson, and D. P. Huenemoerder. An improved HR diagram for Chamaeleon I pre-main-sequence stars. MNRAS, 280:1071–1088, June 1996.

W. A. Lawson, L. A. Crause, E. E. Mamajek, and E. D. Feigelson. The η Chamaeleontis cluster: photometric study of the ROSAT-detected weak-lined T Tauri stars. MNRAS, 321:57–66, February 2001. doi: 10.1046/j.1365-8711.2001.03967.x.

W. A. Lawson, A.-R. Lyo, and J. Muzerolle. Long-lived disc accretion in the η Chamaeleontis pre-main sequence star cluster. MNRAS, 351:L39–L43, June 2004. doi: 10.1111/j.1365-2966.2004.07959.x.

N. Lehner, E. B. Jenkins, C. Gry, H. W. Moos, P. Chayer, and S. Lacour. Far Ultraviolet Spectroscopic Explorer Survey of the Local Interstellar Medium within 200 Parsecs. ApJ, 595:858–879, October 2003. doi: 10.1086/377493.

C. et al. Leitherer. STIS Instrument Handbook for Cycle 11 (v5.1; Baltimore: STScI). 2001.

S. Lepp and J. M. Shull. The kinetic theory of H2 dissociation. ApJ, 270:578–582, July 1983. doi: 10.1086/161149.

H. F. Levison, E. Thommes, and M. J. Duncan. Modeling the Formation of Giant Planet Cores. I. Evaluating Key Processes. AJ, 139:1297–1314, April 2010. doi: 10.1088/0004-6256/139/4/1297.

H. F. Levison, K. A. Kretke, and M. J. Duncan. Growing the gas-giant planets by the gradual accumulation of pebbles. Nature, 524:322–324, August 2015a. doi: 10.1038/nature14675.

H. F. Levison, K. A. Kretke, K. J. Walsh, and W. F. Bottke. Growing the terrestrial planets from the gradual accumulation of sub-meter sized objects. Proceedings of the National Academy of Science, 112:14180–14185, November 2015b. doi: 10.1073/pnas.1513364112.

D. N. C. Lin and J. Papaloizou. On the tidal interaction between protoplanets and the protoplanetary disk. III - Orbital migration of protoplanets. ApJ, 309:846–857, October 1986. doi: 10.1086/164653.

D. Lindler. CALSTIS Reference Guide (Greenbelt: NASA/LASP). 1999.

J. L. Linsky and B. E. Wood. The alpha Centauri Line of Sight: D/H Ratio, Physical Properties of Local Interstellar Gas, and Measurement of Heated Hydrogen (The 'Hydrogen Wall') Near the Heliopause. ApJ, 463:254–270, May 1996. doi: 10.1086/177238.

J. L. Linsky, S. Redfield, B. E. Wood, and N. Piskunov. The Three-dimensional Structure of the Warm Local Interstellar Medium. I. Methodology. ApJ, 528:756–766, January 2000. doi: 10.1086/308205.

W. Liu and A. Dalgarno. The Ultraviolet Spectra of the Jovian Aurora. ApJ, 467:446, August 1996. doi: 10.1086/177618.

L. Loinard, R. M. Torres, A. J. Mioduszewski, L. F. Rodríguez, R. A. González-Lópezlira, R. Lachaume, V. Vázquez, and E. González. VLBA Determination of the Distance to Nearby Star-forming Regions. I. The Distance to T Tauri with 0.4% Accuracy. ApJ, 671:546–554, December 2007. doi: 10.1086/522493.

S. H. Lubow and G. D'Angelo. Gas Flow across Gaps in Protoplanetary Disks. ApJ, 641:526–533, April 2006. doi: 10.1086/500356.

S. H. Lubow, M. Seibert, and P. Artymowicz. Disk Accretion onto High-Mass Planets. ApJ, 526:1001–1012, December 1999. doi: 10.1086/308045.

K. L. Luhman. New Brown Dwarfs and an Updated Initial Mass Function in Taurus. ApJ, 617:1216–1232, December 2004. doi: 10.1086/425647.

D. Lynden-Bell and J. E. Pringle. The evolution of viscous discs and the origin of the nebular variables. MNRAS, 168:603–637, September 1974.

A.-R. Lyo, N. Ohashi, C. Qi, D. J. Wilner, and Y.-N. Su. Millimeter Observations of the Transition Disk around HD 135344B (SAO 206462). AJ, 142:151, November 2011. doi: 10.1088/0004-6256/142/5/151.

K. Malfait, C. Waelkens, L. B. F. M. Waters, B. Vandenbussche, E. Huygen, and M. S. de Graauw. The spectrum of the young star HD 100546 observed with the Infrared Space Observatory. A&A, 332:L25–L28, April 1998.

E. E. Mamajek, W. A. Lawson, and E. D. Feigelson. A Radio Survey of Older T Tauri Stars in the η Chamaeleontis Cluster. PASA, 16:257–261, December 1999. doi: 10.1071/AS99257.

A. M. Mandell, M. J. Mumma, G. A. Blake, B. P. Bonev, G. L. Villanueva, and C. Salyk. Discovery of OH in Circumstellar Disks around Young Intermediate-Mass Stars. ApJL, 681:L25–L28, July 2008. doi: 10.1086/590180.

A. M. Mandell, J. Bast, E. F. van Dishoeck, G. A. Blake, C. Salyk, M. J. Mumma, and G. Villanueva. First Detection of Near-infrared Line Emission from Organics in Young Circumstellar Disks. ApJ, 747:92, March 2012. doi: 10.1088/0004-637X/747/2/92.

M. E. Mandy. State-specific Dissociation Rates for $H_2(v, j) + H_2(v', j')$. ApJ, 827:62, August 2016. doi: 10.3847/0004-637X/827/1/62.

M. E. Mandy and P. G. Martin. Collisional excitation of H2 molecules by H atoms. ApJ, 86: 199–210, May 1993. doi: 10.1086/191775.

C. B. Markwardt. Non-linear Least-squares Fitting in IDL with MPFIT. In D. A. Bohlender, D. Durand, and P. Dowler, editors, Astronomical Data Analysis Software and Systems XVIII, volume 411 of Astronomical Society of the Pacific Conference Series, page 251, September 2009.

E. R. Martin and D. G. York. Components in the interstellar medium toward Epsilon Persei and Delta Persei. ApJ, 257:135–144, June 1982. doi: 10.1086/159971.

R. G. Martin and M. Livio. On the Evolution of the CO Snow Line in Protoplanetary Disks. ApJL, 783:L28, March 2014. doi: 10.1088/2041-8205/783/2/L28.

J. R. Martínez-Galarza, A. M. Glauser, A. Hernán-Caballero, R. Azzollini, A. Glasse, S. Kendrew, B. Brandl, and F. Lahuis. Wavelength calibration of the JWST-MIRI medium resolution spectrometer. Proc. SPIE, pages 7731–3Q, July 2010.

E. E. Martínez-García, R. A. González-Lópezlira, and G. Bruzual. Triggered star formation in spiral arms. In Revista Mexicana de Astronomia y Astrofisica Conference Series, volume 35 of Revista Mexicana de Astronomia y Astrofisica Conference Series, pages 231–232, May 2009.

P. Martini, K. Sellgren, and D. L. DePoy. Near-Infrared Spectroscopy of Molecular Hydrogen Emission in Four Reflection Nebulae: NGC 1333, NGC 2023, NGC 2068, and NGC 7023. ApJ, 526:772–787, December 1999. doi: 10.1086/308040.

H. Maruta, F. Nakamura, R. Nishi, N. Ikeda, and Y. Kitamura. Physical Properties of Dense Cores in the ρ Ophiuchi Main Cloud and a Significant Role of External Pressures in Clustered Star Formation. ApJ, 714:680–698, May 2010. doi: 10.1088/0004-637X/714/1/680.

F. S. Masset and J. C. B. Papaloizou. Runaway Migration and the Formation of Hot Jupiters. ApJ, 588:494–508, May 2003. doi: 10.1086/373892.

G. S. Mathews, P. D. Klaassen, A. Juhász, D. Harsono, E. Chapillon, E. F. van Dishoeck, D. Espada, I. de Gregorio-Monsalvo, A. Hales, M. R. Hogerheijde, J. C. Mottram, M. G. Rawlings, S. Takahashi, and L. Testi. ALMA imaging of the CO snowline of the HD 163296 disk with DCO^+. A&A, 557:A132, September 2013. doi: 10.1051/0004-6361/201321600.

S. R. McCandliss. Molecular Hydrogen Optical Depth Templates for FUSE Data Analysis. PASP, 115:651–661, June 2003. doi: 10.1086/375387.

S. R. McCandliss, E. B. Burgh, and P. D. Feldman. Flyable windowless calibration lamps for far-UV spectroscopy. In Instrumentation for UV/EUV Astronomy and Solar Missions, volume 4139 of Proc. SPIE, page 413970, 2000.

S. R. McCandliss, K. France, S. Osterman, J. C. Green, J. B. McPhate, and E. Wilkinson. Far-Ultraviolet Sensitivity of the Cosmic Origins Spectrograph. ApJL, 709:L183–L187, February 2010. doi: 10.1088/2041-8205/709/2/L183.

M. A. McCord and M. J. Rooks. SPIE Handbook of Microlithography, Micromachining and Microfabrication, volume 1. SPIE, 2000.

M. McJunkin, K. France, E. B. Burgh, G. J. Herczeg, E. Schindhelm, J. M. Brown, and A. Brown. Probing the Inner Regions of Protoplanetary Disks with CO Absorption Line Spectroscopy. ApJ, 766:12, March 2013. doi: 10.1088/0004-637X/766/1/12.

M. McJunkin, K. France, P. C. Schneider, G. J. Herczeg, A. Brown, L. Hillenbrand, E. Schindhelm, and S. Edwards. Direct Measurement of Interstellar Extinction toward Young Stars Using Atomic Hydrogen Lyα Absorption. ApJ, 780:150, January 2014. doi: 10.1088/0004-637X/780/2/150.

M. McJunkin, K. France, E. Schindhelm, G. Herczeg, P. C. Schneider, and A. Brown. Empirically Estimated Far-UV Extinction Curves for Classical T Tauri Stars. ApJ, 828:69, September 2016. doi: 10.3847/0004-637X/828/2/69.

R. Meijerink, K. M. Pontoppidan, G. A. Blake, D. R. Poelman, and C. P. Dullemond. Radiative Transfer Models of Mid-Infrared H_2O Lines in the Planet-Forming Region of Circumstellar Disks. ApJ, 704:1471–1481, October 2009. doi: 10.1088/0004-637X/704/2/1471.

M. Meixner, P. McCullough, J. Hartman, M. Son, and A. Speck. The Multitude of Molecular Hydrogen Knots in the Helix Nebula. AJ, 130:1784–1794, October 2005. doi: 10.1086/444539.

H. Mizuno, K. Nakazawa, and C. Hayashi. Instability of a gaseous envelope surrounding a planetary core and formation of giant planets. Progress of Theoretical Physics, 60:699–710, September 1978. doi: 10.1143/PTP.60.699.

D. C. Morton. Interstellar absorption lines in the spectrum of zeta Ophiuchi. ApJ, 197:85–115, April 1975. doi: 10.1086/153490.

D. C. Morton, E. B. Jenkins, and W. W. Macy. Rocket-Ultraviolet Spectra of Six Stars in Perseus. ApJ, 177:235, October 1972. doi: 10.1086/151700.

T. C. Mouschovias. Magnetic braking of self-gravitating, oblate interstellar clouds. ApJ, 228: 159–162, February 1979. doi: 10.1086/156832.

K. Muraoka, M. Takeda, K. Yanagitani, H. Kaneko, K. Nakanishi, N. Kuno, K. Sorai, T. Tosaki, and K. Kohno. CO(J = 3-2) on-the-fly mapping of the nearby spiral galaxies NGC 628 and NGC 7793: Spatially resolved CO(J = 3-2) star-formation law. PASJ, 68:18, April 2016. doi: 10.1093/pasj/psv134.

J. Muzerolle, N. Calvet, C. Briceño, L. Hartmann, and L. Hillenbrand. Disk Accretion in the 10 MYR Old T Tauri Stars TW Hydrae and Hen 3-600A. ApJL, 535:L47–L50, May 2000. doi: 10.1086/312691.

J. Najita, J. S. Carr, and R. D. Mathieu. Gas in the Terrestrial Planet Region of Disks: CO Fundamental Emission from T Tauri Stars. ApJ, 589:931–952, June 2003. doi: 10.1086/374809.

J. R. Najita, M. Ádámkovics, and A. E. Glassgold. Formation of Organic Molecules and Water in Warm Disk Atmospheres. ApJ, 743:147, December 2011. doi: 10.1088/0004-637X/743/2/147.

D. C. Nguyen, A. Brandeker, M. H. van Kerkwijk, and R. Jayawardhana. Close Companions to Young Stars. I. A Large Spectroscopic Survey in Chamaeleon I and Taurus-Auriga. ApJ, 745: 119, February 2012. doi: 10.1088/0004-637X/745/2/119.

H. Nomura. Structure and Instabilities of Irradiated Protoplanetary Disks: Effects of Dust Particle Growth. APSS, 292:435–438, August 2004. doi: 10.1023/B:ASTR.0000045110.90202.ce.

H. Nomura and T. J. Millar. Molecular hydrogen emission from protoplanetary disks. A&A, 438: 923–938, August 2005. doi: 10.1051/0004-6361:20052809.

H. Nomura and Y. Nakagawa. Dust Size Growth and Settling in a Protoplanetary Disk. ApJ, 640: 1099–1109, April 2006. doi: 10.1086/500251.

H. Nomura, Y. Aikawa, Y. Nakagawa, and T. J. Millar. Molecular Hydrogen Emission from Protoplanetary Disks: Effects of Dust Size Growth and Settling. In Protostars and Planets V Posters, page 8157, 2005.

H. Nomura, Y. Aikawa, M. Tsujimoto, Y. Nakagawa, and T. J. Millar. Molecular Hydrogen Emission from Protoplanetary Disks. II. Effects of X-Ray Irradiation and Dust Evolution. ApJ, 661: 334–353, May 2007. doi: 10.1086/513419.

M. L. Norman, J. R. Wilson, and R. T. Barton. A new calculation on rotating protostar collapse. ApJ, 239:968–981, August 1980. doi: 10.1086/158185.

K. I. Öberg, E. F. van Dishoeck, H. Linnartz, and S. Andersson. The Effect of H_2O on Ice Photochemistry. ApJ, 718:832–840, August 2010. doi: 10.1088/0004-637X/718/2/832.

S. Osterman, J. Green, C. Froning, S. Béland, E. Burgh, K. France, S. Penton, T. Delker, D. Ebbets, D. Sahnow, J. Bacinski, R. Kimble, J. Andrews, E. Wilkinson, J. McPhate, O. Siegmund, T. Ake, A. Aloisi, C. Biagetti, R. Diaz, W. Dixon, S. Friedman, P. Ghavamian, P. Goudfrooij, G. Hartig, C. Keyes, D. Lennon, D. Massa, S. Niemi, C. Oliveira, R. Osten, C. Proffitt, T. Smith, and D. Soderblom. The Cosmic Origins Spectrograph: on-orbit instrument performance. Ap&SS, 335:257–265, September 2011. doi: 10.1007/s10509-011-0699-5.

J. E. Owen. The Origin and Evolution of Transition Discs: Successes, Problems, and Open Questions. PASA, 33:e005, February 2016. doi: 10.1017/pasa.2016.2.

J. E. Owen, B. Ercolano, C. J. Clarke, and R. D. Alexander. Radiation-hydrodynamic models of X-ray and EUV photoevaporating protoplanetary discs. MNRAS, 401:1415–1428, January 2010. doi: 10.1111/j.1365-2966.2009.15771.x.

L. Pagani, J. Steinacker, A. Bacmann, A. Stutz, and T. Henning. The Ubiquity of Micrometer-Sized Dust Grains in the Dense Interstellar Medium. Science, 329:1622, September 2010. doi: 10.1126/science.1193211.

F. Palla, E. E. Salpeter, and S. W. Stahler. Primordial star formation - The role of molecular hydrogen. ApJ, 271:632–641, August 1983. doi: 10.1086/161231.

I. Pascucci, M. Sterzik, R. D. Alexander, S. H. P. Alencar, U. Gorti, D. Hollenbach, J. Owen, B. Ercolano, and S. Edwards. The Photoevaporative Wind from the Disk of TW Hya. ApJ, 736: 13, July 2011. doi: 10.1088/0004-637X/736/1/13.

M. V. Penston. A Numerical Integration of the Non-Linear Equations of Spherical Collapse. In Liege International Astrophysical Colloquia, volume 14 of Liege International Astrophysical Colloquia, page 305, 1967.

S. V. Penton, S. N. Osterman, K. France, C. Oliveira, and D. J. Sahnow. Announcing A New HST+COS Central Wavelength: G130M/1222. In American Astronomical Society Meeting Abstracts #219, volume 219 of American Astronomical Society Meeting Abstracts, page 241.19, January 2012.

S. V. Penton, A. Aloisi, K. A. Bostroem, E. Elliott, K. France, S. A. Lockwood, C. M. Oliveira, S. Osterman, C. R. Proffitt, J. Roman-Duval, and D. J. Sahnow. Sensing the "LUV" with HST+COS in Cycle 20 and Beyond. In American Astronomical Society Meeting Abstracts #221, volume 221 of American Astronomical Society Meeting Abstracts, page 344.04, January 2013.

J. B. Pollack, O. Hubickyj, P. Bodenheimer, J. J. Lissauer, M. Podolak, and Y. Greenzweig. Formation of the Giant Planets by Concurrent Accretion of Solids and Gas. Icarus, 124:62–85, November 1996. doi: 10.1006/icar.1996.0190.

K. M. Pontoppidan, G. A. Blake, E. F. van Dishoeck, A. Smette, M. J. Ireland, and J. Brown. Spectroastrometric Imaging of Molecular Gas within Protoplanetary Disk Gaps. ApJ, 684:1323–1329, September 2008. doi: 10.1086/590400.

S. S. Prasad and W. T. Huntress, Jr. A model for gas phase chemistry in interstellar clouds. I - The basic model, library of chemical reactions, and chemistry among C, N, and O compounds. ApJ, 43:1–35, May 1980. doi: 10.1086/190665.

R. K. Prinja, D. Massa, A. W. Fullerton, I. D. Howarth, and M. Pontefract. Wind variability of B supergiants. II. The two-component stellar wind of γ Arae. A&A, 318:157–170, February 1997.

C. Qi, P. D'Alessio, K. I. Öberg, D. J. Wilner, A. M. Hughes, S. M. Andrews, and S. Ayala. Resolving the CO Snow Line in the Disk around HD 163296. ApJ, 740:84, October 2011. doi: 10.1088/0004-637X/740/2/84.

C. Qi, K. I. Öberg, D. J. Wilner, P. D'Alessio, E. Bergin, S. M. Andrews, G. A. Blake, M. R. Hogerheijde, and E. F. van Dishoeck. Imaging of the CO Snow Line in a Solar Nebula Analog. Science, 341:630–632, August 2013. doi: 10.1126/science.1239560.

G. R. Quast, C. A. O. Torres, R. de La Reza, L. da Silva, and M. Mayor. V4046 Sgr, a key young binary system. In IAU Symposium, volume 200 of IAU Symposium, page 28P, 2000.

M. A. Quijada, J. Del Hoyo, and S. Rice. Enhanced far-ultraviolet reflectance of MgF_2 and LiF over-coated Al mirrors. In Space Telescopes and Instrumentation 2014: Ultraviolet to Gamma Ray, volume 9144 of Proc. SPIE, page 91444G, July 2014. doi: 10.1117/12.2057438.

B. L. Rachford, T. P. Snow, J. Tumlinson, J. M. Shull, W. P. Blair, R. Ferlet, S. D. Friedman, C. Gry, E. B. Jenkins, D. C. Morton, B. D. Savage, P. Sonnentrucker, A. Vidal-Madjar, D. E. Welty, and D. G. York. A Far Ultraviolet Spectroscopic Explorer Survey of Interstellar Molecular Hydrogen in Translucent Clouds. ApJ, 577:221–244, September 2002. doi: 10.1086/342146.

B. L. Rachford, T. P. Snow, J. D. Destree, T. L. Ross, R. Ferlet, S. D. Friedman, C. Gry, E. B. Jenkins, D. C. Morton, B. D. Savage, J. M. Shull, P. Sonnentrucker, J. Tumlinson, A. Vidal-Madjar, D. E. Welty, and D. G. York. Molecular Hydrogen in the Far Ultraviolet Spectroscopic Explorer Translucent Lines of Sight: The Full Sample. ApJ, 180:125–137, January 2009. doi: 10.1088/0067-0049/180/1/125.

S. K. Ramsay Howat and J. S. Greaves. Molecular hydrogen emission from discs in the η Chamaeleontis cluster. MNRAS, 379:1658–1664, August 2007. doi: 10.1111/j.1365-2966.2007.12049.x.

V. A. Rapson, J. H. Kastner, S. M. Andrews, D. C. Hines, B. Macintosh, M. Millar-Blanchaer, and M. Tamura. Scattered Light from Dust in the Cavity of the V4046 Sgr Transition Disk. ApJL, 803:L10, April 2015. doi: 10.1088/2041-8205/803/1/L10.

L. Reboussin, V. Wakelam, S. Guilloteau, F. Hersant, and A. Dutrey. Chemistry in protoplanetary disks: the gas-phase CO/H_2 ratio and the carbon reservoir. A&A, 579:A82, July 2015. doi: 10.1051/0004-6361/201525885.

S. Redfield. The Local Interstellar Medium. In S. J. Kannappan, S. Redfield, J. E. Kessler-Silacci, M. Landriau, and N. Drory, editors, New Horizons in Astronomy: Frank N. Bash Symposium, volume 352 of Astronomical Society of the Pacific Conference Series, page 79, September 2006.

S. Redfield. Physical Properties of the Local Interstellar Medium, page 323. 2009. doi: 10.1007/978-1-4419-0247-4_26.

S. Redfield and J. L. Linsky. The Structure of the Local Interstellar Medium. I. High-Resolution Observations of Fe II, Mg II, and Ca II toward Stars within 100 Parsecs. ApJS, 139:439–465, April 2002. doi: 10.1086/338650.

S. Redfield and J. L. Linsky. The Structure of the Local Interstellar Medium. II. Observations of D I, C II, N I, O I, Al II, and Si II toward Stars within 100 Parsecs. ApJ, 602:776–802, February 2004.

S. Redfield and J. L. Linsky. The Structure of the Local Interstellar Medium. IV. Dynamics, Morphology, Physical Properties, and Implications of Cloud-Cloud Interactions. ApJ, 673:283-314, January 2008. doi: 10.1086/524002.

Z. Regály, Z. Sándor, C. P. Dullemond, and R. van Boekel. Detectability of giant planets in protoplanetary disks by CO emission lines. A&A, 523:A69, November 2010. doi: 10.1051/0004-6361/201014427.

F. Reif. Fundamentals of Statistical and Thermal Physics. Waveland Press, 1965.

T. W. Rettig, J. Haywood, T. Simon, S. D. Brittain, and E. Gibb. Discovery of CO Gas in the Inner Disk of TW Hydrae. ApJL, 616:L163–L166, December 2004. doi: 10.1086/426433.

Á. Ribas, B. Merín, H. Bouy, and L. T. Maud. Disk evolution in the solar neighborhood. I. Disk frequencies from 1 to 100 Myr. A&A, 561:A54, January 2014. doi: 10.1051/0004-6361/201322597.

L. Ricci, L. Testi, A. Natta, R. Neri, S. Cabrit, and G. J. Herczeg. Dust properties of protoplanetary disks in the Taurus-Auriga star forming region from millimeter wavelengths. A&A, 512:A15, March 2010. doi: 10.1051/0004-6361/200913403.

W. K. M. Rice, K. Wood, P. J. Armitage, B. A. Whitney, and J. E. Bjorkman. Constraints on a planetary origin for the gap in the protoplanetary disc of GM Aurigae. MNRAS, 342:79–85, June 2003. doi: 10.1046/j.1365-8711.2003.06515.x.

W. K. M. Rice, G. Lodato, J. E. Pringle, P. J. Armitage, and I. A. Bonnell. Accelerated planetesimal growth in self-gravitating protoplanetary discs. MNRAS, 355:543–552, December 2004. doi: 10.1111/j.1365-2966.2004.08339.x.

W. Roberge and A. Dalgarno. Collision-induced dissociation of H2 and CO molecules. ApJ, 255: 176–180, April 1982. doi: 10.1086/159815.

D. R. Rodriguez, J. H. Kastner, D. Wilner, and C. Qi. Imaging the Molecular Disk Orbiting the Twin Young Suns of V4046 Sgr. ApJ, 720:1684–1690, September 2010. doi: 10.1088/0004-637X/720/2/1684.

J.-Y. Roncin and F. Launay. Atlas of the Vacuum Ultraviolet Emission Spectrum of H2. In A. J. Sauval, R. Blomme, and N. Grevesse, editors, Laboratory and Astronomical High Resolution Spectra, volume 81 of Astronomical Society of the Pacific Conference Series, page 310, 1995.

K. A. Rosenfeld, S. M. Andrews, D. J. Wilner, and H. C. Stempels. A Disk-based Dynamical Mass Estimate for the Young Binary V4046 Sgr. ApJ, 759:119, November 2012a. doi: 10.1088/0004-637X/759/2/119.

K. A. Rosenfeld, C. Qi, S. M. Andrews, D. J. Wilner, S. A. Corder, C. P. Dullemond, S.-Y. Lin, A. M. Hughes, P. D'Alessio, and P. T. P. Ho. Kinematics of the CO Gas in the Inner Regions of the TW Hya Disk. ApJ, 757:129, October 2012b. doi: 10.1088/0004-637X/757/2/129.

K. A. Rosenfeld, S. M. Andrews, D. J. Wilner, J. H. Kastner, and M. K. McClure. The Structure of the Evolved Circumbinary Disk around V4046 Sgr. ApJ, 775:136, October 2013. doi: 10.1088/0004-637X/775/2/136.

D. Rosenthal, F. Bertoldi, and S. Drapatz. ISO-SWS observations of OMC-1: H_2 and fine structure lines. A&A, 356:705–723, April 2000.

M. Salaris and S. Cassisi. Evolution of Stars and Stellar Populations. 2005.

R. Salmeron, A. Königl, and M. Wardle. Angular momentum transport in protostellar discs. MNRAS, 375:177–183, February 2007. doi: 10.1111/j.1365-2966.2006.11277.x.

C. Salyk, G. A. Blake, A. C. A. Boogert, and J. M. Brown. Molecular Gas in the Inner 1 AU of the TW Hya and GM Aur Transitional Disks. ApJL, 655:L105–L108, February 2007. doi: 10.1086/512012.

C. Salyk, K. M. Pontoppidan, G. A. Blake, F. Lahuis, E. F. van Dishoeck, and N. J. Evans, II. H_2O and OH Gas in the Terrestrial Planet-forming Zones of Protoplanetary Disks. ApJL, 676: L49–L52, March 2008. doi: 10.1086/586894.

C. Salyk, G. A. Blake, A. C. A. Boogert, and J. M. Brown. High-resolution 5 μm Spectroscopy of Transitional Disks. ApJ, 699:330–347, July 2009. doi: 10.1088/0004-637X/699/1/330.

C. Salyk, G. A. Blake, A. C. A. Boogert, and J. M. Brown. CO Rovibrational Emission as a Probe of Inner Disk Structure. ApJ, 743:112, December 2011a. doi: 10.1088/0004-637X/743/2/112.

C. Salyk, K. M. Pontoppidan, G. A. Blake, J. R. Najita, and J. S. Carr. A Spitzer Survey of Mid-infrared Molecular Emission from Protoplanetary Disks. II. Correlations and Local Thermal Equilibrium Models. ApJ, 731:130, April 2011b. doi: 10.1088/0004-637X/731/2/130.

Y. Sato and Y. Nakagawa. Spectral Energy Distributions of Protoplanetary Disks: Effects of Growth and Settling of Dust Particles. In T. Nakamoto, editor, Star Formation 1999, pages 235–236, December 1999.

B. D. Savage, R. C. Bohlin, J. F. Drake, and W. Budich. A survey of interstellar molecular hydrogen. I. ApJ, 216:291–307, August 1977. doi: 10.1086/155471.

J. Schaye. Star Formation Thresholds and Galaxy Edges: Why and Where. ApJ, 609:667–682, July 2004. doi: 10.1086/421232.

E. Schindhelm, K. France, E. B. Burgh, G. J. Herczeg, J. C. Green, A. Brown, J. M. Brown, and J. A. Valenti. Characterizing CO Fourth Positive Emission in Young Circumstellar Disks. ApJ, 746:97, February 2012a. doi: 10.1088/0004-637X/746/1/97.

E. Schindhelm, K. France, G. J. Herczeg, E. Bergin, H. Yang, A. Brown, J. M. Brown, J. L. Linsky, and J. Valenti. Lyα Dominance of the Classical T Tauri Far-ultraviolet Radiation Field. ApJL, 756:L23, September 2012b. doi: 10.1088/2041-8205/756/1/L23.

E. Schinnerer, S. E. Meidt, D. Colombo, R. Chandar, C. L. Dobbs, S. García-Burillo, A. Hughes, A. K. Leroy, J. Pety, M. Querejeta, C. Kramer, and K. F. Schuster. The PdBI Arcsecond Whirlpool Survey (PAWS): The Role of Spiral Arms in Cloud and Star Formation. ApJ, 836:62, February 2017. doi: 10.3847/1538-4357/836/1/62.

M. Schmidt. The Rate of Star Formation. ApJ, 129:243, March 1959. doi: 10.1086/146614.

P. C. Schneider, H. M. Günther, J. Robrade, S. Facchini, K. W. Hodapp, C. F. Manara, V. Perdelwitz, J. H. M. M. Schmitt, S. Skinner, and S. J. Wolk. The nature of the 2014-2015 dim state of RW Aurigae revealed by X-ray, optical, and near-IR observations. A&A, 584:L9, December 2015. doi: 10.1051/0004-6361/201527237.

A. Schruba, A. K. Leroy, F. Walter, F. Bigiel, E. Brinks, W. J. G. de Blok, G. Dumas, C. Kramer, E. Rosolowsky, K. Sandstrom, K. Schuster, A. Usero, A. Weiss, and H. Wiesemeyer. A Molecular Star Formation Law in the Atomic-gas-dominated Regime in Nearby Galaxies. AJ, 142:37, August 2011. doi: 10.1088/0004-6256/142/2/37.

M. Schultheis, B. Q. Chen, B. W. Jiang, O. A. Gonzalez, R. Enokiya, Y. Fukui, K. Torii, M. Rejkuba, and D. Minniti. Mapping the Milky Way bulge at high resolution: the 3D dust extinction, CO, and X factor maps. A&A, 566:A120, June 2014. doi: 10.1051/0004-6361/201322788.

K. R. Schwarz, E. A. Bergin, L. I. Cleeves, G. A. Blake, K. Zhang, K. I. Öberg, E. F. van Dishoeck, and C. Qi. The Radial Distribution of H_2 and CO in TW Hya as Revealed by Resolved ALMA Observations of CO Isotopologues. ApJ, 823:91, June 2016. doi: 10.3847/0004-637X/823/2/91.

K. Sellgren. The near-infrared continuum emission of visual reflection nebulae. ApJ, 277:623–633, February 1984. doi: 10.1086/161733.

K. Sellgren, M. W. Werner, and H. L. Dinerstein. Extended near-infrared emission from visual reflection nebulae. ApJL, 271:L13–L17, August 1983. doi: 10.1086/184083.

R. Shetty, J. Roman-Duval, S. Hony, D. Cormier, R. S. Klessen, L. K. Konstandin, T. Loredo, E. W. Pellegrini, and D. Ruppert. Simultaneously modelling far-infrared dust emission and its relation to CO emission in star-forming galaxies. MNRAS, 460:67–81, July 2016. doi: 10.1093/mnras/stw930.

A. Shukurov, G. R. Sarson, Å. Nordlund, B. Gudiksen, and A. Brandenburg. The effects of spiral arms on the multi-phase ISM. A&SS, 289:319–322, February 2004. doi: 10.1023/B:ASTR.0000014960.35780.2e.

J. M. Shull. H2 resonance fluorescence with Lyman-alpha. ApJ, 224:841–847, September 1978. doi: 10.1086/156433.

J. M. Shull and S. Beckwith. Interstellar molecular hydrogen. ARA&A, 20:163–190, 1982. doi: 10.1146/annurev.aa.20.090182.001115.

O. H. W. Siegmund, A. S. Tremsin, and J. V. Vallerga. Development of cross strip MCP detectors for UV and optical instruments. In UV, X-Ray, and Gamma-Ray Space Instrumentation for Astronomy XVI, volume 7435 of Proc. SPIE, page 74350L, August 2009.

M. Simon, A. Dutrey, and S. Guilloteau. Dynamical Masses of T Tauri Stars and Calibration of Pre-Main-Sequence Evolution. ApJ, 545:1034–1043, December 2000. doi: 10.1086/317838.

D. Smith, N. G. Adams, and E. Alge. Some H/D exchange reactions involved in the deuteration of interstellar molecules. ApJ, 263:123–129, December 1982. doi: 10.1086/160487.

T. P. Snow and A. G. Jensen. Interstellar Abundances and Depletions Based On FUSE Spectra. In G. Sonneborn, H. W. Moos, and B.-G. Andersson, editors, Astrophysics in the Far Ultraviolet: Five Years of Discovery with FUSE, volume 348 of Astronomical Society of the Pacific Conference Series, page 457, June 2006.

T. P. Snow, Jr. and E. B. Jenkins. Interstellar depletions and far-ultraviolet extinction in the Rho Ophiuchi cloud. ApJ, 241:161–172, October 1980. doi: 10.1086/158328.

P. M. Solomon, A. R. Rivolo, J. Barrett, and A. Yahil. Mass, luminosity, and line width relations of Galactic molecular clouds. ApJ, 319:730–741, August 1987. doi: 10.1086/165493.

A. K. Speck, M. Meixner, D. Fong, P. R. McCullough, D. E. Moser, and T. Ueta. Large-Scale Extended Emission around the Helix Nebula: Dust, Molecules, Atoms, and Ions. AJ, 123:346–361, January 2002. doi: 10.1086/338089.

L. Spitzer, J. F. Drake, E. B. Jenkins, D. C. Morton, J. B. Rogerson, and D. G. York. Spectrophotometric Results from the Copernicus Satellite.IV. Molecular Hydrogen in Interstellar Space. ApJL, 181:L116, May 1973. doi: 10.1086/181197.

L. Spitzer, Jr., W. D. Cochran, and A. Hirshfeld. Column densities of interstellar molecular hydrogen. ApJS, 28:373–389, October 1974. doi: 10.1086/190323.

T. P. Stecher and D. A. Williams. Photodestruction of Hydrogen Molecules in H I Regions. ApJL, 149:L29, July 1967. doi: 10.1086/180047.

H. C. Stempels and N. Piskunov. Spectroscopy of T Tauri stars with UVES. Observations and analysis of RU Lup. A&A, 391:595–608, August 2002. doi: 10.1051/0004-6361:20020814.

H. C. Stempels, G. F. Gahm, and P. P. Petrov. Periodic radial velocity variations in RU Lupi. A&A, 461:253–259, January 2007. doi: 10.1051/0004-6361:20065268.

K. M. Strom, S. E. Strom, S. Edwards, S. Cabrit, and M. F. Skrutskie. Circumstellar material associated with solar-type pre-main-sequence stars - A possible constraint on the timescale for planet building. AJ, 97:1451–1470, May 1989. doi: 10.1086/115085.

J. Takahashi, K. Masuda, and M. Nagaoka. Product Energy Distribution of Molecular Hydrogen Formed on Icy Mantles of Interstellar Dust. ApJ, 520:724–731, August 1999. doi: 10.1086/307461.

T. Takeuchi and P. Artymowicz. Dust Migration and Morphology in Optically Thin Circumstellar Gas Disks. ApJ, 557:990–1006, August 2001. doi: 10.1086/322252.

T. Takeuchi and D. N. C. Lin. Radial Flow of Dust Particles in Accretion Disks. ApJ, 581: 1344–1355, December 2002. doi: 10.1086/344437.

T. Takeuchi, C. J. Clarke, and D. N. C. Lin. The Differential Lifetimes of Protostellar Gas and Dust Disks. ApJ, 627:286–292, July 2005. doi: 10.1086/430393.

H. Tanaka, Y. Himeno, and S. Ida. Dust Growth and Settling in Protoplanetary Disks and Disk Spectral Energy Distributions. I. Laminar Disks. ApJ, 625:414–426, May 2005. doi: 10.1086/429658.

Y.-W. Tang, S. Guilloteau, V. Piétu, A. Dutrey, N. Ohashi, and P. T. P. Ho. The circumstellar disk of AB Aurigae: evidence for envelope accretion at late stages of star formation? A&A, 547: A84, November 2012. doi: 10.1051/0004-6361/201219414.

S. P. Tarafdar and K. S. Krishna Swamy. Molecules in celestial objects. III - Study of CO in interstellar diffuse clouds. MNRAS, 200:431–444, August 1982. doi: 10.1093/mnras/200.2.431.

R. J. Thomas. Toroidal varied-line space (TVLS) gratings. In S. L. Keil and S. V. Avakyan, editors, Innovative Telescopes and Instrumentation for Solar Astrophysics, volume 4853 of Proc. SPIE, pages 411–418, February 2003.

I. Tilling, P. Woitke, G. Meeus, A. Mora, B. Montesinos, P. Riviere-Marichalar, C. Eiroa, W.-F. Thi, A. Isella, A. Roberge, C. Martin-Zaidi, I. Kamp, C. Pinte, G. Sandell, W. D. Vacca, F. Ménard, I. Mendigutía, G. Duchêne, W. R. F. Dent, G. Aresu, R. Meijerink, and M. Spaans. Gas modelling in the disc of HD 163296. A&A, 538:A20, February 2012. doi: 10.1051/0004-6361/201116919.

D. E. Trilling, J. I. Lunine, and W. Benz. Orbital migration and the frequency of giant planet formation. A&A, 394:241–251, October 2002. doi: 10.1051/0004-6361:20021108.

J. Vallerga, R. Raffanti, A. Tremsin, O. Siegmund, J. McPhate, and G. Varner. Large-format high-spatial resolution cross-strip readout MCP detectors for UV astronomy. In Space Telescopes and Instrumentation 2010: Ultraviolet to Gamma Ray, volume 7732 of Proc. SPIE, page 773203, July 2010.

R. van Boekel, M. Min, L. B. F. M. Waters, A. de Koter, C. Dominik, M. E. van den Ancker, and J. Bouwman. A 10 μm spectroscopic survey of Herbig Ae star disks: Grain growth and crystallization. A&A, 437:189–208, July 2005. doi: 10.1051/0004-6361:20042339.

M. E. van den Ancker, D. de Winter, and H. R. E. Tjin A Djie. HIPPARCOS photometry of Herbig Ae/Be stars. A&A, 330:145–154, February 1998.

N. van der Marel, E. F. van Dishoeck, S. Bruderer, L. Pérez, and A. Isella. Gas density drops inside dust cavities of transitional disks around young stars observed with ALMA. A&A, 579: A106, July 2015. doi: 10.1051/0004-6361/201525658.

F. van Leeuwen. Validation of the new Hipparcos reduction. A&A, 474:653–664, November 2007. doi: 10.1051/0004-6361:20078357.

M. E. van Steenberg and J. M. Shull. IUE-IRAS studies of the infrared cirrus. ApJ, 335:197–214, December 1988.

A. Vidal-Madjar, C. Laurent, R. Ferlet, and D. G. York. Neutral interstellar gas toward epsilon Persei - H I, H2, D I, N I, O I, and AR I. ApJ, 260:128–140, September 1982. doi: 10.1086/160240.

A. Vidal-Madjar, C. Laurent, C. Gry, P. Bruston, R. Ferlet, and D. G. York. The ratio of deuterium to hydrogen in interstellar space. V The line of sight to Epsilon Persei. A&A, 120:58–62, April 1983.

C. Walsh, H. Nomura, T. J. Millar, and Y. Aikawa. Chemical Processes in Protoplanetary Disks. II. On the Importance of Photochemistry and X-Ray Ionization. ApJ, 747:114, March 2012. doi: 10.1088/0004-637X/747/2/114.

C. Walsh, H. Nomura, and E. van Dishoeck. The molecular composition of the planet-forming regions of protoplanetary disks across the luminosity regime. A&A, 582:A88, October 2015. doi: 10.1051/0004-6361/201526751.

R. A. Webb, B. Zuckerman, I. Platais, J. Patience, R. J. White, M. J. Schwartz, and C. McCarthy. Discovery of Seven T Tauri Stars and a Brown Dwarf Candidatein the Nearby TW Hydrae Association. ApJL, 512:L63–L67, February 1999. doi: 10.1086/311856.

S. J. Weidenschilling. Aerodynamics of solid bodies in the solar nebula. MNRAS, 180:57–70, July 1977. doi: 10.1093/mnras/180.1.57.

S. J. Weidenschilling and J. N. Cuzzi. Formation of planetesimals in the solar nebula. In E. H. Levy and J. I. Lunine, editors, Protostars and Planets III, pages 1031–1060, 1993.

R. J. White and A. M. Ghez. Observational Constraints on the Formation and Evolution of Binary Stars. ApJ, 556:265–295, July 2001. doi: 10.1086/321542.

K. Willacy and P. M. Woods. Deuterium Chemistry in Protoplanetary Disks. II. The Inner 30 AU. ApJ, 703:479–499, September 2009. doi: 10.1088/0004-637X/703/1/479.

D. Williams and P. Murdin. Physics of Molecules. November 2000. doi: 10.1888/0333750888/2101.

D. W. Wilson, P. D. Maker, R. E. Muller, P. Z. Mouroulis, and J. Backlund. Recent advances in blazed grating fabrication by electron-beam lithography. In P. Z. Mouroulis, W. J. Smith, and R. B. Johnson, editors, Current Developments in Lens Design and Optical Engineering IV, volume 5173 of Proc. SPIE, pages 115–126, November 2003.

P. Woitke, B. Dent, W.-F. Thi, B. Sibthorpe, K. Rice, J. Williams, A. Sicilia-Aguilar, J. Brown, I. Kamp, I. Pascucci, R. Alexander, and A. Roberge. Gas Evolution in Protoplanetary Disks. In E. Stempels, editor, 15th Cambridge Workshop on Cool Stars, Stellar Systems, and the Sun, volume 1094 of American Institute of Physics Conference Series, pages 225–233, February 2009a. doi: 10.1063/1.3099095.

P. Woitke, I. Kamp, and W.-F. Thi. Radiation thermo-chemical models of protoplanetary disks. I. Hydrostatic disk structure and inner rim. A&A, 501:383–406, July 2009b. doi: 10.1051/0004-6361/200911821.

P. Woitke, B. Riaz, G. Duchêne, I. Pascucci, A.-R. Lyo, W. R. F. Dent, N. Phillips, W.-F. Thi, F. Ménard, G. J. Herczeg, E. Bergin, A. Brown, A. Mora, I. Kamp, G. Aresu, S. Brittain, I. de Gregorio-Monsalvo, and G. Sandell. The unusual protoplanetary disk around the T Tauri star ET Chamaeleontis. A&A, 534:A44, October 2011. doi: 10.1051/0004-6361/201116684.

P. Woitke, W. R. F. Dent, W.-F. Thi, F. Menard, C. Pinte, G. Duchene, G. Sandell, W. Lawson, and I. Kamp. ET Cha - a single T Tauri star with a disk of radius ~ 5 AU ? In Protostars and Planets VI Posters, page 13, July 2013.

L. Wolniewicz, I. Simbotin, and A. Dalgarno. Quadrupole Transition Probabilities for the Excited Rovibrational States of H_2. ApJ, 115:293–313, April 1998. doi: 10.1086/313091.

B. C. Wolven, P. D. Feldman, D. F. Strobel, and M. A. McGrath. Lyα-induced Fluorescence of H_2 and Co in Hubble Space Telescope Spectra of a Comet Shoemaker-Levy 9 Impact Site on Jupiter. ApJ, 475:835–842, February 1997.

T. Wong and L. Blitz. The Relationship between Gas Content and Star Formation in Molecule-rich Spiral Galaxies. ApJ, 569:157–183, April 2002. doi: 10.1086/339287.

B. E. Woodgate, R. A. Kimble, C. W. Bowers, S. Kraemer, M. E. Kaiser, A. C. Danks, J. F. Grady, J. J. Loiacono, M. Brumfield, L. Feinberg, T. R. Gull, S. R. Heap, S. P. Maran, D. Lindler, D. Hood, W. Meyer, C. Vanhouten, V. Argabright, S. Franka, R. Bybee, D. Dorn, M. Bottema, R. Woodruff, D. Michika, J. Sullivan, J. Hetlinger, C. Ludtke, R. Stocker, A. Delamere, D. Rose, I. Becker, H. Garner, J. G. Timothy, M. Blouke, C. L. Joseph, G. Hartig, R. F. Green, E. B. Jenkins, J. L. Linsky, J. B. Hutchings, H. W. Moos, A. Boggess, F. Roesler, and D. Weistrop.

The Space Telescope Imaging Spectrograph Design. PASP, 110:1183–1204, October 1998. doi: 10.1086/316243.

G. Wuchterl, T. Guillot, and J. J. Lissauer. Giant Planet Formation. Protostars and Planets IV, page 1081, May 2000.

G. Wurm and J. Blum. Experiments on Preplanetary Dust Aggregation. Icarus, 132:125–136, March 1998. doi: 10.1006/icar.1998.5891.

M. C. Wyatt. Evolution of Debris Disks. ARA&A, 46:339–383, September 2008. doi: 10.1146/annurev.astro.45.051806.110525.

H. Yang, J. L. Linsky, and K. France. HST/COS Spectra of DF Tau and V4046 Sgr: First Detection of Molecular Hydrogen Absorption Against the Lyα Emission Line. ApJL, 730:L10, March 2011. doi: 10.1088/2041-8205/730/1/L10.

H.-W. Yen, H. B. Liu, P.-G. Gu, N. Hirano, C.-F. Lee, E. Puspitaningrum, and S. Takakuwa. Gas Gaps in the Protoplanetary Disk around the Young Protostar HL Tau. ApJL, 820:L25, April 2016. doi: 10.3847/2041-8205/820/2/L25.

A. N. Youdin. On the Formation of Planetesimals Via Secular Gravitational Instabilities with Turbulent Stirring. ApJ, 731:99, April 2011. doi: 10.1088/0004-637X/731/2/99.

A. N. Youdin and J. Goodman. Streaming Instabilities in Protoplanetary Disks. ApJ, 620:459–469, February 2005. doi: 10.1086/426895.

K. Zhang, N. Crockett, C. Salyk, K. Pontoppidan, N. J. Turner, J. M. Carpenter, and G. A. Blake. Dimming and CO absorption toward the AA Tau protoplanetary disk: An infalling flow caused by disk instability? ApJ, 805:55, May 2015. doi: 10.1088/0004-637X/805/1/55.

Z. Zhu, R. P. Nelson, L. Hartmann, C. Espaillat, and N. Calvet. Transitional and Pre-transitional Disks: Gap Opening by Multiple Planets? ApJ, 729:47, March 2011. doi: 10.1088/0004-637X/729/1/47.

B. Zuckerman and I. Gatley. Molecular hydrogen maps of extended planetary nebulae - The Dumbbell, the Ring, and NGC 2346. ApJ, 324:501–515, January 1988. doi: 10.1086/165910.

Appendix A

Supplemental Material: Chapter 2

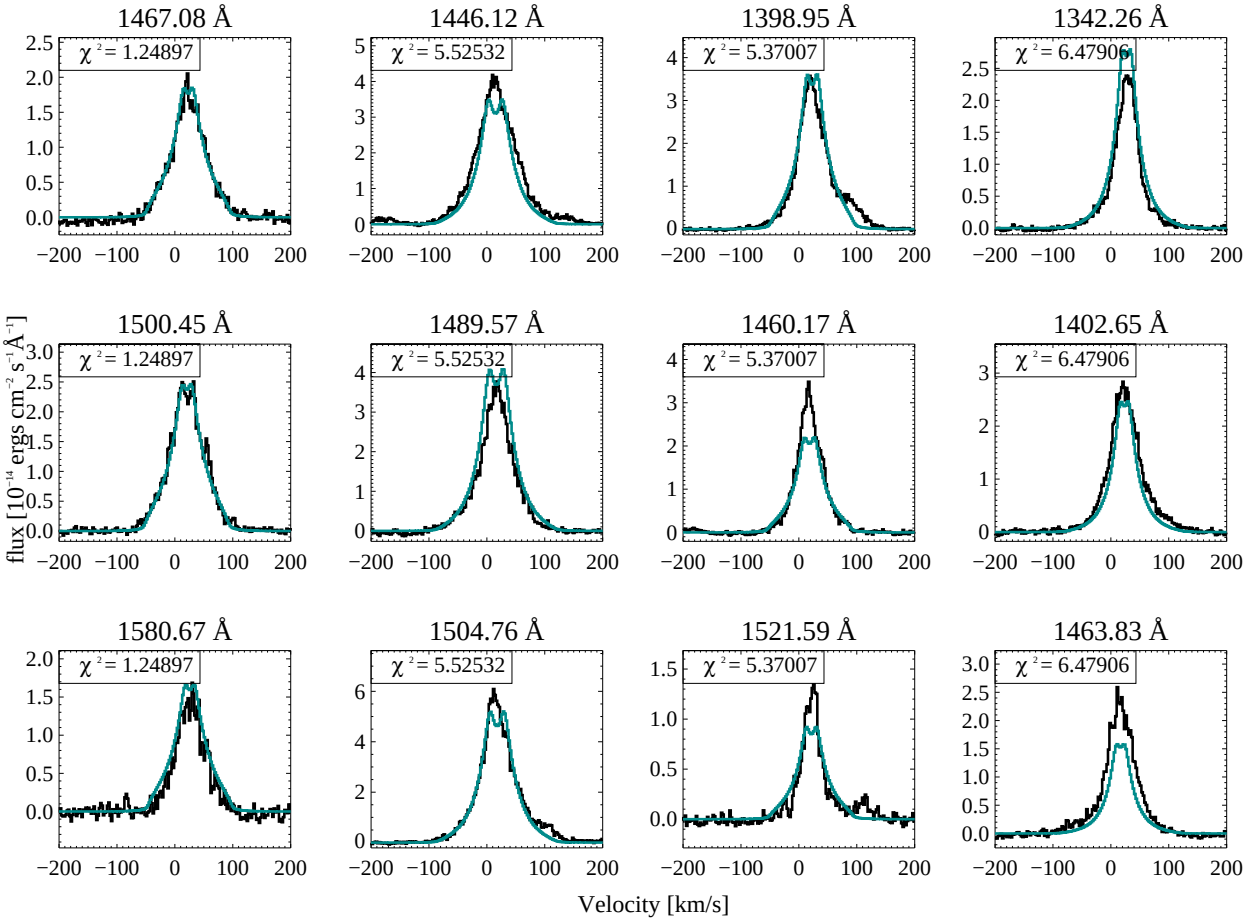

Figure A.1 Model Fits for All Protoplanetary Disk Targets: AA Tau (2011).

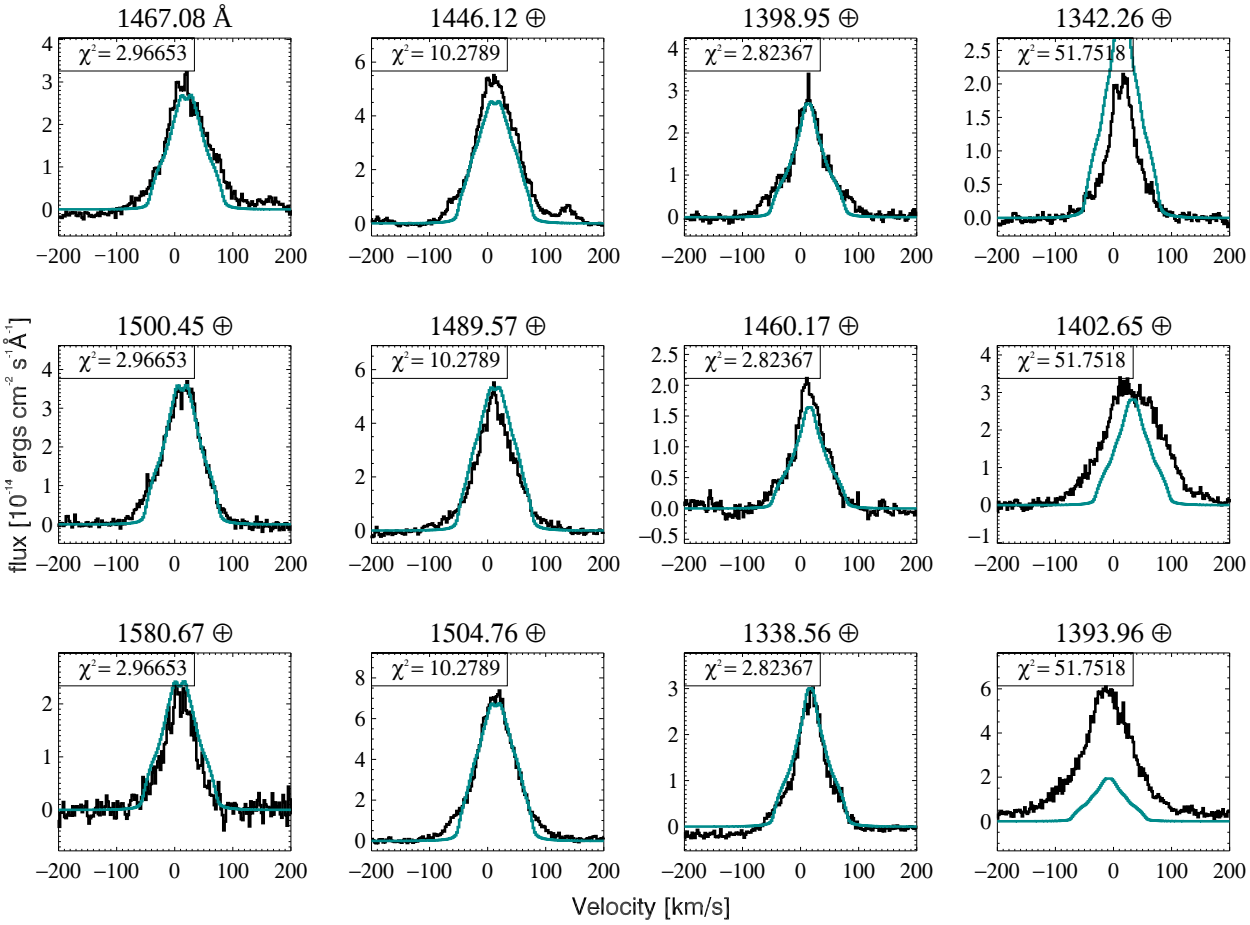

Figure A.2 Model Fits for All Protoplanetary Disk Targets: BP Tau.

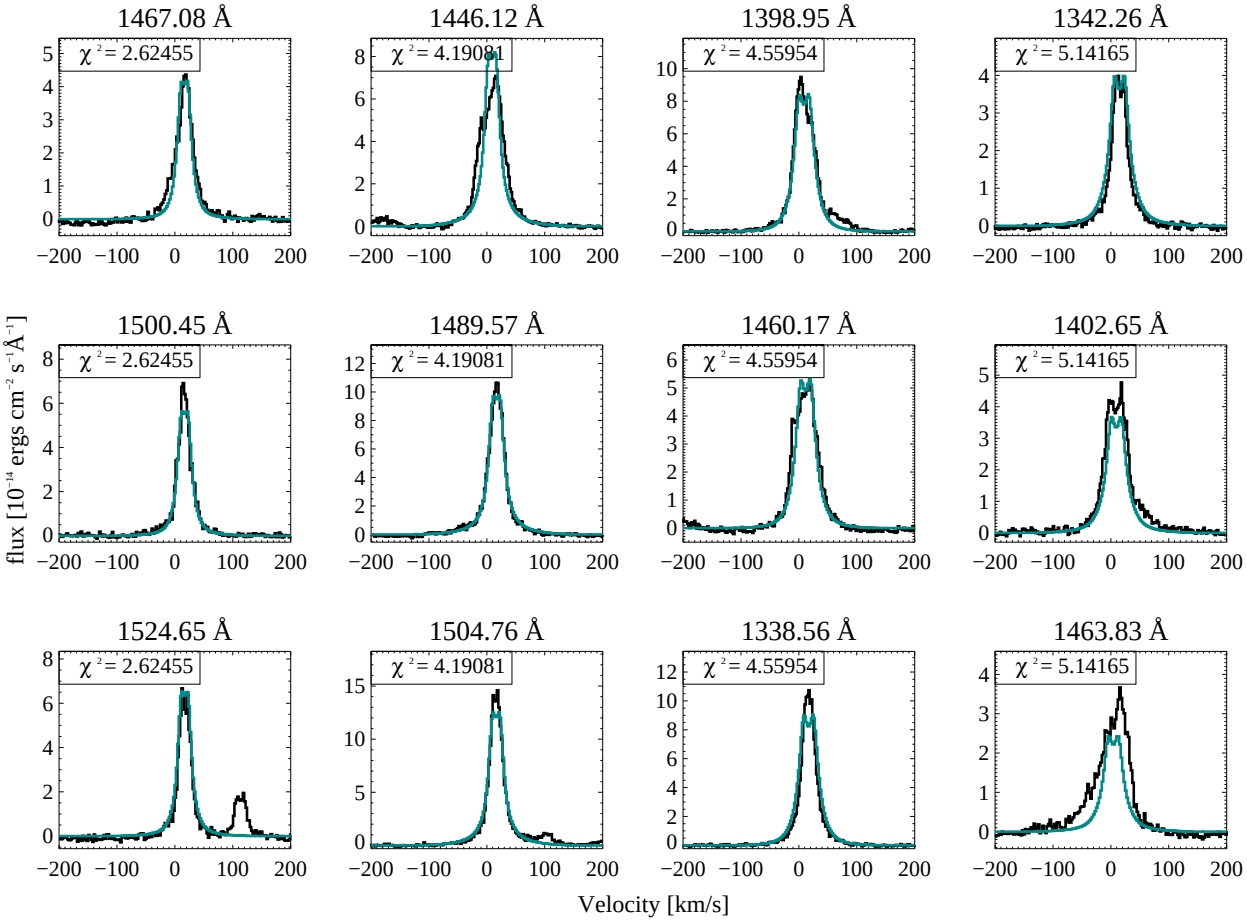

Figure A.3 Model Fits for All Protoplanetary Disk Targets: CS Cha.

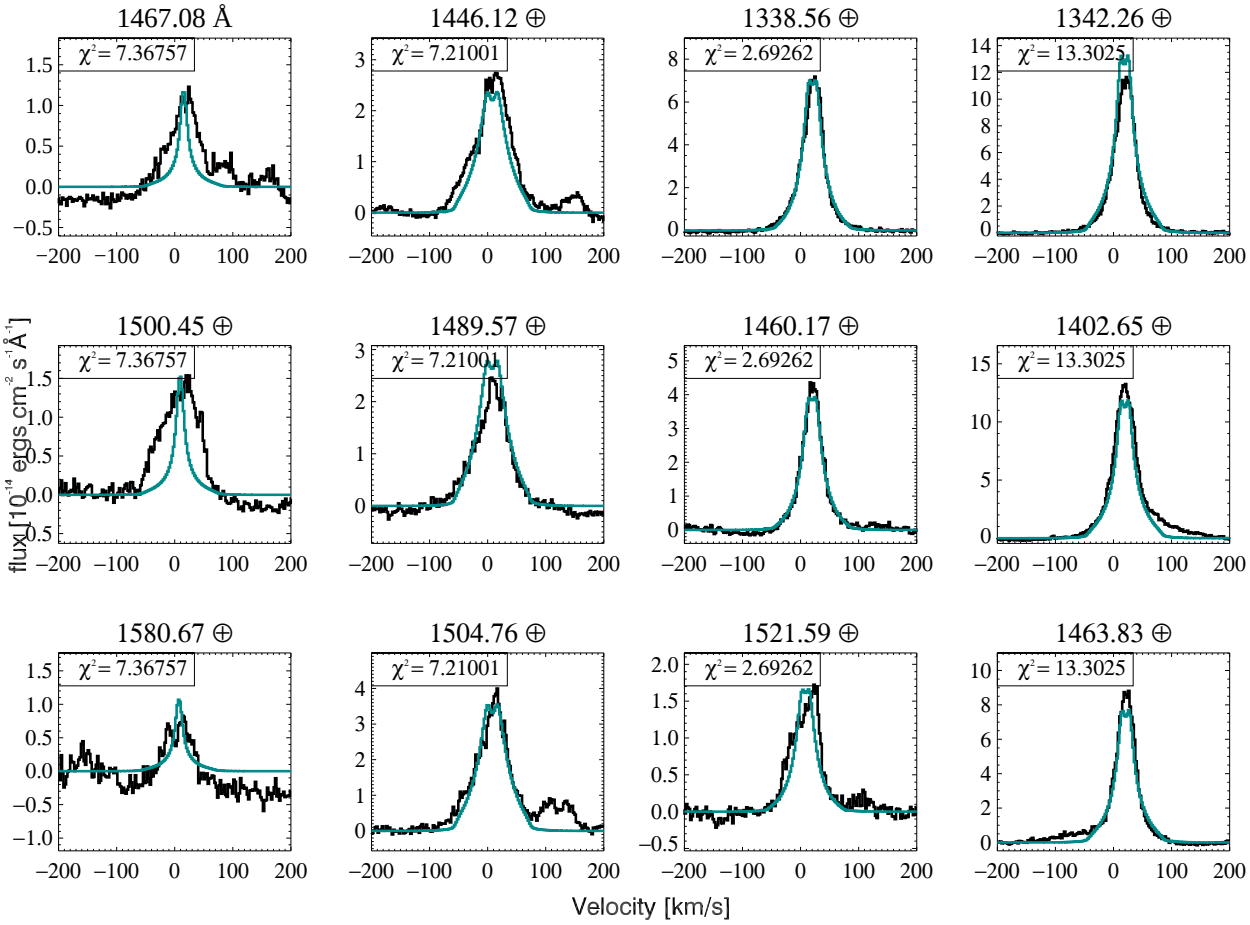

Figure A.4 Model Fits for All Protoplanetary Disk Targets: DF Tau.

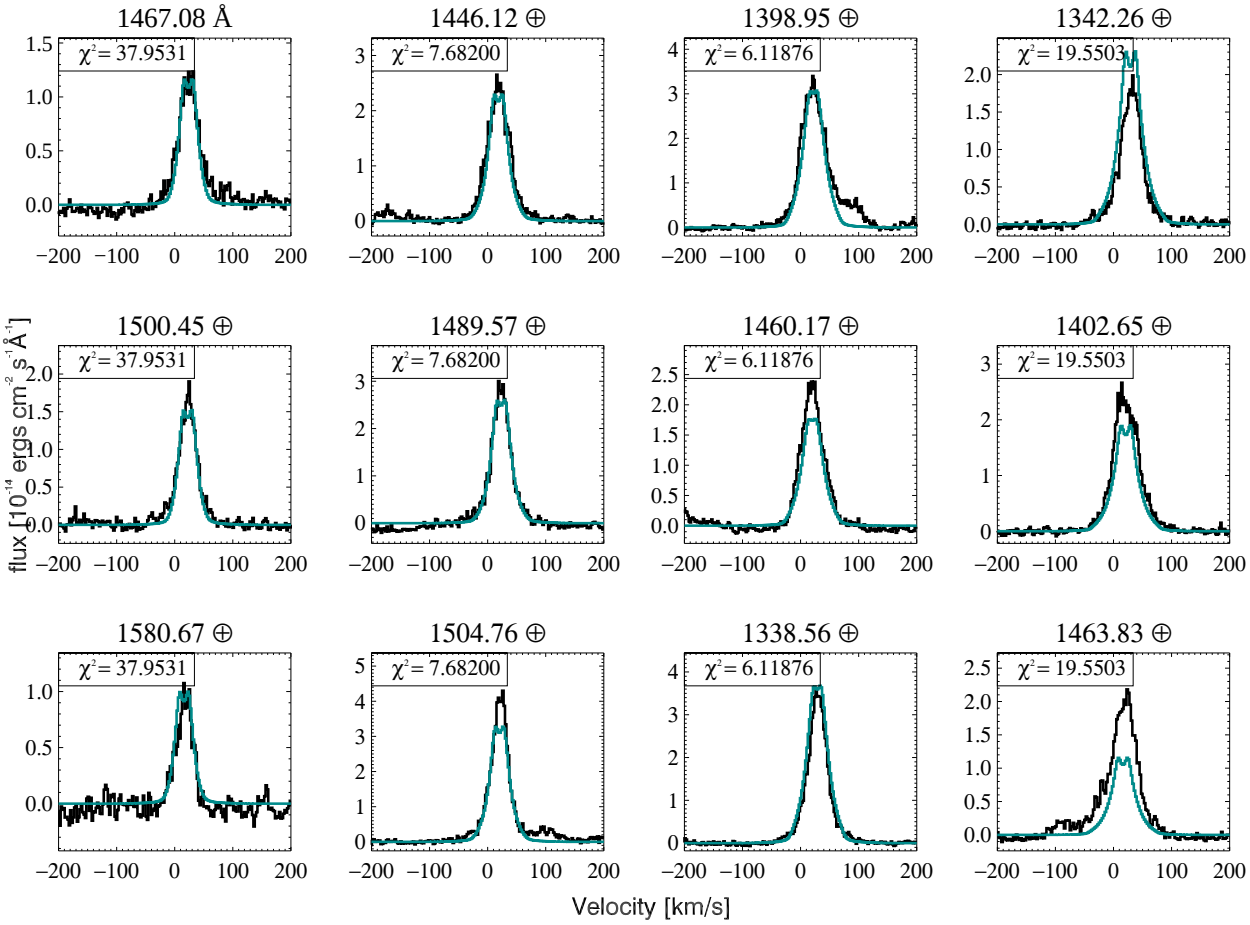

Figure A.5 Model Fits for All Protoplanetary Disk Targets: DM Tau.

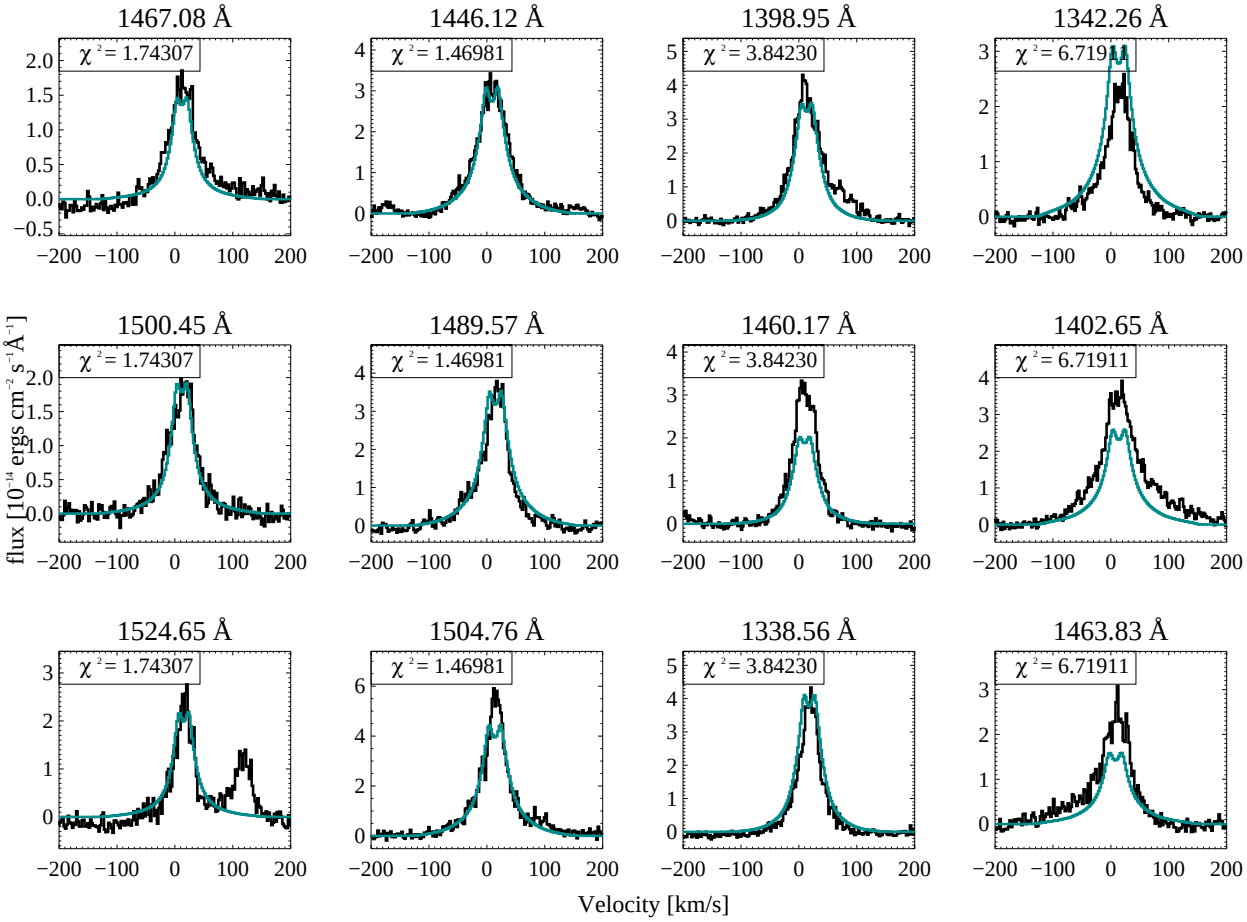

Figure A.6 Model Fits for All Protoplanetary Disk Targets: GM Aur.

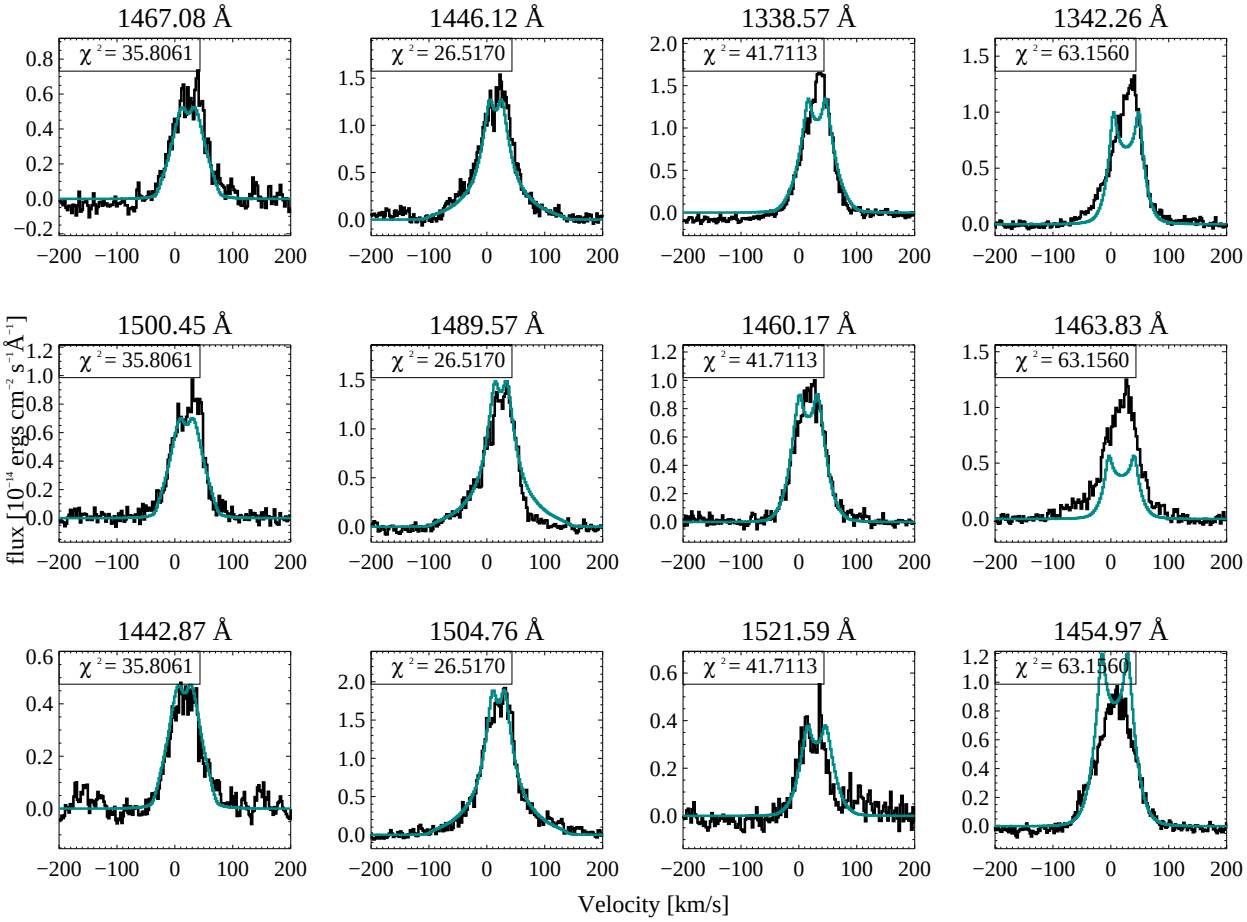

Figure A.7 Model Fits for All Protoplanetary Disk Targets: HN Tau.

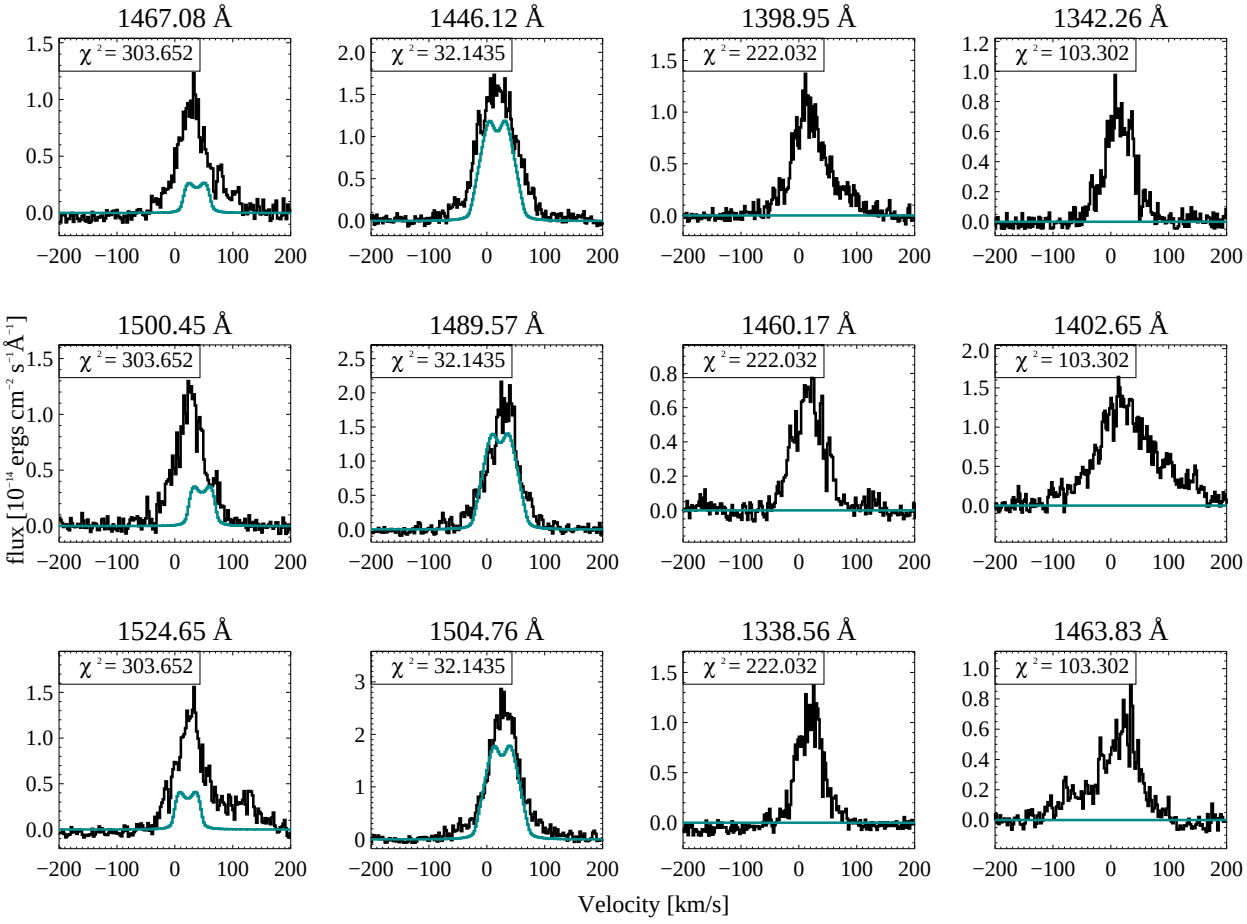

Figure A.8 Model Fits for All Protoplanetary Disk Targets: LkCa 15.

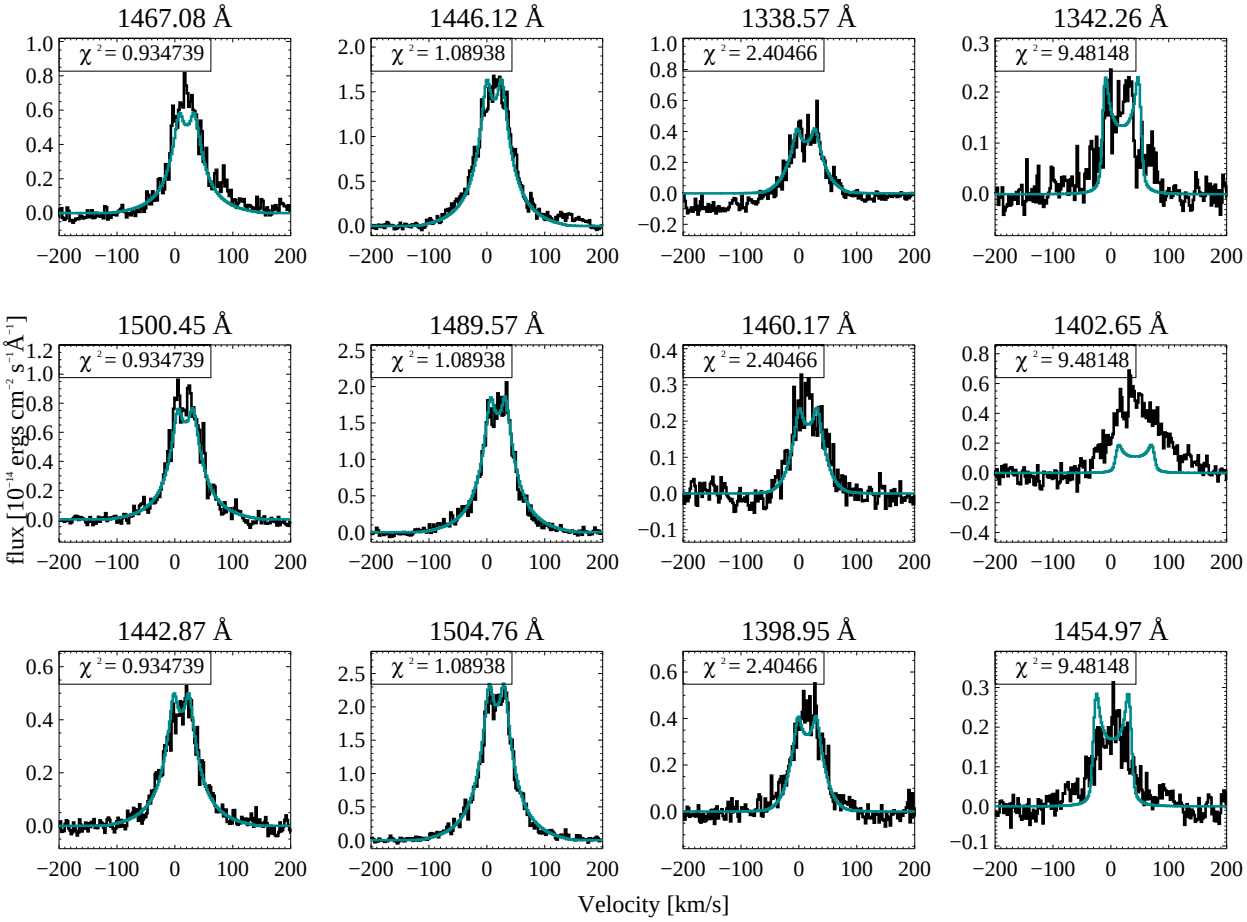

Figure A.9 Model Fits for All Protoplanetary Disk Targets: RECX-11.

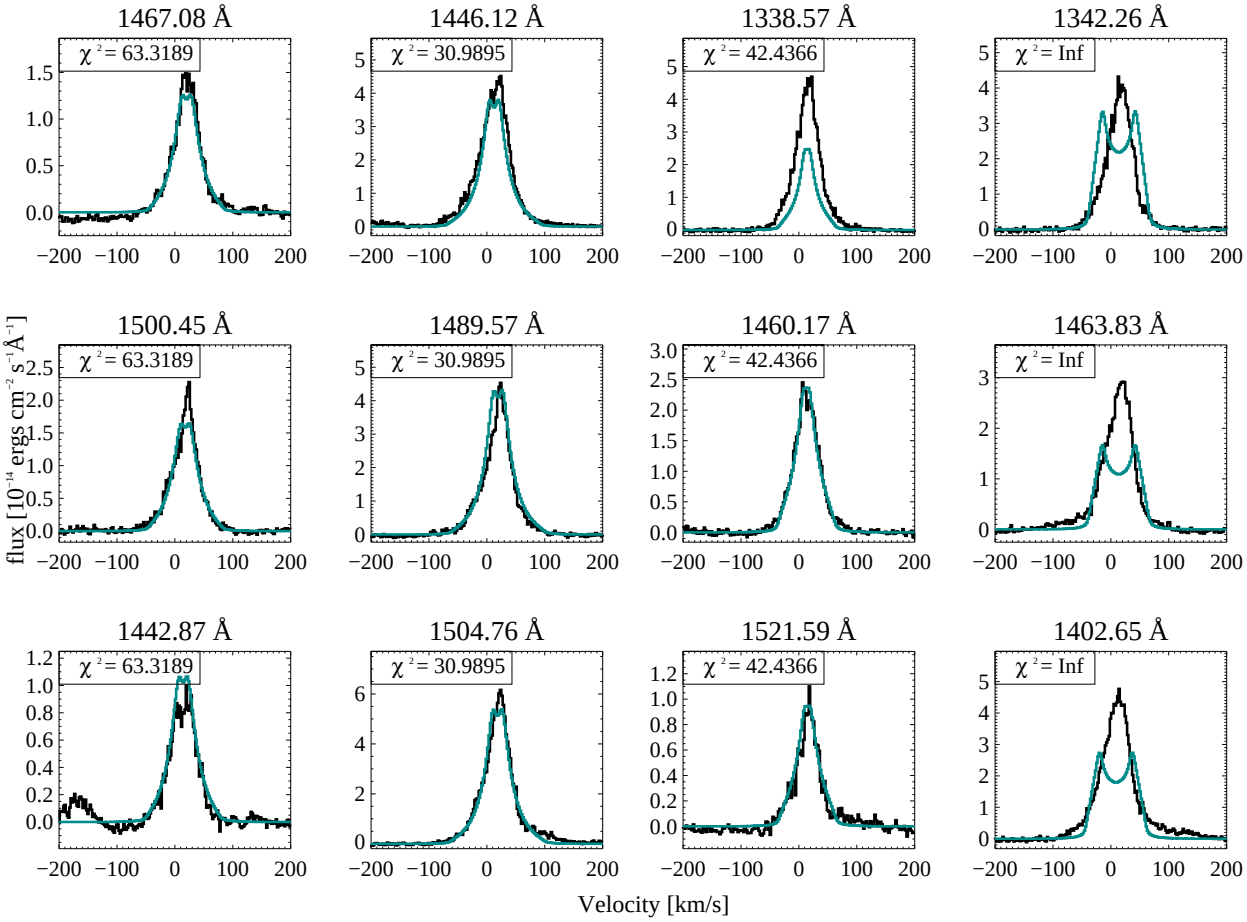

Figure A.10 Model Fits for All Protoplanetary Disk Targets: RECX-15.

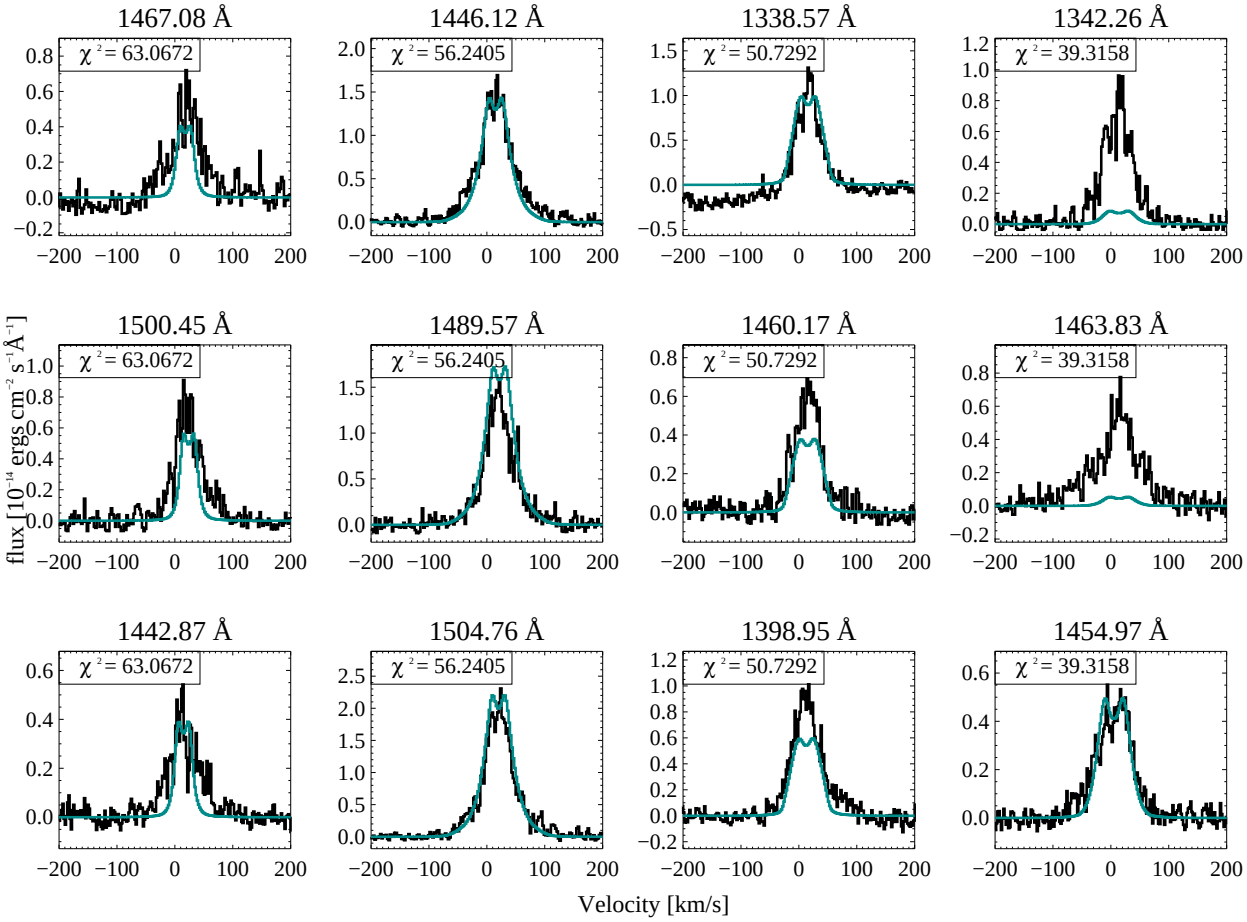

Figure A.11 Model Fits for All Protoplanetary Disk Targets: SU Aur.

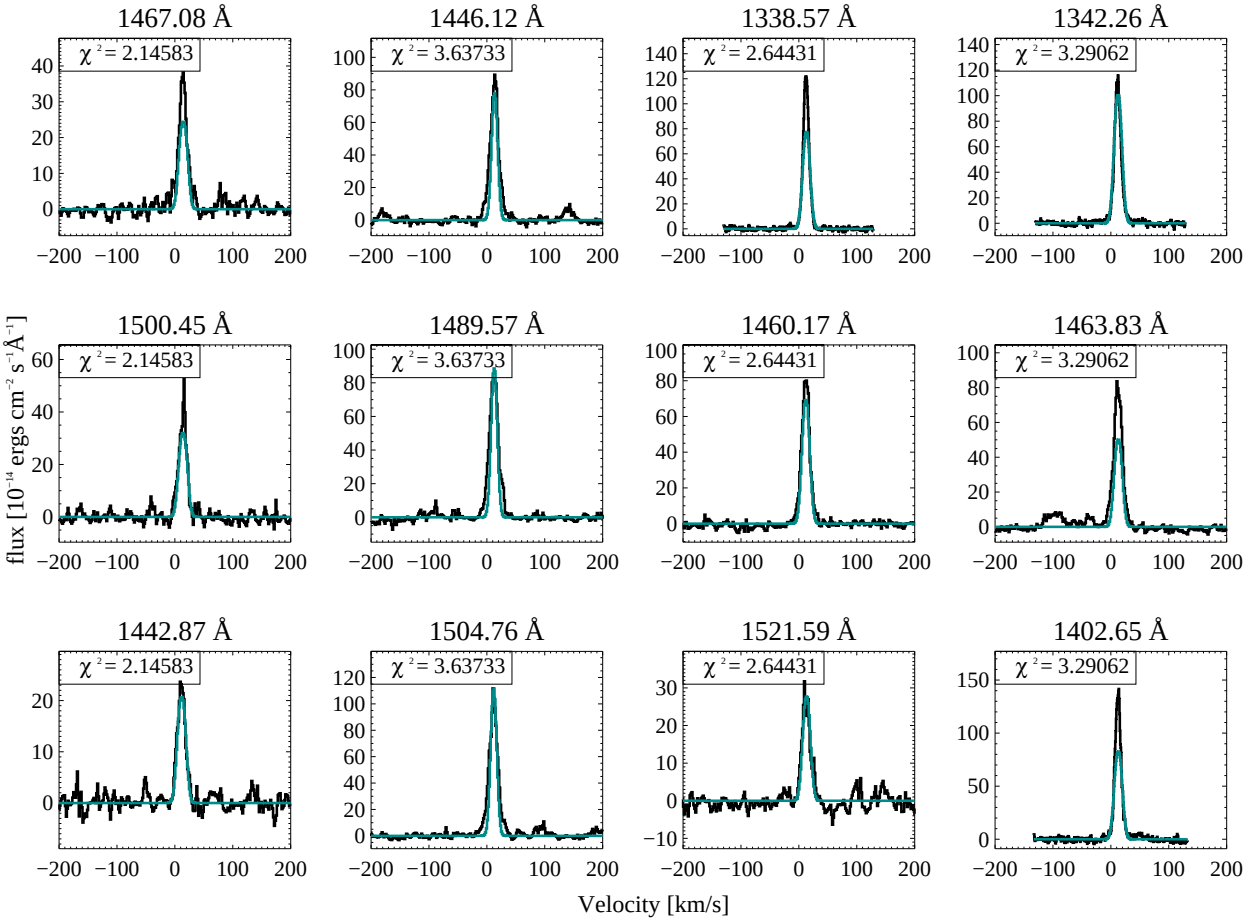

Figure A.12 Model Fits for All Protoplanetary Disk Targets: TW Hya.

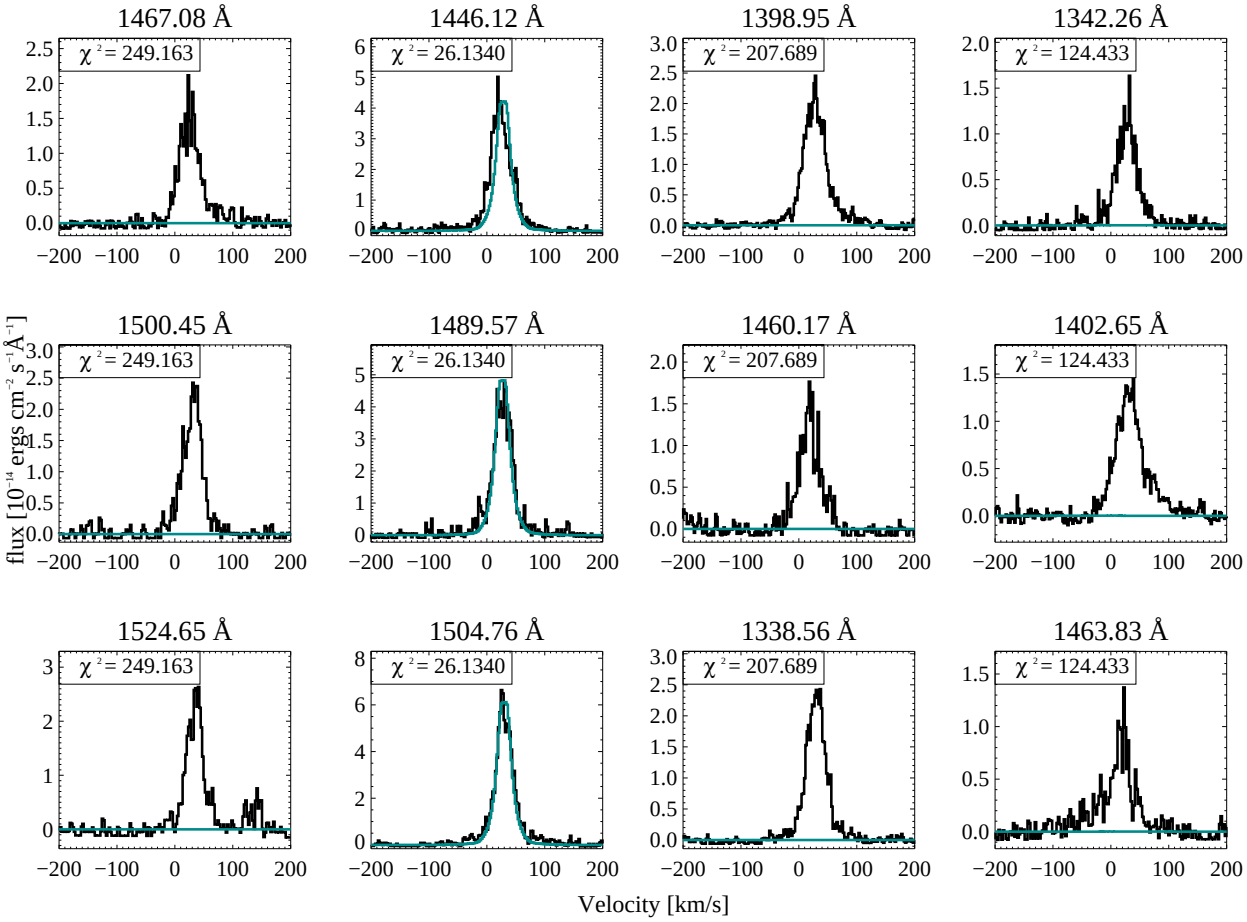

Figure A.13 Model Fits for All Protoplanetary Disk Targets: UX Tau.

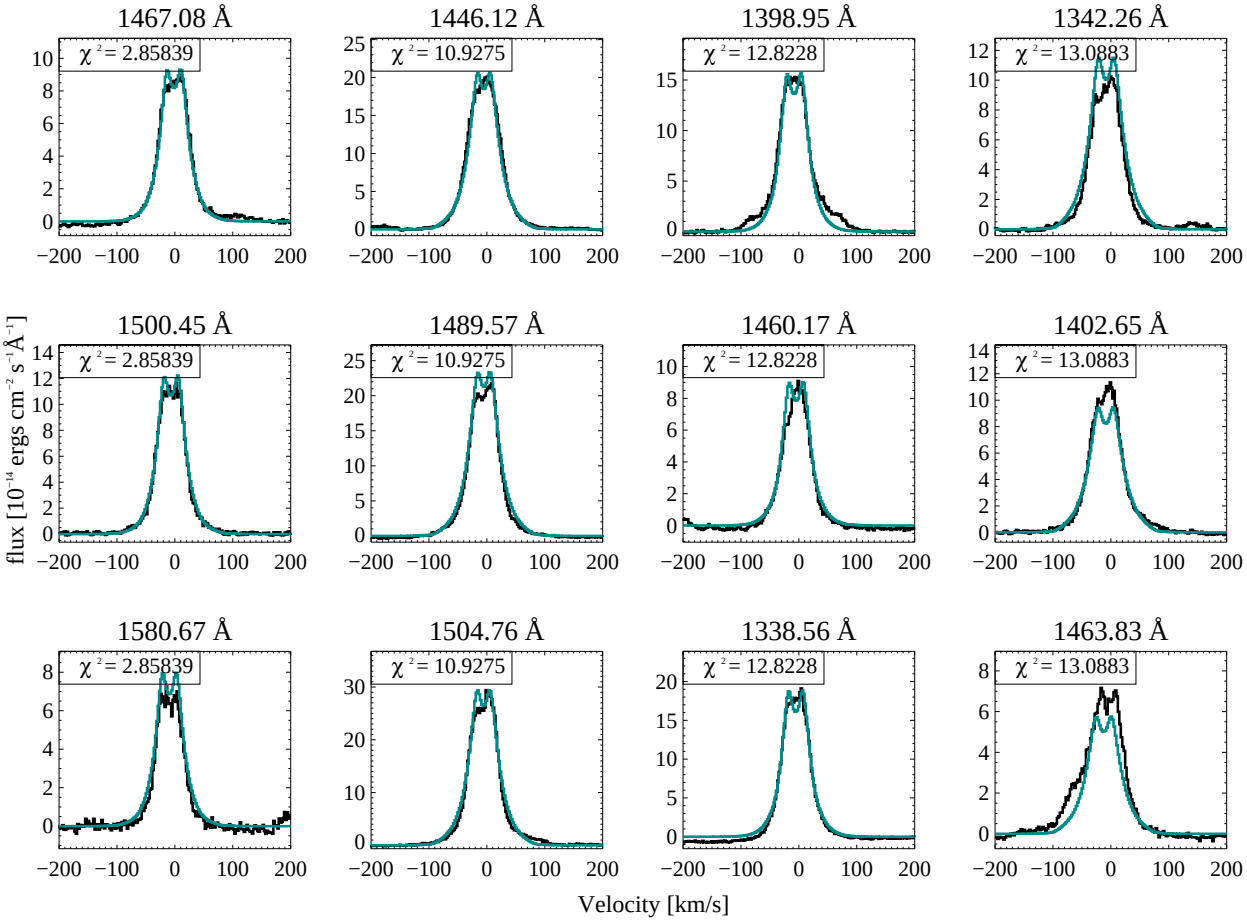

Figure A.14 Model Fits for All Protoplanetary Disk Targets: V4046 Sgr.

Appendix B

Supplemental Material: Chapter 3 - Additional Lyα Profiles, Continuum Fits, and Synthesized H_2 Absorption Models

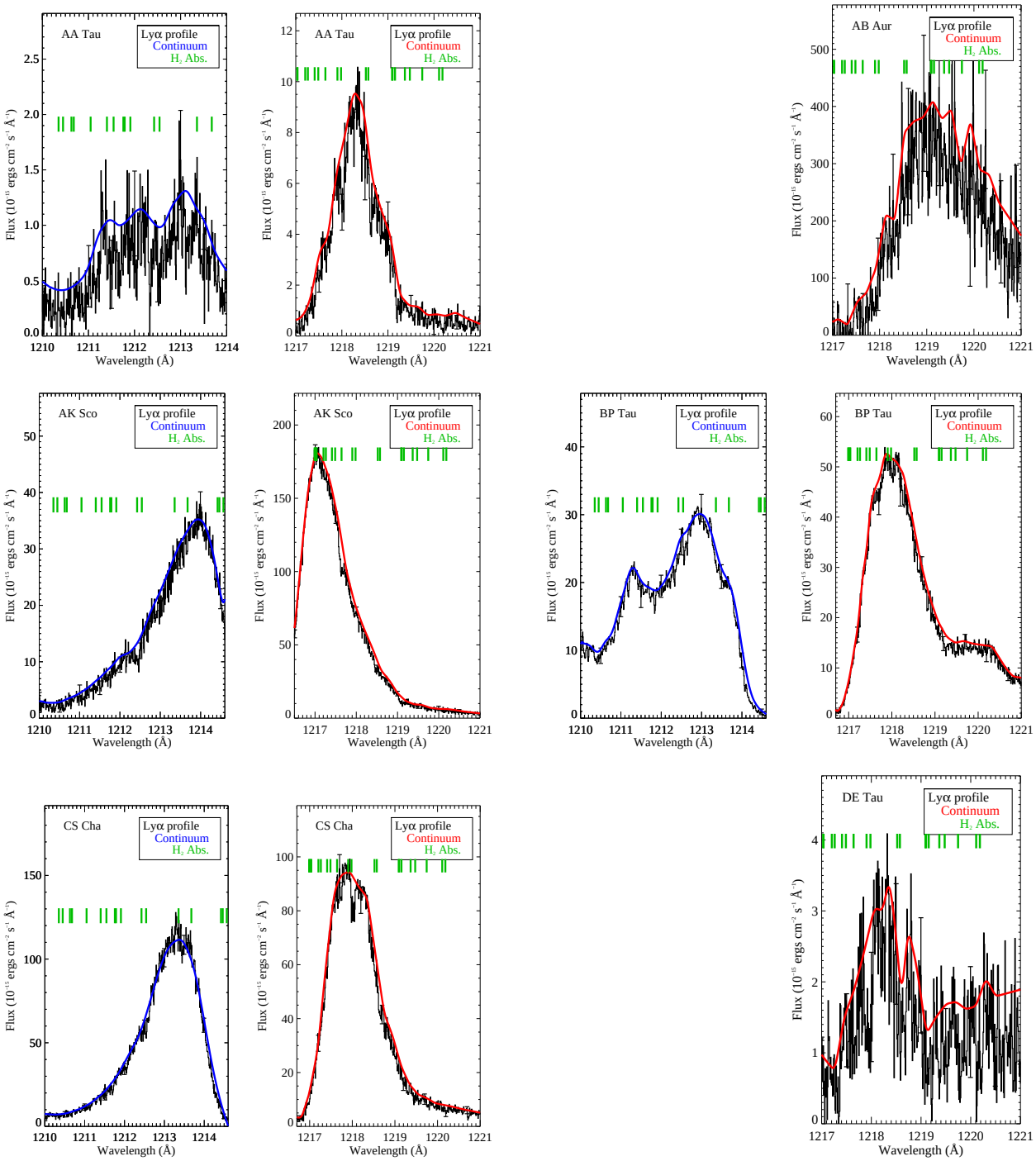

Figure B.1 The Lyα profiles of each target, overlaid with the Lyα "continuum" fit determined from our functional processes (Section 3.3). Two targets are shown per row, where the blue and red Lyα profiles are presented. The Lyα mean flux arrays are over-plotted in blue (over the blue-wing Lyα component) and red (over the red-wing Lyα component). We mark the location of H_2 absorption transitions in the Lyα profiles with green hashes. The continuum fit is determined to normalize the Lyα emission profile, which is achieved by dividing the mean flux continuum through the emission line, creating a normalized spectral region across the Lyα wing.

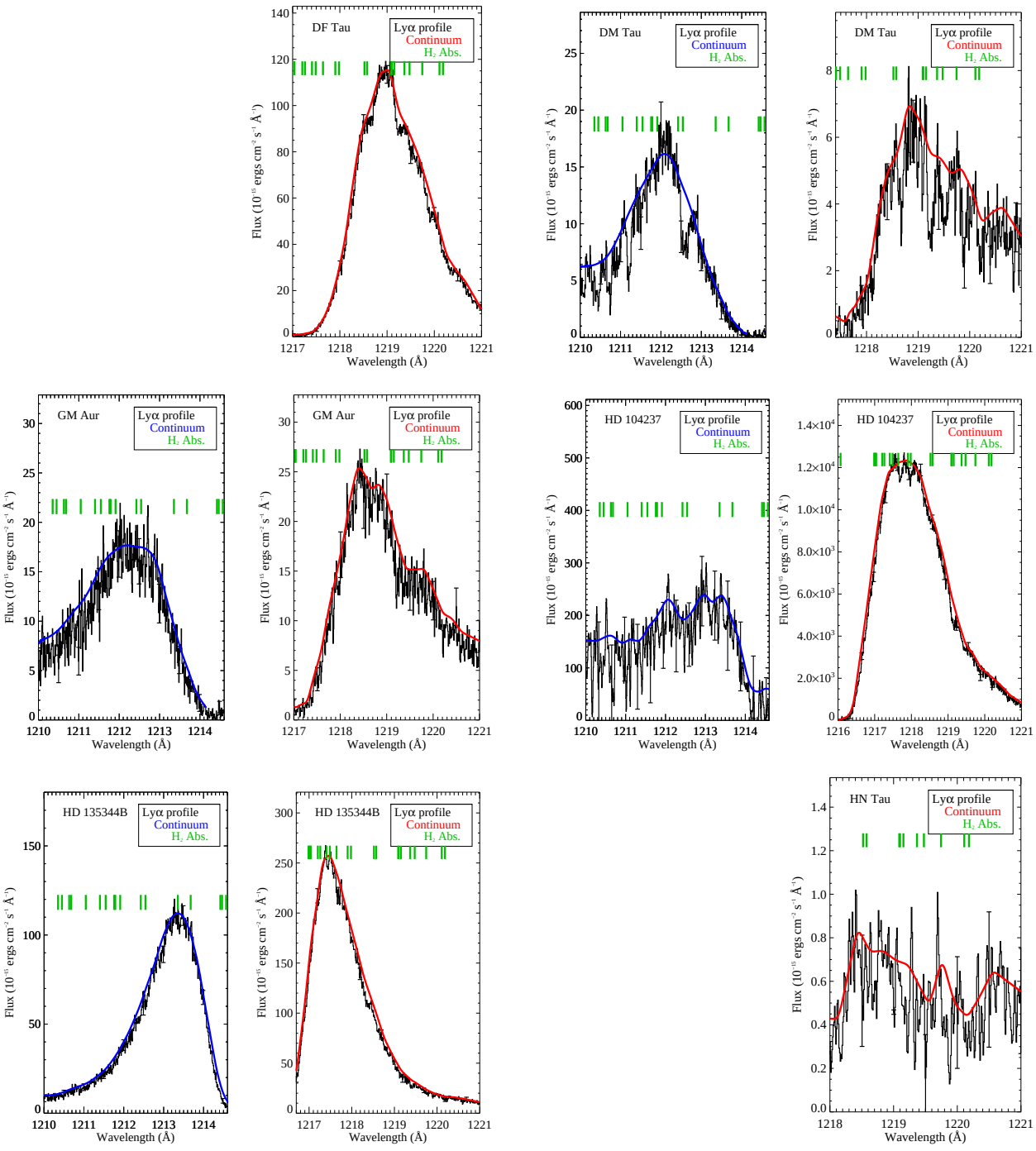

Figure B.1 Continued...

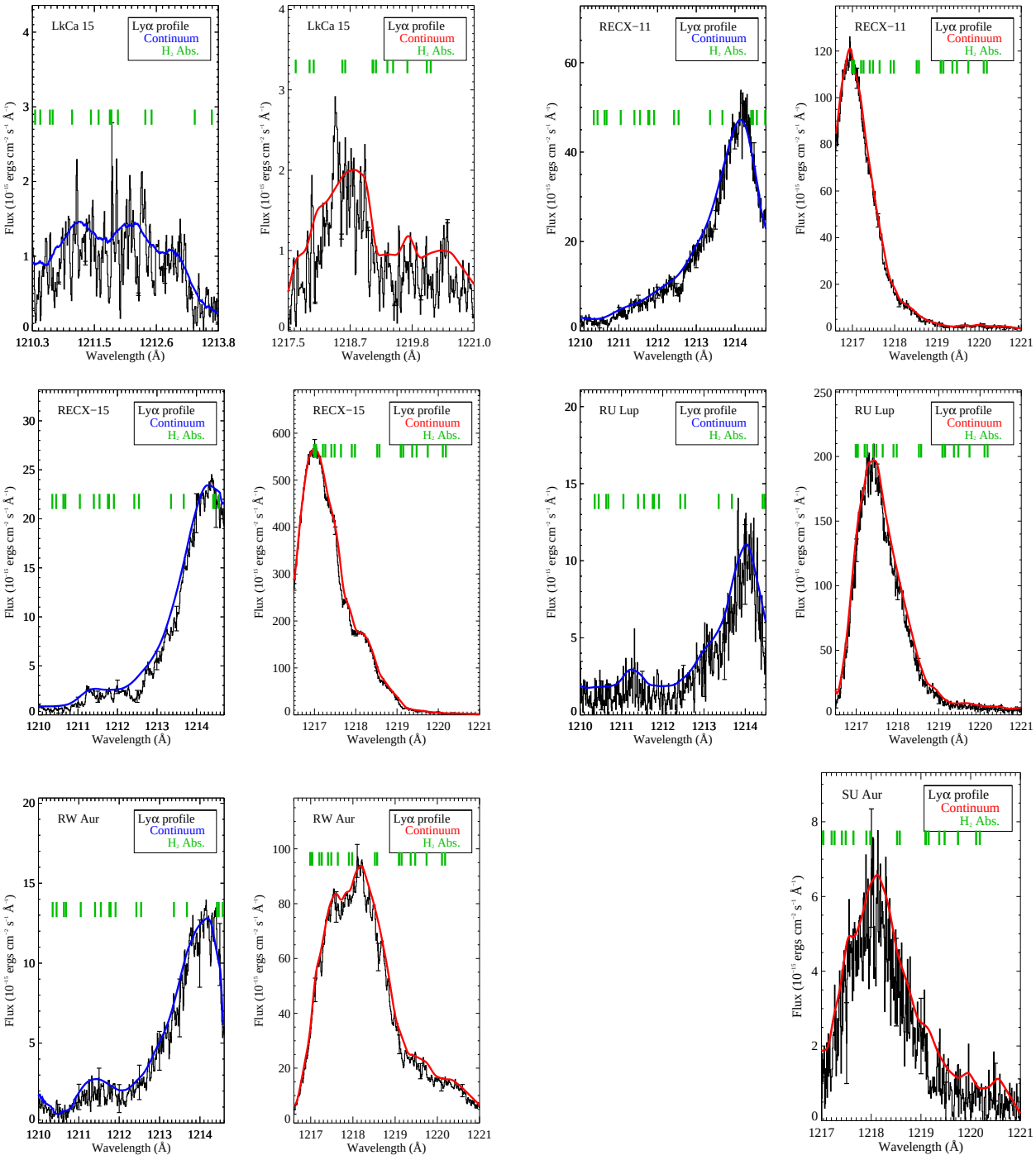

Figure B.1 Continued...

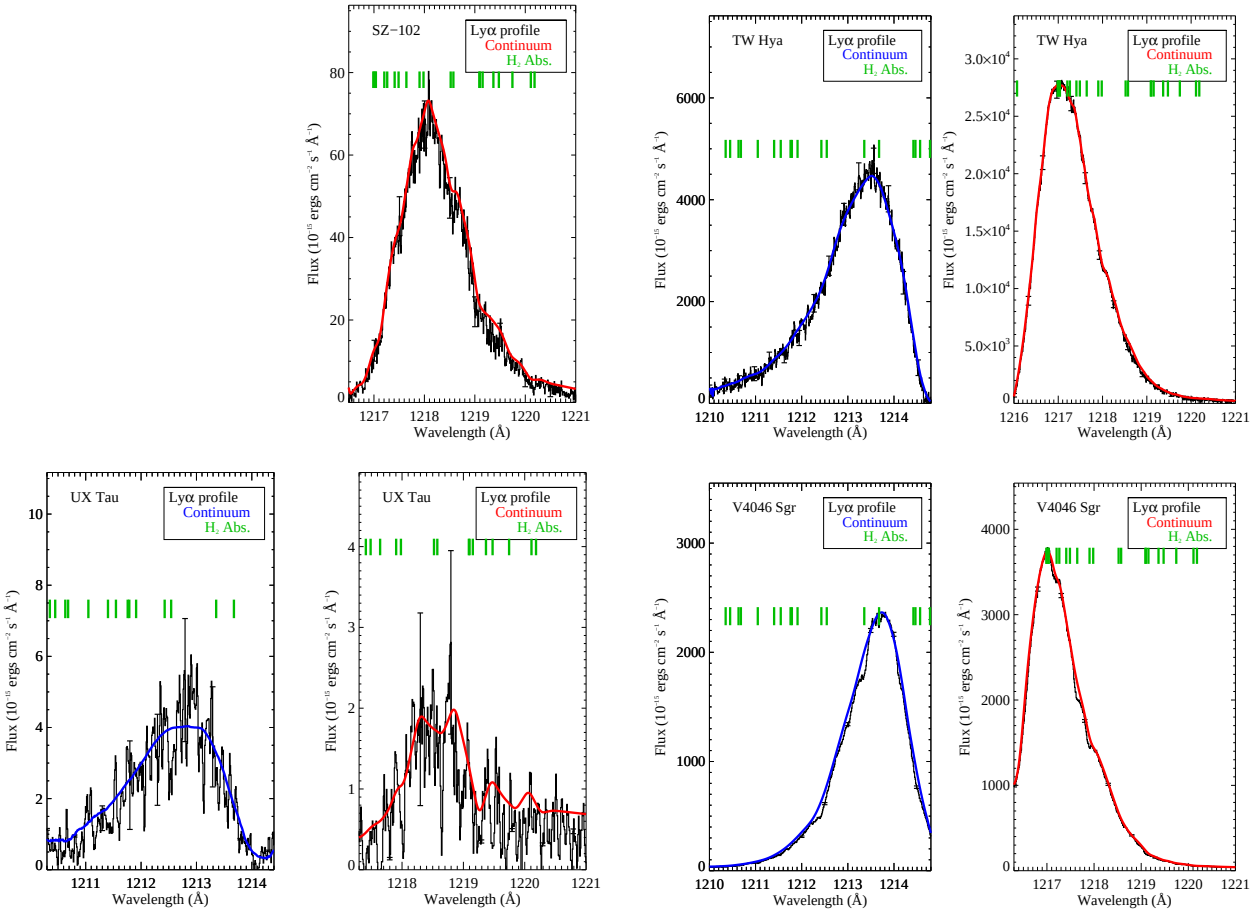

Figure B.1 Continued...

Appendix C

Supplemental Material: Chapter 3 - H_2 Absorption Line Analysis

Information about each H_2 absorption transition was found either in Abgrall et al. (1993a) or Abgrall et al. (1993b), specifically the Einstein A-coefficient, describing the rate of spontaneous decay from state $u \rightarrow l$ (A_{ul}), and the wavenumber. All H_2 transitions were selected from Roncin and Launay (1995) between 1210 - 1221 Å, with transitions preferentially considered from those previously called out by Herczeg et al. (2002) and France et al. (2012b). Other H_2 transitions included in the line-fitting analysis met a minimum (A_{ul}) $\geq 3.0\times10^7$ s^{-1}, to ensure that the absorption transition probabilities were large enough for detection, assuming a warm thermal population of H_2. The energy levels of ground state H_2 in vibration and rotation levels [v,J] (E_{gr}) were derived from equations outlined in `H2ools` (McCandliss 2003), with physical constants taken from Herzberg (1950), Jennings et al. (1984), and Draine (2011). The physical properties of the H_2 transition were derived from intrinsic properties of the molecule:

$$\sigma(\lambda) = \left(\frac{\lambda_\lambda^3}{8\pi c}\right)\left(\frac{g_u}{g_l}\right) A_{ul} \tag{C.1}$$

$$f_{lu} = \left(\frac{m_e c}{8\pi^2 e^2}\right)\left(\frac{g_u}{g_l}\right) \lambda_{lu}^2 A_{ul} \tag{C.2}$$

where λ_λ is the photo-excitation wavelength, Lyα, of H_2 in ground state [v,J]; g_u and g_l are the statistical weights of the electronically-excited [v',J'] and ground [v,J] states, respectively; and ($\pi e^2/m_e c$) is the definition of the classical cross section, expressed as 0.6670 cm^2 s^{-1} in cgs units. Table 3.3 shows all transitions used in our H_2 synthetic absorption model, including physical properties (E_{gr}, f_{lu}, A_{ul}) and level transition information. Not all transitions were implemented

for every target. Depending on the effective range of the stellar Lyα wing in wavelength space, many of the transitions found on the edges of the wings (1210 - 1212: 1213.5 - 1215.2 Å for the blue wing; 1216 - 1218: 1219.5 - 1221 Å for the red wing) were omitted.

The modeled b-value is fixed in all synthetic absorption spectra to replicate the thermal width of a warm bulk population of H_2 ($T(H_2) \geq 2500$ K) in the absence of turbulent velocity broadening. If the b-value were larger, the broadening acts to widen the absorption feature and diminish the depth of the line center, which causes degeneracy between the estimated rovibrational [v,J] level column densities and the thermal/turbulent parameters of the models. When we increased b_{H_2} = 10 km s^{-1}, the column densities of the rovibrational [v,J] levels were systematically reduced by 0.1-0.7 dex for all survey samples.

The multi-component fit of H_2 absorption was mostly insensitive to initial conditions. Initially, we set the same initial conditions for the start of the run (v_r = 0 km s^{-1}; $T(H_2)$ = 2500 K; $\log_{10}$ N(H_2;v,J) varied by transition properties) and allowed the parameters float. Once an effective range of values was determined for all targets, $T(H_2)$ and b_{H_2} were fixed, and only v_r was allowed to float. This produces column density estimates that are relatively comparable for all targets in our survey.

As discussed in France et al. (2012b), only the (0-2)R(2) and (2-2)P(9) levels, whose wavelengths differed by $\Delta\lambda$ = 0.01 Å (at 1219.09 and 1219.10 Å, respectively), were sensitive to the initial conditions. The total column density at this wavelength range is robust, while the relative columns shared between the two transitions was not. To mitigate this, we weighed the individual columns by the product of their oscillator strengths and relative populations of the two levels at $T(H_2)$ = 2500 K. Using the methodology laid out in `H2ools` and Equation C.2, we calculate the oscillator strengths and relative populations of the two lines to be [$f_{R(2)} = 25.5 \times 10^{-3}$; $P_{R(2)} = 5.76 \times 10^{-4}$] and [$f_{R(9)} = 31.8 \times 10^{-3}$; $P_{R(9)} = 6.24 \times 10^{-4}$], respectively. Therefore, N(2,2) contributes 0.425 of the total column density determined at 1219.10 Å, while N(2,9) contributes 0.575 of the total column. Column 2 of Figure C.1 show the minimized multi-component synthetic spectra plotted over the normalized Lyα wings for the red-ward and blue-ward profile components,

respectively.

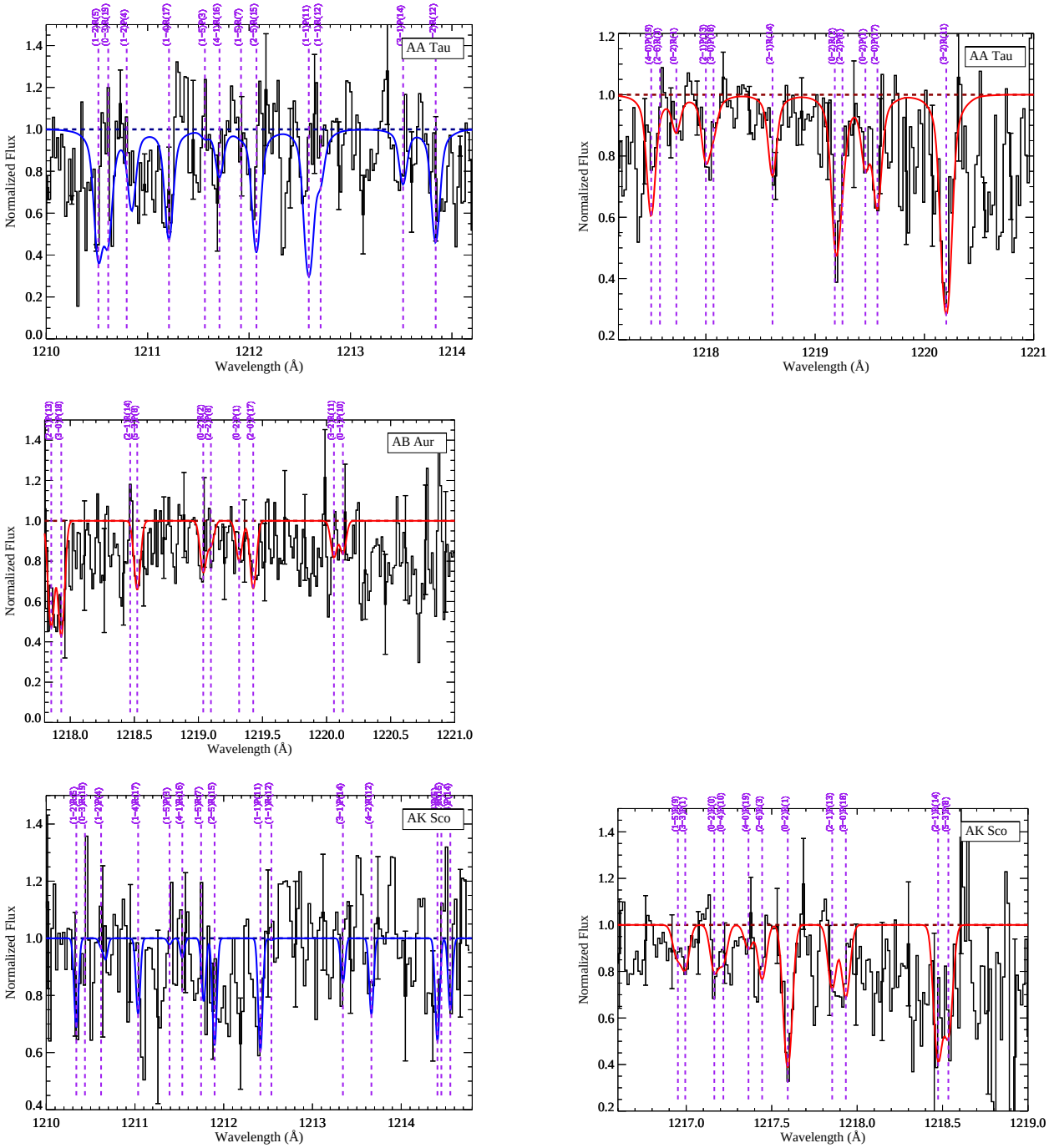

Figure C.1 The final, synthesized absorption spectra of warm H_2 against the Lyα transmission spectra. For targets that have transmission spectra for both blue and red Lyα wings, blue wing spectra are shown on the **left** (blue H_2 absorption fit) and red wing spectra are on the **right** (red H_2 absorption fit). For targets with only a red-wing transmission spectrum, red-wing fits are shown on the **left** (red H_2 absorption fit).

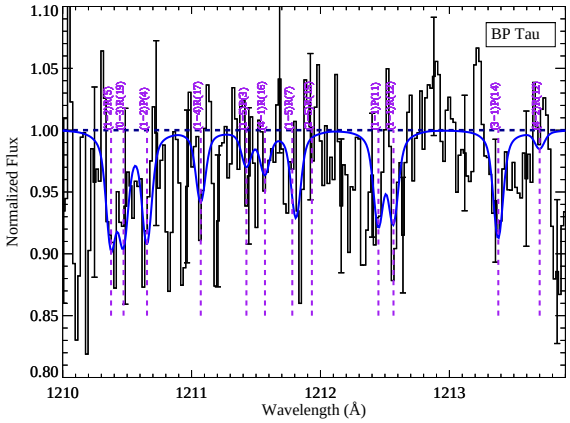

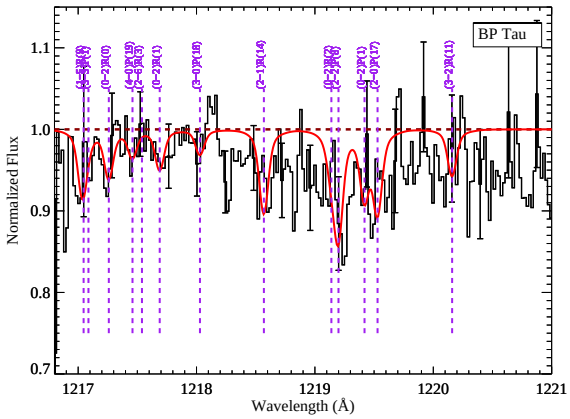

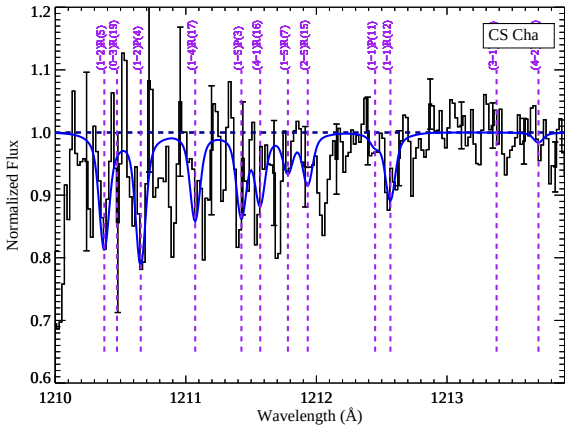

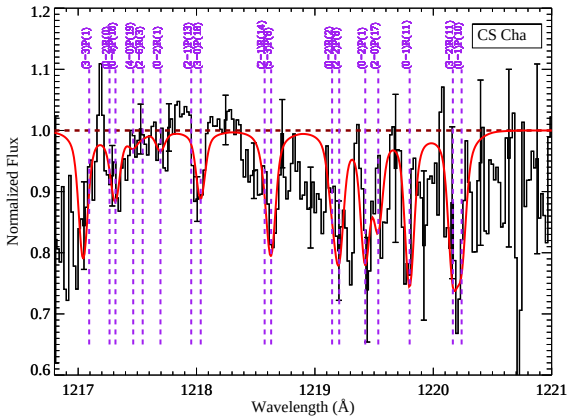

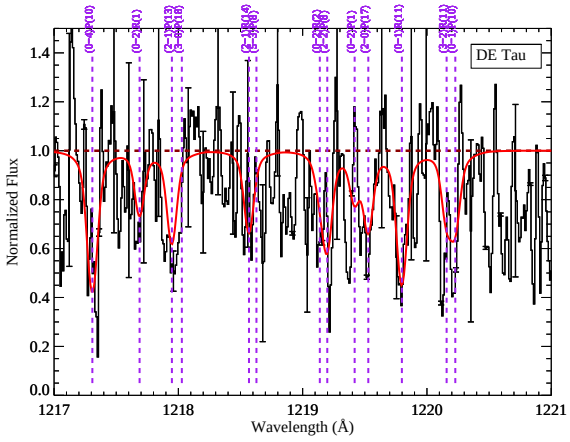

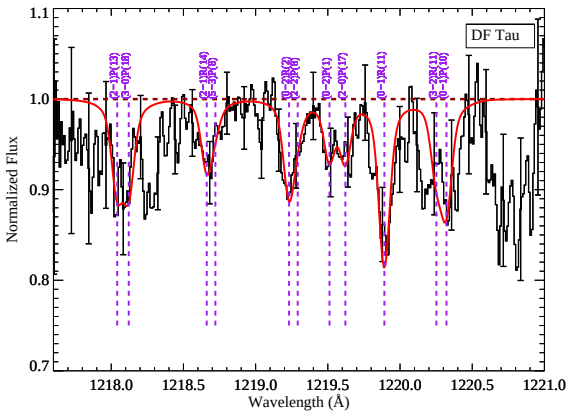

Figure C.1 Continued...

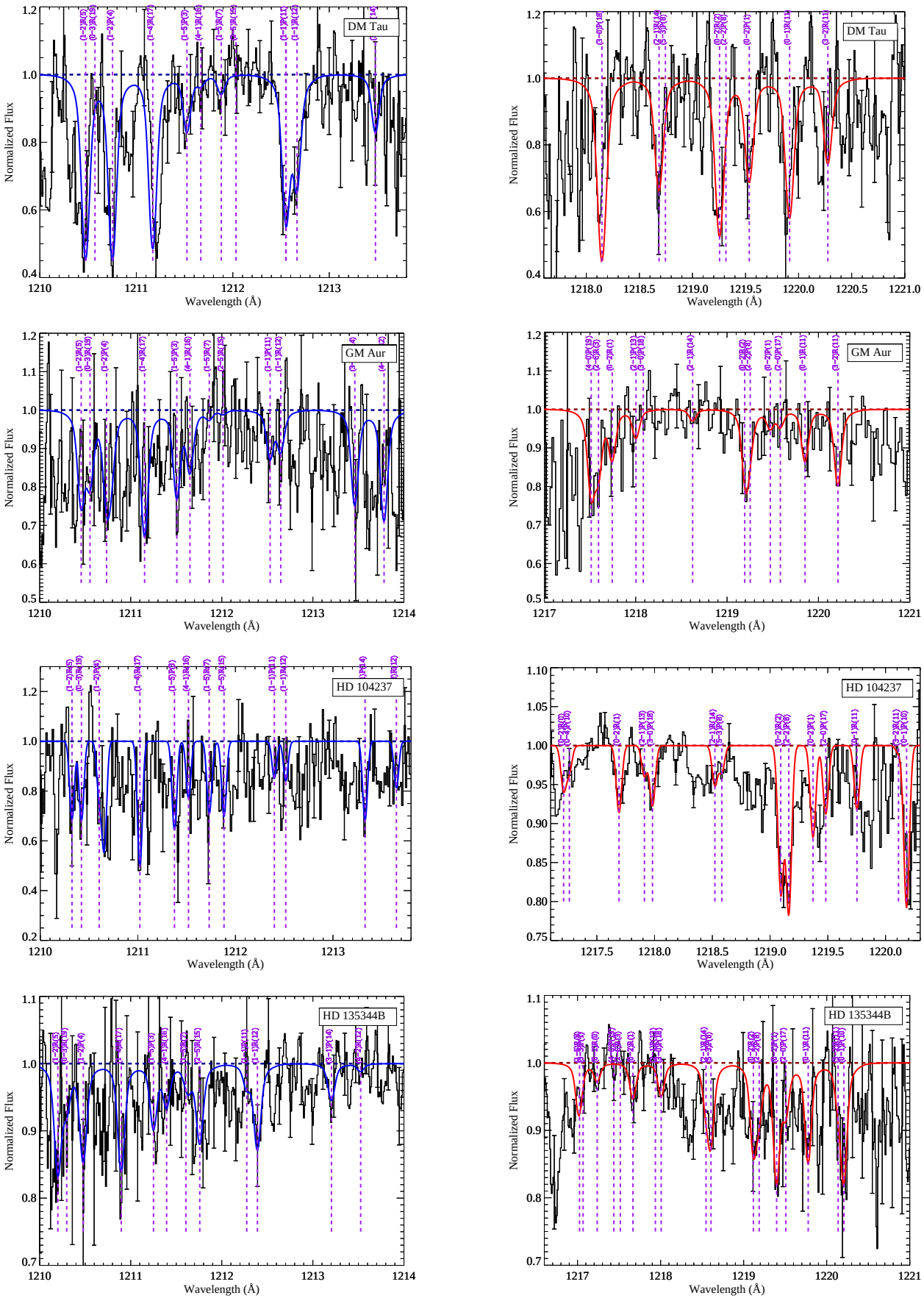

Figure C.1 Continued...

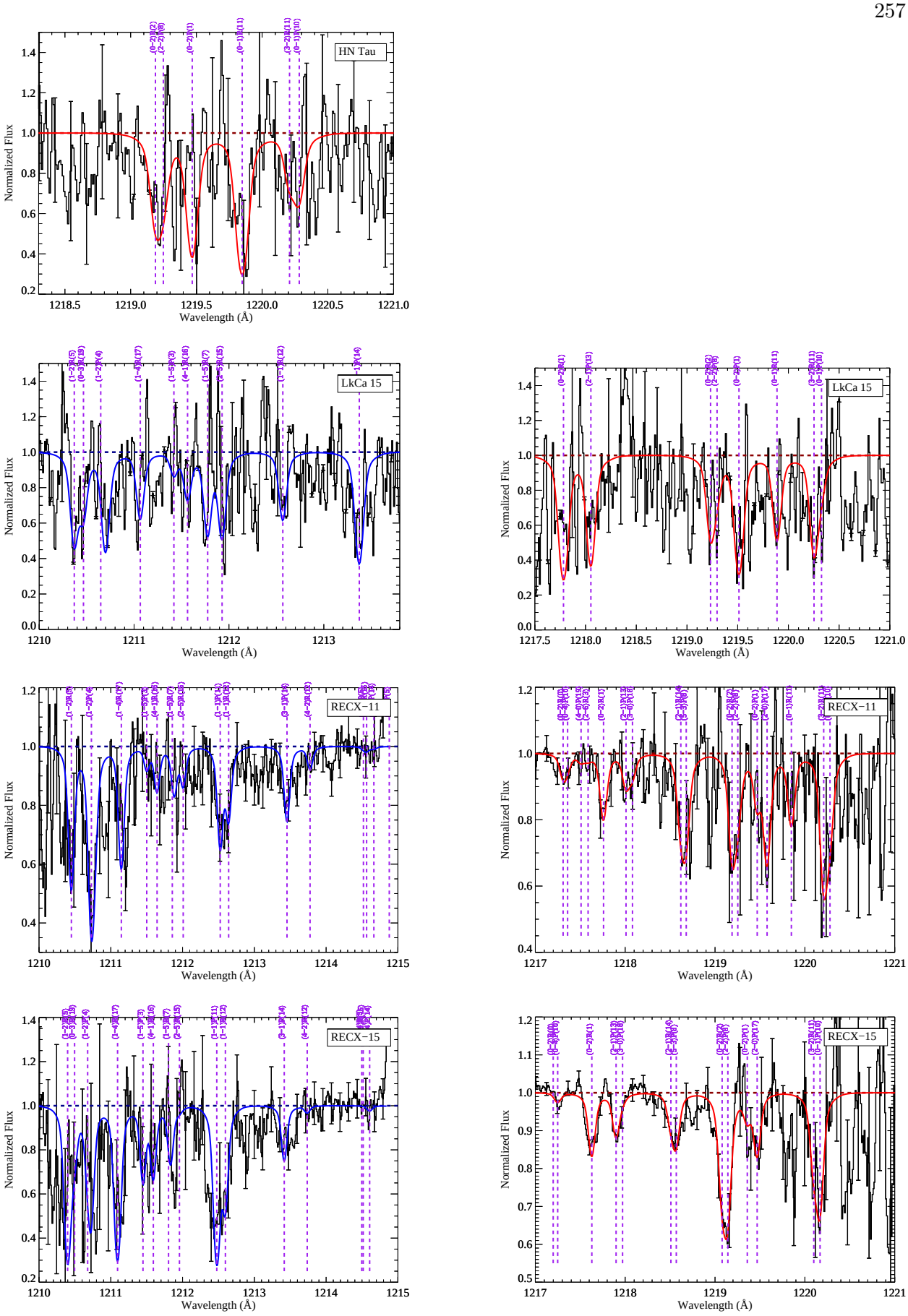

Figure C.1 Continued...

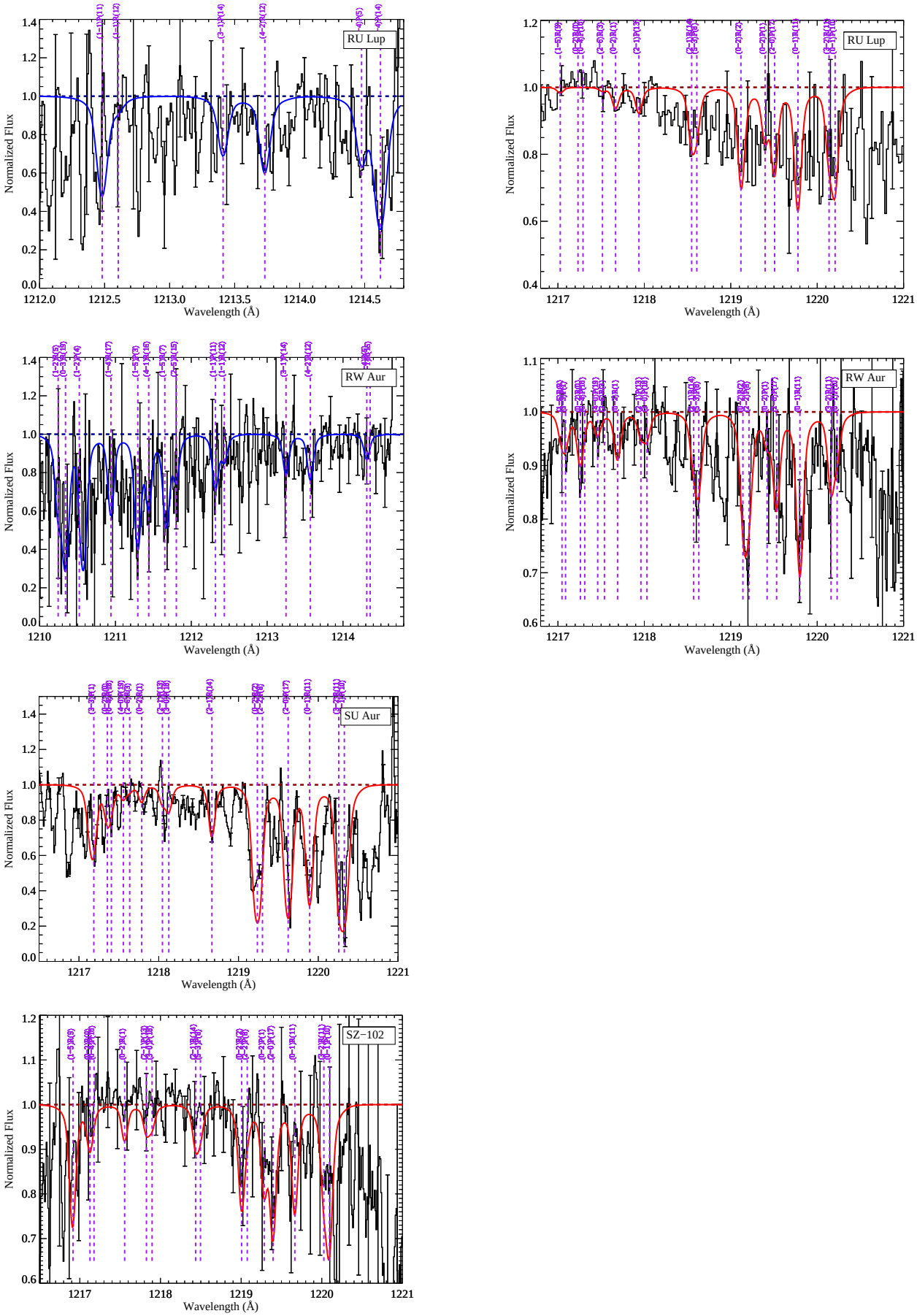

Figure C.1 Continued...

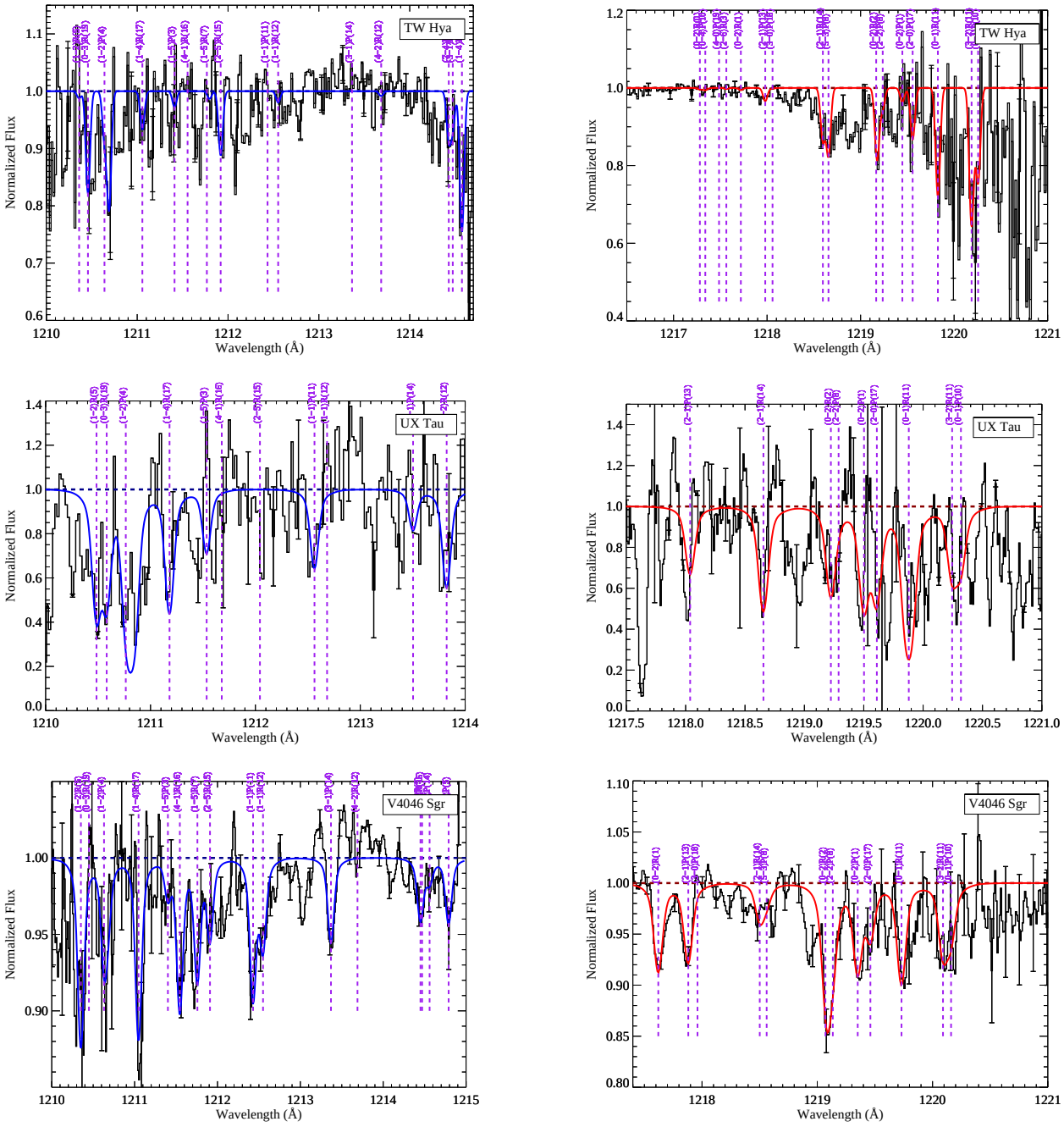

Figure C.1 Continued...

Appendix D

Supplemental Material: Chapter 3 - H_2 Model Details and Monte Carlo Simulations

D.0.1 Models 1 & 2: Thermal H_2 Populations only

Models 1 and 2 are simple models that follow the `H2ools` layout: Given the derived column densities for observed H_2 ground states against the stellar Lyα wing N(H_2;v,J), we use first principles molecular physics to determine the theoretical population column densities of a bulk H_2 population N(H_2) described by a shared thermal profile T(H_2). The level column densities are calculated using Boltzmann populations, assuming LTE conditions, and each ground state energy level is determined by calculating the electronic, vibrational, and rotational energy levels for a ground state [v,J], as described in McCandliss (2003).

Model 1 assumes that all data points extracted from the absorption features of each target are thermally-populated. Model 2 assumes only H_2 populations with ground state energies $E_{gr} <$ 1.5 eV ($T_{exc} \lesssim$ 17500 K) are thermally-populated, with the possibility that H_2 in ground states with $E_{gr} >$ 1.5 eV are pumped additionally by some unknown non-thermal process(es), and so are not considered in the model-data comparison. We use Model 2 as a baseline of the minimum N(H_2) and T(H_2) of thermal H_2 in the disk atmosphere for each target, assuming any of the observed, absorbing H_2 against the Lyα wing is purely thermally excited.

Figure D.1 shows an example of how the relative [v,J] states are populated by the thermal distribution of H_2. While the total column density of H_2 regulates the column densities of H_2 found in ground state [v,J], T(H_2) determines the relative abundances of each [v,J] to others in

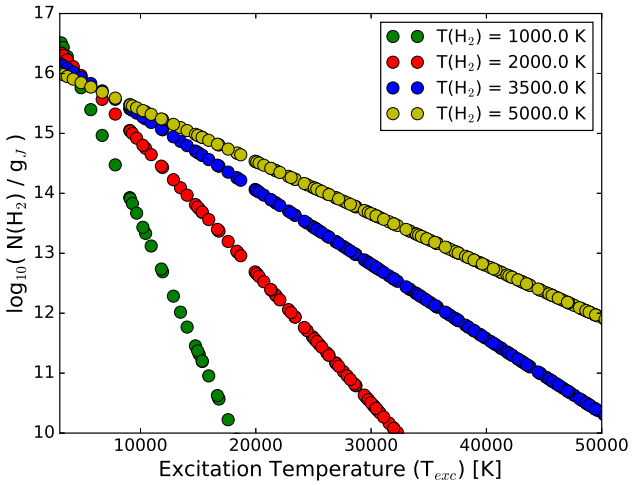

Figure D.1 Modeled rotation diagram of H_2 populations found in thermal equilibrium with a set $N(H_2) = 10^{17}$ cm^{-2} and varying thermal descriptions $T(H_2)$. As $T(H_2)$ increases, more H_2 populations with higher excitation temperatures, T_{exc}, become populated, increasing the relative ratio of higher T_{exc} state to lower T_{exc} states, which decreases the slope of the distribution towards zero. This model is used to compare the observed rotation profiles of H_2 to thermally-populated states of H_2 for Models 1 and 2.

the ground state. For example, a lower T(H_2) means that, statistically, more H_2 is found in ground states with low [v,J] because the overall excess energy in the H_2 populations is low. However, as T(H_2) increases, the ratio of the abundances of H_2 found in higher [v,J] states to those in low [v,J] states increases. This appears as a "flattening" of the slope of H_2 populations in Figure D.1.

D.1 MCMC Simulations

Each model is compared to the resulting rotation diagrams derived from the relative H_2 absorption column densities derived as explained in Section 3.3. This is done using a MCMC routine, which randomly-generates initial parameter conditions and minimizes the likelihood function ($\ln \mathcal{L}$(x,θ)) between the H_2 rovibration column densities and model parameters. We define $\ln \mathcal{L}$(x,θ) as a χ^2 statistic, with an additional term to explore the weight of standard deviations on each rovibrational column density:

$$\ln \mathcal{L}(\mathrm{x}, \theta, f) = \frac{(y(\mathrm{x}) - y(\mathrm{x}, \theta))^2}{\sigma^2} - \ln((\sigma^2 + y(\mathrm{x}, \theta)^2 \exp(2f))^{-1}) \tag{D.1}$$

In Equation D.1, x represents the ground state energy of H_2 in rovibration level [v,J], y(x) is the observed column density of H_2, y(x,θ) is the modeled column density of H_2 derived from the thermal model, σ^2 is the variance in the column densities, and f is an estimation on the accuracy of the column density standard deviations. For parameters shared between all thermal model runs (N(H_2), T(H_2), $\ln f$), we set prior information about each to keep the model outputs physically viable. We let the total thermal H_2 column density range from N(H_2) = 12.0 − 25.0 cm^{-2}. Below N(H_2) = 12.0 cm^{-2}, there is not enough column in individual rovibrational levels to produce measurable absorption features in the data. Additionally, N(H_2) $\geq$ 25.0 cm^{-2} will significantly saturate the features in the absorption spectra, which we do not see for any target in our survey. The thermal populations of H_2 are allowed to range from T(H_2) = 100 − 5000 K. The H_2 populations must be warm enough to populate the correct rovibrational levels that absorb Lyα photons, while simultaneously cooler than the dissociation temperature of H_2 (T$(H_2)_{diss} \approx$ 5000 K).

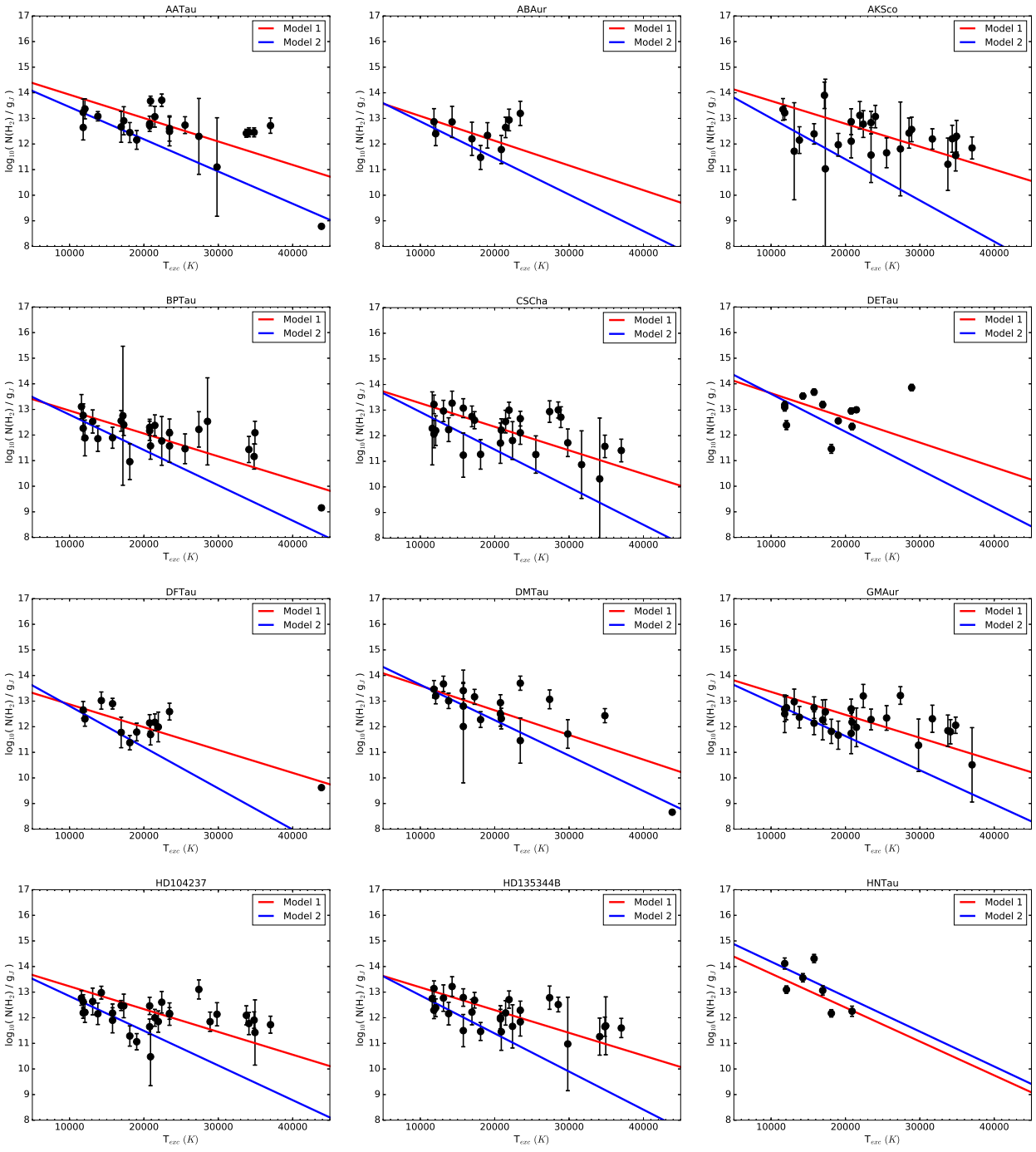

Figure D.2 All rotation diagrams are presented here. Each H_2 ground state column density is weighed by its statistical weight, g_J. Model 1 attempts to fit one thermally-populated bulk H_2 population through all data points extracted from the *HST* data sets. Model 2 does the same as Model 1, but only for H_2 states with lower energy ground states ($E_{gr} \leq 1.5$ eV; $T_{exc} \leq 17{,}500$ K).

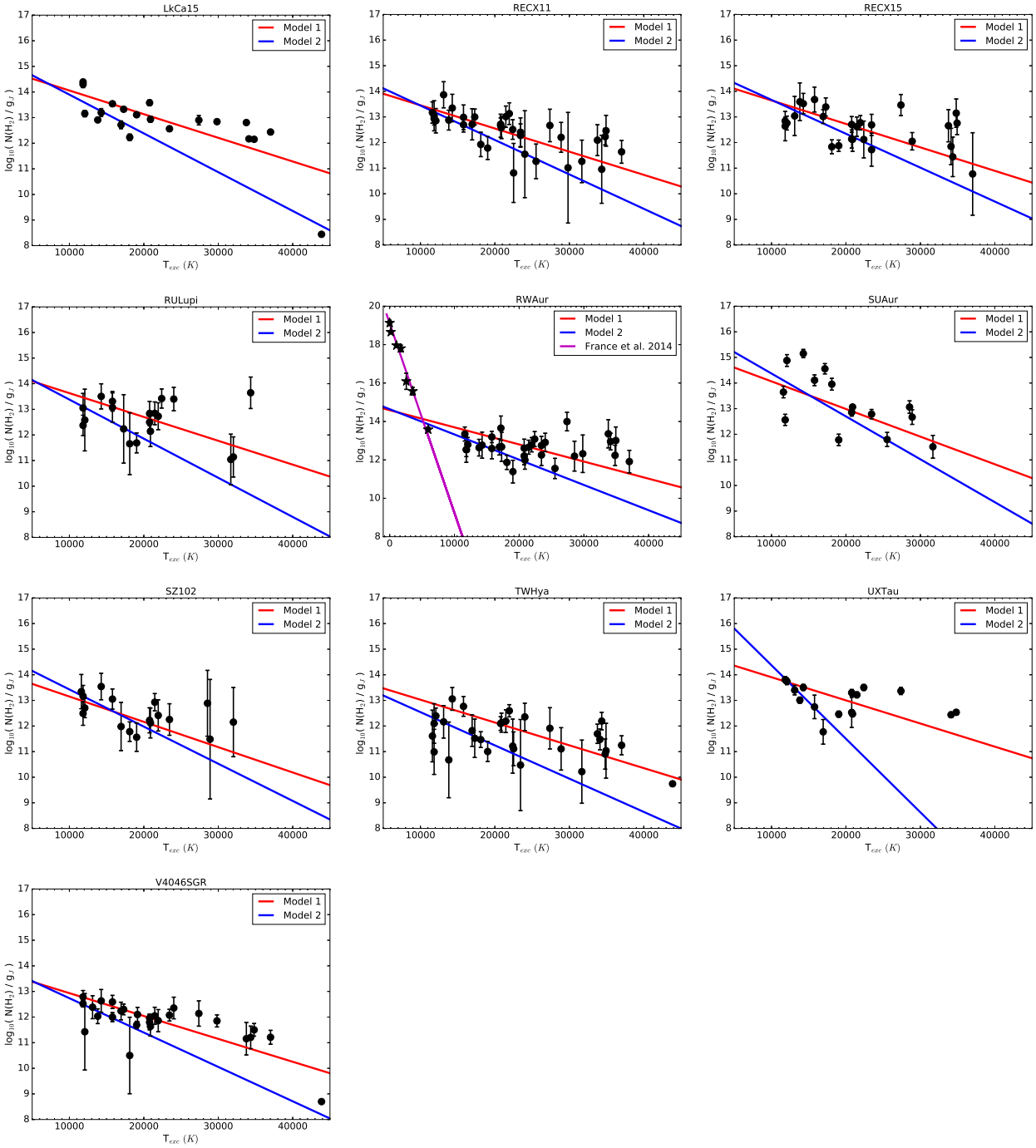

Figure D.2 Continued...

For Models 1 and 2, MCMC simulations were run with 300 independent initial randomly-generated parameter realizations (walkers) and allowed to vary over 1000 steps to converge on the best representation of the observations.

D.1.1 Model 3: Thermal H_2 Populations Photo-excited by HI-Lyα

Model 3 uses the same thermal populations of Models 1 and 2 and adds an additional photo-pumping mechanism to show how thermal populations reach an equilibrium state in the presence of an external radiation field. First, because we observe H_2 absorption against the Lyα wings of these targets and Lyα radiation makes up the vast majority of the FUV radiation that photo-excited H_2 to fluorescence, we assume the radiation pumping the thermal states to new equilibrium populations is dominated by Lyα. To describe the amount of radiation being absorbed by H_2, we add two additional parameters that describe the flux input to the system, $F_n(\lambda)$ and $F_b(\lambda)$, which represent a narrow and broad flux component from the stellar Lyα radiation incident on the H_2 populations. Following the results and analysis from McJunkin et al. (2014), we assume the Lyα radiation profile incident with the H_2 on the disk surface is described by two Gaussian components - a narrow component, where the bilk of the flux is located, and a broad component, which describes the shape of the observed outer wings. McJunkin et al. (2014) find full width at half maximum (FWHM) fits for both the narrow and broad Gaussian components of the radiation distribution, and we use those results to describe the width of our input flux. We allow the peak fluxes of both the narrow and broad flux distributions to vary and have final input Lyα flux distributions described by:

$$\begin{aligned} F_{\mathrm{Ly}\alpha}(\lambda) &= F_n(\lambda) + F_b(\lambda) \\ &= F_n \exp\left(\frac{-\Delta\lambda^2}{2\sigma_n^2}\right) + F_b \exp\left(\frac{-\Delta\lambda^2}{2\sigma_b^2}\right), \end{aligned} \tag{D.2}$$

where F_n and F_b are free parameters in the models, and σ_n and σ_b are derived from the FWHM found in McJunkin et al. (2014), and $\Delta\lambda = \lambda - \lambda_{lab}$, where λ_{lab} is the rest wavelength of HI-Lyα (1215.67 Å). Each flux distribution is kept constant throughout the model run, assuming the output

radiation from the star over the time it takes to equalize the photo-pumped populations of H_2 is isotropic. We assume $F_n(\lambda)$ and $F_b(\lambda)$ are observed flux rates, and we therefore infer the flux back to the star by reddening the flux with ISM extinction values determined by McJunkin et al. (2014). The allowed ranges of observed total Lyα flux are outlined in Schindhelm et al. (2012b) for reconstructed Lyα profiles seen in at the PPDs. We constrain the Lyα flux to $\log_{10}(F_n(\lambda))$ = -13 to -5 ergs cm^{-2} s^{-1} and $\log_{10}(F_b(\lambda))$ = -16 to -5 ergs cm^{-2} s^{-1}, which are integrated over each Gaussian function in Equation D.2.

Once flux and thermal H_2 population parameters are chosen, we follow the change in thermal populations in states [v,J] of H_2 being exposed to the pumping radiation in time iterations of the pumping process, t_{step}, where each t_{step} is considered over some arbitrary Δt. First, we find how much H_2 in state [v,J] is lost to be pumped to some electronic excited state [v',J'] because of the interaction with a discrete Lyα photon with wavelength λ. We determine how much H_2 is photo-excited by λ by calculating the cross section for absorption of photon λ, given the transition probabilities of the H_2 rovibration levels. Once all [v,J] state losses via λ absorption have been determined, we allow the excited state H_2 to fluoresce back to the ground state via the branching ratios, or transition probabilities, to some final ground state [v'',J''].

For this simple model, we assume that dissociation of H_2 molecules by Lyα-pumping is negligible. As Dalgarno and Stephens (1970) describe, nearly all Lyα-pumped excited states have bound de-exciation levels, such that transitions from the Lyman band are expected to have very low probabilities of dissociation. While there exist a handful of Werner-band transitions, which likely prose the greatest probability for molecular dissociation upon decay, this simple model does not contain a source term of H_2, such that we cannot control the formation of H_2 at any point in the model. To keep the modeled distributions of H_2 constant throughout the simulated experiment, therefore, we assume that all H_2 transitions result only in the decay of H_2 to arbitrary ground states, with no probability that H_2 dissociates via these fluorescence routes.

This process is repeated until the H_2 populations reach a steady-state equilibrium, such that the absorption out of state [v,J] equalizes with the cascade back to [v'',J'']. For T(H_2) $\leq$ 5000 K,

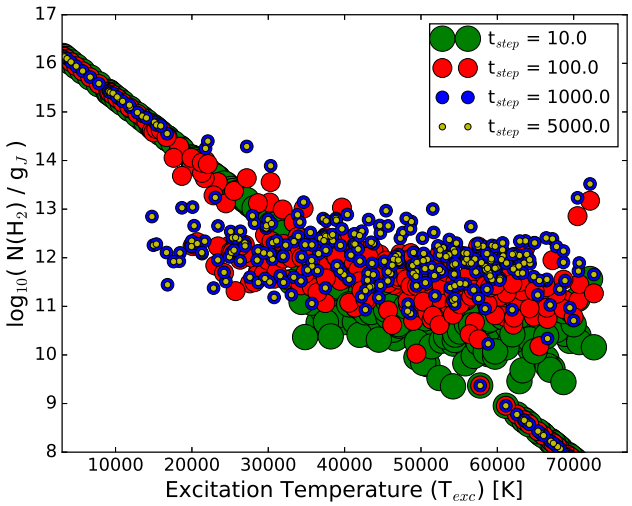

Figure D.3 Modeled thermal distributions of H_2 with N(H_2) = 10^{17} cm^{-2} and T(H_2) = 4500 K, assuming thermal populations of H_2 are constantly photo-excited by an external HI-Lyα radiation field to an equilibrium state. The Lyα radiation field is assumed to be Gaussian in shape when interacting with H_2 molecules, with a peak flux of 10^{-9} ergs cm^{-2} s^{-1} at 1215.67 Å. We show how the number of iterations of time the H_2 is exposed to the Lyα flux affects the distribution of H_2 ground states. We find that iterations t$_{step}$ = 1000 reaches a final equilibrium state. The thermal distribution + Lyα pumping mechanics are used to calculate theoretical H_2 populations in Model 3.

this equilibrium is reached by $t_{step} = 1000$. With higher $N(H_2)$, we find that it takes more t_{step} to reach equilibrium, but for $N(H_2) < 10^{20}$ cm^{-2} and high $T(H_2)$, an equilibrium state is reached after $t_{step} \approx 3000$ steps. Figure D.3 shows how the distributions of thermal H_2 populations change when exposed to a constant Lyα flux from the host star, as a function of time steps from first exposure. If we assume the distributions of H_2 ground states are primarily affected by photo-pumping via Lyα photons and no other physical mechanisms to drive the populations to non-LTE states (collisions with other species, chemical evolution, etc), then equilibrium of H_2 states is reached fairly quickly and does not change from the final equilibrium state of populations.

We perform the same MCMC data-model reduction for Model 3 and the observed rotation diagrams. Model 3 required time iterations and, therefore, took longer to run. We ran two separate iteration of Model 3, the first MCMC simulation having 100 independent walkers varying over the parameter space iterating over 2000 steps with 1000 time iterations of the Lyα-pumping. We determined that, after about 100 converging steps for each walker, we were able to settle into the best realization of the data. We also determined that longer time iterations were necessary to settle the Lyα-pumping mechanism into equilibrium for larger column densities ($N(H_2) > 10^{20}$ cm^{-2}) and temperatures ($T(H_2) > 4500$ K). We ran a second iteration of MCMC simulations for Model 3 using $t_{step} = 5000$ per model realization, with 100 independent MCMC walkers iterating over 500 steps to convergence. Because of the extensive computation time of Model 3 with 5000 time steps per model realization, we chose to cut the total number of convergence steps to keep the same number of walker realizations in the MCMC.

Table 3.5 presents parameter results for all modeled H_2 thermal distributions. For all Model 3 realizations, $F_b(\lambda)$ has been excluded, since the majority of the integrated flux of Lyα is dominated by $F_n(\lambda)$ ($F_n(\lambda) >> F_b(\lambda)$). Figure D.4 shows the best-fit, median model parameters for Model 3 with observed rovibration H_2 levels plotted with the data. We mark each modeled rovibration level with a green plus symbol, and we mark modeled rovibration levels which are probed in the observed Lyα wing(s) of the target with cyan crosses.

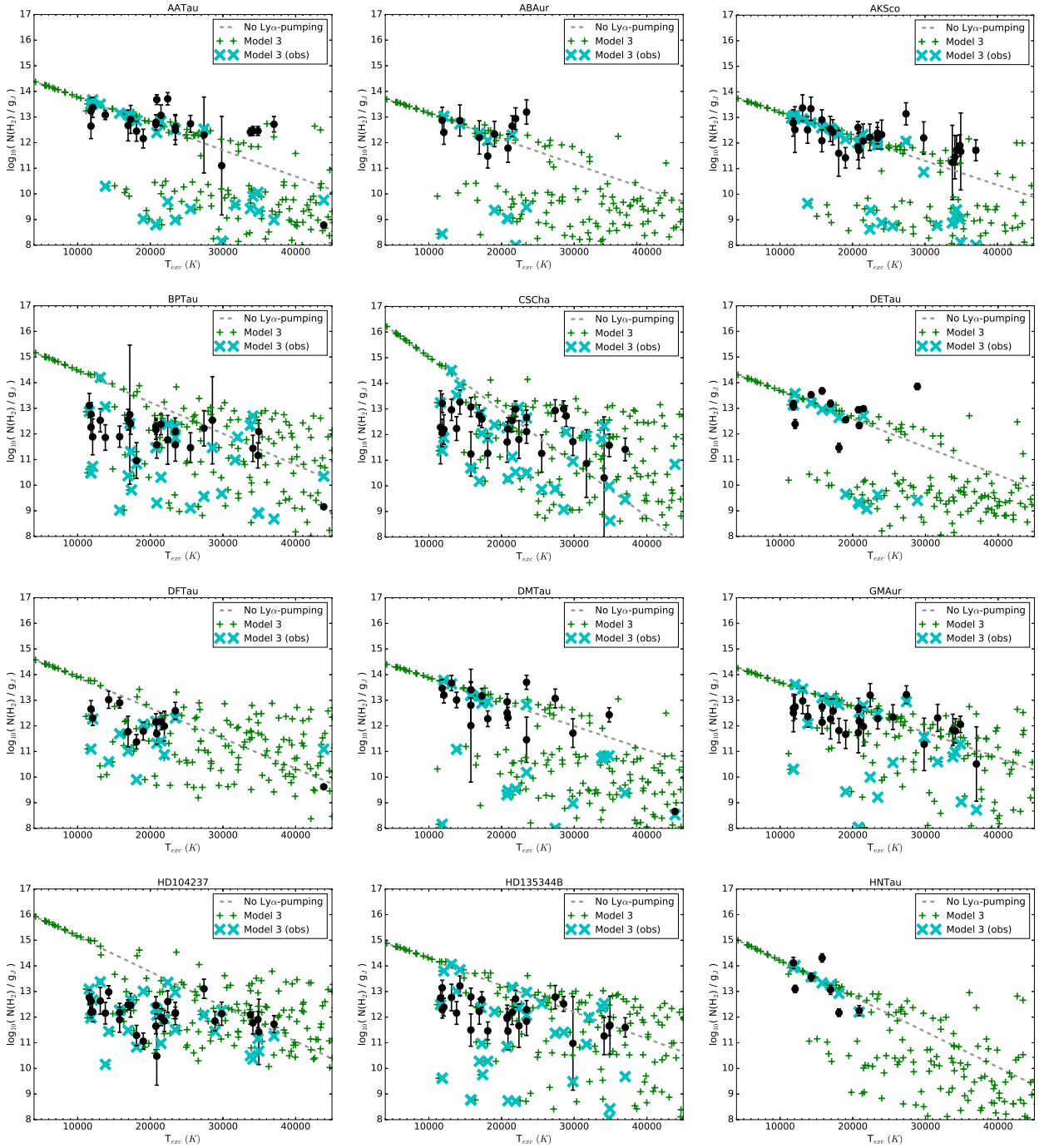

Figure D.4 All rotation diagrams are presented here. Each H_2 ground state column density is weighed by its statistical weight, g_J. Model 3 takes a thermally-populated H_2 population and photo-excites it with Lyα photons to re-distribute the states, based on the photon flux and H_2 states responsive to Lyα radiation. Green plus symbols represent all rovibrational H_2 level rotation-weighed column densities, after radiative equilibrium has been reached for the initial thermal distribution of molecules and radiative flux of Lyα. We mark modeled rovibration levels that are probed in the observations with cyan crosses.

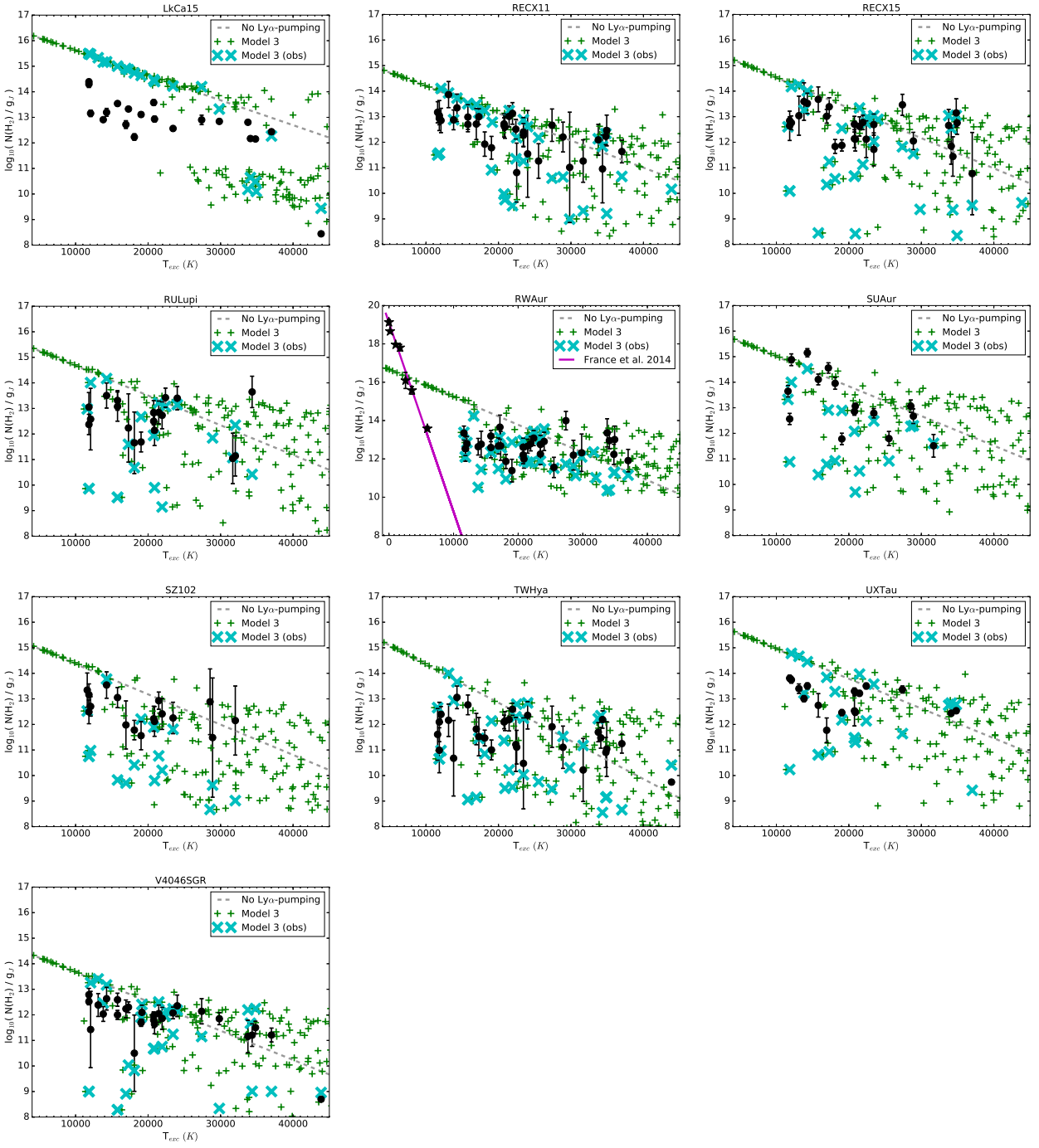

Figure D.4 Continued...